UNIVERSITÀ POLITECNICA DELLE MARCHE

DOCTORAL THESIS

Biophysical and toxicological properties of rhamnolipids as potential agents in bioremediation processes

PhD Student
Benedetta Come

Tutor:
Prof. Francesco Spinozzi

Co-tutor:

Prof. Paolo Mariani
Prof.ssa Rosangela Itri

Department of Life and Environmental Sciences (DiSVA)

XXXI cycle

Ancona, 2017-2018

Ai miei genitori che hanno sempre creduto in me,
che mi hanno fatto vedere la luce anche quando era tutto buio.

"The scientist is not the man who provides the true answers; that's what asks the real questions ".

(Claude Lévi-Strauss)

Content

Declaration of Authorship

I, Benedetta Come, declare that this thesis titled “Biophysical and toxicological properties of rhamnolipids as potential agents in bioremediation processes” and the work presented it are my own and has been generated by me as the result of my own original research.

I confirm that:

- This work was done wholly or mainly while in candidature for a research degree at this University;
- where any part of this thesis has previously been submitted for a degree or any other qualification at the University or any other institution, this has been clearly stated;
- where I have consulted the published work of others, this is always clearly attributed;
- where I have quoted from the work of others, the source is always given. With the exception of such
- quotations, this thesis is entirely my own work;
- where the thesis is based on work done by myself jointly with others, I have made clear exactly what done by others and what I have contributed myself.

Abstract

This thesis reports the study of a particular class of natural surfactants, the RLs, to be used in bioremediation processes, especially in the petroleum industry. The case study of this thesis stems from a very important and frequent problem in the last decades, namely the environmental pollution of water and soils by hydrocarbons, petrochemical products and their derivatives. Rhamnolipids are a class of glycolipids produced by Pseudomonas aeruginosa (Desai & Banat, 1997a). RLs have been starting to became relevant for bioremediation, a waste management technique that involves the use of organisms to neutralize pollutants from a contaminated site. The low solubility and adsorption are two major properties of high molecular weight hydrocarbons, which limit their availability to microorganisms. For this reason, the addition of surfactants enhances the solubility and removal of those contaminants (De Cássia et al., 2014). It has also been demonstrated that the addition of biosurfactants into the soil may improve the bioremediation rates and they are promising due to their biodegradability, low toxicity (Mulligan, 2005a).

The first part of my thesis focuses on the physical chemical characterization of ramnolipids through techniques such as dynamic light scattering and X-ray diffraction. Subsequently we have conducted toxicity tests through interaction with model membrane systems by testing different surfactant concentrations. We have initially used a class of liposomes: GUVs, giant unilamellar vesicles, prepared by varying their lipid composition and by the electroforming method. Then we have used the erythrocytes and analyzed the effect by spectrophotometric analysis and by an optical microscope evaluating their lysis and their morphological change. Finally we have analyzed their toxicity on HaCat cells, spontaneously transformed aneuploid immortal keratinocyte cell line from adult human skin (Boukamp et al., 1988a).

The final part of my thesis project focuses on the analysis of the structure assumed by single rhamnolipid molecules in diluted conditions. The tests were carried out on pure water and on water with precise salt concentrations in order to get closer and closer to the model of brackish water. To evaluate the effect of this biosurfactant on the hydrocarbons, different concentrations of oil (kirkuk oil) have also been added. This last part of the research was carried out using the SAXS (Small-Angle X-ray Scattering) technique in various European and extra-European synchrotrons (ELETTRA, Trieste; ESRF, Grenoble; LNLS, Campinas, Brazil) obtaining

information on the structural parameters, stability, counter-ion effects and interactions between the different molecules of rhamnolipids in different conditions.

List of Abbreviations

CMC: Critical Micellar Concentration

EOR: Enhanced Oil Recovery

ESI: Electrospray Ionisation

GUV: Giant Unilamellar Vesicle

ITO: Indium Tin Oxide

KC: Keratinocyte

IMPS: Infinite Periodic Minimal Surface

IFT: Interfacial Tension

LUV: Large Unilamellar Vesicle

MIC: Minimum Inhibitory Concentration

MLV: Multilamellar Vesicle

MDR: Multidrug-Resistant

NAPL: Non-aqueous phase liquids

OM: Optical Microscopy

PAH: Polycyclic Aromatic Hydrocarbons

POM: Polarized Optical Microscopy

RBC: Red Blood Cell

RL: Rhamnolipid

SAN: Self-Assembled Nanomaterials

SAS: Small-Angle Scattering

SAXS: Small Angle X-ray Scattering

ST: Surface Tension

SUV: Small Unilamellar Vesicle

TIRF: Total Internal Reflection Fluorescence Microscope

TM: Melting Temperature

TC: Critical Temperature

XRD: X-Ray Diffraction

List of Figures

Chapter 1

Introduction

1.1 Bioremediation

Bioremediation is a process that uses naturally occurring microorganisms (yeast, fungi, or bacteria) to break down, or degrade, hazardous substances into less toxic or nontoxic substances. Microorganisms eat and digest organic substances for nutrition and energy purposes. In chemical terms, "organic" compounds are those that contain carbon and hydrogen atoms. Certain microorganisms can digest organic substances such as fuels or solvents that are hazardous to humans. Such microorganisms break down the organic contaminants and transform them in harmless products mainly carbon dioxide and water (Figure 1.1). Once the contaminants are degraded, the microorganism population is reduced because they have used all of their food source. Dead microorganisms or small populations in the absence of food pose no contamination risk.

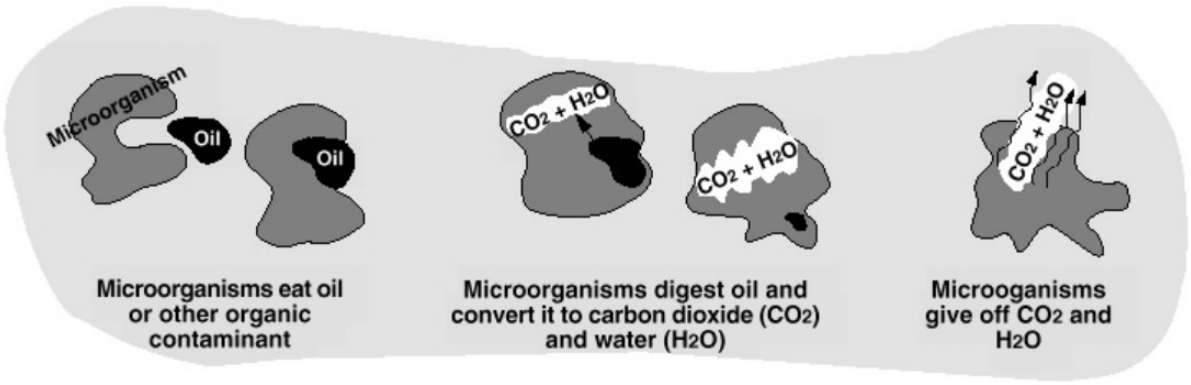

Figure 1.1: Schematic Diagram of Aerobic Biodegradation in Soil

Bioremediation processes are a series of techniques developed as a result of environmental disasters that have caused a lot of damage to the environment.

1.2 Black tides: the 10 worst oil disasters in history

The environmental disaster caused by the explosion and sinking of the Deepwater Horizon oil rig in the Gulf of Mexico is just the latest in a long series of episodes that, starring oil, have held the world in suspense and threatened or upset whole ecosystems. The following are the 10 most serious accidents in terms of quantity of crude oil dispersed in the environment, bearing in mind that, in cases like these, it is always very difficult to make precise estimates.

1. Gulf War, Persian Gulf, 1991

On January 21st, 1991, during the first Gulf War, a very serious oil spill occurs in the Persian Gulf: soon it will be discovered that the Iraqi army deliberately opened the valves of the oil pipelines in Kuwait, in order to prevent or at least to hinder the landing of American soldiers. The oil spill affected the coasts of Kuwait, Saudi Arabia and Iran, causing heavy damage to the ecosystems of those regions. According to the estimates by analysts and researchers, the amount of oil dispersed in the environment on this occasion would have been between 1.36 and 1.5 millions of tons.

2. Ixtoc I, Campeche Bay, Gulf of Mexico, 1979-1980

On June 3rd, 1979, the Mexican oil rig Ixtoc I was engaged in some exploration operations in the Gulf of Mexico, 600 miles from the Texas coast. For an error in the maneuvers, the platform catches fire and begins to disperse oil at sea: the loss, which went on for 9 months, until March 23, 1980, was between 0.454 and 0.480 millions of tons.

3. Nowruz, Persian Gulf, 1983

On February 10th, 1983, a tanker collided with the Nowruz oil platform in the Persian Gulf, a short distance from the Iranian coast. The collision took place during the Iran-Iraq war and caused a first oil spill that was exacerbated, about a month later, by the Iraqi aviation attack.

The bombing caused a fire of large proportions. The loss of crude oil was arrested only a few months later, in September 1983: it has been estimated that in this very long span about 0.3 millions of tons of oil was dispersed in the waters of the Persian Gulf.

4. Atlantic Empress - Aegean Captain, Trinidad and Tobago, 1979

On July 19th, 1979, during a tropical storm, the Greek tanker Atlantic Empress clashed with the Aegean Captain off Trinidad and Tobago. Both boats report very serious damage, releasing a good 0.287 millions of tons of oil at sea.

5. Fergana Valley, Uzbekistan, 1992

An environmental disaster less known but of enormous proportions was the accident that on March 2nd,1992, provoked the dispersion of about 0.285 millions of tons of crude oil in the Fergana Valley, in Uzbekistan. The Fergana Valley is a region with a predominantly agricultural economy, but rich in oil and gas deposits, so much so that it has been subjected to drilling for extraction purposes since the early twentieth century. It was during this ordinary mining activity that the loss occurs, probably due to a failure of a extraction machine.

6. ABT Summer, Angola, 1991

In May 1991 a violent explosion occurred on board the Liberian tanker Abt Summer, sailing off the coast of Angola. The blast killed some members of the crew and causes a terrible fire: the boat burned for three days before sinking and disperses in the Atlantic Ocean about 0.260 millions of tons of oil.

7. Castillo de Beliver, Saldanha Bay, South Africa, 1983

On August 6th, 1983, the Spanish oil tanker Castillo de Beliver caught fire while sailing off South Africa. The fire followed a violent explosion, which caused the sinking of the boat. The accident caused the spillage of about 0.227 millions of tons of crude into the sea.

8. Amoco Cadiz Brittany, France, 1978

On March 16th, 1978, Amoco Cadiz, a 330-meter Liberian super-tanker headed by the American company Amoco, crashed off the Breton coast, facing the coast of the small village of Portsall. The accident caused the dispersion of about 0.223 millions of tons of crude into the sea and affected about 150 km of coastline, with considerable damage to local ecosystems and in particular marine fauna.

9. Amoco Haven, Genoa, Italy, 1991

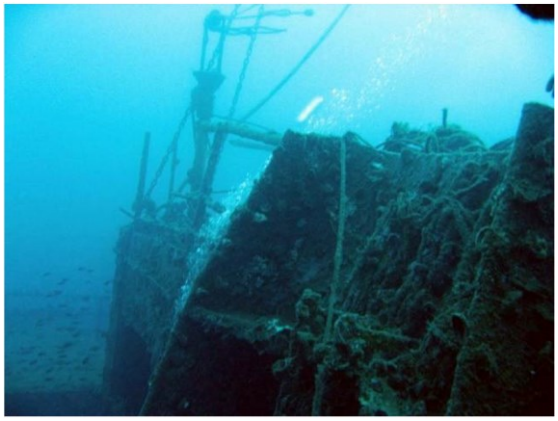

In April 1991, the Cypriot tanker Amoco Milford Haven, also known as M / C Haven, sinked into the Gulf of Genoa, probably due to an explosion that occurred during a routine procedure. The accident caused the deaths of some crew members and the spillage of about 0.144 millions of tons of crude into the sea. Today, the wreck of the M / C Haven lies about 80 meters deep in the waters in front of the Municipality of Arenzano and is the largest "visitable" wreck of the entire Mediterranean sea.

10. Odyssey, Nova Scotia, Canada, 1988

In November 1988, on the American drilling platform Odyssey, off the east coast of Canada, there was a violent explosion. The accident caused the spillage of about 0.132 millions of tons of oil into the sea.

All the 10 episodes we have mentioned had serious consequences on the surrounding environment, and in particular on the atmosphere and marine fauna. Just like the infamous Exxon Valdez oil tanker, which in March 1989 ran around in the waters of Prince William Strait, Alaska, dispersing about 0.038 million tons of crude oil into the sea.

1.3 Bioremediation processes

Microorganisms should be active and healthy in order for bioremediation to take place. Bioremediation technologies assist microorganisms' growth and increase microbial populations by creating optimum environmental conditions for them to detoxify the maximum amount of contaminants. The specific bioremediation technology to be used is determined by several factors, such as the species of microorganisms present, the site conditions and the quantity and toxicity of contaminant chemicals. Different microorganisms degrade different types of compounds and survive under different conditions. Bioremediation can be used as a cleanup method for contaminated soil and water.

Indigenous microorganisms are those microorganisms that are found already living at a given site. To stimulate the growth of these indigenous microorganisms, the proper soil temperature, oxygen, and nutrient content may need to be provided.

If the biological activity needed to degrade a particular contaminant is not present in the soil at the site, microorganisms from other locations, whose effectiveness has been tested, can be added to the contaminated soil. These are called *exogenous* microorganisms. The soil conditions at the new site may need to be adjusted to ensure that the exogenous microorganisms will thrive. Bioremediation can take place under *aerobic* and *anaerobic* conditions. In aerobic conditions, microorganisms use available atmospheric oxygen for their needs. With sufficient oxygen, microorganisms will convert many organic contaminants to carbon dioxide and water. *Anaerobic* conditions support biological activity in which no oxygen is present so themicroorganisms break down chemical compounds in the soil to release the energy they need. Sometimes, during aerobic and anaerobic processes of breaking down the original

contaminants, intermediate products that are less, equally, or more toxic than the original contaminants are created.

Bioremediation can be used as a cleanup method for contaminated soil and water. Bioremediation applications fall into two broad categories: *in situ* or *ex situ*. In situ bioremediation treats the contaminated soil or groundwater in the location in which it was found. Ex situ bioremediation processes require excavation of contaminated soil or pumping of groundwater before they can be treated.

1.3.1 In Situ Bioremediation of Soil

In situ techniques do not require excavation of the contaminated soils so may be less expensive, create less dust, and cause less release of contaminants than ex situ techniques. Also, it is possible to treat a large volume of soil at once. In situ techniques, however, may be slower than ex situ techniques, may be difficult to manage, and are most effective at sites with *permeable* (sandy or uncompacted) soil.

The goal of aerobic in situ bioremediation is to supply oxygen and nutrients to the microorganisms in the soil. Aerobic in situ techniques can vary in the way they supply oxygen to the organisms that degrade the contaminants. Two of methods are bioventing and injection of hydrogen peroxide**.** Oxygen can be provided by pumping air into the soil above the water table (bioventing) or by delivering the oxygen in liquid form as hydrogen peroxide. In situ bioremediation may not work well in clays or in highly layered subsurface environments because oxygen cannot be evenly distributed throughout the treatment area. In situ remediation often requires years to reach cleanup goals, depending mainly on how biodegradable specific contaminants are. Less time may be required with easily degraded contaminants.

***Bioventing*.** Bioventing systems deliver air from the atmosphere into the soil above the water table through injection wells placed in the ground where the contamination exists. The number, location, and depth of the wells depend on many geological factors and engineering considerations.

An air blower may be used to push or pull air into the soil through the injection wells. Air flows through the soil and the oxygen in it is used by the microorganisms. Nutrients may be pumped into the soil through the injection wells. Nitrogen and phosphorous may be added to increase the growth rate of the microorganisms.

Injection of Hydrogen Peroxide. This process delivers oxygen to stimulate the activity of naturally occurring microorganisms by circulating hydrogen peroxide through contaminated soils to speed the bioremediation of organic contaminants. Since it involves putting a chemical (hydrogen peroxide) into the ground (which may eventually seep into the groundwater), this process is used only at sites where the groundwater is already contaminated. A system of pipes or a sprinkler system is typically used to deliver hydrogen peroxide to shallow contaminated soils. Injection wells are used for deeper contaminated soils.

1.3.2 In Situ Bioremediation of Groundwater

In situ bioremediation of groundwater speeds the natural biodegradation processes that take place in the water-soaked underground region that lies below the water table. For sites at which both the soil and groundwater are contaminated, this single technology is effective at treating both.

Generally, an in situ groundwater bioremediation system consists of an extraction well to remove groundwater from the ground, an above-ground water treatment system where nutrients and an oxygen source may be added to the contaminated groundwater, and injection wells to return the "conditioned" groundwater to the subsurface where the microorganisms degrade the contaminants.

One limitation of this technology is that differences in underground soil layering and density may cause reinjected conditioned groundwater to follow certain preferred flow paths. Consequently, the conditioned water may not reach some areas of contamination.

Another frequently used method of in situ groundwater treatment is air sparging, which means pumping air into the groundwater to help flush out contaminants. Air sparging is used in conjunction with a technology called soil vapor extraction and is described in detail in the document entitled A Citizen's Guide to Soil Vapor Extraction and Air Sparging (see bottom of document).

1.3.3 Ex Situ Bioremediation of Soil

Ex situ techniques can be faster, easier to control, and used to treat a wider range of contaminants and soil types than in situ techniques. However, they require excavation and treatment of the contaminated soil before and, sometimes, after the actual bioremediation step. Ex situ techniques include slurry-phase bioremediation and solid-phase bioremediation.

Slurry-phase bioremediation.

Contaminated soil is combined with water and other additives in a large tank called a "bioreactor" and mixed to keep the microorganisms -- which are already present in the soil -- in contact with the contaminants in the soil. Nutrients and oxygen are added, and conditions in the bioreactor are controlled to create the optimum environment for the microorganisms to degrade the contaminants. Upon completion of the treatment, the water is removed from the solids, which disposed or treated further if they still contain pollutants.
Slurry-phase biological treatment can be a relatively rapid process compared to other biological treatment processes, particularly for contaminated clays. The success of the process is highly dependent on the specific soil and chemical properties of the contaminated material. This technology is particularly useful where rapid remediation is a high priority.

Solid-phase bioremediation.

Solid-phase bioremediation is a process that treats soils in above-ground treatment areas equipped with collection systems to prevent any contaminant from escaping the treatment. Moisture, heat, nutrients, or oxygen are controlled to enhance biodegradation for the application of this treatment. Solid-phase systems are relatively simple to operate and maintain, require a large amount of space, and cleanups require more time to complete than with slurry-phase processes. Solid-phase soil treatment processes include landfarming, soil biopiles, and composting

Landfarming.

In this relatively simple treatment method, contaminated soils are excavated and spread on a pad with a built-in system to collect any "leachate" or contaminated liquids that seep out of contaminant soaked soil. The soils are periodically turned over to mix air into the waste. Moisture and nutrients are controlled to enhance bioremediation. The length of time for bioremediation to occur will be longer if nutrients, oxygen or temperature are not properly controlled. In some cases, reduction of contaminant concentrations actually may be attributed more to volatilization than biodegradation. When the process is conducted in enclosures controlling escaping volatile contaminants, volatilization losses are minimized.

Soil biopiles.

Contaminated soil is piled in heaps several meters high over an air distribution system. Aeration is provided by pulling air through the heap with a vacuum pump. Moisture and nutrient levels are maintained at levels that maximize bioremediation. The soil heaps can be placed in enclosures. Volatile contaminants are easily controlled since they are usually part of the air stream being pulled through the pile.

Composting.

Biodegradable waste is mixed with a bulking agent such as straw, hay, or corn cobs to make it easier to deliver the optimum levels of air and water to the microorganisms. Three common designs are static pile composting (compost is formed into piles and aerated with blowers or vacuum pumps), mechanically agitated in-vessel composting (compost is placed in a treatment vessel where it is mixed and aerated), and windrow composting (compost is placed in long piles known as windrows and periodically mixed by tractors or similar equipment).

Chapter 2

Surfactants and Biosurfactants: Rhamnolipids

2.1 Surfactant chemistry and general phase behaviour

The term colloid (which means "glue" in Greek) was first introduced in 1861 by Thomas Graham to describe the "pseudosolutions" in aqueous systems of silver chloride, sulfur, and Prussian blue which were prepared by Francesco Selmi in the mid-nineteenth century (Evans & Wennerström, 1999). Such systems were characterised by a lack of sedimentation under the influence of gravity, as well as low diffusion rates. Graham thus deduced that the colloidal size range is approximately 1 μm down to 1 nm (i.e., 10^{-6} – 10^{-9} m). This characteristic still holds today and colloids are generally described as systems consisting of one substance finely dispersed in another. These substances are referred to as the dispersed phase and dispersion medium (or continuous phase) respectively, and can be a solid, a liquid, or a gas. Such combinations together with large surface areas associated with the characteristic size of colloidal particles give rise to a large variety of systems, practical applications and interfacial phenomena.

Amongst these systems, the most common and ancient class is probably the lyophobic ("liquid-hating") colloids, composed of insoluble or immiscible components. They can be traced back to the 1850's when Michael Faraday prepared colloidal gold sols, which involve solid particles in water (Faraday, 1857). More commonly encountered examples of lyophobic colloids are milk (liquid fat dispersed as fine drops in an aqueous phase), smoke (solid particles dispersed in air), fog (small liquid droplets dispersed in air), paints (small solid particles dispersed in liquid), jelly (large protein molecules dispersed in water), and bone (small particles of calcium phosphate dispersed in a solid matrix of collagen). A second and more recent class includes the lyophilic ("liquid-loving") colloids, which are solutions that form spontaneously and are thermodynamically stable. These systems consist of solute molecules that are polymers (i.e., of much larger size than the solvent molecules), and as such form a large and distinct area of research (polymer science).

Another major group of colloidal systems, also classified as lyophilic, is that of the so-called association colloids. These are aggregates of amphiphilic (both "oil and water-loving") molecules that associate in a dynamic and thermodynamically driven process that may be simultaneously a molecular solution and a true colloidal system. Such molecules are commonly

termed “surfactants”, a contraction of the term surface-active agents. As will be introduced below and described in more detail in Chapter 2, surfactants are an important and versatile class of chemicals. Due to their dual nature, they are associated with many useful interfacial phenomena, e.g., wetting, and as such are found in many diverse industrial products and processes.

Surface-active agents are organic molecules that, when dissolved in a solvent at low concentration, have the ability to adsorb (or locate) at interfaces, thereby altering significantly the physical properties of those interfaces. The term “interface” is commonly employed here to describe the boundary in liquid/liquid, solid/liquid and gas/liquid systems, although in the latter case the term “surface” can also be used. This adsorption behaviour can be attributed to the solvent nature and to a chemical structure for surfactants that combine both a polar and a non-polar (amphiphilic) group into a single molecule. To accommodate for their dual nature, amphiphiles therefore “sit” at interfaces so that their lyophobic moiety keeps away from strong solvent interactions while the lyophilic part remains in solution. Since water is the most common solvent, and is the liquid of most academic and industrial interest, amphiphiles will be described with regard to their “hydrophilic” and “hydrophobic” moieties, or “head” and “tail” respectively.

Adsorption is associated with significant energetic changes since the free energy of a surfactant molecule located at the interface is lower than that of a molecule solubilised in either bulk phase. Accumulation of amphiphiles at the interface (liquid/liquid or gas/liquid) is therefore a spontaneous process and results in a decrease of the interfacial (surface) tension. However, such a definition applies to many substances: medium- or long-chain alcohols are surface active (e.g., n-hexanol, dodecanol) but these are not considered as surfactants. True surfactants are distinguished by an ability to form oriented monolayers at the interface (here air/water or oil/water) and, most importantly, self-assembly structures (micelles, vesicles) in bulk phases. They also stand out from the more general class of surface-active agents owing to emulsification, dispersion, wetting, foaming or detergency properties.

Both adsorption and aggregation phenomena result from the hydrophobic effect (Krimm, 1980); i.e., the expulsion of surfactant tails from water. Basically this originates from water−water intermolecular interactions being stronger than those between water−tail. Finally, another characteristic of surfactants, when their aqueous concentration exceeds approximately

40%, is an ability to form liquid crystalline phases (or lyotropic mesophases). These systems consist of extended aggregation of surfactant molecules into large organised structures.

Owing to such a versatile phase behaviour and diversity in colloidal structures, surfactants find application in many industrial processes, essentially where high surface areas, modification of the interfacial activity or stability of colloidal systems are required. The variety of surfactants and the synergism offered by mixed-surfactant systems also explains the ever-growing interest in fundamental studies and practical applications. Listing the various physical properties and associated uses of surfactants is beyond the scope of this chapter. However, a few relevant examples are presented in the following section, giving an idea of their widespread industrial use.

The surface activity of surfactants derives from their amphiphilic structure, meaning that their molecules contain both water soluble and water insoluble portions *(*West and Harwell, 1992*)*. The water solubility of the surfactants is due to the hydrophilic portion (polar group), while the hydrophobic portion (nonpolar chain) tends to concentrate at the air-water interfaces or in the center of micelles, reducing the surface tension of the solution *(*West and Harwell, 1992*;* Desai and Banat, 1997; Volkering et al., 1998*)*. Surfactants form aggregates or micelles; this ability confers certain properties such as emulsifying, foaming, dispersing, and the capacity to act as a detergent, making surfactants very versatile chemical compounds. They are applied in several industrial sectors such as the cosmetics, pharmaceuticals and food, petroleum, agrochemical and fertilizer industries, as it has been reviewed by Kosaric (1992), Deleu and Paquot (2004) and Banat et al. (2010).

Surfactants are characterized by properties such as critical micelle concentration (CMC), hydrophilic-lipophilic balance (HLB), chemical structure and charge, as well as properties from their origin source (Van Hamme et al., 2006). The surfactants exist as monomers or single.

molecules at low concentration in aqueous solutions; over the CMC, the surfactant molecules assemble together, forming aggregates. The CMC depends on surfactant structure, composition, temperature, ionic strength, and the presence and types of organic additives in the solutions (Fuget et al., 2005). At the CMC of surfactant solutions, a drastic change occurs in many physico-chemical properties (surface tension, conductivity, or turbidity) (Figure 2.1) (Hanna et al., 2005; Zana, 2005). Micelles are capable of dissolving hydrophobic contaminants in their hydrophobic core, which results in an increased apparent aqueous solubility of the pollutants (Edwards et al., 1991; Prak and Pritchard, 2002).

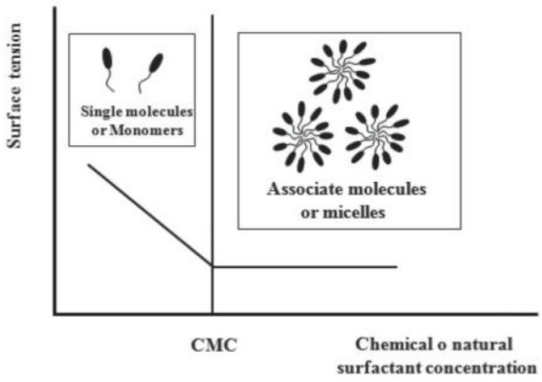

Figure 2.1: surface tension as a function of chemical or natural surfactant concentration, CMC represents critical micelle concentration (Patist et al., 2000; Whang et al., 2008).

The HLB number is also an important parameter of the surfactants, describing their physical properties and is specific for each surfactant. This number is determined by the relationship of the hydrophilic and the hydrophobic parts of the surfactant molecule (Tiehm, 1994). This indicates the types of oils that can emulsify them and can be also used to determine their suitability for use. Surfactants with a low HLB are lipophilic where- as a high HLB is indicative of better water solubility (West and Harwell, 1992; Tiehm, 1994). In terms of the hydrophilic portion, surfactants are classified as anionic (negative charge), cationic (positive charge), zwitter-ionic (both negative and positive charges), or nonionic (no charge) (West and Harwell, 1992; Volkering et al., 1998)

2.1.1 Classification of surfactants

Numerous variations are possible within the structure of both the head and tail group of surfactants. The head group can be charged or neutral, small and compact in size, or a polymeric chain. The tail group is usually a single or double, straight or branched hydrocarbon chain, but may also be a fluorocarbon, or a siloxane, or contain aromatic group(s).

Since the hydrophilic part normally achieves its solubility either by ionic interactions or by hydrogen bonding, the simplest classification is based on surfactant head group type, with further subgroups according to the nature of the lyophobic moiety. Four basic classes therefore emerge as:

- the anionics and cationics, which dissociate in water into two oppositely charged species (the surfactant ion and its counterion),
- the non-ionics, which include a highly polar (non charged) moiety, such as polyoxyethylene ($-OCH_2CH_2-$) or polyol groups,

• the zwitterionics (or amphoterics), which combine both a positive and a negative group.

With the continuous search for improving surfactant properties, new structures have recently emerged that exhibit interesting synergistic interactions or enhanced surface and aggregation properties. These novel surfactants have attracted much interest, and include the catanionics, bolaforms, gemini (or dimeric) surfactants, polymeric and polymerisable surfactants (Robb, 1997). Another important driving force for this research is the need for enhanced surfactant biodegradability. To note, for personal care products and household detergents, regulations [Hollis, G. Ed. 'Surfactants UK' Tergo-Data, 1976.] require high biodegradability and non-toxicity of each component present in the formulation.

2.1.2 Surfactant uses and development

Surfactants may derive from natural or synthetic sources. The first category includes naturally occurring amphiphiles such as the lipids, which are surfactants based on glycerol and are vital components of the cell membrane. Also there are the so-called "soaps", the first recognised surfactants. These can be traced back to Egyptian times; by combining animal and vegetable oils with alkaline salts a soap-like material was formed, and this was used for treating skin diseases, as well as for washing. Soaps remained the only source of natural detergents from the seventh century till the early twentieth century, with gradually more varieties becoming available for shaving and shampooing, as well as bathing and laundering. In 1916, in response to a World War I-related shortage of fats for making soap, the first synthetic detergent was developed in Germany. Known today simply as detergents, synthetic detergents are washing and cleaning products obtained from a variety of raw materials.

Nowadays, synthetic surfactants are essential components in many industrial processes and formulations (Karsa, Goode, & Donnelly, 1991). Depending on the precise chemical nature of the product, the properties of emulsification, detergency and foaming may be exhibited in varying degree. The number and arrangement of the hydrocarbon groups together with the nature and the position of the hydrophilic groups combine to determine the surface-active properties of the molecule. For example, C_{12} to C_{20} is generally regarded as the range covering optimum detergency, whilst wetting and foaming are best achieved with shorter chain lengths. Structure-performance relationships and chemical compatibility are therefore key elements in surfactant-based formulations, so that much research is devoted to this area.

Among the different classes of surfactants, anionics are often used in applications, mainly because of the ease and low cost of manufacture. They contain negatively charged head group, e.g., carboxylates, used in soaps, sulfate, and sulfonates groups. Their main applications are in detergency, personal care products, emulsifiers and soaps.

Cationics have positively charged head groups – e.g., trimethylammonium ion and are mainly involved in applications related to their absorption at surfaces. These are generally negatively charged (e.g., metal, plastics, minerals, fibers, hairs and cell membranes) so that they can be modified upon treatment with cationic surfactants. They are therefore used as anticorrosion and antistatic agents, flotation collectors, fabric softeners, hair conditioners and bactericides.

Non-ionics contain groups with a strong affinity for water due to strong dipole-dipole interactions arising from hydrogen bonding, e.g., ethoxylates. One advantage over ionics is that the length of both the hydrophilic and hydrophobic groups can be varied to obtain maximum efficiency in use. They find applications in low temperature detergents and emulsifiers.

Zwitterionics constitute the smallest surfactant class due to their high cost of manufacture. They are characterised by excellent dermatological properties and skin compatibility. Because of their low eye and skin irritation, common uses are in shampoos and cosmetics.

2.2 Biosurfactants

Natural surfactants or biosurfactants can be produced extracellularly or as part of the cell membrane by a wide variety of microorganisms such as bacteria, fungi, and yeast. Some examples include Pseudomonas aeruginosa (produces rhamnoplids), Bacillus subtilis (produces a lipopeptide called surfactin) (Ron and Rosenberg, 2001; Mata-Sandoval et al., 2002; Mulligan, 2005), Nocardia amarae (Moussa et al., 2006), and Saccharomyces lipolytica CCT-0913 (Lima and Alegre, 2009). Most biosurfactants are either anionic or neutral, only a few are cationic, containing amine groups. The hydrophobic part is based on long chain fatty acids, hydroxyl fatty acids or α-alkyl-β-hydroxy fatty acids. The hydrophilic group can be a carbohydrate, amino acid, cyclic peptide, phosphate, carboxylic acid or alcohol (Mulligan et al, 2001).

Biosurfactants are grouped mainly by their chemical composition and their microbial origin. The main classes of these compounds include glycolipids; lipopeptides and lipoproteins; fatty acids, phospholipids, and neutral lipids; and polymeric biosurfactants, as has been reviewed by Desai and Banat (1997), Kosaric (2001), Rahman and Gakpe (2008) and Gautam and Tyagi

(2006). Besides, biosurfactants can be classified according to their molecular weight into two main classes, low-molecular-weight molecules called biosurfactants and high-molecular-weight polymers or bioemulsans (Neu, 1996; Rosenberg and Ron, 1999). Biosurfactants lower surface and interfacial tension; this group includes glycolipids, lipopeptides, phospholipids, and proteins. On the other hand, bioemulsans are more effective as emulsion-stabilizing agents, i.e. stabilize oil-in-water; this group includes polymers of polisaccharides, lipoproteins, and particulate surfactants (Neu, 1996; Rosenberg and Ron, 1999; Perfumo et al., 2010). In this context, surfactin and rhamnolipids are low-molecular mass biosurfactants with molecular weight of 1036 and 802 Da, respectively (Mulligan and Gibbs, 1990). Besides, emulsan an extracellular lipopolysaccaharide biosurfactant produced by Acinetobacter calcoaceticus, is a high-molecular-weight bioemulsifier with an average molecular weight of about 1000 kDa (Kim et al., 1997). Alasan is another bioemulsifier complex produced by Acinetobacter radioresistens KA53, with an average molecular weight of 1 MDa (Navon-Venezia et al, 1995). Biosurfactants can be synthesized using different microorganisms and carbon sources and production is influenced by the composition of the medium and by culture conditions (Desai and Banat, 1997; Franzetti et al., 2009). The carbon sources used for biosurfactant production are hydrocarbons, carbohydrates, vegetable oils and oil wastes, olive oil mill effluent, lactic whey and distiller wastes, starchy substrates, renewable resources, industrial and/ or municipal wastewater, under aerobic conditions (Kosaric, 1992; Desai and Banat, 1997; Gautam and Tyagi, 2006). In this context, Franzetti et al. (2008) found three new bacterial strains hydrocarbon-degrading Gordonia genus. They were isolated from a site chronically

contaminated by diesel. These strains were able to grow using a wide range of straight and branched aliphatic hydrocarbons as carbon and energy sources and to produce at least two classes of surface-active compounds, emulsifying agents and water-soluble substrates. Cell-bound biosurfactants, which reduce surface tension, were produced in hydrocarbons. However, their production was lower in water soluble substrates. Gordonia sp. BS29 synthesized and then released extracellularly, bioemulsions during the exponential phase with n-hexadecane as carbon and energy source. The production of biosurfactants started in the exponential phase and their concentration increased following linear growth. Calvo et al. (2008) isolated Ochrobactrum anthropi strain AD2 from the waste water treatment plant of an oil refinery. This bacterium produced exopolysaccharide AD2 (exopolysaccharide emulsi-fiers) in glucose nutrient broth media with various added hydrocarbons; such as n-octane, mineral light and heavy oils and crude oils. In addition, Franzetti et al. (2009) studied the cultural factors that

affecting the production of the cell-bound biosurfactants by Gordonia sp. BS29. Their research has evaluated the type and concentration of the carbon source, the concentration of phosphates and sodium chloride, and the interactions among these factors. The results showed that with the optimized cultural conditions a 5-fold increase in the biosurfactant concentration, compared to the un-optimized medium, was obtained. The optimization did not change the number and type of the glycolipid biosurfactants produced by Gordonia sp. BS29.

The phytogenic surfactant is another group of biosurfactants, such as saponins and lecithins (Soeder et al., 1996), and humic acids (Conte et al., 2005). The phytogenic surfactants are released from decaying roots and can be found in considerable amounts in the rhizosphere, where phosphatidylcholine, the most important component of lecithin, is the major phospholipid (Soeder et al, 1996). Cyclodextrins are another group of substances that enhanced the apparent solubility and biodegradation of hydrophobic organic compounds (HOCs) in aqueous solutions and contaminated soil (Boyle, 2006). These substances can imitate the function of surfactants since they can form soluble complexes with hydrophobic compounds. Cyclodextrins have a non-polar cavity into which the HOCs partition to form inclusion complexes and a polar exterior that provides the molecule with a relatively high aqueous solubility. Moreover, they are of interest in microbial processes because they do not exhibit the toxicity of many synthetic surfactants (Singh et al., 2007).

The most important characteristic of biosurfactants is their environmental acceptability, as they are biodegradable, have lower toxicity than synthetic surfactants, their own specific action, effectiveness at extremes of temperature, pH and salinity, and are ecologically safe, as it has been reviewed by Kosaric (1992) and Desai and Banat (1997). These properties have allowed the use of biosurfactants in the remediation of inorganic compounds such as heavy metals (Kosaric, 1992; Zouboulis et al., 2003), and in the remediation of organic compounds such as hydrocarbons (Franzetti et al., 2008). Also, the ability to reduce the interfacial tension of oil in water has allowed applied of biosurfactants for the removal of water from emulsions prior to processing (Mulligan, 2005) and therefore they are applied in oil recovery (Plaza et al., 2008; Abdolhamid et al., 2009). Moreover, natural surfactants have been used in the food processing industry, and the health care and cosmetics industries (Desai and Banat, 1997). The properties of biosurfactants have generated a large number of investigations, which have allowed identification of new microorganism producers of natural surfactants, determination of their structure, finding new sources of carbon and energy, enhancing the production processes, and generating several patents (Shete et al., 2006).

2.2.1 Advantages of biosurfactants

Biosurfactants have many advantages when compared to their chemically synthesized counterparts, some of these are:

Biodegradability: Biological surfactants are easily degraded by microorganism (Mohan, Nakhla, & Yanful, 2006).

Low toxicity: Biosurfactant demonstrate lower toxicity than the chemical-derived surfactants. It was also reported that biosurfactants showed higher EC 50 (effective concentration to decrease 50% of test population) values than synthetic dispersants (Desai & Banat, 1997b).

Availability of raw materials: Biosurfactants can be produced from very cheap raw materials which are available in large quantities. The carbon source may come from hydrocarbons, carbohydrates and /or lipids, which may be used separately or in combination with each other.

Physical factors: Many biosurfactants are not affected by environmental factors such as temperature, pH and ionic strength tolerances. Lichenysin produced by Bacillus licheniformis strain was not affected by temperature ranges of up to 50°C, a pH range of 4-5- 9.0, and NaCl concentration of 50g/l and Ca concentration of 25g/l. (Muthusamy, Gopalakrishnan, Ravi, & Sivachidambaram, n.d.-a).

Surface and interface activity: Mulligan (Mulligan, 2005b) has stated that a good surfactant can lower surface tension of water from 75 to 35 mN/m and the interfacial tension water/hexadecane from 40 to 1 mN/m. Surfactin possess the ability to reduce the surface tension of water to 25 mN/m and the interfacial tension of water/hexadecane to < 1 mN/m (Muthusamy, Gopalakrishnan, Ravi, & Sivachidambaram, 2008).

Other advantages (kosaric, 2001) are biocompatibility and digestibility, which allows their application in cosmetic, pharmaceuticals and as functional food additives

2.2.2 Commercial Applications of Biosurfactants

The worldwide production of surfactants amount increased to 17 million tonnes in 2000 (including soaps) expected future growth rates of 3-4% per year globally (Rahman & Gakpe, 2008). These chemically synthesized surfactants are mainly petroleum based and are usually non-biodegradable thus remain toxic to the environment they find themselves. Moreover, these compounds may bio-accumulate and their production processes and by-products can be

environmentally hazardous, due to the increasing awareness on the need to protect the ecosystem, environmental scientists have been tightening environment regulations thus necessitating an increased interest in surfactants of microbial origin as possible alternatives to chemically synthesized ones (Benincasa, 2007). Biosurfactants have several applications in agriculture, medicine, petroleum and industry.

Application of Biosurfactants in Agriculture

One way to enhance the solubility of bio-hazardous chemical compounds such as PAH is to apply surfactants as mobilizing agents.

This increases the apparent solubility of Hydrophobic Organic Contaminants (HOC). Surfactants can also help microbes to adsorb from soil particles occupied by pollutants, thus decreasing the diffusion path length between the site of absorption and the site of biouptake by the microorganisms (Makkar & Rockne, 2003). Also in agriculture, surfactants are used for hydrophilization of heavy soils to obtain good wettability and to achieve even distribution of fertilizer in the soil. They also prevent the caking of certain fertilizer during storage and promote spreading and penetration of the toxicants in pesticides (Makkar & Rockne, 2003).

The rhamnolipid biosurfactant, mostly produced by the genus Pseudomonas is known to possess potent antimicrobial activity. Further, no adverse effects on humans or the environments are anticipated from aggregate exposure to rhamnolipid biosurfactants. Fengycins are also reported to possess antifungal activity and therefore may be employed in biocontrol of plant diseases (Traudel & Merten, 2017).

Biosurfactants as Biopesticide

Conventional arthropod control strategy involves applications of broad-spectrum chemicals and pesticides, which often produce undesirable effects. Further, emergence of pesticide resistant insect populations as well as rising prices of new chemical pesticides have stimulated the search for new eco-friendly vector control tools.

Lipopeptide biosurfactants produced by several bacteria exhibit insecticidal activity against fruit fly Drosophila melanogaster and hence are promising to be used as biopesticide (Mulligan, 2005a)

Application of biosurfactants in medicine

Mukherjee et al. (Das & Mukherjee, 2007) elucidated on the wide range of applications of biosurfactants in medicine they include:

Antimicrobial activity: The diverse structures of biosurfactants confer them the ability to display versatile performance. By its structure, biosurfactants exerts its toxicity on the cell membrane permeability bearing the similitude of a detergent like effect (Zhao et al., 2010). Gharaei-Fathabad (Gharaei-Fa, 2011) reported that several biosurfactants have strong antibacterial, antifungal and antivirus activity; these surfactants play the role of anti adhesive agents to pathogens making them useful for treating many diseases as well as its use as therapeutic and probiotic agent. A good example is the biosurfactant produced by marine *B. circulans* that had a potent antimicrobial activity against Gram positive and Gram negative pathogens and Semi pathogenic microbial strains including MDR strain.

Anti-cancer activity: Some microbial extracellular glycolipids induce cell differentiation instead of cell proliferation in the human promyelocytic leukemia cell line, also, exposure of PC 12 cells to MEL enhanced the activity of acetylcholine esterase and interrupted the cell cycle at the G1 phase with resulting overgrowth of neurites and partial cellular differentiation, this suggest that MEL induces neuronal differentiation in PC 12 cells and provides the ground work for the use of microbial extracellular glycolipids as novel reagents for the treatment of cancer cells (Muthusamy et al., 2008).

Anti-adhesive agents: Biosurfactants have been found to inhibit the adhesion of pathogenic organisms to solid surfaces or to infection sites, Rodrigues et al. (Rodrigues, Banat, Teixeira, & Oliveira, 2006) demonstrated that pre-coating vinyl urethral catheter by running the surfactin solution through them before inoculation with media resulted in the decrease in the amount of -biofilm formed by Salmonella typhimurium, Salmonella enterica, E. coli and Proteus mirabilis. Muthusamy et al. (Muthusamy et al., 2008) reported that pretreatment of silicone rubber with S. thermophilus surfactant inhibited 85% adhesion of C. albicans and surfactants from L. fermentum and L. acidophilus adsorbed on glass, reduced by 77% the number of adhering uropathogenic cells of Enterococcus faecalis.

Immunological adjuvants: Bacterial lipopeptides constitute potent non-toxic, nonpyrogenic immunological adjuvants when mixed with conventional antigens. An improvement of the

humoral humane response was demonstrated when low molecular mass antigens Iturin AL and herbicolin A (Gharaei-Fa, 2011).

Antiviral activity: Antibiotic effects and inhibition of growth of human immunodeficiency virus in leucocytes by biosurfactants have been cited in literature (Desai & Banat, 1997a); (Muthusamy et al., 2008). Furthermore, Muthusamy et al. reported that, due to the increased incidence of HIV in women, the need for a female controlled, efficacious and safe vaginal topical microbicide arise. Sophorolipids surfactants from C. bombicola and its structural analogues such as the sophorolipid diacetate ethyl ester is the most potent spermicidal and virucidal agent. It was also reported that this substance has a virucidal activity similar to nonoxynol – 9 against the human semen.

Gene delivery: Gharaei-Fathabad (Gharaei-Fa, 2011) stated that the establishment of an efficient and safe method for introducing exogenous nucleotides into mammalian cells is critical for basic sciences and clinical applications.

Other: Other advantages and applications of biosurfactant in medicine are their use as agents for stimulating stem fibroblast metabolism and immunomodulatory action. It has been reported in literature that in the case of deficiency of pulmonary surfactant, a phospholipids protein complex is responsible for the failure of respiration in prematurely born infants (Gharaei-Fa, 2011). Other studies have shown that the isolation of genes for protein molecules of this surfactant and cloning in bacteria have made possible its fermentation production for medical application.

Application of biosurfactant in food processing industry

Biosurfactants have been used for various food processing application but they usually play a role as food formulation ingredient and anti-adhesive agents. Concerning food formulation ingredient,

they promote the formation and stabilization of emulsion due to their ability to decrease the surface and interfacial tension. They are is also used to control the agglomeration of fat globules, stabilize aerated systems, improve texture and shelf -life of starch-containing products, modify rheological properties of wheat dough and improve consistency and texture of fat-based products.

Application of biosurfactant in cosmetic industry

In the cosmetic industry, due to their emulsification, foaming, water binding capacity, spreading and wetting properties effect on viscosity and on product consistency, biosurfactants have been proposed to replace chemically synthesized surfactants. These surfactants are used as emulsifiers, foaming agents, solubilizers, wetting agents, cleansers, antimicrobial agents, mediators of enzyme action, in insect repellents, antacids, bath products, acne pads, anti dandruff products, contact lens solutions, baby products, mascara, lipsticks, toothpaste, dentine cleansers to mention but a few (Gharaei-Fa, 2011).

Application of biosurfactant in petroleum

Biosurfactant and bioemulsifiers are novel group of molecules and among the most powerful and versatile by-product that modern microbial technology can offer in fields such as bio-

corrosion and biofouling degradation of hydrocarbons within oil reservoirs, enzymes and biocatalysts for petroleum up-grading (Perfumo, Rancich, & Banat, 2010). Furthermore, biosurfactants play a major role in petroleum extraction, transportation, upgrading and refining and petrochemical manufacturing.

Application of biosurfactant in microbial enhanced oil recovery

Microbial enhanced oil recovery includes the use of microorganisms and the exploitation of their metabolic processes to increase production of oil from marginally producing reservoirs. Microbial surfactants are widely used in oil recovery in recent times. The mechanism responsible for oil release is acidification of the solid phase. Certain microorganisms, such as Bacillus subtilis, Pseudomonas aeruginosa and Torulopsis bombicola have been reported to utilize crude oil and hydrocarbons as sole carbon sources and can be used for oil spill clean-ups (Das & Mukherjee, 2007).

2.3 Rhamnolipids

Rhamnolipids are members of the glycolipid biosurfactants and were discovered and first identified from Pseudomonas sp. in 1949 (Jarvis 1949). Since then, numerous producing microorganisms, including bacteria, fungi and yeast, have been reported to produce rhamnolipids. Pseudomonas aeruginosa species of soil bacteria have been identified as the most frequently isolated rhamnolipid producers (Nie, Yin et al. 2010). Other Pseudomonas species that have been reported to produce rhamnolipids are P. chlororaphis, P. plantarii, P. putida, and

P. fluorescens. Some bacteria are known to produce only mono-rhamnolipids while some produce both. The ratio of mono and di-rhamnolipid can also be controlled in the production method. There are available enzymes that can convert mono-rhamnolipids into di-rhamnolipids. In 1984, the first patent to produce rhamnolipids was filed by Kaeppeli and Guerra-Santos and obtained in 1986 as a result of their work on Pseudomonas aeruginosa (Kaeppeli and Guerra-Santos, 1986). Subsequently, Wagner et al. filed a patent in 1985 for the biotechnical production of rhamnolipids from Pseudomonas sp. and obtained the same in 1989 (Wagner et al., 1989); (Randhawa & Rahman, 2014). An amphiphilic rhamnolipid molecule is composed of two moieties. One half is the hydrophilic sugar part, mono- or di-rhamnose, and the hydrophobic lipid part possessing one or two 3-hydroxy fatty acid residues. These residues may either be both fully saturated or one may be saturated and the other unsaturated with either one or two double bonds. The lipid moiety is attached to the sugar by O-glycosidic linkage while the two 3-hydroxy acyl groups are joined together by the formation of an ester bond. The structure diversity of rhamnolipids is determined by the number of rhamnose (one or two) and fatty acid (one or two), and the fatty acid composition. The length of the constituent fatty acids and their combinations have been found to be largely variable. To date, over 40 different rhamnolipid congeners have been described in the scientific literature, although Rha-C10-C10 and Rha-Rha-C10-C10 are typically found to be the dominant components in a naturally occurring mixture. Rhamnolipids, members of glycolipids, are the most extensively studied biosurfactant. They are commonly classified into two groups: monorhamnolipids and dirhamnolipids.

The functions of monorhamnolipids and dirhamnolipids include that of a natural surfactant, emulsifier, foaming/wetting agent, solubilizer, bactericide and fungicide, and anionic complexation agent. Rhamnolipids may be manufactured in different forms such as raw or pure powder, pure paste, like honey, like syrup, like wax, like and aqueous solution.

2.3.1 Applications of rhamnolipids

Over the years, rhamnolipids are becoming broadly pertinent in various industries and are posing a serious threat to the synthetic surfactants. Before venturing into the current production economics of rhamnolipids, it is imperative to evaluate the major applications of rhamnolipids that make them noticeable among other biosurfactants. A list of five major applications of rhamnolipids that cater to the wide range of industrial demands includes:

Bioremediation and enhanced oil recovery (EOR): Rhamnolipids show excellent emulsification properties, efficiently remove crude oil from contaminated soil and facilitate bioremediation of oil spills (Rahman et al., 2003; Costa et al., 2010).

Pharmaceuticals and therapeutics: Rhamnolipids show low toxicity, surface active properties and antimicrobial activities against several microbes (Bacillus cereus, Micrococcus luteus, Staphylococcus aureus, Listeria monocytogenes) thereby showing promising applications in pharmaceuticals and therapeutics (Magalhaes and Nitschke, 2013).

Cosmetics: Rhamnolipid as an active ingredient is found to be effective for several skin treatments i.e., wound healing with reduced fibrosis, cure of burn shock, treatment of wrinkles. Hence, they are demanded in the health and beauty industry (Piljac and Piljac, 2007).

Detergents and cleaners: Rhamnolipids are natural emulsifiers and surface-active agents leading to their wide spread usage in detergent compositions, laundry products, shampoos and soaps

Agriculture: Rhamnolipids are already used for soil remediation for improving soil quality and are now further getting explored for plant pathogen elimination, for aiding the absorption of fertilizers and nutrients through roots and as biopesticides (Sachdev and Cameotra, 2013).

Bioremediation

RLs have been studied and shown to have potential in bioremediation of organics, as organic flushing agents, as metal flushing agents, and in the biodegradation of organics in metal–organic co-contaminated systems (Maier & Soberón-Chávez, 2000a).

Biodegradation and uptake of hydrocarbons

Numerous studies confirmed that biosurfactants, especially RLs, could affect the biodegradation of hydrocarbons, both aliphatic and aromatic (Rikalović, Vrvić, & Karadžić, 2015). Furthermore, it has been shown that the addition of RLs to pure cultures of P. aeruginosa enhanced the biodegradation of hexadecane, octadecane, n-paraffins and phenanthrene, (Shreve GS, Inguva S, 1995) as well as degradation in soil systems in the presence of hexadecane, tetradecane, pristane, creosote or hydrocarbon mixtures. Additionally, besides the role of RLs in the biodegradation of hydrocarbons, reports showed that RLs facilitate the uptake of hydrocarbons by P. aeruginosa. Although some studies reported positive effects on the biodegradation of petroleum hydrocarbons in presence of RL biosurfactant, a lack of influence

or even a negative effect of biosurfactant supplementation was observed just as frequently. Some reports indicated that the potential reason for inhibition of degradation is that RLs are favored as the carbon source for bacterial metabolism.
Recently, it was observed that the presence of RLs, or other surfactant compounds, may induce changes in the microbial community, which in turn corresponded to differences in the degradation patterns (Chrzanowski, Ławniczak, & Czaczyk, 2012).

Some earlier reports have suggested mechanisms of hydrocarbon biodegradation facilitated by RL, and assumed that RLs, due to their physicochemical properties, increased the hydrocarbon solubility and bioavailability or that RLs interact with the bacterial cell, making the cell surface more hydrophobic and easily accessible to hydrophobic substrates (Sandrin, Chech, & Maier, 2000). On the other hand, some recently published studies have proposed three mechanisms of interaction between microorganisms and hydrocarbons: access to water-solubilized hydrocarbons, direct contact of cells with large oil drops and contact with pseudo-solubilized or emulsified oil, (Microbial Biosurfacyants Role in Oil Products Biodegradation, 2010) as well as combinations of these interactions (Chrzanowski et al., 2012). However, regardless of whether the biodegradation process is enhanced or inhibited, the effects are bacterial strain-specific in the sense of strain characteristics and response to environmental conditions (Zhang et al., 2007). Although much work has been carried out by many groups to explain the role of RLs, and biosurfactants generally, in the degradation of water-immiscible substrate, their significance and exact purpose in these processes remain still unclear.

Flushing agents for organic pollution

Biodegradation of NAPL and soil-phase organics, such as PAH, is often a slow and non-feasible process. The addition of surfactants to a flushing solution could enhance the flushing efficiency, either by mobilization or by an increase in the solubilization of these compounds. (Maier & Soberón-Chávez, 2000b). Thus, to be effective, a surfactant must have good solubilization capacity and/or be able to reduce interfacial tension.

RLs were shown to have an MSR for the model NAPL, hexadecane that was 20 times greater than the MSR for hexadecane alkyl benzyl sulfonate. In studies examining the use of RLs for the removal of residual hexadecane from soil, it has been shown that RL (20 % removal) was more effective than either SDS (negligible removal) or Tween 80 (6 % removal). Additionally, it has been shown that the optimal removal of NAPL compounds (60 %) could be achieved by

altering the pH and ionic strength, thereby maximizing the reduction of the surface tension. Similar results has been obtained for RL solubilization of solid phase materials. For example, the MSR of rhamnolipid–octadecane was ten and five times higher than the MSRs for Triton-X-114–octadecane and for Corexit 0600–octadecane, respectively. 3 Moreover, the MSR of rhamnolipid-phenanthrene was from 1.7 to 2.8 times higher than for 13 different synthetic surfactants that have been tested (Maier & Soberón-Chávez, 2000).

Furthermore, in a comparison of the removal of a hydrocarbon mixture (undecane, pentadecane, hexadecane, octadecane, pristane, naphthalene, phenanthrene and pyrene) from soil, RLs have been shown to be more effective than Triton X-100 or Tween 60 for all hydrocarbon components. Finally, RL-enhanced removal of phenanthrene, pyrene and polychlorinated biphenyls and a variety of PAH from soil have been reported (Maier & Soberón-Chávez, 2000).

Bioremediation of heavy metals

Juwarkar et al. (Juwarkar, Dubey, Nair, & Singh, 2008) have conducted column experiments to evaluate the potential of environmentally compatible RL biosurfactants produced by P. aeruginosa BS2, to remove Cd and Pb from artificially contaminated soil. Results show that dirhamnolipid removes not only the leachable or available fraction of Cd and Pb, but also the bound metals, whereas tap water removed only the mobile fraction (Juwarkar et al., 2008).

Washing contaminated soil with tap water have revealed that only ≈ 2.7 % of Cd and 9.8 % of Pb in contaminated soils are freely available or weakly bound forms and are able to be removed, whereas washing with RL has removed 92 % of Cd and 88 % of Pb after 36 h of leaching (Juwarkar et al., 2008). Wang and Mulligan80 evaluated the feasibility of using RL foam to remove Cd and Ni from a sandy soil. Application of RL foam increases the efficiency and enables the removal of 73.2 % and 68.1% of Cd and Ni, respectively, whereas the RL solution alone flushes 61.7 % and 51 % of Cd and Ni, respectively (S. Wang & Mulligan, 2004). Mulligan et al. designed batch washing experiments to evaluate the feasibility of using biosurfactants to remove heavy metals from sediments. Thus, surfactant from Bacillus subtilis, RLs from P. aeruginosa, and sophorolipid from Torulopsis bombicola were evaluated on a sediment containing 110 mg kg^{-1} of Cu and 3300 mg kg^{-1} of Zn. A single washing with 0.5 % RL removes 65 % of the copper and 18% of the zinc, whereas 4 % sophorolipid removes 25 % of Cu and 60 % of Zn. (Mulligan, Yong, & Gibbs, 2001). Avramovic et al. (Rikalovic, Avramovic, & Karadzic, 2017) have studied the chromium (VI) tolerance of P. aeruginosa

NCAIM (P) B001380 and have showed that the strain was chromium tolerant and had potential for application in heavy metal bioremediation.

Bioremediation of co-contaminated sites

Sandrin (Sandrin et al., 2000) has studied the effectiveness of RL biosurfactants in the remediation of a Cd and naphthalene co-contaminated site. They have observed that reduced cadmium toxicity as a result of the addition of P. aeruginosa RL lead to enhanced naphthalene biodegradation by Burkholderia sp. These authors suggest that the reduction of metal toxicity by RL might involve a combination of RL complexation with cadmium and RL interaction with the cell surface to alter Cd uptake, resulting in enhanced rates of bioremediation. In another co-contaminant study, it has been observed that the inhibition of phenanthrene mineralization in the presence of Cd was reduced by the pulsed addition of RL. Dahrazma and Mulligan (Dahrazma & Mulligan, 2007) have reported higher rates of Cu and Ni removal from sediments by adding 1 % NaOH to a solution of RL. Efficient removal of Zn and Cu from co-contaminated soil with a 12.6 % oil content using RLs has also been demonstrated (Mulligan et al., 2001).

Food industry

Some properties of RLs, such as emulsion formulation and stabilization, as well as anti-adhesive and antimicrobial activity, make them interesting for the food industry as multipurpose ingredients (Nitschke & Costa, 2007). Apart from their role as surface active agents, there are reports that RLs could have several other functions in food (Kosaric, 1992; Muthusamy et al., 2008). Some examples are an improvement of dough stability, texture, volume and conservation of bakery products, obtained by the addition of RL surfactants, while some other authors suggested the use of RLs for improvement of properties of butter cream, croissants and frozen confectionery products. Finally, RLs could serve a source of L-rhamnose, a compound used commercially in the production of high quality flavor compounds. L-Rhamnose is a methyl pentose natural sugar, classified as one of the rarer sugars, and is found in several animal, plant and bacterial polysaccharides, as well in RLs. This compound has been already successfully obtained by hydrolyzing RL surfactants produced by P. aeruginosa. (Linhardt, Bakhit, Daniels, Mayerl, & Pickenhagen, 1989). L-Rhamnose is a sugar that the Food and Drug Administration (FDA) has approved as a food additive and hence it has found use in the flavor industry as a precursor for the production of 2,5-dimethyl-4-hydroxy- -3 (2H)-furanone, the high-quality flavor aroma furaneol (trademark of Firmenich SA, Geneva), which resembles strawberry and

raspberry. It is also the starting raw material in the reaction of flavors developed during the preparation of various foods, such as bread, grilled meats, etc. Thus, there is a great deal of interest in obtaining commercial quantities of rhamnolipids to provide a source of L-rhamnose, which already has the above mentioned applications in the food industry.

Surface conditioning

Bacterial biofilms present on surfaces in the food industry are potential sources of contamination, which may lead to food spoilage and disease transmission, and thus, controlling the adherence of microorganisms to food contact surfaces is an essential step in providing safe and quality products to consumers (Hood & Zottola, 1995). The promising results from studies of the disruption of Bordetella bronchiseptica biofilm by RL (Irie, O'Toole, & Yuk, 2005) and reduction of adhesion of Streptococcus salivarius and C. tropicalis by RL (L. R. Rodrigues, Banat, Mei, Teixeira, & Oliveira, 2006) have suggested a potential application of RLs for surface conditioning in the food industry. Moreover, studies by Meylheuc et al. (Meylheuc, van Oss, & Bellon-Fontaine, 2001) have shown the inhibition of the adhesion of the pathogen Listeria monocytogenes to two types of surfaces typically used in the food industry using biosurfactant obtained from P. fluorescens, while Dagbert et al. (Dagbert, Meylheuc, & Bellon-Fontaine, 2006) showed that the surfactant produced by P. fluorescens also has good potential as a corrosion inhibitor. It is important to note that RLs, as products obtained from P. aeruginosa, which are considered to be opportunistic pathogens, still face some difficulties (particularly the long process required by regulations for the approval required by governmental agencies) related to application in food industry as food ingredients or integration of these biosurfactants in industrial processes on any large scale level (Nitschke & Costa, 2007). This obstacle could, in the future, be prevented by using RL produced by, as already mentioned, non-pathogenic bacterial species, such as P. chlororophasis.

Cosmetic and pharmacy industries

Cosmetic surfactants perform detergency, wetting, emulsifying, solubilizing, dispersing and foaming effects (Lourith & Kanlayavattanakul, 2009). Biodegradability, low toxicity and ecological acceptability, which, at the same time, are the benefits of a naturally derived surfactant that promises cosmetic safety are, therefore, in high demand. In particular, the application of RLs in the field of cosmetics and pharmaceuticals as emulsifiers, penetrating

agents and drug delivery systems is an emerging area of research (Sánchez et al., 2010). RLs are used in health care products in several different formulations, (Lourith & Kanlayavattanakul, 2009). For example, in insect repellents, antacids, acne pads, anti-dandruff products, contact lens solutions, deodorants, nail care products and toothpastes (Maier & Soberón-Chávez, 2000). These formulations require surfactants with high surface activity and, in particular, emulsifying activities (Vasileva-Tonkova, Galabova, Karpenko, & Shulga, 2001), which is the essence of the texture consistency of these products (E. Haba, Abalos, Jáuregui, Espuny, & Manresa, 2003).

Furthermore, requirements for the biological activities for cosmetics should expand the application of RLs, and a delivery system has been achieved, not only for emulsions but also

for liposomes. Patents for cosmetics containing RLs have been granted for anti-wrinkle and anti-aging products, which were launched in several dosage forms as commercial skin care cosmetics 108 because of their skin compatibility and extremely low skin irritation (E. Haba et al., 2003).

Biomedicine

Early on, the wide-ranging antimicrobial properties of RLs had been noted. Interestingly, they have been shown to be active against a large variety of bacteria, including both Gram-negative and Gram-positive species. In several studies, the antimicrobial properties of mixtures of RL congeners produced by three different strains of P. aeruginosa were investigated (M. Benincasa, Abalos, Oliveira, & Manresa, 2004; E. Haba et al., 2003; Ester Haba et al., 2014). The various RL combinations displayed antimicrobial activity against nearly all the tested Gram-positive spe-cies, including Staphylococcus, Mycobacterium, and Bacillus, and significant activity against a number of Gram-negative species, with Serratia marcescens, Enterobacter aerogenes, and Klebsiella pneumoniae being especially sensitive.

Rhamnolipids have been also shown to affect cellular immunosuppression and wound healing, treatment and prevention of gum disease and periodontal regeneration, and to display differential effects on human keratinocytes and fibroblast cultures. Moreover, Piljac et al. have reported the successful treatment of a decubitus ulcer with an ointment containing 0.1 % of a di-rhamnolipid.

Thanomsub et al. have tested the cytotoxic activity of a crude RL extract, Rha–Rha–C10–C10 and Rha–Rha–C10–C12, produced by P. aeruginosa B189 isolated from a milk factory, against

herpes simplex virus, insect and cancer cell lines. Rha–Rha–C10–C10 exhibits significant inhibition of growth of human breast cancer cell lines (MCF-7), with minimum inhibitory concentration (MIC) of 6.25 μg/mL, Rha–Rha–C10–C12 has got an MIC of 50 μg/mL against insect cell line C6/36, while the crude RL extract shows no cytotoxic activity. The potential mechanism of activity, regarding the structure of the biosurfactant, is a toxicological effect on the cell membrane permeability. Furthermore, Rha–Rha–C10–C10 and Rha–Rha–C10–C12 haave no inhibition effect on the normal cell line (Vero cell) at concentrations up to 50 μg/mL.

This result confirms the specific toxicity of these compounds to the cell lines used. However, the inhibitory mechanisms against these cell lines are yet unknown and are under investigation. (Thanomsub et al., 2007)

Agronomy

RLs also show the ability to control certain zoosporic plant pathogens, including Phytophthora cryptogea and Pythium spp. Purified mono- and di-RL, in concentrations ranging from 5 to 30 mg/L, caused cessation of motility and lysis of the entire zoosporic population in less than 1 min. This observation led to the development of a RL-containing biofungicide formulation, used to prevent crop contamination by pathogenic fungi (Nitschke & Costa, 2007). This product is considered to be non-mutagenic and of low acute toxicity to mammals. It was approved by the FDA for direct use on vegetables, legumes and fruit crops. Dorey et al. reported the role of RLs in triggering defense responses and protection against the fungus Botrytis cinerea in grapevines. The authors have shown that RLs inhibit spore germination and mycelium growth, thus efficiently protecting grapevines against the fungus by inducing the plant defense system. A product based on an aqueous RL solution (0.01 %) has been claimed to act as a novel agent for stimulating the natural defence reactions of plants against pathogenic fungi.

One of the major commercial domestic applications of biosurfactants is in the field of cleaning and laundry products. The interfacial chemistry created by adsorbed surface-active molecules, of either biological or chemical origin, dominates the end-use properties of materials in many different applications (Nitschke & Costa, 2007). The properties and efficacy of detergent formulations are critically dependent on the interfacial activity of various surfactants, which are present in their composition (Özdemir & Malayoglu, 2004). At present, the liquids and powders generally contain alkyl sulfonates, such as linear alkylbenzene sulfonates, but the glycolipid biosurfactants and among them rhamnolipids, produced by P. aeruginosa, are possible

candidates to be used for the, at least, partial replacements of these synthetic compounds (Marchant & Banat, 2012). One of the major challenges in the use of RLs is the fact that they are produced as a mixture of different congeners, which affects their physicochemical properties and behavior, as mentioned previously.

Bafghi and Fazaelipoor (Arutchelvi & Doble, 2011) have investigated RLs in the formulation of a washing powder. The results show that the biosurfactant was effective in removal of oil from the samples. The formulation presented in this study has also been compared with some commercial powders for the removal of edible oil, chocolate and albumen stains. These results show that the RL-inclusive formulation are comparable to the commercial powders in terms of stain removal. Biodegradability tests performed on pure RL and the RL-inclusive formulation have confirmed the good biodegradability of this biosurfactant.

Özdemir and Malayoglu (Özdemir & Malayoglu, 2004) have investigated the wetting behavior of a mixture of mono- and di-rhamnolipid (in 1:1 ratio of mono: di-rhamnolipid) on glass, PET and gold surfaces by measuring the advancing contact angle and have elucidated the preferences of the surfactant molecules adsorbed onto SL–SV and L–V interfaces, with SDS as the reference surfactant. The study shows that at low concentrations of RL and reference surfactant, the contact angle varies in a certain range, depending on the character of the surfactant interactions with the surface (Özdemir & Malayoglu, 2004).

Moreover, on hydrophobic surfaces, the adhesion tension had a specific dynamic, depending on surfactant concentration, while on hydrophilic surfaces a steady decrease in adhesion tension has been observed with both surfactant solutions. Dinasarapu et al. (2011) have also studied the wetting behavior of RLs produced by P. aeruginosa LBI grown on a waste oil substrate, and the chemical surfactant SDS, on glass, PET, poly (vinyl chloride) (PVC), poly(ε-caprolactone) (PCL) and a polymer blend (PVC–PCL) by measuring the contact angle of sessile drops. The comparison of the wetting profiles shows dynamic changes in the contact angle at low SDS and RL concentrations – the contact angle increases when the concentration of the surfactant increases further, the contact angle decreases. The results show that RLs produced by P. aeruginosa LBI exhibited superior wetting abilities compared to SDS. This is the first work that evaluated the wetting properties of RLs on polymer blends.

Drug delivery systems

In 1988, RL liposomes were patented as drug delivery systems, useful as microcapsules for drugs, proteins, nucleic acids, dyes and other compounds, as biomimetic models for biological membranes and as sensors for detecting pH variations. (Fracchia, Cavallo, Giovanna, & M., 2012). These novel liposomes have been described as safe and biologically decomposable, with suitable affinity for biological organisms, stable and with long service and shelf life. Recently, in a study of Sharma et al., (Sharma, Yngard, & Lin, 2009) RLs and sophorolipids have been mixed with lecithins to prepare biocompatible microemulsions in which the phase behavior was unaffected by changes in temperature and electrolyte concentration, making them desirable for cosmetic and drug delivery applications (Fracchia et al., 2012).

Chapter 3

Lipid phase and Membrane Models

3.1 Lipid polymorphism

Amphiphilic molecules, being constituted by a hydrophilic and a hydrophobic part, when are placed in an aqueous solvent, are affected by the hydrophobic effect, which represents their propensity to organize themselves in order to avoid the contact between their hydrophobic domains with the solvent. Based on the geometrical characteristics of the lipid molecules, they will tend to give rise to aggregates of different shapes.

The following parameters are considered:

• the area of area a_0 occupied by the head group (due to the electrostatic repulsion between neighbour molecules, for polar lipids this parameter strongly depends on the pH and ionic strength of the solution);

• the length of the aliphatic chains l_c, which also establishes the size of the micelle;

• the volume of the aliphatic chains v.

From these three parameters it is possible to calculate the shape factor of the lipid:

eq. 3.1

$$\eta = \frac{v}{a_0 \; l_c}$$

When the phospholipids or surfactants are in an aqueous environment they tend to be disposed at the air-water interface to form a monolayer in which the polar heads are completely immersed in the polar solvent and the hydrophobic tails are directed towards the gas phase. In solution small amounts of molecules in the form of monomers will reamsin, which tend to fold the hydrophobic tail in order to minimize the interactions with the solvent. By increasing the concentration of phospholipids / surfactants, the Critical Micellar Concentration (CMC) is reached, defined as the concentration at which lipids self-aggregate forming complexes in which the tails form a hydrophobic core shielded by the hydrophilic heads called micelle.

The micelles

The micelles are the simplest lipid structure that can be formed in aqueous solvent.

Lipids that form micelles should possess large polar heads and short, voluminous hydrophobic tails. For a micelle, the shape factor must be <1/3. Lipids with these geometrical characteristics are called tapered.

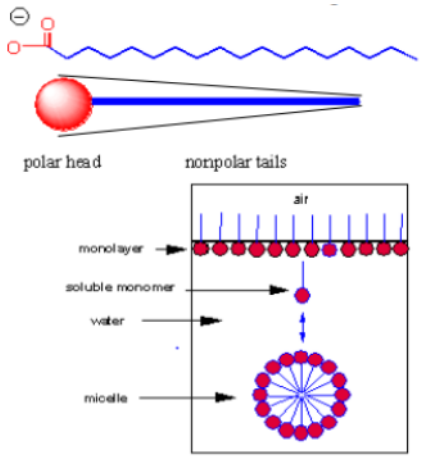

Figure 3.1: Conical shape. Micellar phase of lipids

The shape and size of these aggregates depend on numerous factors, such as: the length of the apolar tail, the nature and the size of the polar or ionic head, the acidity of the solution, the temperature and the presence of added salts. The number of amphiphilic molecules that form the micellar structure is called aggregation number, and is a useful parameter to describe the size of the micelles.

In the presence of a non-polar organic solvent, the amphiphilic molecules tend to form the inverse micelles. These aggregates indeed show an 'upside down' arrangement with respect to the previous situation. In fact, the hydrocarbon tails are exposed to the non-polar solvent, while the polar heads are directed inside the aggregate to avoid contact with the solvent (Baeurle & Kroener, 2004).

In this way an ideal "pocket" is created to melt and transport polar solutes through a non-polar solvent (Hartley & Runnicles, 1938).

Lipid bilayers

The second structure that lipids can form are double layers or lipid bilayers. The lipids that tend to form this structure should have a tail and a head of similar dimensions so that they are attributable to the shape of a cylinder. They are in fact called cylindrical lipids ($1/2 < \eta < 1$)

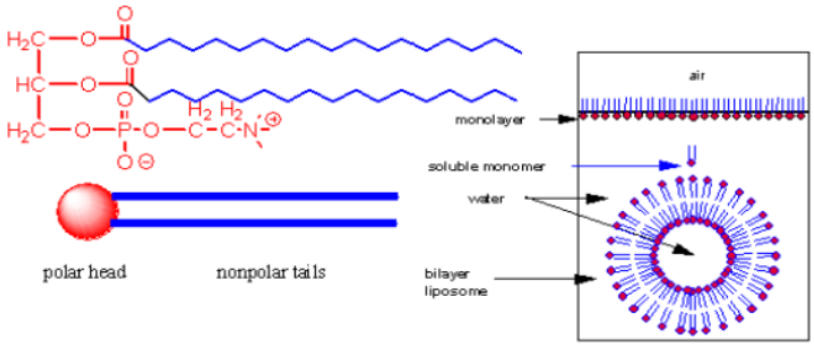

Figure 3.2: Cylindrical form of lipids. Linear bilayer and formation of liposomes.

In the double layer the lipids arrange the two hydrocarbon tails inwards and the heads in contact with the aqueous solvent. In order to avoid the solvent exposure of the hydrophobic part of the lipids placed at the ends of the double layer, this structure tends to close on itself by joining the ends and then to maintain the tails within a single hydrophobic environment. The resulting structure is a spherical shell called vesicle or liposome. The strong tension that is created between the lipids in the inner layer prevents pore formation in the vesicle unless they are destabilized by the presence of conical proteins or surfactants. The structure is maintained by non-covalent interactions (Schindler, 1980).

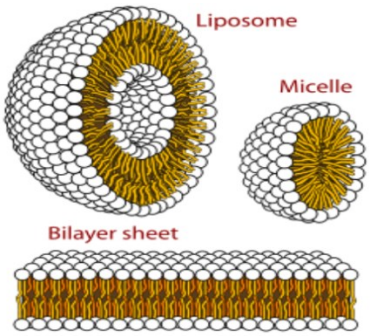

Figure 3.3: Different lipids create diffeent structures: Liposome, Micelles, Bilayer sheet

The lipid phases

All the possible spatial organizations that lipids can take are called phases. Among the various morphologies we can find: spheres of lipid molecules (micelles), lamellar phases, in which the two double phospholipid layers are arranged in parallel, a tubular arrangement of the lipid molecules (hexagonal) and various cubic phases. More complex aggregations and therefore rhombohedral, tetragonal and orthorhombic phases have been observed. The structural phase of the aggregation is also influenced by the ratio of the lipids present, the temperature, the hydration, the pressure and the ionic strength. The determination of the topology of a lipid system is possible thanks to several methods. The most informative technique is X-ray

diffraction. An X-ray beam hits the sample which causes it to be scattered as a function of the phase structure. As a result, a diffraction spectrum can be obtained formed by a series of peaks centered on particular scattering angles. By analyzing the relative ratio of the positions of the diffraction peaks, it is possible to determine the lipid phase or the lipid phases present in the analyzed sample.

The structural characteristics of the lipids (elongated shape, marked asymmetry, polar character present in a narrow portion of the molecule, with a clear division of the polar portion from the apolar, possibility of forming two orders of bonds, strong interactions between the polar heads and weak interactions between the aliphatic tails) allow them to acquire liquid-crystalline phases. The liquid-crystalline (or liquid crystal) phase is an intermediate phase (or mesophase) between the solid phase and the liquid phase, which shows some characteristic properties of the former state (e.g. ordered arrangement of the molecules) and some of the latter (e.g. fluidity). The property of phospholipids to form liquid-crystalline phases is at the basis of the structure of cell membranes. The possibility of a single lipid species to present different liquid-crystalline phases is called polymorphism. The specific liquid-crystalline phase in which the phospholipids can be found, besides being dependent on temperature and concentration, is a function of the molecule's shape which, in turn, is given by the shape of the head, tail and their steric bulk. The size of the head depends on its charge, on the degree of hydrophilia and on repulsions or electrostatic attractions with the heads of the adjacent molecules. In the case of tails, the length and degree of unsaturation of the aliphatic chains determine the volume occupied by the phospholipid tail. The temperature has a very important influence, since it determines the degree of thermal agitation of the aliphatic chains and, therefore, leads to strongly change the volume occupied by the tails.

Conical molecules, in which the section of the area occupied by the fatty acid chains is greater than that occupied by the polar head (e.g. phosphatidylethanolamine, plasmenylethanolamine), tend to form H_{II} phases (inverted Hexagonal Phase).

The inverted cone-shaped molecules, in which the section of the area occupied by the apolar part is smaller than that occupied by the polar head, form micelles (Micellar phase, M) and H_I phases (Hexagonal Phase). Only gangliosides (glycosphingophospholipids) and lysophospholipids belong to this group, which are produced by the hydrolysis of phospholipids by phospholipases and therefore possess only one fatty acid. The cylindrical molecules, in which the sections of the areas occupied by fatty acids and those of the head are similar (e.g.

phosphatidylcholine), form bimolecular laminae (Lamellar phase, L). There is also another important liquid-crystalline phase: the cubic phase.

This structural typology occurs when the aggregates are arranged within a cubic lattice. The aggregates can be curved lamellae or micelle. Structurally, the lipid cubic phase consists of a single lipid bilayer that follows an infinite periodic minimal surface (IMPS), dividing the space into two networks of aqueous channels that do not intersect. There are different types of cubic phases that have different spatial symmetries (e.g. Q_{223}, Q_{230} and Q_{229}). (Figure 3.4)

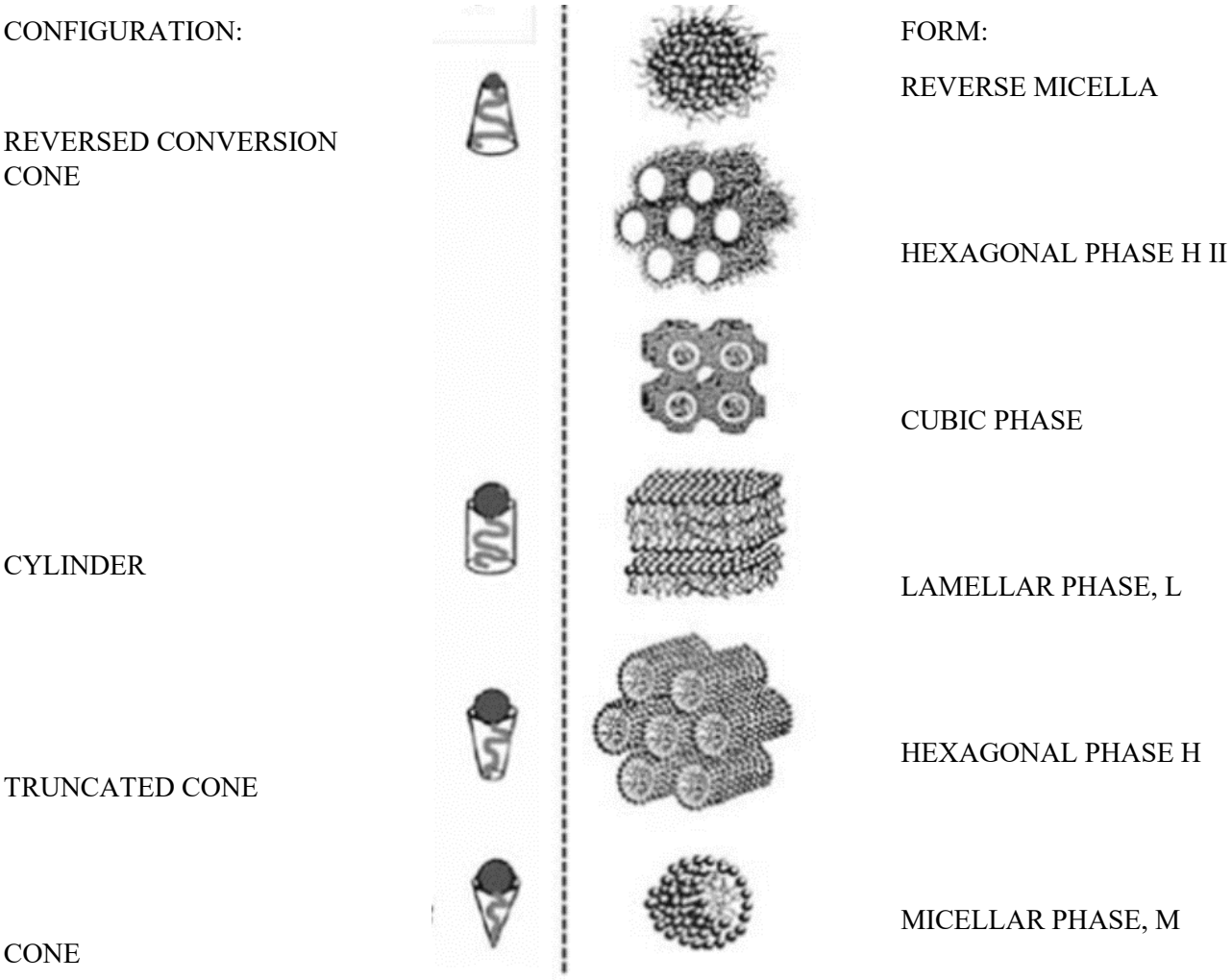

Figure 3.4: Lipid polymorphism; lipid form and corresponding lipid phase

The lamellar liquid-crystalline phases are of extreme importance in the case of phospholipids, since they form the structural units of the lipid bilayer of biological membranes. The phospholipid bilayers undergo phase transitions, generally defined as the passage from one aggregation layer to another, which derives from an alteration in the packaging and the mobility of the lipids obtained by varying the temperature.

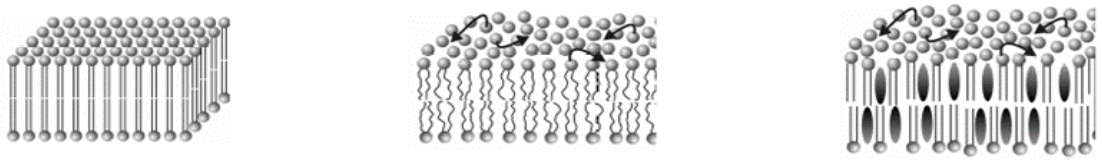

A) GEL PHASE Lβ | B) CRYSTALLINE LIQUID PHASE Lα | C) ORDERED LIQUID PHASE Lo

Figure 3.5: Lipid bilayers can exist in different physical states.

At low temperatures the acyl chains of the phospholipids are tightly packed and placed perpendicular to the plane of the bilayer. The individual molecules are limited in their movements and cannot spread laterally. This highly compact state is the Lβ gel phase (or crystalline phase). Increasing the temperature leads to the transition to the liquid-crystalline phase Lα. The double layer undergoes a phase transition and becomes fluid; consequentely, the molecules of the phospholipid start to rotate around its axis and there is a flexion of the acyl chains and the diffusion of the molecules from one position to the other of the double layer.

The transition from one phase to another takes place at a specific temperature, called critical temperature TC (or transition temperature or melting temperature Tm), characteristic for each phospholipid species. Several factors affect the transition temperature:

• Length of fatty acids;

• Degree of unsaturation of fatty acids;

• Hydrophilicity of the polar head.

Cholesterol can intermingle in the phospholipid double layer and establish hydrophobic interactions with lipid chains. A new phase is obtained, the liquid-ordered phase (fig. 3.5 C), in which the lipid chains are packaged in an orderly manner thanks to the interaction with the cholesterol, allowing however the diffusion of the lipid molecules inside the bilayer. The introduction of cholesterol in the bilayer has a double effect:

• at low temperatures there is a decrease in the order of the aliphatic chains of fatty acids, an effect that prevents crystallization.

• at temperatures above the Tm, the order of the proximal tract of the fatty acid chains increases, an effect that limits the movement of the acyl chains, leading overall to a reduction in the fluidity of the membrane.

Lipid phase diagram

The phase diagram (or lipid status) identifies which lipid liquid-crystalline phases are present when two or more thermodynamic coordinates (temperature and pressure) change and, in the case of lipid mixtures, as the composition changes. It is difficult to produce a phase diagram of a complex lipid mixture such as the plasma membrane. The study of simple systems, with distinct phase transitions, serves to understand at least some of the phenomena that occur in real membranes. Data relating to the membrane as a whole cannot be reproduced, but local phenomena can be observed such as lipid domain formation (lipid phase domains or rafts) or lipid melting phenomena in the vicinity of membrane proteins.

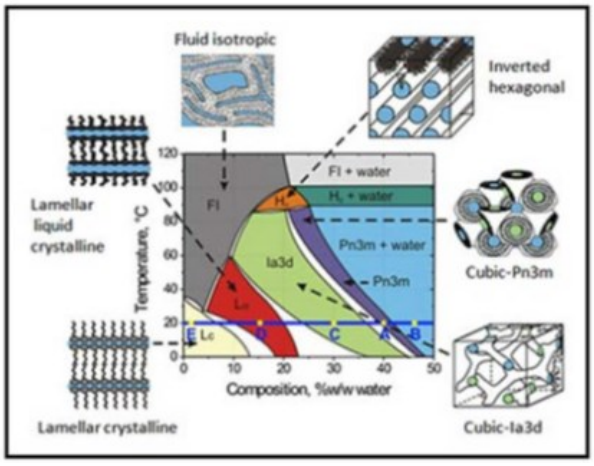

Figure 3.6: State diagram of a single lipid: monolein

3.2 Membrane Models:

3.2.1 Liposomes

The most common systems used to understand the properties and structures of cell membranes are lipid vesicles called liposomes. The term liposome derives from the two Greek words: Lipos, fat and Soma body.

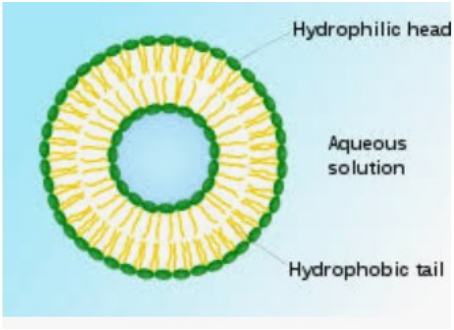

Figure 3.7 Structure of liposome

These vesicles normally consist of one or more closed double phospholipidic layers, in which the aqueous solvent is confined. Liposomes can therefore have a uni- or multi-lamellar structure, with a diameter ranging between 20 nm and 1 μm.

The liposomes, being constituted by phospholipids that are also found in the natural plasma membranes, show a remarkable affinity with the latter and consequently, through membrane fusion phenomena, the water-soluble substances present in the aqueous core or the hydrophobic substances present can be released in the phospholipid double layer. Because of this characteristic they are used as "vectors", able to convey different compounds such as: drugs of various kinds, vaccines, genetic material and functional substances from the cosmetic point of view.

Based on their size and the number of bilayers, liposomes are classified into one of two categories: multilamellar vesicles (MLV) and unilamellar vesicles. Unilamellar vesicles can also be classified into: large unilamellar vesicles (LUV), small unilamellar vesicles (SUV) and giant unilamellar vesicles (GUV). In unilamellar liposomes, the vesicle has a single phospholipid double layer that encloses the aqueous solution. In multilamellar liposomes, the vesicles have an onion structure. As different unilamellar vesicles will form within the other

with gradually smaller dimensions, creating a multilamellar structure of concentric spheres of phospholipids separated by layers of water (Akbarzadeh et al., 2013).

3.2.1.1 GUVs, Giant Unilamellar Vesicles

Among the categories of liposomes, in this thesis we are interested in the GUV, as they imitate the structure of plasma cell membranes. GUVs are also used to study membrane phenomena such as those affecting lipid raft. Lipid rafters are lipid plates i.e. planar membrane microdomains (not invaginated). In the cellular membrane there are highly dynamic microdomains, composed of aggregates of lipids rich in saturated and long chains, glycosphingolipids, sphingomyelin and cholesterol and poor in unsaturated lipids such as phosphatidylcholine. Other applications of GUVs include: the study of lateral lipid heterogeneities, budding and membrane fission phenomena, membrane protein reconstitution, and membrane permeabilization studies caused by added chemical compounds. One of the first methods to produce GUVs is the one described by Reeves and Dowben in 1969. A controlled hydration of a thin film of phosphatidylcholine of egg yolk (egg PC) formed by the deposition of a planar solid support of 0.5 ml was carried out of a solution of 5 μM of chloroform / methanol (1: 2, v / v). Before hydrating the film, the solvent was completely evaporated by nitrogen flow taking care not to disturb or stir the solution. An aqueous solution was then added, pouring it very gently into the test tube, and the lipid film was left in incubation for a few hours to promote the swelling process, which refers to the effect of water molecules penetrating between the individual bilayers until reaching the intralamellar space. It follows the formation of a bulge followed by the detachment in the form of vesicles.

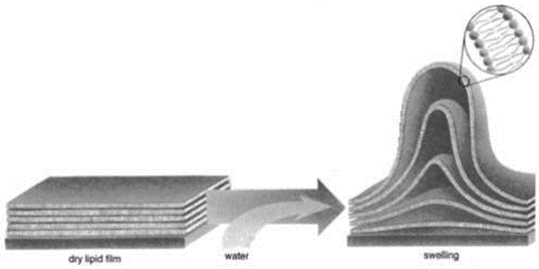

Figure 3.8: Spontaneous swelling of lipid film

This method is known as spontaneous swelling, natural swelling or gentle hydration method. In 1986 Angelova and Dimitrov published a study concerning the effect of an external electric field on the hydration of a lipid film, obtained after evaporation of the organic solvent, on the surface a slide with electrical conductivity (indium tin oxide -ITO-coated glass) or platinum

wires. With this system it is possible to obtain GUVs in aqueous solution or in a buffer with low ionic strength. The obtained GUVs are almost homogeneous, depending on the experimental conditions such as the type, composition and concentration of lipids used, the characteristics of the hydration solution and the applied electric field values. This method is known as electroforming or electroswelling.

3.3 Natural Membrane

3.3.1 Erytrhocytes

The erythrocyte, commonly known as a red blood cell (or RBC), is by far the most common formed element: A single drop of blood contains millions of erythrocytes and just thousands of leukocytes. Specifically, males have about 5.4 million erythrocytes per microliter (μL) of blood, and females have approximately 4.8 million per μL. In fact, erythrocytes are estimated to make up about 25% of the total cells in the body. They are small cells, with a mean diameter of only about 7–8 micrometers (μm).

Erythrocytes are biconcave disks: they are plump at their periphery and very thin in the center (Figure 3.9). Since they lack most organelles, there is more interior space for the presence of the hemoglobin molecules that transport gases. The biconcave shape also provides a greater surface area across which gas exchange can occur, relative to its volume; a sphere of a similar diameter would have a lower surface area-to-volume ratio. In the capillaries, the oxygen carried by the erythrocytes can diffuse into the plasma and then through the capillary walls to reach the cells, whereas some of the carbon dioxide produced by the cells as a waste product diffuses into the capillaries to be picked up by the erythrocytes. Capillary beds are extremely narrow, slowing the passage of the erythrocytes and providing an extended opportunity for gas exchange to occur. However, the space within capillaries can be so minute that, despite their own small size, erythrocytes may have to fold in on themselves if they are to

make their way through. Fortunately, their structural proteins like spectrin are flexible, allowing them to bend over themselves to a surprising degree, then spring back again when they enter a wider vessel.

Production of erythrocytes in the marrow occurs at the staggering rate of more than 2 million cells per second.

Erythrocytes live up to 120 days in the circulation, after which the worn-out cells are removed by a type of myeloid phagocytic cell called a macrophage, located primarily within the bone marrow, liver, and spleen.

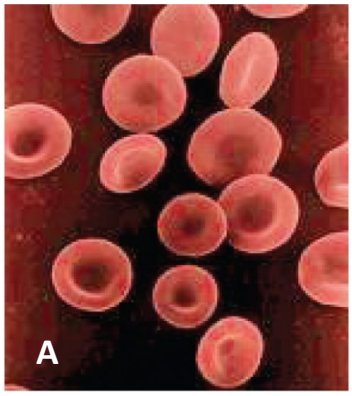

Figure 3.9 A: Shape of Red Blood Cells Erythrocytes are biconcave discs with very shallow centers. This shape optimizes the ratio of surface area to volume, facilitating gas exchange. It also enables them to fold up as they move through narrow blood vessels.

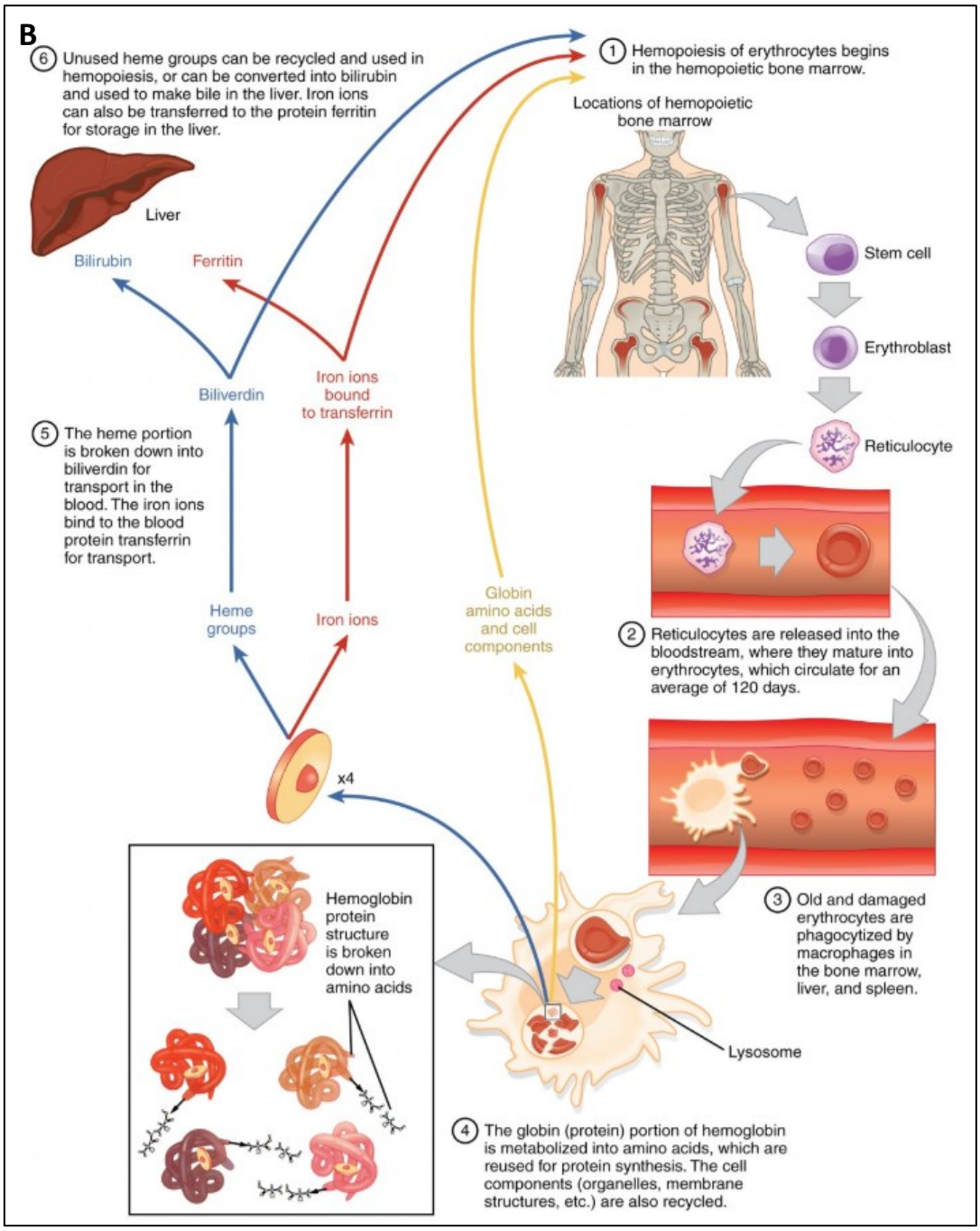

Figure 3.9 B: Erythrocytes are produced in the bone marrow and sent into the circulation. At the end of their lifecycle, they are destroyed by macrophages, and their components are recycled.

3.3.2 HaCat Cell lines

The skin is a continuously self-renewing organ that dynamically manages the outside-inside-outside relationships of the human body and actively participates in the host defenses (Baroni

et al., 2012). Keratinocytes (KCs) represent 95% of the epidermal cells. Primarily, they play the structural and barrier function of the epidermis, but their role in the initiation and perpetuation of skin inflammatory and immunological responses, and wound repair, is also well recognized (Hänel et al., 2013).

HaCaT from adult skin has been proposed as a model for the study of KC functions. HaCaT is a nontumorigenic monoclonal cell line, adapted to long-term growth without feed-layer or supplemented growth factors (Micallef et al., 2009; Schurer, Kohne, Schliep, Barlag, & Goerz, 1993); it exhibits normal morphogenesis and expresses all the major surface markers and functional activities of isolated KC (Micallef et al., 2009). Upon stimulation, HaCaT cells differentiate and express specific markers of differentiation, such as K14, K10, and involucrin. They can also form stratified epidermal structure (Boukamp et al., 1988b), but they can revert, back and forth, between a differentiated and a basal state upon changes in Ca^{2+} concentration in the medium (Deyrieux & Wilson, 2007). They retain the capacity to reconstitute a well-structured epidermis after transplantation in vivo (Garach-Jehoshua et al., 1998).

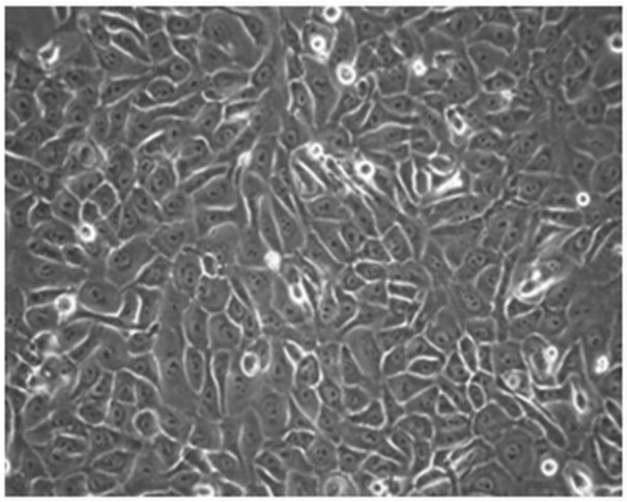

Figure 3.10: Light microscopy images of HaCaT keratinocytes. About 100,000 cells were infected with S. aureus ATCC 25923 (1 × 107 CFU/ml) for 2 h, washed with PBS, treated with gentamicin to remove extracellular bacteria.

Chapter 4

Instrumental techniques

4.1 X-Ray diffraction (XRD)

X-rays make up X-radiation, a form of electromagnetic radiation. Most X-rays have a wavelength ranging from 0.01 to 10 nanometers, corresponding to frequencies in the range 30 petahertz to 30 exahertz (3×10^{16} Hz to 3×10^{19} Hz) and energies in the range 100 eV to 100 keV. The wavelengths frequently used for diffraction experiments can vary from 0.5 Å to 2.5 Å and their speed in vacuum is the light velocity c = 2.99792458 10^8 ms^{-1}.

The X-rays that strike the matter are mainly scattered as spherical waves in all directions. The XRD depends on scattering of electron radiation and the intensity of the scattered X-ray is proportional to the number of electrons in the structure. When the X-ray beam collides with the atoms of the structure investigated it can produce a constructive and a destructive interference; only when the interference is constructive the XRD pattern is generated. The X-ray beam when passes througth the matter is attenuated and the photon can follow two different ways: they can be deflected from their path without loss of energy and this is the elastic scattering radiation (Thomson scattering), which has the same wavelength of the incident radiation, or they can be deviated with a small loss of energy and a consequent slight variation of the wavelength. This latter is the Compton or inchoerent scattering.

The energy carried by the radiation is given by

$E = h\upsilon$ (where h is Planck constant and υ is the frequency).

X-rays can be divided into soft and hard X-rays according to the wavelength:

- $\lambda \geq 0.1$ nm soft X-ray
- $\lambda \leq 0.1$ nm hard X-ray

Hard X-rays are very close to γ-rays but different from them since X-ray photons are produced by atomic electrons (electronic sources), while γ-rays are generated by sub-atomic (nuclear) transitions.

The XRD is a technique mainly used for structural investigations, allowing to reach resolutions of about 1.5 Å, comparable with the interatomic distances of condensed matter. The molecular crystalline structures are able to scatter X-rays, according to specific angles that depend on the nature and arrangement of the atoms in molecules of the system to be examined.

Max von Laue (1879-1960) suggested that a crystalline solid, consisting of ordered arrays of atoms, could serve as a diffraction lattice for electromagnetic waves displaying wavelengths comparable with the inter atomic distances. The experiments proved soon that the X-rays scattered by a crystal really showed the peaks and troughs of a diffraction pattern. XRD technique has revealed to be very efficient for the exploring the world of atoms and molecules. Today, this technique plays a key role in the study of crystals. A crystal is constituted by simple structural units called "elementary cells", which regularly repeat in space forming the entire crystalline lattice.

4.1.1 X-ray diffractometer

In general, a diffractometer consists of an X-ray source, a monochromator and collimator of the incident beam, a support for positioning the sample and a detector system.

The X-ray source consists of a tube where a heated tungsten filament releases thermal electrons, which are accelerated by a high-potential electric field and hit the metal anode. Following this interaction, X-rays are emitted at different wavelengths characteristic of each substance.

The monochromatization system consists of quartz monochromator crystals that have the function of selecting the chosen radiation (typically 1.5 Å)

The collimation system makes it possible to define the shape and size of the beam, for this purpose a sequence of slits that control the angular divergence of the beam is used.

The radius thus obtained hits the sample inserted in a particular sample holder specially constructed for biological samples.

The incident ray is diffracted from the sample and collected on a detector that measures the intensity of the radiation (I) as a function of the diffraction angle 2θ.

Between the detector and the sample, a small lead plate is positioned to block the transmitted beam (beam stop)

Figure 4.1: A) Operating scheme of an x-ray diffractometer B) sample holder, brass ring

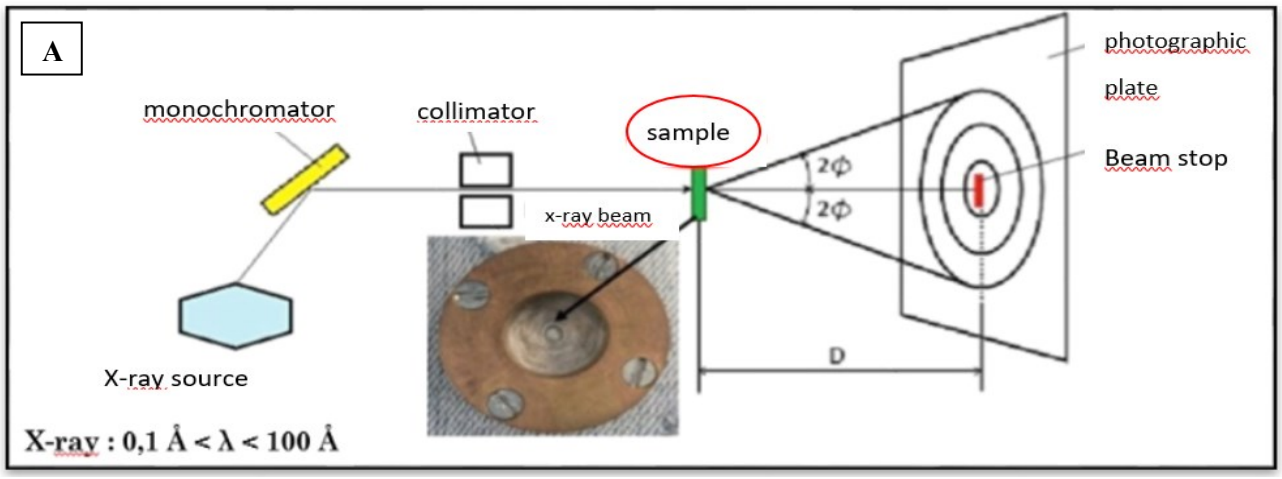

The detection system used is a photographic plate with active phosphors (Image Plate) in which the blackening of the emulsion is proportional to the intensity of the diffracted beam. The image is impressed on the plate, displayed using a scanner and processed by a computer.

The tricosane is used to obtain a calibration line necessary to convert the values of the screen pixels into the modulus of the scattering vector defined as $q=4\pi\sin\theta/\lambda$. This molecule, extensively described in the literature, forms a precise lamellar phase characterized by a sequence of interference peaks whose positions are known. Therefore, from the calibration line it is possible to convert the value of the pixels on the abscissa axis into q values for any sample.

4.1.2 Fundamental of X-ray diffraction and Bragg's law

The interaction of waves with periodic structures produces diffraction effects if the wavelength and the periodicity of the crystals are of similar magnitude. X-rays may easily be produced with wavelengths matching the unit cell dimensions of crystals, but electrons or neutrons of appropriate energy can also be used for diffraction experiments on crystals.

Considering that atoms in molecules are at distances in the order of Ångströms (1 Å = 10^{-10} m), the unit cells have dimensions of several Å. This implies that crystals with sizes of microns or larger consist of billions of unit cells, which repeat periodically in all three dimensions, i.e., they possess long-range order. This kind of order distinguishes crystalline materials from amorphous ones, e.g., glasses, which have only short-range order. Since the "quality" of diffraction effects in XRD strongly depends on the strict and undisturbed periodicity of atoms, any kind of deviation from the ideal order is shown in the X-ray diffraction diagram. Even small crystallite size is a deviation from the theoretically infinite perfect crystal.

Without any diffraction effects, the incidence of a primary X-ray beam onto a sample volume would produce scattering in all directions. Diffraction redistributes intensity from the whole scattering sphere into distinct directions. Therefore, intensity peaks arise in certain directions, whereas in directions between peaks the intensity decreases drastically.

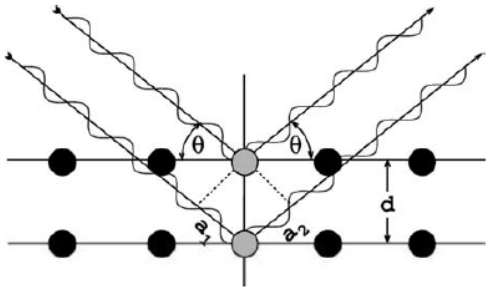

Figure 4.2. Geometric derivation of Bragg's law: Constructive interference occures when the delay between waves scattered from adjacent lattice planes given by $a_1 + a_2$ is an integer multiple of thewavelength λ.

The intensity integrated over the sphere, however, remains constant due to energy conservation. One way of describing these directions is the notion of scattering lattice planes and interference between the wavelength scattered by neighbouring lattice planes. The figure illustrates this situation. Constructive interference and hence a so called Bragg reflection is obtained when the difference in the path of two beams scattered by atoms two different lattice planes is equal to an integer number of wavelengths λ. The constructive interference will thus occur when:

$$n\lambda = 2d \sin \theta \qquad \text{eq. 4.1}$$

This is the so-called Bragg equation, where λ is the wavelength of the radiation, n is an integer number, σ is the angle between the lattice planes and the incident beam and d is the distance of the lattice planes for which the peak occurs.

4.2 Small Angle X-Ray Scattering (SAXS)

In solution small-angel scattering (SAS) of X-rays or neutrons (SAXS and SANS or SAS in general) is a powerful tool for determining the structural features of biologically relevant macromolecules in the solution. SAS can provide not only precise information concerning the size and shape of single molecules (also in terms of molecular weight, volume, compactness degree and aggregation state) but also detailed information from large, multicomponent macromolecular complexes such as protein complexes. Moreover size and shape of the protein in solution can be obtained in very different experimental conditions, for example as a function of pH (Barbosa et al., 2010), salt concentration (Zhang et al., 2007), temperature or pressure (Ortore et al., 2009) presence of cosolvents, ligands or denaturing agents. In a SAXS experiments, the elastic scattering of X-rays (typical wavelength λ~ 1 Å) by a sample with nm range inhomogeneities is recorded at very low angles (scattering angles 2θ typically from 0.1° to 10°). A standard setup can be appreciated in the Figure 4.3.

Basically, a polychromatic X-ray beam coming from a conventional X-ray generator or synchrotron storage ring passes through a monochromator that selects a rather narrow wavelength window. Thus, the monochromatic incoming beam passes through a collimation system and hits the sample ($\vec{k}_{in}$). On one hand, the transmitted X-ray beam ($\vec{k}_{in}$) goes directly to the detector and hits the beam stopper, which is usually a piece of metal that absorbs the incident radiation avoiding detector damage. On the other hand the scattered X-ray $\vec{k}_{out}$ reaches the detector at a certain position, which is defined by the scattering angle 2θ ($\vec{q}$ is defined as $\vec{q} = \vec{k}_{out} - \vec{k}_{in}$). The measured data comprises the variation of X-ray scattered intensity as a function of the scattering angle, 2θ, and , hence the scattering vector, $\vec{q}$.

The whole system is enclosed in vacuum chambers in order to avoid the non-negligible SAS of air. If the sample consists of particles or aggregates dispersed in a homogeneous solution, the intensity scattered in this angular region contains information about the shape, size, and interactions of the dispersed particles. The analysis of the SAS curve can be limited to the determination of few parameters, but other information can be also derived. The first is the particle *form factor,* which is directly related to the in-solution structure of the scattering

particles. When the particle-particle interactions cannot be neglected, an additional scattering signal related to the spatial distribution of the particles is detected and the presence of a structure factor should be considered. In this context, an analysis of the structure factor leads to the correlation function, which describes the spatial arrangement of the particles and, hence, the direct pair potential that describes particle-particle interaction force (Barbosa et al., 2010; Ortore et al., 2009; Sinibaldi et al., 2007; Zhang et al., 2007).

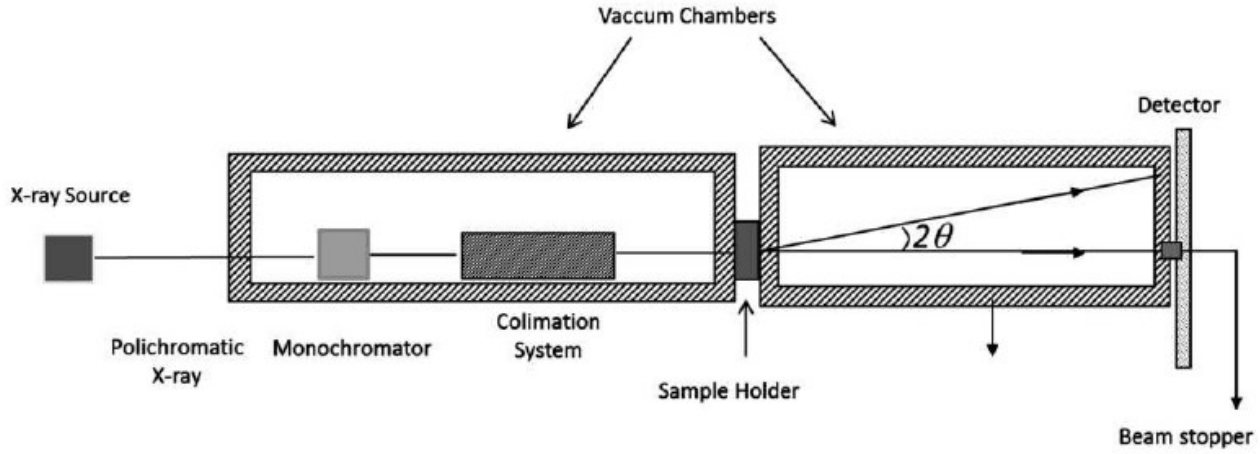

Figure 4.3: A basic SAXS setup. A collimated, monochromatic X-ray beam incident on the sample generates scattered X-rays, which are imaged by a detector.

4.2.1 General Equation of SAXS

The most general equation of Small Angle Scattering is (A. Guinier, G.Fournet, 1955.)

eq. 4.2
$$\frac{d\Sigma}{d\Omega}(q) = V^{-1}\left\langle \left| \int_V \delta\rho(\vec{r}) d\vec{r} e^{i\vec{q}.\vec{r}} \right|^2 \right\rangle$$

where $\frac{d\Sigma}{d\Omega}(q)$ is the scattering intensity (more precisely called macroscopic differential excess scattering cross section) as a function of the exchanged wave vector $\vec{q}$. The modulus of q is defined as:

eq. 4.3
$$q = \frac{4\pi}{\lambda}\sin\theta$$

In Equation 4.2 the integral is extended over the total sample volume V and and $\vec{r}$ is the position vector; the angular brackets $\langle ... \rangle$ indicate an average over all positions, orientations and microstates of the particles in the systems. Finally, $\rho(\vec{r})$ is the electron density multiplied for the electron radius (for X-rays its value is $r_e = 2.8 \times 10^{-13}$ cm).

In absence of long range order, the scattering density can be thought as having a uniform value ρ_0 on which fluctuations $\delta\rho(\vec{r})$ are superimposed. The amplitude factor $F(\vec{q})$ is defined as the normalized Fourier Transform of $\delta\rho(\vec{r})$ function as

eq. 4.4 $$F(\vec{q}) = \frac{1}{f} \int_{Vp} d\vec{r}\, \delta\rho(\vec{r}) e^{i\vec{q}\vec{r}}$$

where f is the scattering amplitude at $\vec{q}$=0 and V_p is the volume of the scattering particles.

eq. 4.5 $$f = \int_{Vp} d\vec{r}\, \delta\rho(\vec{r}).$$

Let us consider a polydisperse system which can be regarded as a mixture with p components. By introducing the effective form factor $P(q)$ as

eq. 4.6 $$P(q) = \frac{\sum_{i=1}^{p} n_i f_i{}^2 \langle |F_i^2(\vec{q})| \rangle}{\sum_{i=1}^{p} n_i f_i{}^2 \langle |F_i^2(\vec{q})| \rangle}$$

n_i being the number density of species i in the equation, the scattering intensity can be written as

eq. 4.7 $$\frac{d\Sigma}{d\Omega}(q) = n_p P(q) S_M(q)$$

where n_p is the particle number density, $r_e = 2.8\ 10^{-13}$ cm is the classical radius of the electron, $P(q)$ is defined as the average squared form factor and $S_M(q)$ is the effective structure factor, which takes into account the correlations among the centers of the scattering particles.

4.3 Optical spectroscopy

The UV / VIS spectrophotometry is based on the selective absorption, by molecules, of the radiations with a wavelength between 10 nm and 780 nm that are distinguished in the following spectral regions:

• Far UV (10 - 200 nm)

• Near UV (200 - 380 nm)

• Visible (380 - 780 nm)

From an analytical point of view, the most interesting regions are the near UV and the visible. When energy is supplied to the molecules, the excitation of the valence electrons is promoted, which can cause electronic transitions that take place starting from molecular binding orbiting (σ or π) or non-binding (n) orbitals. These transitions are characteristic of both organic compounds and inorganic compounds that possess valence electrons of type *s* and *p*.

The experimental law that describes the phenomena of absorption of electromagnetic radiation is the Lambert-Beer law, which in the case of monochromatic radiation takes the form:

eq. 4.8 $$A\ (\lambda) = \varepsilon\ (\lambda)\ b\ C$$

where:

• A (λ) = absorbance of the radiation at a specific wavelength;

• b = optical path, thickness of the solution crossed by the radiation;

• C = molar concentration of the absorbent species;

• ε (λ) = molar absorption coefficient at a specific wavelength.

By fixing a constant value of the optical path, Beer's law becomes A (λ) = K (λ) C, corresponding to the equation of a line passing through the origin of which K (λ) is the angular coefficient. In the case of b = 1 cm, this angular coefficient defines the molar absorption coefficient. Another useful quantity to express the absorption of radiation in quantitative terms is the transmittance:

eq. 4.9 $$T\ (\lambda) = I\ (\lambda) / I_0\ (\lambda)$$

where I (λ) is the intensity of the radiation leaving the sample and I_0 (λ) is that of the incident radiation. Transmittance and absorbance are related to each other by the relationship

eq. 4.10 $$A(\lambda) = \log [1 / T(\lambda)] = \log [I_0(\lambda) / I(\lambda)]$$

Generally, the transmittance is expressed as a percentage transmittance

$$T(\lambda)\% = T(\lambda)\ 100$$

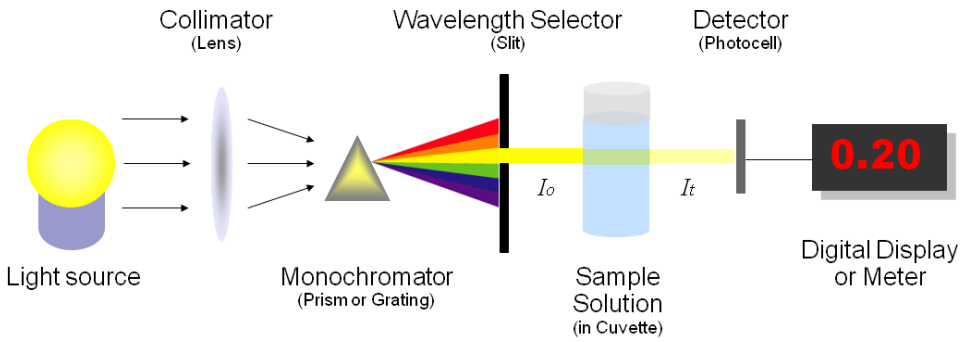

Figure 4.4: Spectrophotometer setup

The instruments used to measure the absorption of radiation by solutions are called spectrophotometers. Schematically a spectrophotometer consists of:

- source: lamp that can emit in the UV or Visible field;
- monochromator: decomposes the radiation into monochromatic bands;
- cuvettes: containing the sample;
- detectors: transforms the radiant energy into an electrical signal that is transferred to an analog or digital indicator and to a recorder;
- the reading system: converts the signal coming from the detector into a form that can be used by the analyst.

Spectrophometry allows qualitative as well as quantitative analysis. The qualitative analysis is possible because the molecular absorption spectrum obtained in the UV / VIS depends on the electronic structure of the molecule it absorbs and therefore on its possible transitions The quantitative analysis makes use of the Lambert-Beer law which, as already shown, expresses a relationship of direct proportionality between the concentration of a species in solution and the absorbance A (λ) of a radiation at a given wavelength.

In order to avoid deviations of the Lambert-Beer law it is necessary to take into account that as the solute concentration increases, considerable deviations occur with consequent lack of

reliability of the analytical data, therefore solutions must always be very diluted, compatibly with the sensitivity of the instrument, to have acceptable absorbance values. It should also be noted that chemical equilibria amog the species in solution can modify their nominal concentration.

4.4 Microscopy

4.4.1 Polarized Light Optical Microscopy

Polarized optical microscopy (POM) is a technique that employs polarized light to study the microstructure of materials. For example, with the aid of POM, researchers can observe crystalline and amorphous area of polymers. Usually the normal unpolarized light is constituted by many sinusoidal waves describing the amplitude of both electric and magnetic fields that can oscillate in any plane that contains the propagating beam. On the contrary, in the case of POM, due to the presence of polarizer devices, the waves can oscillate only in one plane.

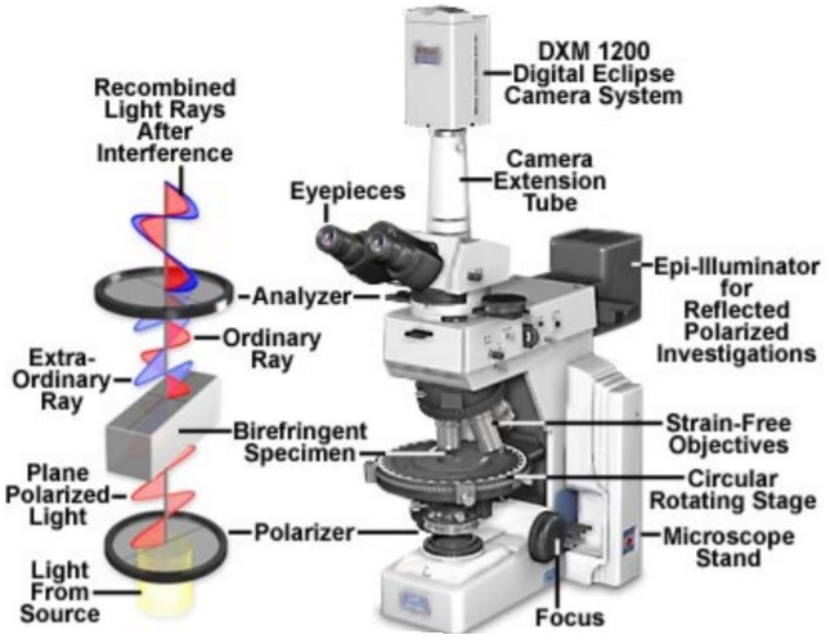

Figure 4.5: Classical configuration of Polarized Optical Microscope

Figure 4.5 shows the concept of light polarization: the unpolarized incoming light passes through the first polarizer, in which only the waves that are vertical in the incident beam will pass. Waves passed through polarizer 1 will blocked by polarizer 2. The use of two polarizers is fundamental for the practice of polarized light microscopy. And it is called crossed polarization. Other different components are the circular rotating stage, the special plates or

filters placed between the object and light path. (Figure 4.5). The microscope configuration uses crossed polarizers where the first polarizer (polarizer) is placed below the sample in the light path and the second polarizer (analyzer) is placed above the sample, between the objective and the eyepieces. With no sample on the microscope stage, the light polarized by the polarizer is blocked by the analyzer and no light will be visible.

When samples that are birefringent are viewed on the stage between crossed polarizers, the microscopist can visualize aspects of the samples through light rotated by the sample and then able to pass through the analyzer.

To increases the quality of image, the polarizer can be used at the same time with other observation techniques, such as dark or brightfield illumination, DIC, fluorescence and phase contrast. The polarized light microscope is characterized by a high degree of sensitivity and it is a valid method for both quantitative and qualitative studies targeted at a wide range of anisotropic specimens. The qualitative analysis is very popular in practice, otherwise the quantitative aspects which is primarily employed in crystallography, represent a specific subject that is usually restricted to geologists, mineralogists, and chemists. In the last few decades the biologists have applied this technique to study the birefringent character of many anisotropic sub-cellular assemblies so the method can be used both qualitatively and quantitatively with success for a wide range of discipline such as materials sciences, geology, chemistry, biology, metallurgy and even medicine.

4.4.2 Fluorescence Microscopy

A fluorescence microscope is an optical microscope that uses fluorescence and phosphorescence instead of, or in addition to, scattering, reflection, and attenuation or absorption, to study properties of organic or inorganic substances. In most cases, a component of interest in the specimen is specifically labeled with a fluorescent molecule called a fluorophore (such as green fluorescent protein (GFP), fluorescein or DyLight 488) (Spring KR, n.d.) The specimen is illuminated with light of a specific wavelength (or wavelengths) which is absorbed by the fluorophores, causing them to emit longer wavelengths of light (of a different color than the absorbed light). The illumination light is separated from the much weaker emitted fluorescence through the use of an emission filter.

Typical components of a fluorescence microscope are the light source (xenon arc lamp or mercury-vapor lamp), the excitation filter, the dichroic mirror (or dichromatic beamsplitter), and the emission filter (see figure below). The filters and the dichroic are chosen to match the spectral excitation and emission characteristics of the fluorophore used to label the specimen. In this manner, a single fluorophore (color) is imaged at a time. Multi-color images of several fluorophores must be composed by combining several single-color images. (Figure 4.6)

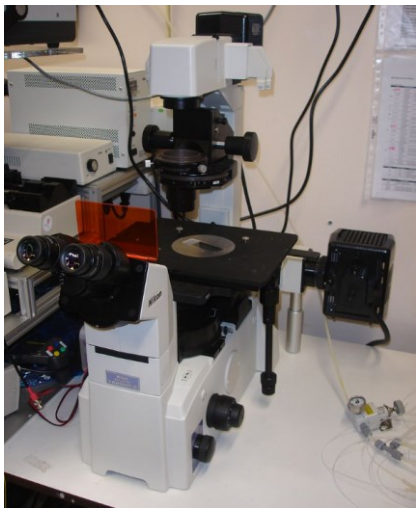

Figure 4.6: Fluorence Microscopy

An inverted fluorescence microscope (Nikon TE2000). Note the orange platform that allows the operator to see the sample, but at the same time protects it from the UV light used for excitation.

Most fluorescence microscopes in use are epifluorescence microscopes (i.e. excitation and observation of the fluorescence are from above (epi–) the specimen). These microscopes have become an important part in the field of biology, opening the doors for more advanced microscope designs, such as the confocal microscope and the total internal reflection fluorescence microscope (TIRF). The Vertico SMI combining localisation microscopy with spatially modulated illumination uses standard fluorescence dyes and reaches an optical resolution below 10 nanometers. Fluorophores lose their ability to fluoresce as they are illuminated in a process called photobleaching. Special care must be taken to prevent photobleaching through the use of more robust fluorophores, by minimizing illumination, or by introducing a scavenger system to reduce the rate of photobleaching.

Chapter 5

5.1 Chemical-physical characterization of rhamnolipids

Rhamnolipids from Pseudomonas Aeruginosa (90% purity) were purchased from Sigma-Aldrich (Poole, UK).

5.1.1 Mass analysis

For mass analysis, approximately 5 mg of the rhamnolipid mixture was dissolved in water and analysed by direct injection in an electrospray ionisation (ESI) mass apparatus (HP 1100 LC/MSD, Agilent), equipped with a single quadrupole detector. The sample was analysed in negative mode at different fragmentor voltages (0, 30, 60, 90 V).

5.1.2 HPLC analysis

HPLC runs were performed using a HPLC system (HP1100, Agilent) equipped with a photodiode array detector (DAD). Rhamnolipids were analysed after derivatization using 2-bromoacetophenone (Schenk et al., 1995). The separation of rhamnolipids was achieved using a reverse phase liquid chromatograpy with a C18 Discovery column (5 µm, 15 cm x 4.6 mm) (Supelco, USA). The elution was made using water/acetonitrile mixture at 70:30 ratio. Flow rate was 0.8 ml/min. Estimation of the relative amount (as a percentage) of the mono-and di-rhamnolipids in the mixture was performed by the ratio of the integrated area over time relative to the chromatographic peaks measured at 254 nm (ChemStation, Agilent).

5.1.3 Surface tension measurements

Surface tension measurements were performed at 37°C by tensiometry, using the Du-Noüy ring method (DCA-100 contact angle tensiometer; First Ten Angstrom, USA). A stock solution of rhamnolipids was prepared in HBSS and then diluted to obtain different concentrations. The critical micelle concentration (CMC) and the surface tension at CMC (γCMC) were determined from the breakpoint of the surface tension versus log surfactant concentration (mM). measurements were performed in triplicates.

5.1.4 Dynamic light scattering

Dynamic light scattering measurements were performed using a Malvern Zetasizer NanoS instrument (Malvern, Worchestershire, UK). Counts (Kcps) of different concentration of rhamnolipids solutions were recorded as previously reported (Perinelli et al., 2016). CMC was determined by the straight-line interception method. Measurements were performed in triplicates.

5.1.5 Chemical characterization of rhamnolipid mixture

The negative ESI mass spectrum obtained after direct injection of the rhamnolipid mixture clearly shows two main molecular ions (M-1) with a larger relative abundance. These ions have 503 m/z and 649 m/z, denoting the predominance in the mixture of rhamnolipids with molecular weight of 504 and 650 Da. According to the literature, these molecular weights can be attributed to mono-rhamnolipids (Rha-C8-C12 and Rha-C10-C10) and di-rhamnolipids (Rha-Rha-C8-C10 or Rha-Rha C10-C10) (Déziel et al., 2000). The other ions in the range between 450 m/z and 700 m/z have a relative abundance less than 20% and they can be attributed to the presence in the mixture of smaller amounts of additional rhamnolipids such as Rha-C8-C10 (475 m/z), Rha-C10-C12:1 (529 m/z), Rha-C10-C12 (531 m/z), Rha-Rha C10-C8 (621 m/z) (Figure 5.3). Considering the fragmentation ions, the most abundant are 333 m/z and 187 m/z, which can be ascribed to Rha-C10 (334 MW) and 3-hydroxydecanoic acid (188 MW), suggesting that the main rhamnolipids of the mixture are Rha-C10-C10 (504 MW) and Rha-Rha-C10-C10 (650 MW). This was also confirmed by repeating the mass spectra at increasing fragmentor voltage (from 0 to 120 V) in order to increase the fragmentation of the molecules. In this case, an increase in the relative percentage of 333 m/z ion (Rha-C10) was observed, confirming the presence, as main components of the mixture, of rhamnolipids bearing a C10-hydrocarbon chain (SF1). Mass analysis also confirmed the purity of the rhamnolipid mixture as declared by the manufacturer (90%). An estimation (semi-quantitative determination) of the relative amounts (%) of the mono- and di-rhamnolipids in the mixture after derivatization was achieved through HPLC. Figure 5.2 A reports the obtained chromatogram, which presents three distinctive eluted peaks. The sharper peak with the lowest retention time is ascribed to the excess of the derivatization agent (2-bromo acetophenone). The other two peaks are referred to mono- (3.8 min of retention time) and di-rhamnolipids (7.9 min of retention time) in the mixture detected as phenacyl esters. These peaks were identified according to literature (Vijaya et al.,

2014). An additional proof of their identification can be given by UV spectra related to the peak (Fig. 5.2 B). From the ratio of the integrated area the relative percentage of the components were calculated as 63-67% of the di-rhamnolipids and 37-33% of the mono-rhamnolipids.

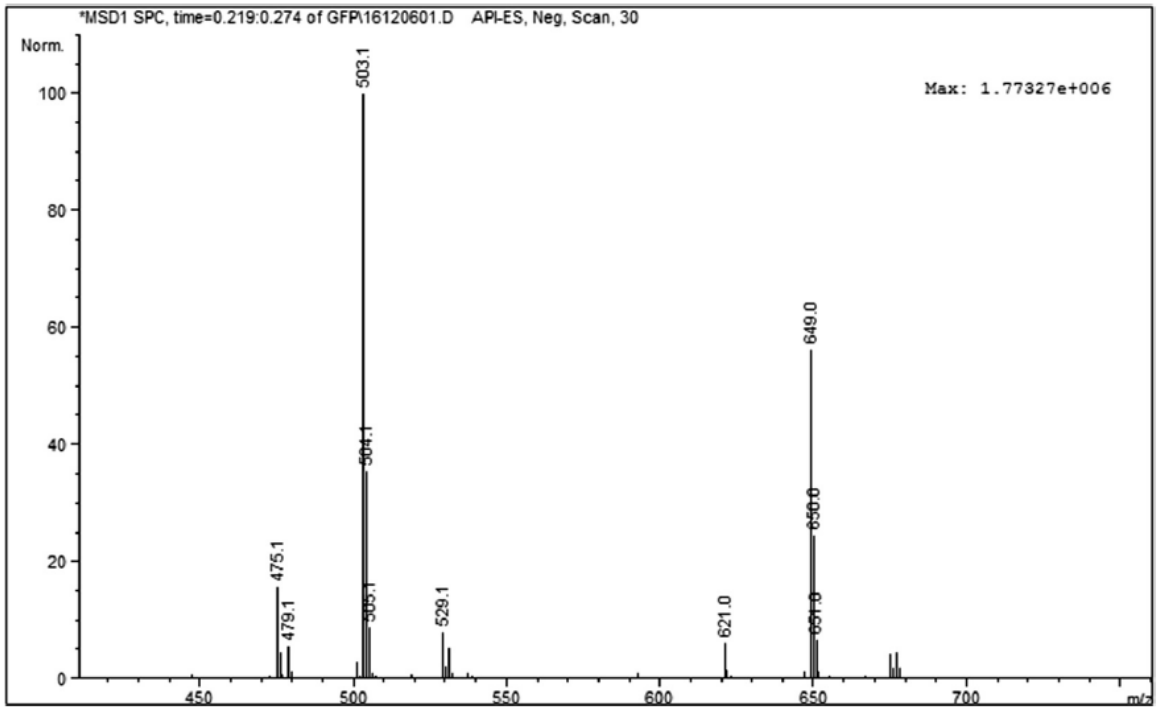

Figure 5.1: ESI negative mass spectrum of rhamnolipid mixture (Fragmentor voltage 30 V).

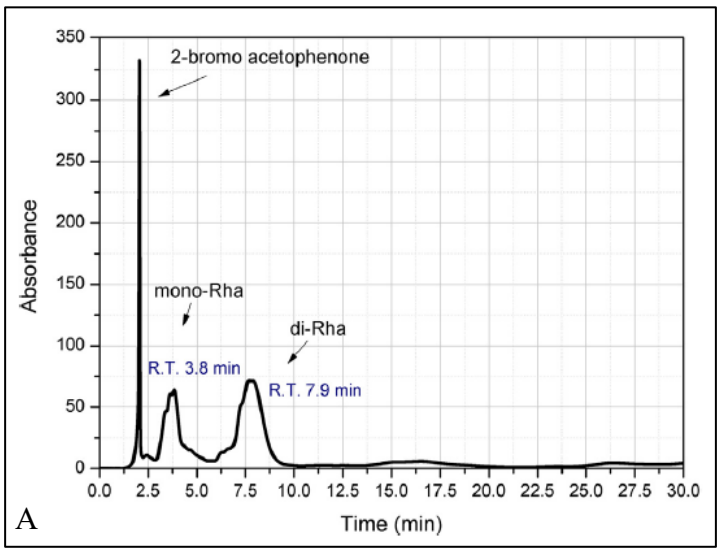

Figure 5.2: A) Chromatogram obtained from the HPLC separation of mono- and dirhamnolipids after derivatization as phenacyl esters.

B) UV spectra referred to the eluted peaks obtained from HPLC separation of mono- and di-rhamnolipids after derivatization as phenacyl esters

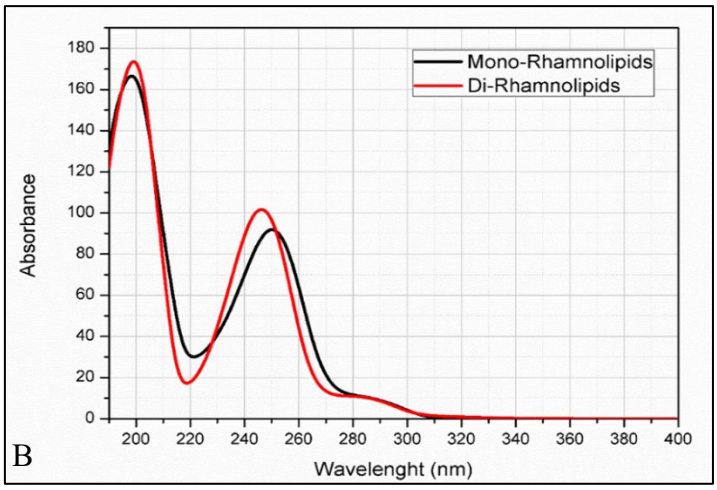

Surface tension and CMC determination

Figure 5.3 shows the results obtained from tensiometry and dynamic light scattering (counts) analysis. These techniques were employed to determine the critical micelle concentration (CMC) of the rhamnolipid mixture. Both plots display two evident breakpoints of the experimental data, which can be considered as the CMC of the surfactant mixtures. In the surface tension vs concentration plot, the plateau indicates the concentration at which the air-water interface is completely saturated by the rhamnolipids. On the other hand, in the counts vs concentration plot, the increase in the scattered light to the detector (counts) is associated with the formation of mixed rhamnolipid surfactant micelles and/or aggregates (Topel et al., 2013). The CMC values calculated by the two techniques were found to be 88±7 µg/ml by tensiometry and 112±7 µg/ml by DLS. Surface tension at CMC (γCMC) was 27.3±0.6 mN/m.

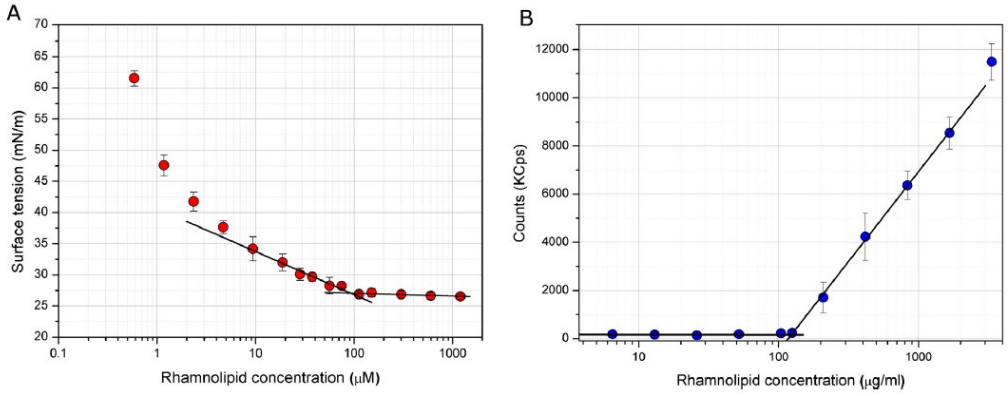

Figure 5.3. Surface tension vs different concentrations of rhamnolipids in HBSS measured by force tensiometry at 37 °C (A). Counts vs different concentrations of rhamnolipids in HBSS measured by dynamic light scattering at 37 °C (B).

5.2 Characterization of the lipid structures of rhamnolipid:

5.2.1 X-ray diffraction experiments: Structural organization of rhamnolipid molecules in concentrated conditions

5.2.1.1 Preparation of samples for diffraction measurements (XRD)

For the preparation of the samples for XRD measurements, we used:

- 90% purity rhamnolipid: produced by Sgma-Aldirich. It has a grainy appearance and yellow-ocher color. As already explained, it consists of a mixture of mono and di-rhamnolipids;
- milliQ water.

Several rhamnolipid concentrations were prepared in water milliQ for a total amount of 30 mg of sample. The water weight concentrations used are reported in Table 5.1.

[Concentration w/w]	Rhamnolipid (g)	H_2O milliQ (µl)
10 %	0.027	3
15 %	0.025	5
20 %	0.024	6
30 %	0.021	9
40 %	0.018	12
45%	0.017	13.5

Table 5.1: Rhamnolipid concentrations in water milliQ

The samples are inserted inside the 1 mm thick Teflon disk hole and sealed by two thin sheets of mylar which make up the windows through which the X radiations pass. Externally two perforated aluminum discs are positioned. The whole is sealed by a brass shirt formed by two cylindrical parts that close together and sealed with four screws to prevent the sample from drying out. In this operation the formation of air bubbles which would produce interferences with the X-ray diffraction spectra must be avoided. The samples were measured as a function of temperature, from 20 to 60°C, increasing the temperature by 10°C. At the end of each measurement before moving on to the next one, the image printed on the photographic plate is scanned and displayed on the computer with the ImageJ Launcher software. Subsequently, the diffraction analysis is performed with the IgorPro program.

5.2.1.2 Spectral analysis of rhamnolipid diffraction

Rhamnolipid solutions in water at different concentrations have been analyzed as the temperature changed.

The X-ray diffraction spectra have been digitized and subsequently analyzed with the Image J and IgorPro programs.

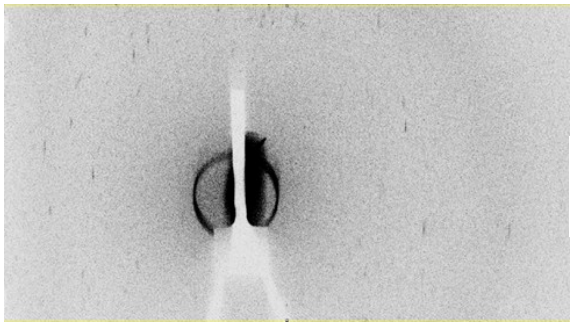

Figure 5.4 Sample diffraction image at 10% w / w at 20 ° C

The first image obtained after a diffraction experiment (Figure 5.4) has a central white portion due to the presence of the beam stop which blocks the direct X-ray beam. Around this there are concentric circles that are the result of diffraction. By selecting a radial portion of the image, pixels are converted to intensity and reported as a function of the distance (in pixels) on a two-dimensional graph which can be saved as a text file and loaded onto the IgorPro program. Before performing the sample data analysis, it is necessary to calibrate the instrument through the model spectrum of the tricosane. From the trichosane diffrattometric analysis we can obtain the calibration line that allows the conversion from the distance measured in pixels from the center of the beam into the values of the q (the modulus of the scattering vector), measured in $Å^{-1}$. The rhamnolipid diffraction spectra are shown in Fig. 5.5 at water concentrations from 10 to 45 w/w % measured at different temperatures from 20 to 60°C.

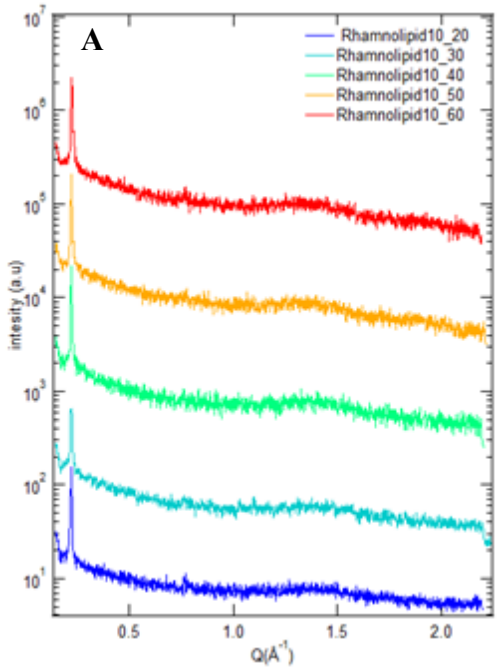
A
Rhamnolipid10_20
Rhamnolipid10_30
Rhamnolipid10_40
Rhamnolipid10_50
Rhamnolipid10_60
intesity (a.u)
Q(Å^{-1})

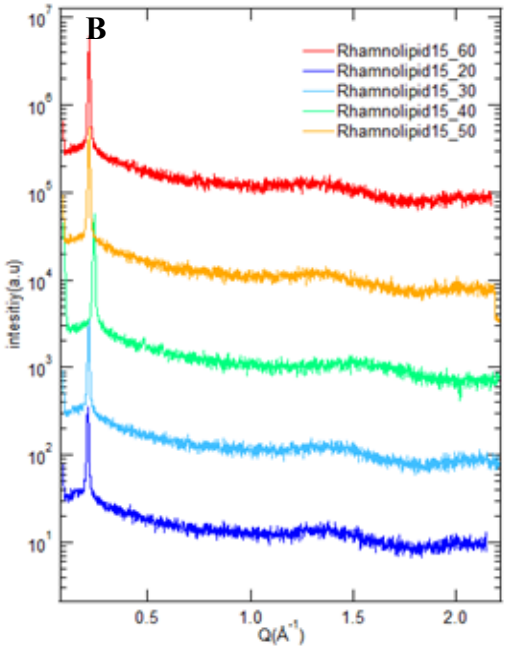
B
Rhamnolipid15_60
Rhamnolipid15_20
Rhamnolipid15_30
Rhamnolipid15_40
Rhamnolipid15_50
intesity(a.u)
Q(Å^{-1})

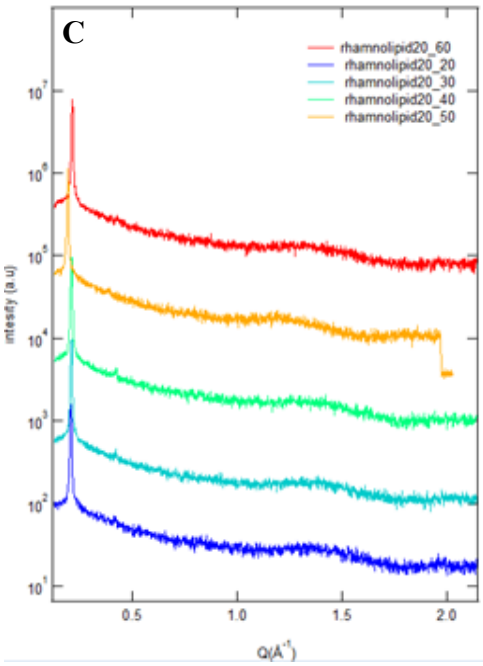
C
rhamnolipid20_60
rhamnolipid20_20
rhamnolipid20_30
rhamnolipid20_40
rhamnolipid20_50
intesity (a.u)
Q(Å^{-1})

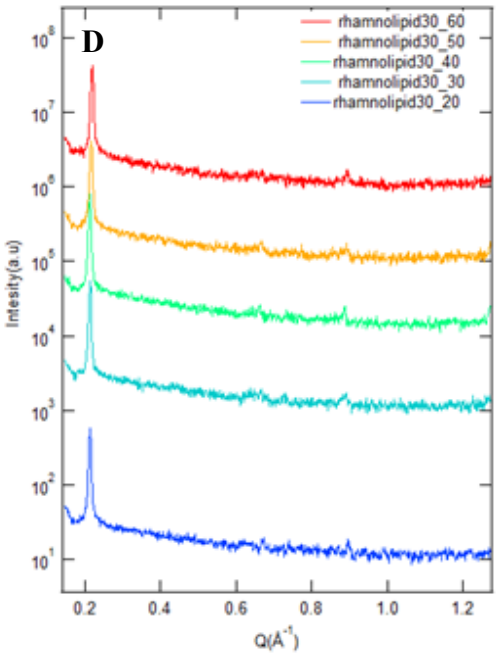
D
rhamnolipid30_60
rhamnolipid30_50
rhamnolipid30_40
rhamnolipid30_30
rhamnolipid30_20
Intesity(a.u)
Q(Å^{-1})

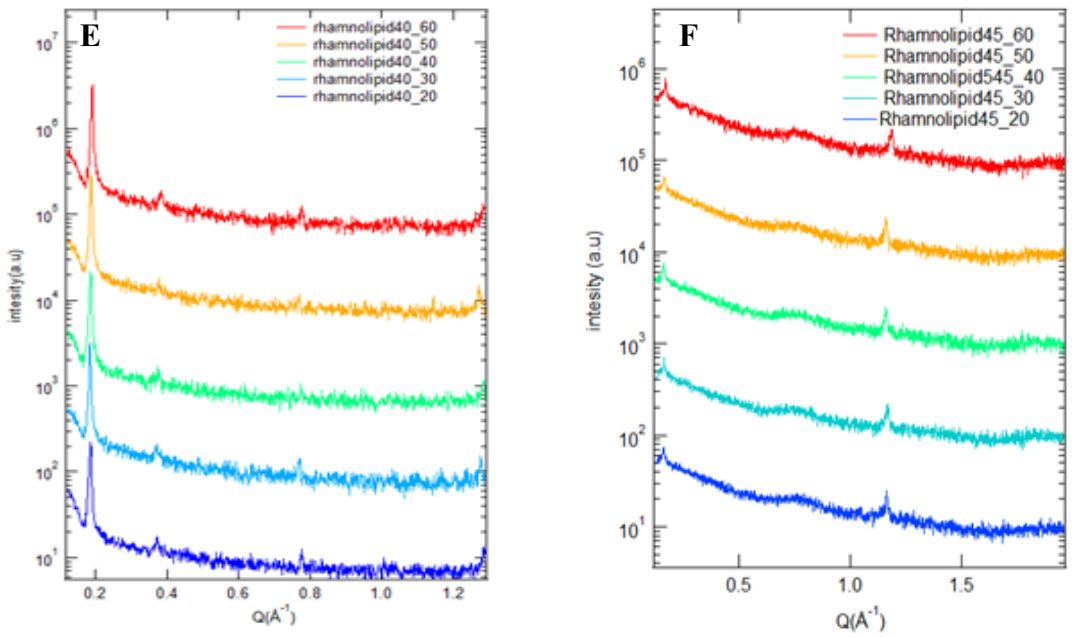

Figure 5.5: Rhamnolipid diffraction spectra at different temperatures and water concentrations. In each panel, from top to bottom, red, orange, green, cyan and blue curves refer to 10°, 20°, 30°, 40°, 50° and 60°C, respectively. A) 10% w/w; B) 15% w/w; C) 20% w/w; D) 30% w/w; E) 40% w/w; F) 45% w/w.

The experiments have been conducted in the temperature range from 20 ° C to 60 ° C. We highlight the presence of a low q peak due to a lamellar phase (L), present in all concentrations. It is worth noting that the unit cell d of a lamellar system (Figure 5.6) is given by the contribution of the lipid layer and the water that interposes among them. By combining the Bragg law (eq. 4.1) and the definition of q (eq. 4.3) it is possible to calculate the cell parameter d from the position q_1 of the first Bragg peak (n=1):

eq. 5.1 $$d = 2\pi / q_1$$

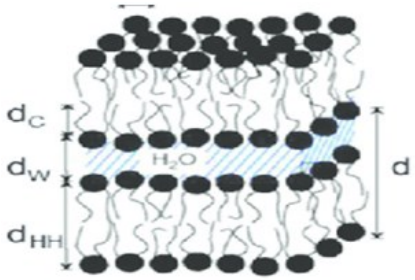

Figure 5.6: cell parameter d of the lamellar phase is given by the sum of the thickness of the bilayes d_{HH} and the thickness of the water d_W

Cell parameters *d* have been determined for each curve. Results, reported in Fig. 5.7, clearly show that, by increasing the temperature, the cell parameter remains almost constant, indicating that temperature does not determine a phase change of RL.

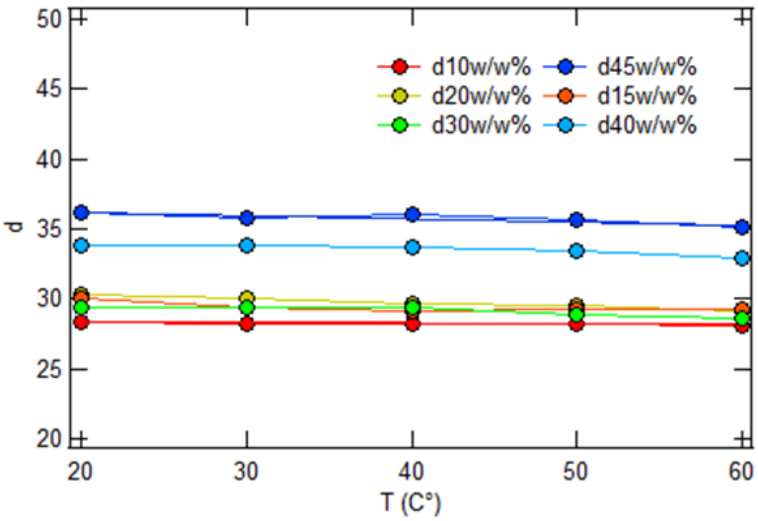

Figure 5.7: Graph of cell parameter *d* as a function of temperature variation

Placing in a single graph all the concentrations investigated at the temperature of 30°C (Fig. 5.8 A), it is noted that the Bragg peak, as the water concentration increases, shifts towards lowe *q* values lower, compatible with an increase in the cell values *d* (Figure 5.8 B).

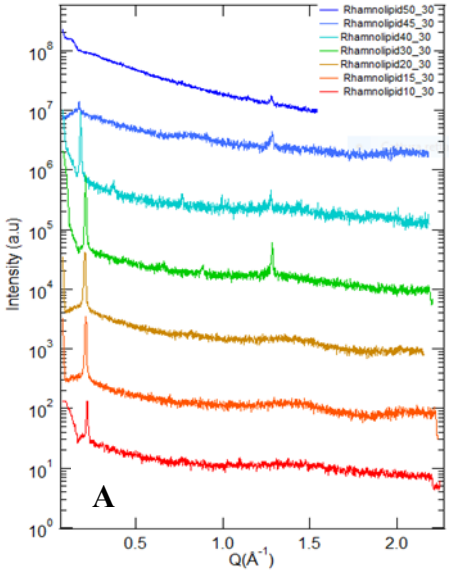

Figure 5.8 A) Diffraction of the Ramnolipide at different concentrations keeping the temperature constant B) Graph d according to the concentration w / w% at the same temperature

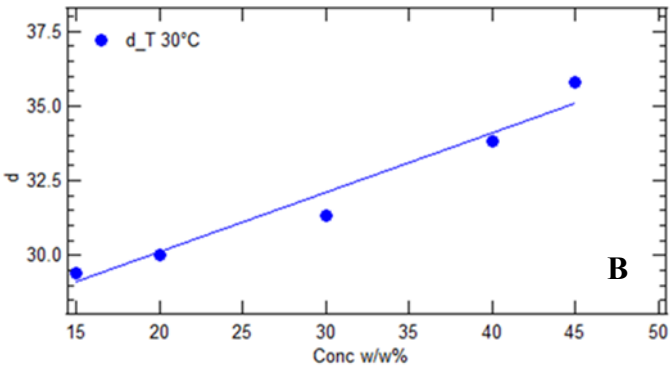

At concentrations of water greater than 50% w/w (Fig. 5.9) the samples become more diluted, losing their previously observed lamellar organization. In fact, it passes from a lamellar to an isotropic phase that can not be observed with simple diffraction. The technique to be used in

this case is SAXS (Small Angle X-ray scattering), in which the dispersion of X-rays from the sample is collected at small q values (typically from 0.01 to 0.5 $Å^{-1}$).

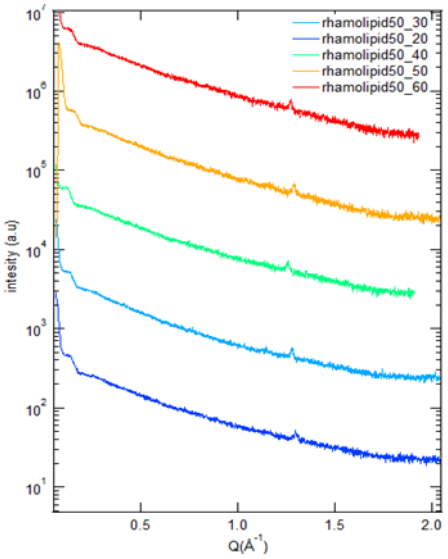

Figure 5.9: 50% w / w sample diffraction spectrum in which the peak of the lamellar phase is no longer present. The sample is undergoing a phase change.

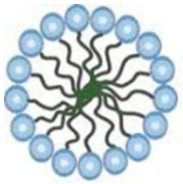

Lam ⟹ Iso

Micelle Phase

5.2.2 SAXS experiments:

5.2.2.1 Structural organization of rhamnolipid molecules in diluted conditions

The prepared samples had the following characteristics:

- Four different rhamnolipid concentrations: 10, 15, 25, 35 and 47 mM

These concentrations were tested in the absence of oil and in the presence of oil at 2 v/v volume fraction ϕ_O= 0.002 and ϕ_O =0.02. SAXS experiments were conducted at the Brazilian LNLS synchrotron at temperature 13° and 22°C.

Before carrying out the synchrotron SAXS experiments preliminary tests with the laboratory Nanostar instrument (University of Sao Paulo, Brazil) have been performed, at 3 RL concentrations and in the absence of oil: 28.2, 42.2 and 84.5 mM. Corresponding curves are shown in Fig. 5.10. These curves show a typical profile of a micellar system, with a bump at high *q* attributed to the electron density contrast between polar and paraffinic domain within a micelle and a broad peak at low *q*, which modifies its position with concentration, indicating a correlation of the positions of the micelle centers. Curve have been then analysed with the GENFIT software (Spinozzi, Ferrero, Ortore, De Maria Antolinos, & Mariani, 2014), by adopting the model of interacting spherocylinders. The the effective structure factor is depicted

with the DLVO potential in the framework of the Random Phase Approximation (RPA) (Spinozzi, Mariani, & Ortore, 2016). A detailed explanation of this model is hereafter reported.

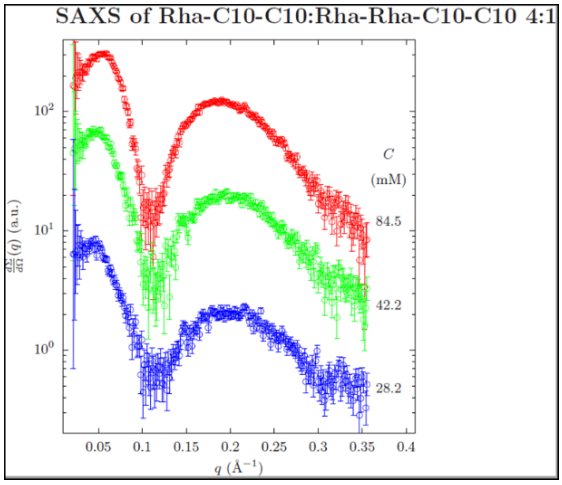

Figure 5.10: Curves obtained at the Nanostar. Three different concentrations of rhamnolipid without the presence of oil.

Form factor of a two-density level spherocylinder

The SAXS amplitude of a two-density level spherocylinder with its long axis forming an angle β with the scattering vector q is:

eq. 5.2 $$A(q,\beta) = 4\pi \sum_{k=1}^{2}(\rho_k - \rho_{k+1})R_k^2 \times \int_0^1 x\left[R + R_k(1-x^2)^{\frac{1}{2}}\right]J_0(qR_k x sin\beta) \times \frac{sin\left[q\left(R + R_k(1-x^2)^{\frac{1}{2}}\right)cos\beta\right]}{q\left(R + R_k(1-x^2)^{\frac{1}{2}}\right)cos\beta}\,dx$$

where L is the length of the cylindrical part, R_1 is the the inner cylinder radius and the inner radius of the two hemispherical caps, R_2=R_1+δ, δ being the shell thickness. The electron densities of core, shell and matrix are ρ_k (with k=1,2 and 3, respectively). J_0 (x) is the zero-th order Bessel function. A graphical representation of the RL molecules organized within the spherocylinder is reported in Fig. 5.11

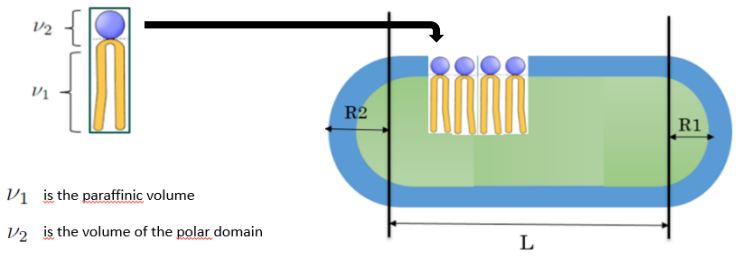

Figure 5.11: Schematic representation of the organization of rhamnolipid molecules in the spherocylinder

The orientational average form factor and squared form factor are

eq. 5.3 $$P_1(q) = \int_0^{\frac{\pi}{2}} sin\beta A(q,\beta)^2 d\beta$$

eq. 5.4 $$P(q) = \int_0^{\frac{\pi}{2}} sin\beta [A(q,\beta)^2] d\beta$$

DLVO Interaction potential

The DLVO interaction potential is the sum of three terms, hard-spheres (HS), screened Coulumbian (C) and Yukawian attractive term (A),

eq. 5.5

$$u(r) = u_{HS}(r) + u_C(r) + u_A(r)$$

$$u_{HS} = \begin{cases} +\infty & r < 2R \\ 0 & r > 2R \end{cases}$$

$$u_C(r) = \frac{Z^2 e^2}{\varepsilon(1+k_D R)^2} \frac{exp[-k_D(r-2R)]}{r}$$

$$u_A(r) = -2JR \frac{exp[-(r-2R)/d]}{r}$$

Parameters of this potential are:

R effective radius of the particle

Ze charge of the particle

ε dielectric constant

K_D reciprocal Debye-Huckel screening length

J depth of the attractive potential at contact (r = 2R)

d range of the attractive potential

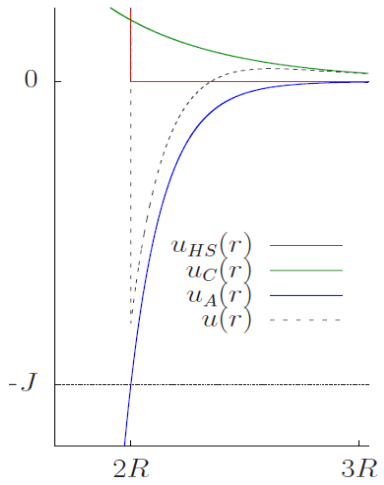

Figure 5.12: DLVO potential and their three contributions

Random Phase Approximation (RPA)

According to this approximation, the particle-particle structure factor is expressed by

eq. 5.6 $$S(q) = \frac{S_0(q)}{1 + \beta n_p S_0(q)[U_C(q) + U_A(q)]}$$

where $S_0(q)$ the MSA structure factor, depending on the volume fraction η,

eq. 5.7 $$[S_0(q)]^{-1} = 1 - \frac{12\eta[\eta(3-\eta^2)-2]}{(1-\eta)^4} \frac{j_1(2Rq)}{2Rq}$$

The other component of eq. 5.7 are

eq. 5.8 $\beta = 1/k_B T$

eq. 5.9 $j_1(x)$: first order spherical Bessel function

eq. 5.10 $\eta = n_p V_p$: particle volume fraction

eq. 5.11 $U_i(q) = 4\pi A_j \frac{k_j sin(2qR)+qcos(2qR)}{q\left(q^2+k_j^2\right)}$: Isotropic Fourier Transform of $u_i(r) = A_j exp\left[-k_j(r-2R)\right]/r$

where kB is Boltzmann's constant and T the absolute temperature.

The effective structure factor is calculated according to the equation

eq. 5.12 $$S_M(q) = 1 + \frac{[P_1(q)]^2}{P(q)}[S(q) - 1]$$

Fitting results

Fitting curve obtained with GENFIT adopting the interacting spherocylinder model are reported as solid black lines in Fig. 5.13. The fitting parameters are shown in Table 5.2.

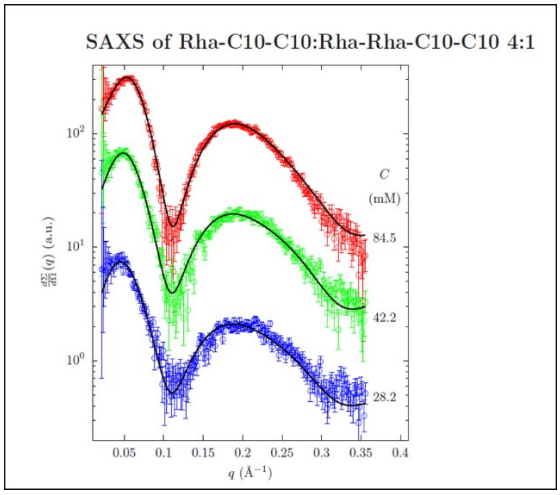

Figure 5.13: Curves obtained at the Nanostar. Three different concentrations of rhamnolipid without the presence of oil with the fitting parameters (Table 5.2)

To note, the small aggregation number, around 40, does not change with RL concentration. Moreover, the net electric charge per RL polar head, which is -0.16, indicating a partial dissociation of carboxylic acids, is the main responsible of the broad interation peak at low q. On the other hand, the small value of J shows that the attractive potential term is negligible.

Fitting Parameters	
R_1 (Å)	10.5 ± 0.6
$\delta = R_2 - R_1$ (Å)	11.9 ± 0.4
N agg (a)	42 ± 3
N agg (b)	47 ± 3
N agg (c)	48 ± 3
v_{CH2} (Å^3)	25.07 ± 0.03
v_{CH3} / v_{CH2}	1.301 ± 0.001
v_w (Å^3)	29.97 ± 0.01
d_W	1.04 ± 0.02
J (k_B T)	0.09 ± 0.06
d (Å)	3 ± 1
z (q_e)	- 0.16 ± 0.01
γ	1.6 ± 0.6
k (10^{-7} a.u.)	9.1 ± 0.6
B (a.u)	0.356 ± 0.008

Table 5.2: Fitting parameters of rhamnolipid without the presence of oil.

Chapter 6

Toxicity tests:

6.1 Interaction with GUVs

6.1.1 Electroformation for the synthesis of GUVs

The classical technique for the formation of giant liposomes is first to dissolve lipids (or mixtures of lipids) in an organic solvent, and a film of lipid solution is then spread on a support, such as glass, (Reeves & Dowben, 1969). The organic solvent is evaporated and the lipids are hydrated at a temperature above the main phase transition temperature (Tm) of the lipid components in the mixture in order to prepare giant liposomes (Akashi, Miyata, Itoh, Kinosita, & Jr, 1996; Hishida, Seto, & Yoshikawa, 2005; Horger, Estes, Capone, & Mayer, 2009; Walde, Cosentino, Engel, & Stano, 2010). Vaz et al. (Vaz, Kapitza, Stuempel, Sackmann, & Jovin, 1981) and Keller et al. (Keller, Hedrich, Vaz, & Criado, 1988) have successfully used this "gentle hydration technique".

It was first shown by Angelova et al. that a high yield of giant unilamellar vesicles is expedited if rehydration of dried lipids plaque is assisted by an electric field (M. I. Angelova, Soléau, Méléard, Faucon, & Bothorel, 1992; Bernardino de la Serna, Perez-Gil, Simonsen, & Bagatolli, 2004; Estes & Mayer, 2005; Husen, Arriaga, Monroy, Ipsen, & Bagatolli, 2012). The process is known as electroformation. It was reported by Husen et al. that the electroformation based GUV preparation method involving dissolution of lipids in an organic solvent produce a system of GUVs with small variability in composition. Electrofusion of a calculable composition of single or two-component GUVs prepared by electroformation to prepare single GUV of three lipid components has been also reported (Bezlyepkina, Gracià, Shchelokovskyy, Lipowsky, & Dimova, 2013), which shows improved compositional homogeneity.

GUVs were prepared by the electroformation procedure (Miglena I. Angelova & Dimitrov, 1986) using POPC; POPC/RHO-PE (1 mol %) and DOPC , SM, CHOL (molar ratio 1:1:1) and RHO-PE (1 mol %). All other chemicals and solvents were purchased from Sigma Aldrich (Saint Louis, MO) and used without further purification: POPC (SIGMA ALDRICH, 2-Oleoyl-1-palmitoyl-sn-glycero-3-phosphocholine, ≥95.5% (GC), ≥98% (TLC), DOPC, (SIGMA ALDRICH 1,2-Di (cis-9-octadecenoyl)-sn-glycero-3-phosphocholine, 3-sn-Phosphatidylcholine, 1,2-dioleoyl, L-α-Phosphatidylcholine, dioleoyl, L-β,γ-Dioleoyl-α-

lecithin) SM (SIGMA ALDRICH, N-Acyl-4-sphingenyl-1-O-phosphorylcholine, N-Acyl-D-sphingosine-1-phosphocholine, Chol (SIGMA ALDRICH, 3β-Hydroxy-5-cholestene, 5-Cholesten-3β-ol) and Rho-PE. Briefly, 20 μL of 2 mg/mL lipid chloroformic solution containing up to 0.1 mol % of RHO-PE were spread on the surfaces of two conductive glass slides coated with indium tin oxide (ITO slides, Sigma Aldrich, Saint Louis, MO. The glass slides were placed with their conductive sides facing each other and separated by a 2 mm thick Teflon frame. The chamber was filled with 0.2 M sucrose solution. The glass plates were connected to a function generator of 2 V with a 10 Hz frequency applied for 2 h. The GUVs were observed in the following day after adding a glucose solution. In detail, a solution containing 600 μl of electroformed GUVs and 100 μl of glucose solution in water 0.2 M, was prepared in eppendorf. The osmolarities of the sucrose and glucose solutions were measured with a cryoscopic osmometer Osmomat 030 (Gonotec, Germany) and carefully matched to avoid osmotic pressure effects. The electroformation of the GUV of DOPC/SM/CHOL was conducted in a thermostat at 40 °C for 2 hours.

Vesicles were observed in the phase contrast mode by means of an inverted microscope Axiovert 200 (Carl Zeiss; Jena, Germany) equipped with a Plan Neo-Fluar 63X Ph2 objective (NA 0.75) and A-plan 10X Ph1 (NA 0.25). Images were recorded with an AxioCam HSm digital camera (Carl Zeiss). All measurements were done at 23±2°C. The observations of both GUV systems were also conducted with a fluorescence and phase contrast microscope (40X) for a maximum time of 40 minutes (Microscope Axiovert 200 (Carl Zeiss; Jena, Germany).

Preparation of GUVs with electroformation

The following reagents were used for the preparation of the GUV and the slides for observation under an optical microscope:

POPC (2-oleoyl-1-palmitoyl-sn-glycero-3-phosphocholine) in solid form

Purity degree < 99%

MW: 760.10

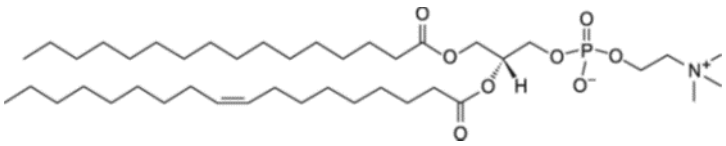

Synthetic origin

Conservation: -20 ° C

Cholesterol:

Solid form, degree of purity <99%,

MW 386.65

Conservation: -20 °C

DOPC (1,2-Dioleoyl-sn-glycero-3-phosphocholine) liquid form

Conservation: -20°C,

MW :786.113

Purity degree <99%

DPPC (1,2-dipalmitoyl-sn-glycero-3-phosphocholine)

MW: 734.039

Purity degree >99%

Conservation -20°C

Sphingomyelin

MW: 815.241

Purity degree > 99%,

Conservation -20 ° C

All of these lipids listed are products of Avanti Polar Lipid ®

Rhodamine

Dye emitting fluorescence that binds vesicle lipids and allows visualization through the fluorescence microscope of any effects on the GUV that are not visible in the bright field.

MW: 1319.75

Conservation -20 ° C

Chloroform: in liquid form

Molecular formula: $CHCl_3$

MW: 119.38

Sucrose: in solid crystalline form

Degree of purity ≥99.0%

Molecular formula $C_{12}H_{22}O_{11}$

MW: 342.30

D - (+) glucose: in solid crystalline form

Molecular formula: $C_6H_{12}O_6$

MW:180.16

Solutions:

- 0.2 M sucrose solution in distilled water
- 0.2 M glucose solution in distilled water
- POPC solution in chloroform 10.3 mg / ml
- POPC / RHODAMINE solution 0.2%
- DOPC / SM / CHOL solution (1: 1: 1) + RHODAMINE 0.2%
- DOPC / DPPC + RHODAMINE 0.2% solution

Instrumentation

- ITO (indium tin oxide) glass slides. They are slides able to conduct electricity on one of the two surfaces and present this darker compared to normal slides precisely following this characteristic.
- Menzel-Gläser storage boxes 26 x76mm
- Thermo-Scientific coverslips 20 x 40 mm, no.1 thickness
- Hamilton syringes with a capacity of 10 µl
- Teflon separators

- GW INSTEK current generator - GFG-8015G
- TeKTromix DMM 249 TRUE RMS meter
- Fluorescence microscope

Preparation for the electroforming chamber

Through a Hamilton syringe 10 µl of the lipid solution are taken and are spread over both conductive surfaces of the two ITO slides, forming a thin and uniform layer. This step is carried out at enviromental temperature and allowed to air-dry until complete evaporation of the organic solvent. The slides are then superimposed with the conductive surfaces facing each other. They are separated by means of a Teflon spacer with a thickness of 2 mm which is made to adhere to the slides and the whole is blocked with clamps. The chamber thus assembled is filled with a 0.2 M sucrose solution, injected through a small hole present on the thickness of the spacer. The application of an electric field accelerates the formation of the vesicles. The slides are connected to the two terminals of the current generator and an alternating current with a frequency of 10 Hz and a potential difference of 1.5 V for 2 hours is applied.

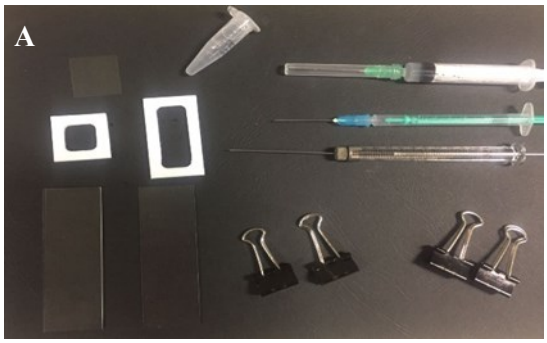

Figure 6.1: A) Laboratory material for the preparation of GUVs. B) Preparation of the electroformation chamber. C) D) Attack of the bedroom to the power generator.

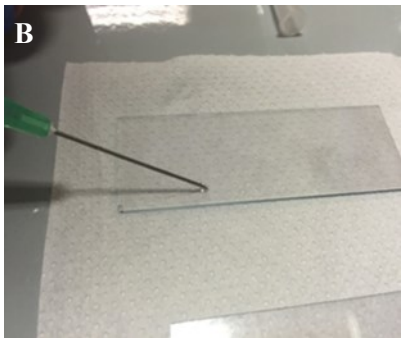

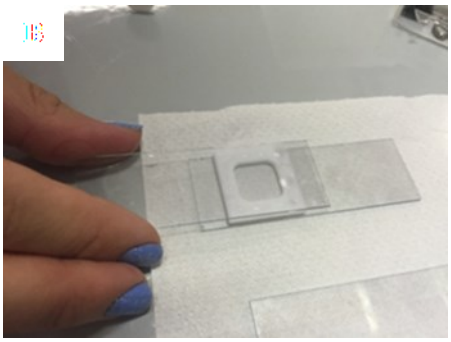

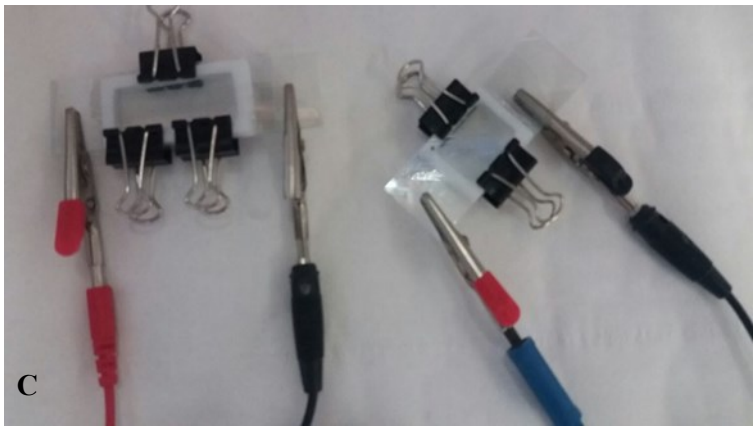

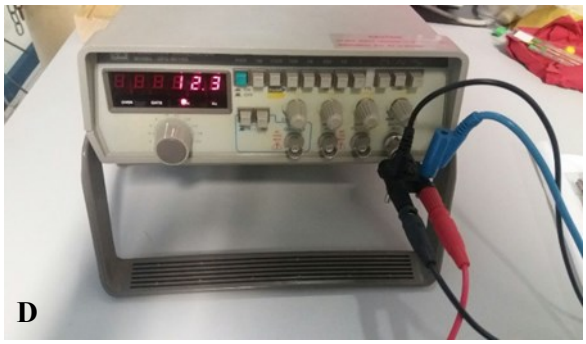

Preparation of microscopy slides

After electroformation, the obtained GUVs were observed under inverted phase and fluorescence contrast microscopy. For the observation an observation room consisting of a:

1) Menzel-Gläser glass slide 26 x76mm

2) Teflon ring 2 mm thick

3) 22 x 22 mm coverslip

The Teflon ring is placed on the glove and the coverslip on it. Then the whole is sealed with silicone placed on both sides of the Teflon ring. The chamber thus formed is turned upside down and a pressure is applied on the sides in order to make the three components adhere to each other better (Figure 6.2).

The Teflon ring is provided with two holes located on opposite sides and through one of these, with the use of a 1 ml insulin syringe, a solution volume of 700 µl is injected into the chamber. The solution consists of 600 µl of glucose and 100 µl of GUV. Once prepared, everything is placed on the microscope and the GUV is expected to settle on the bottom (which takes a few minutes) and stabilize and then go on to observation using the 60X objective.

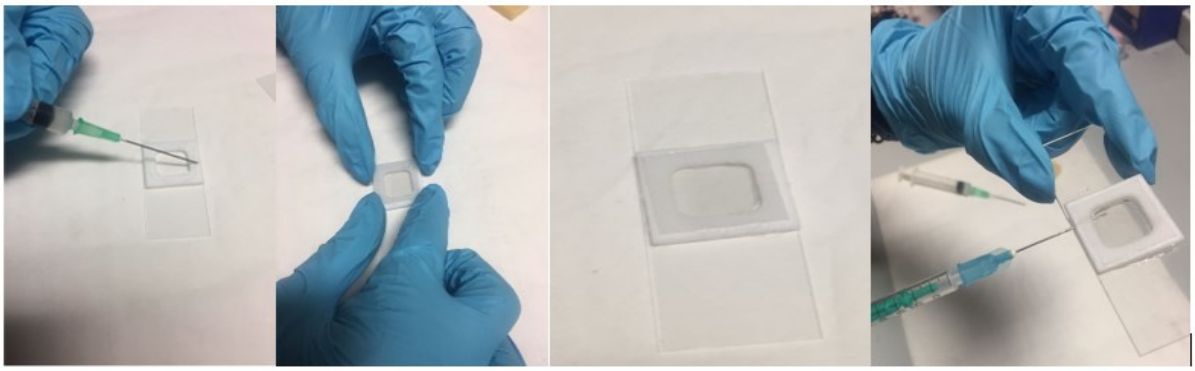

Figure 6.2: Stages of preparation of the observation room

The use of this observation room allows the GUV to be in an isosmotic medium (Glucose 0.2 M) and consequently, being more stable, allows a better monitoring over time.

The use of this system allowed us to follow the effect of the interactions of different concentrations of rhamnolipid on GUV with different composition. The mother solution of the rhamnolipid was obtained by solubilizing 3.6 $x10^{-3}$ g rhamnolipid in 5 ml of glucose, obtaining a concentration of 1.35 Mm.

The 0.2% POPC / RHODAMINE GUVs were tested with the following rhamnolipid concentrations: 0.5 mM, 0.25 mM, 0.16 mM (CMC), 0.05 mM, 0.01 mM.

The GUVs of DOPC, sphingomyelin and cholesterol were made to interact with 0.5 mM and 0.2 mM rhamnolipid solutions.

Considering that the final volume to be introduced into the observation chamber is 700 µl and that the mother solution of rhamnolipid has a concentration of 1.35 mM, the samples were prepared by adding the volumes shown in Table 6.1.

[Rhamnolipid mM]	GUV µl	Glucose µl	Mother Solution Rhamnolipid µl
0.5	100	340	260
0.25	100	470	130
0.20	100	496	104
0.16	100	517	83
0.05	100	574	26
0.01	100	595	5

Table 6.1: Sample preparation

6.1.2 Microscopy analysis with GUVs of POPC

Initially, the RL interactions at different concentrations below and above cmc were conducted on the GUVs of POPC. In the absence of the biosurfactant, GUVs are spherical with very small thermal fluctuations (Figure 6.3).

Water dispersions of GUVs composed by 1 mol % POPC and 0.2 mol % PE-RHO at different concentrations of RL were observed with an inverted microscope in both phase and fluorescence contrast**.**

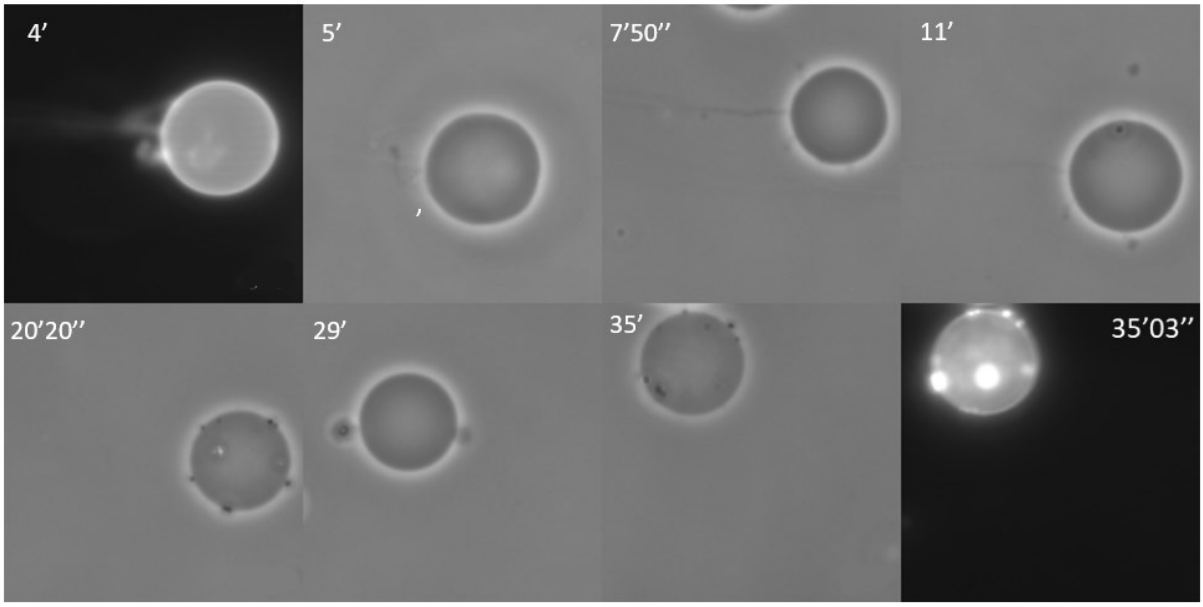

Figure 6.3: GUVs formed by 1 mol % POPC and 0.2 mol % PE-RHO in the presence of 0.16 mM RL (CMC). (63x)

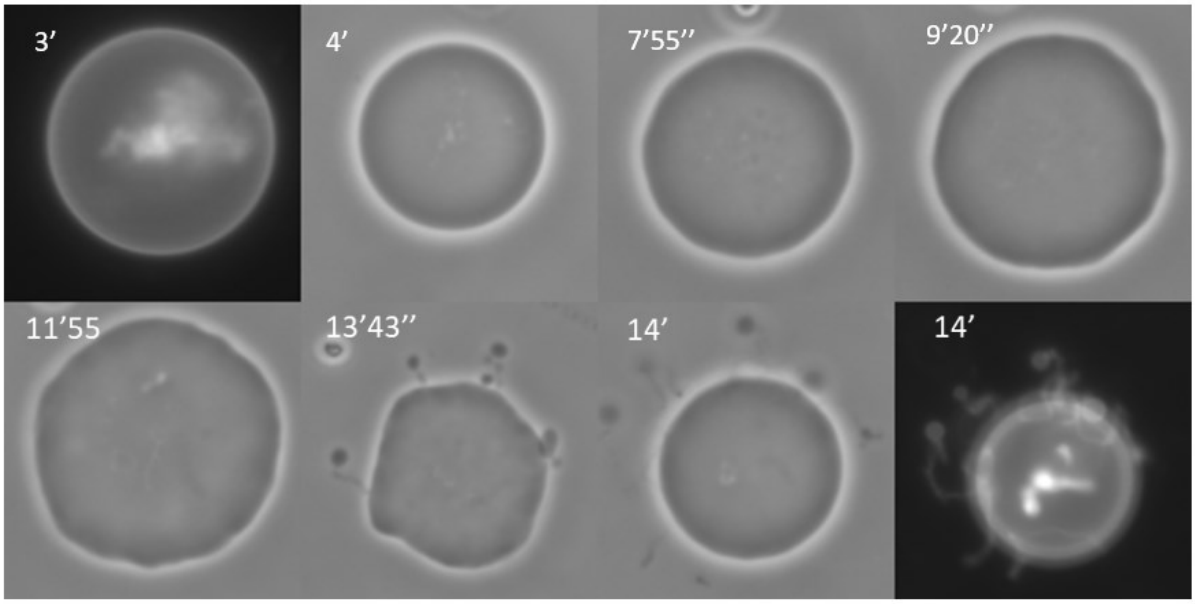

Figura 6.4: GUVs formed by 1 mol % POPC and 0.2 mol % PE-RHO in the presence of 0.50 mM RL. (63x)

At the CMC (Fig. 6.3) the first perturbations are seen after some minutes of incubation. Light perturbations of the native spherical shape of the vesicle are observed, accompanied by some fluctuations.

We can see also the formation of buds. Budding refers to the formation of protrusions that are fluorescent under the microscope and therefore have the lipid composition of the membrane. The formation of these buds are attributed to an excess of air inside the liposomal structure that allows to prevent its "outbreak".

As the concentration of RL increases, these phenomena are more evident and the time intervals in which they occur are lower. In fact, at the concentration of 0.5 mM the effects are observed after 7 minutes (Fig. 6.4), while at 1 mM the first protrusions are observed after 3 minutes.

6.1.3 Microscopy analysis with GUVs of DOPC/SM/CHOL

Subsequently we changed the lipid composition of the membrane system in order to study the effect of RL in the variation of the Lo and Ld phases and therefore when lipid microdomains (referred to as lipid “rafts”) are formed. The lipid mixture used is composed of 1 mol % of DOPC, SM and CHOL in a 1:1:1 ratio.

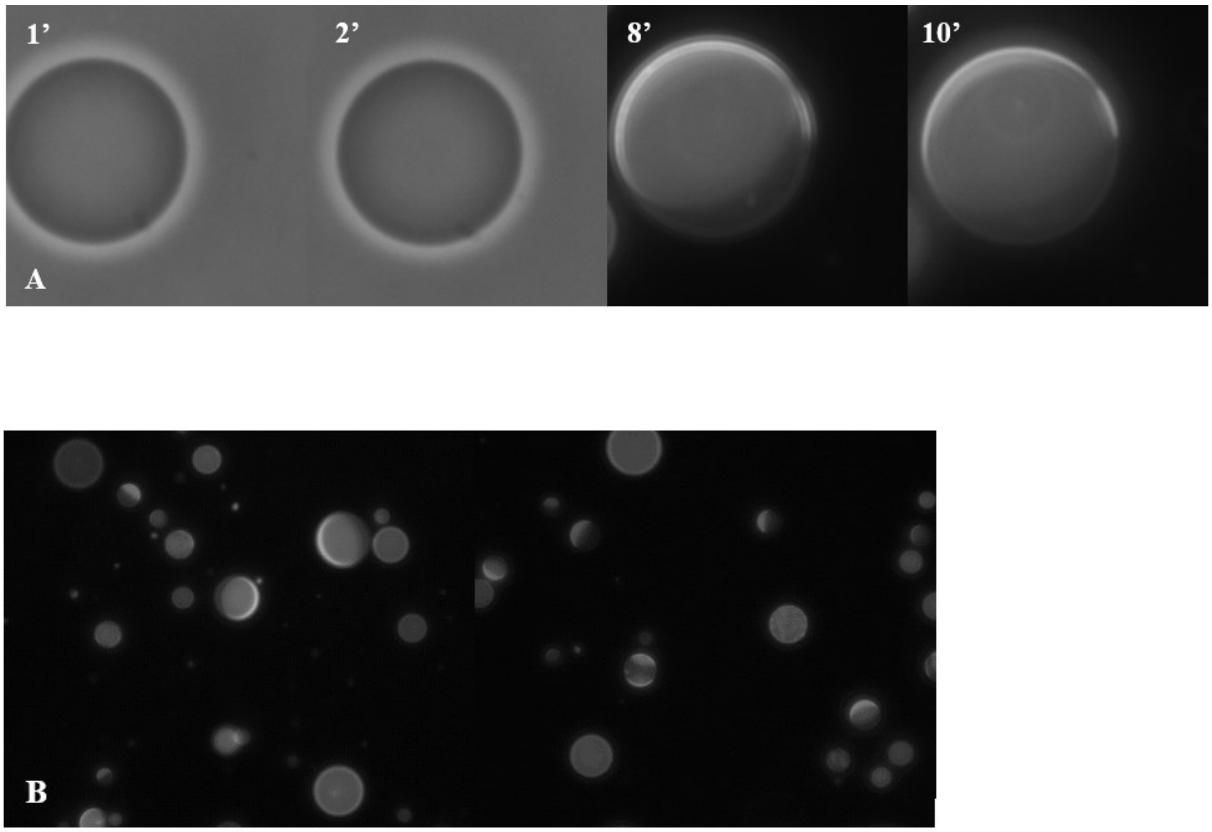

Figure 6.5: A) Control of GUVs of DOPC/SM/CHOL (63x) B) Control of GUVs of DOPC/SM/CHOL (40x)

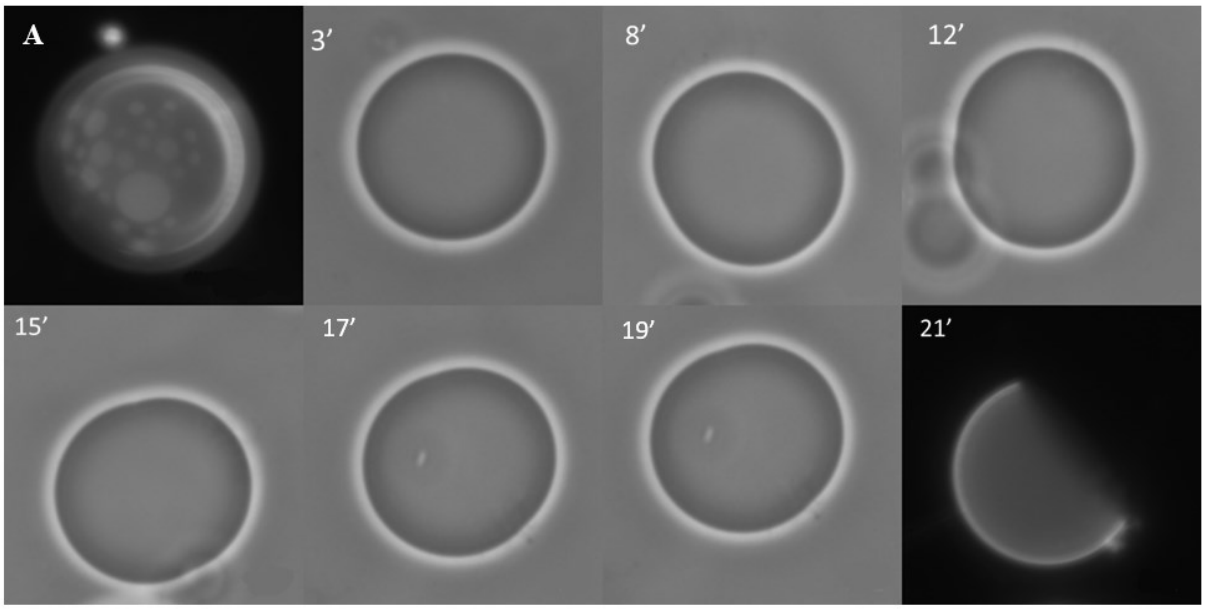

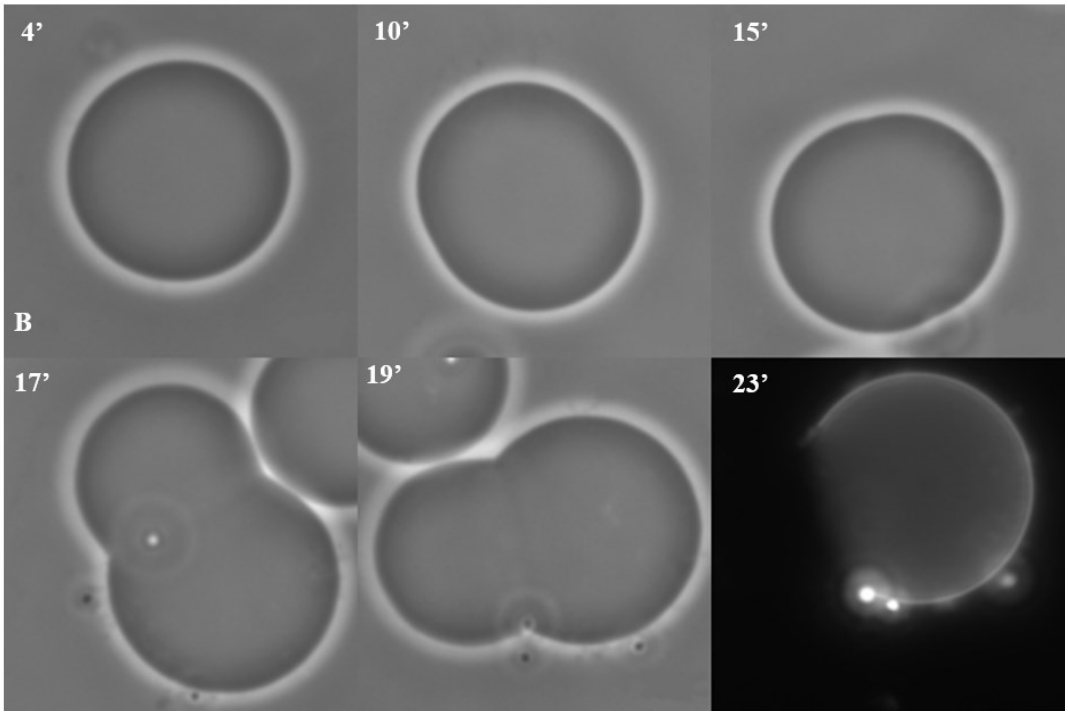

Figure 6.6: GUVs formed by 1 mol % DOPC, SM, CHOL (1:1:1) in the presence of 0.20 mM RL (different GUVs A-B). (63x)

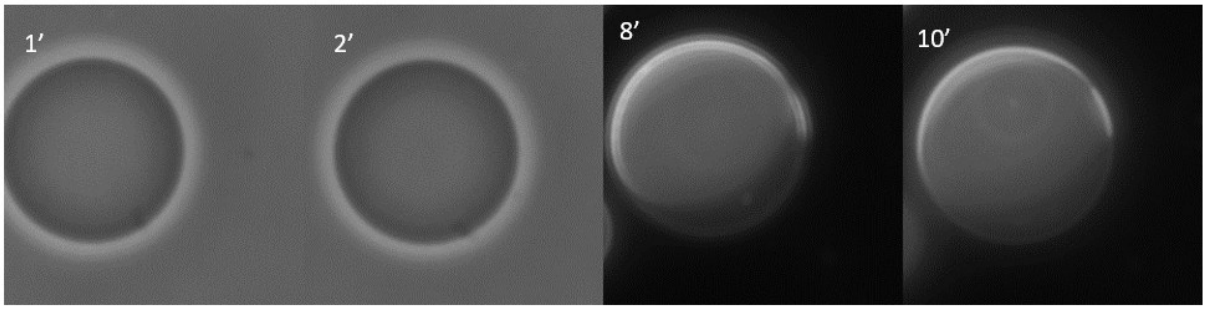

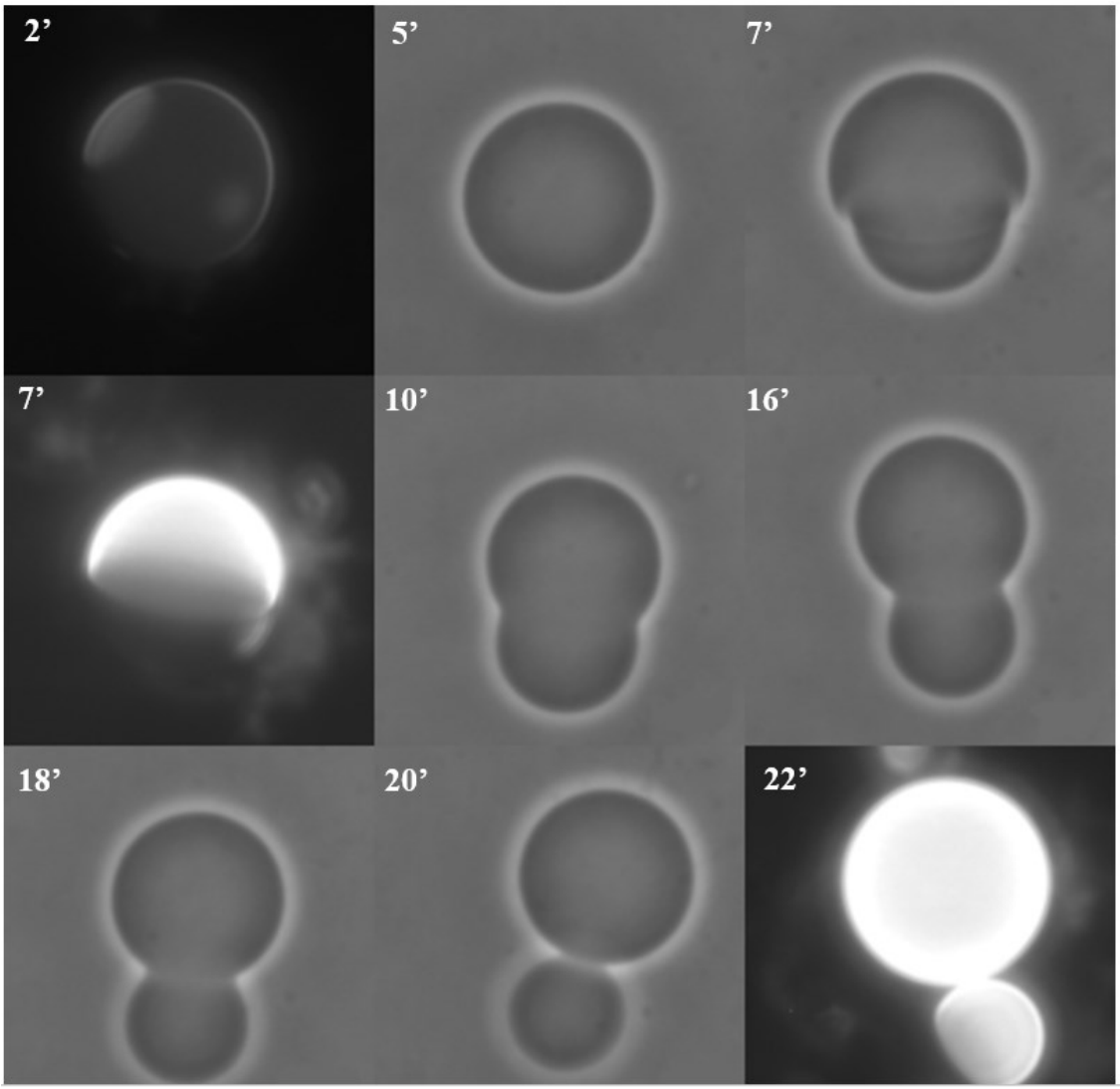

Figura 6.7. GUVs formed by 1 mol % DOPC, SM, CHOL (1:1:1) in the presence of 0.50 mM RL. (63x)

From the images reported in figures. 6.6-6.7 it is observed that RLs induce the fission of the GUV and the speed of this phenomenon increases with increasing concentration. In fact, it can be observed that the fission, at a RL concentration of 0.2 mM, begins after 20 minutes and, in the case of a concentration of 0.5 mM, occurs after 7 minutes (figure 6.7). At the RL concentration of 1 mM the effect is even more rapid and observable after 5 minutes. Furthermore, in this case the budding phenomenon would appear to be observed exclusively in the boundary line between Ld/Ld regions causing the throttling of the GUV.

6.2 Interaction with Erythrocyte

6.2.1 Spectroscopy analysis: Hemolysis rate of erythrocytes

The rate of hemolysis of erythrocytes in the presence of different rhamnolipid concentrations has been monitored over time using three different wavelengths. Hemolysis has been monitored in two ways: by following the scattering light decrease at 650 nm and by following the increase in hemoglobin release (at 415 nm and 575 nm, figure 6.8).

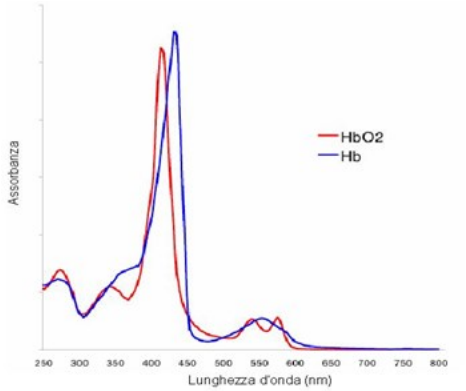

Figure 6.8: Hemoglobin absorption spectrum

We have worked with:

• two rhamnolipid concentrations above the CMC (0.16 mM): 0.5 mM and 0.2 mM;

• two rhamnolipid concentrations below the CMC: 0.1 mM and 0.05 mM.

For the preparation of the samples, the following protocol has been followed (figure 6.9 A,B,C):

• two drops of blood are taken by applying a pressure on the fingertip and are diluted with 1 ml of PBS (PBS = saline phosphate buffer that allows to keep the osmotic pressure unchanged to the whole of erythrocytes);

• the blood suspension is centrifuged for 10 min at 3000 rpm at 25°C;

• centrifugation has been repeated 3 times to ensure that all plasma is eliminated and the isolated erythrocytes;

• 1 ml of PBS is added after washing to resuspend the red blood cell pellet;

• a solution of rhamnolipid (1.35 mM) has been dissolved in PBS at pH 7.4;

• a 96 well plate has been prepared as shown in the next Figure and has been prepared as follows:

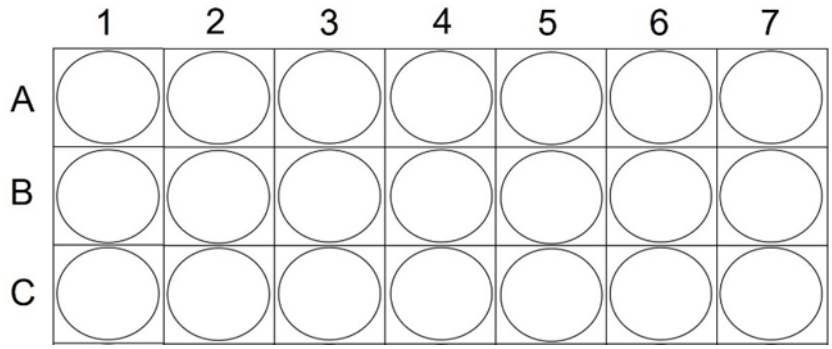

- Column 1- Control (CT): 50 µL PBS + 50 µL RBC;
- Column 2- 0.5 mM Rhamnolipid: 37 µL Rhamnolipid (1.35 mM) + 13 µL PBS + 50 µL RBC;
- Column 3- 0.2 mM Rhamnolipid: 15 µL Rhamnolipid (1.35 mM) + 35 µL PBS + 50 µL RBC;
- Column 4- 0.1 mM Rhamnolipid: 7.5 µL Rhamnolipid (1.35 mM) + 42.5 µL PBS + 50 µL RBC;
- Column 5- 0.05mM Rhamnolipid: 4 µL Rhamnolipid (1.35 mM) + 46 µL PBS + 50 µL RBC;
- Column 6- Lysed Control: 50 µL water + 50 µL RBC + 1 µL Triton X-100;
- Column 7- White: 100 µL PBS.

Each concentration has been repeated three times (A, B, C).

Figure 6.9: A) pellets of red blood cells (in PBS) obtained after centrifugation B) resuspension of pellets with PBS C) distribution of samples in the 96-well.

Once prepared, the microplate has been placed in the Multi-Mode SpectraMax i3x microplate reader and spectral absorbance has been measured at the three wavelengths indicated above.

The measurements have been carried out for about 255 min, after which they have been interrupted because the controls were contaminated and the recorded values showed anomalies.

Results

The hemolytes of the erythrocytes, after the addition of the 4 different concentrations of Rhamnolipid, has been analyzed by recording the absorbance values obtained by subjecting the samples to three different wavelengths: 415 nm and 575 nm, which allow to follow the increase of the hemoglobin release, and 650 nm, in order to evaluate the decrease of scattering light.

Absorbance values, related to the two hemoglobin absorption wavelengths, due to the too high concentrations of erythrocytes, cannot be considered to monitor the rate of hemoglobin release. Hence, the absorbance values for 650 nm have been used in order to calculate the percentage of intact (non-hemolyzed) RBC (% RBC intact) despite the interaction with the biosurfactants. Since the experiments have been conducted in triplicate, 3 absorbance values were obtained for each concentration (≈ every 15-20 min for a total time of 255 min).

In order to plot the percentage of intact RBC as a function of the rhamnolipid concentration, the absorbance values have been converted through the following formula:

eq. 6.1 $$Abs_{(1,2,3)}\% = \frac{Abs_{1,2,3}}{Ma_{Abs(CT)}} 100$$

In this way we obtain the percentage absorbance of each of the three measurements with respect to the arithmetic mean of the absorbance values of the positive control ($Ma_{Abs(CT)}$), where the rhamnolipid is not present and the erythrocytes are intact.

The %RBC intact, relative to a given concentration of rhamnolipid in a given time interval, has been calculated as follows:

eq. 6.2 $$\%\ RBC\ intact = \frac{(Abs\%_1 + Abs\%_2 + Abs\%_3)}{3}$$

Fig. 6.10 shows the obtained values by applying eq 6.2 as a function of time. It is clear that:

• at 0.5 mM, the erythrocytes hemolysis is instantaneous and total;

• at 0.05 mM, hemolysis does not take place during the 200 min;

• at 0.1 and 0.2 mM the hemolysis takes place subsequently. The time instant t_0, in which 50% of the erythrocytes are hemolized, has been derived by analyzing the data with the Boltzmann equation:

eq 6.3 $$\%RBC\ (t)= A2+(A1-A2)/\ (1+ \exp\ [(t-t_0)/\Delta t])$$

which produces a sigmoidal curve that best fit our data, where Δt represents the characteristic time necessary to perform the hemolysis.

As a result, the following information have been derived:

• at 0.2 mM, 50% of the erythrocytes undergoes hemolysis after approximately 6 minutes;

• at 0.1 mM of rhamnolipid, half of the hemolysis takes place after approximately 144 minutes.

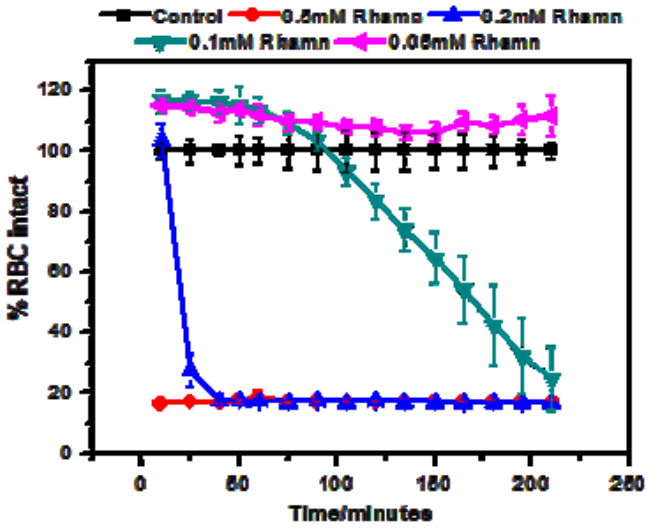

Figure 6.10: %RBC intact at different rhamnolipid concentrations as a function of time.

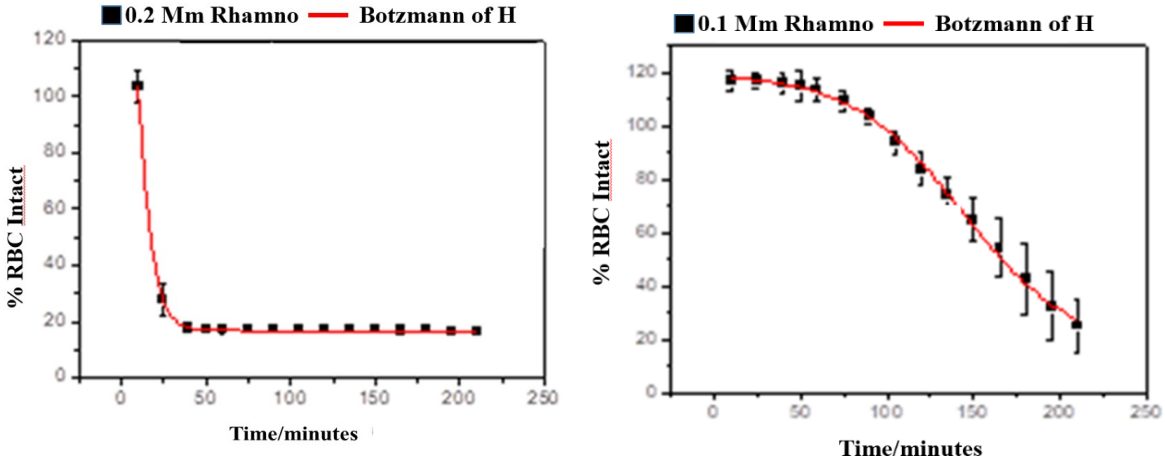

Figure 6.11: 1) and 2) data analysis %RBC intact relative of 0.2 mM rhamnolipid concentration (left panel) and 0.1 mM (right panel) through the Boltzmann equation 6.3.

6.2.2 Microscopy analysis: Morphological changes

In order to display the morphological changes of the erythrocytes induced by the interaction with rhamnolipids, an 8-well plate has been set up were samples observed with the Zeiss phase contrast microscope (without using fluorescence) with 40X objective.

The following protocol was followed:

- rhamnolipids have been solubilized in PBS.
- two drops of blood have been taken from the finger and diluted in 100 µl of 1% BSA in PBS;

Several tests with control RBC have performed to determine the experimental conditions for all samples: 250 µL 1% BSA in PBS + 150 µL PBS (in the case of control) + 1 µL of blood (total of 400 µL for each well / sample).

Four samples have been prepared:

1) 250 µL 1% BSA in PBS + 150 µL PBS + 1 µL blood (control);

2) 0.5 mM rhamnolipid: 250 µL 1% BSA in PBS + 1 µL blood + 150 µL rhamnolipid (1.35mM);

3) 0.35 mM rhamnolipid: 250 µL 1% BSA in PBS + 46 µL PBS + 1 µL Blood + 104 µL Rhamnolipid (1.35 mM);

4) 0.2 mM rhamnolipid: 250 µL 1% BSA in PBS + 90 µL PBS + 1 µL Blood + 60 µL rhamnolipid (1.35 mM).

Results

The erythrocytes in the presence of solutions at different rhamnolipid concentrations in addition to hemolysis, as already described above, undergo morphological changes that have been observed under a phase contrast microscope with a 40x objective. As in the case of GUVs, interaction has been followed over time. In the following, the images of the modification of the morphology of red blood cells are shown.

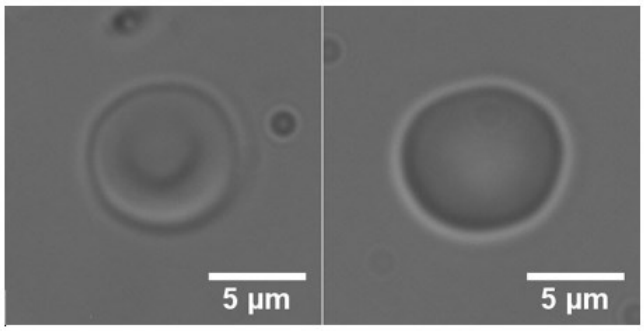

Figure 6.12: Control erythrocytes

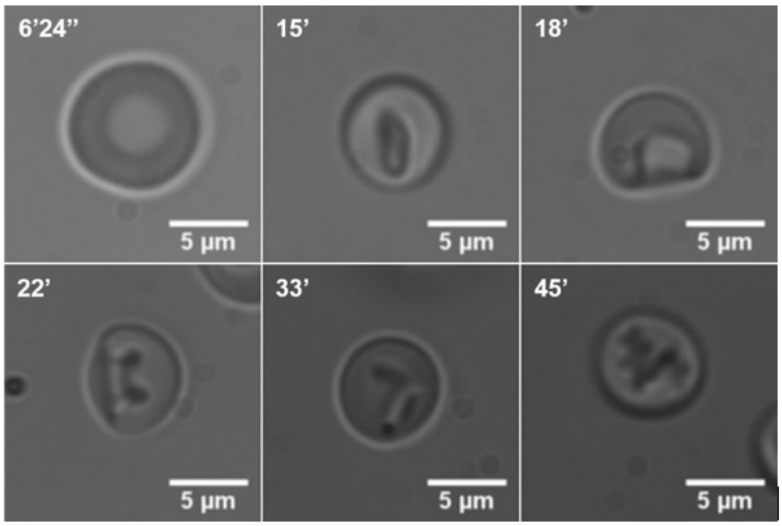

Figure 6.13: Erythrocytes in the presence of 0.2 mM rhamnolipid.

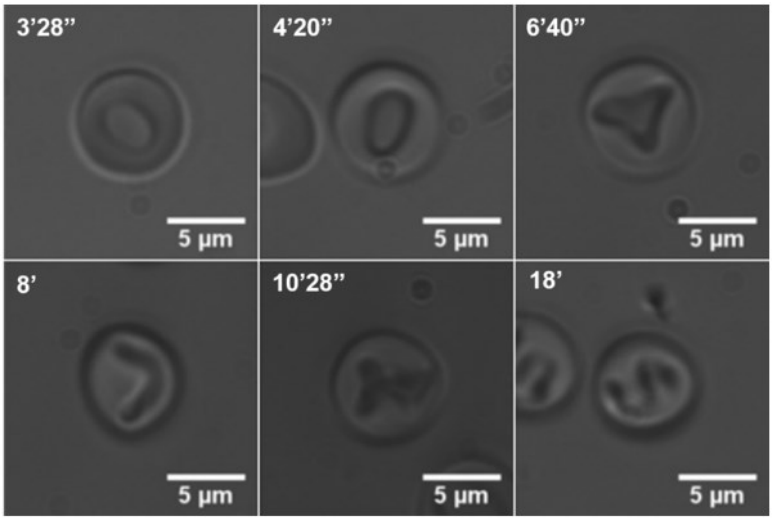

Figure 6.14: Erythrocytes in the presence of 0.35 mM rhamnolipid.

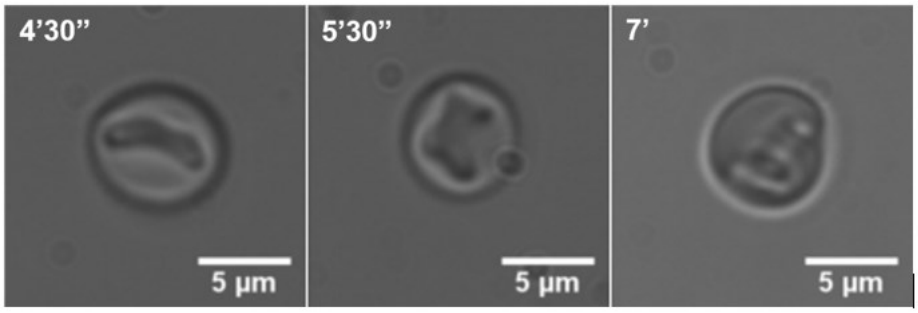

Figure 6.15: Erythrocytes in the presence of 0.5 mM rhamnolipid.

From the obtained images it can be concluded that, with the increase of the rhamnolipid concentration, the effect on the erythrocyte membrane, and therefore on the overall appearance of the erythrocytes, is gradually faster. In fact, at the 0.5 mM, after 7 min from the interaction, the classical biconcave disk aspect of the red blood cells is lost. These results confirm the ones obtained with spectrophotometry, since the morphological changes occur with times similar to the ones observed in the hemolytic process.

On this basis, RLs seems are able to modify the classical biconcave shape of erythrocytes thanks to their structure very similar to that of membrane lipids. Their intercalation disturbs the erythrocyte membrane, leading to conversion into two types of morphologies: echinocytes or stomacities (Manaargadoo-Catin, Ali-Cherif, Pougnas, & Perrin, 2016; Sánchez et al., 2010).

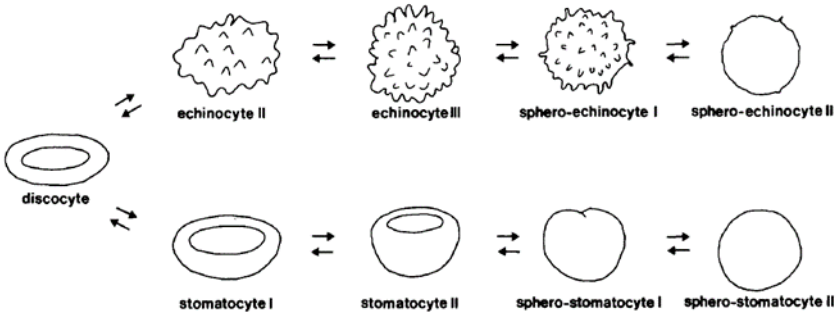

Figure 6.16: Possible morphologies that erythrocytes can take as a result of interaction with surfactants

In our case, we have observed that erythrocytes in the presence of rhamnolipids tend to turn into spherocytes and over time into spherosomites (Muñoz, Sebastián, Sancho, & Álvarez, 2014).

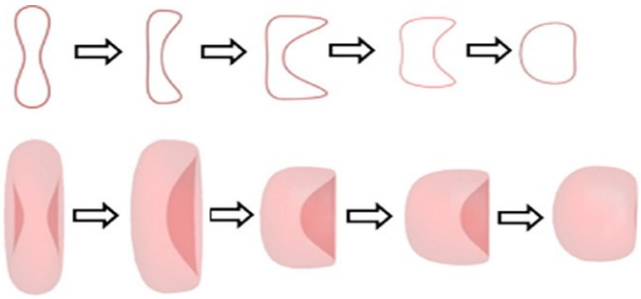

Figure 6.17: Schematic representation of the transformation of the erythrocyte from the biconcave shape to the spherical shape

These changes in erythrocyte form can be mainly the result of a series of cascade effects. Its indeed known that the alteration of the lipid membrane is followed by a reorganization of the whole proteins and finally effects on the cytoskeleton will be verified.

6.3 Interaction with HaCat cells

HaCaT is a spontaneously transformed aneuploid immortal keratinocyte cell line from adult human skin, (Boukamp et al., 1988b) widely used in scientific research (Schoop, Fusenig, & Mirancea, 1999). HaCaT cells are utilized for their high capacity to differentiate and proliferate in vitro (Schurer et al., 1993). Their use in research allows for the characterization of human keratinocyte using a model that is reproducible and addresses issues such as short culture lifespan and variations between cell lines that would otherwise be encountered.

Human skin keratinocyte cell line (HaCaT) was cultured in Dulbecco's Modified Eagle Medium (DMEM, Sigma-Aldrich) supplemented with 10% (v/v) fetal bovine serum (FBS), 100 U/mL of penicillin, and 100 pg/mL of streptomycin in a 37°C incubator at a moist atmosphere of 5% carbon dioxide. The 1:1 mixture of EDTA (stock 0.05%) and trypsin (stock 0.1%) must be prepared each time ahead of detaching the cells using PBS without Ca^{2+} and Mg^{2+} to provide a physiologic osmolarity.

Steps to set up a cell culture of Hacat cells are:

1) remove the culture medium and rinse the adherent cells using PBS without calcium and magnesium (3-5 ml PBS for T25, 5-10 ml for T75 cell culture flasks);

2) add freshly prepared 0.05% EDTA solution, 1-2 ml per T25, 2.5 ml per T75 cell culture flask; the cell sheet must be covered completely and incubated at 37°C for 10 min;

3) add freshly prepared trypsin/EDTA, 0.05% / 0.025% in duplicate (1 ml per T25, 2.5 ml per T75 cell culture flask); the cell sheet must be covered completely; the cells must detach within 1-2 min;

4) stop the trypsin activity using FBS-containing cell culture medium; dispense into new flasks which contain fresh cell culture medium.

6.3.1 MTT assay

Cell viability was evaluated by usual chemical staining methods, such as MTT and CVS (Crystal Violet Staining), as well as by clonogenic assay (see below). The MTT assay is a colorimetric assay for assessing cell metabolic activity. NAD(P)H-dependent cellular oxidoreductase enzymes may, under defined conditions, reflect the number of viable cells present. These enzymes are capable of reducing the tetrazolium dye MTT (3-(4,5-dimethylthiazol-2-yl)-2,5-diphenyltetrazolium bromide) to its insoluble formazan, which has a purple color. MTT and CVS have been performed as described in literature (Martins, Severino, Souza, Stolf, & Baptista, 2013). Briefly, in each sample we have added 0.2 mL of DMEM supplemented with 50 μg/mL MTT, 1% (v/v) FBS, 100 U/mL of penicillin, and 100 pg/mL of streptomycin. Samples have been incubated at 37 °C for 2 h. At the end of the incubation, the DMEM with MTT has been removed and 0.1 mL DMSO (Sigma-Aldrich) has been added. The plate has been shaken and absorbance values read at 550 nm (Infinite M-200 Tecan microplate reader, Switzerland). For the CVS assay, NR-labeled wells were washed twice with distilled water and stained with 0.02 % (w/v) Crystal Violet (CV, Sigma-Aldrich) for 5 min at room temperature. After washing with distilled water, CV has been eluted by 50% (v/v) ethanol containing 0.1 M sodium citrate, and absorbance has been read at 585 nm. For both assays, cell survival rates have been normalized to the absorbance values of untreated cells.

Figure 6.18: A microtiter plate after an MTT assay. Increasing amounts of cells resulted in increased purple colouring.

Results

Interaction experiments have been performed with cell cultures using HaCat cells, keratocinotic cells. We have set up cell cultures (Martins et al., 2013) that we have used for interactions with different concentrations of rhamnolipid (from 200 µM to 450 µM) until reaching a 50% cell viability. Cell viability has been evaluated by usual chemical staining methods, such as MTT assay. Here we reported cell viability after a 24 hours of interactions with the tested detergent and at different concentrations. To evaluate its toxicity, a comparison was made with the SDS detergent.

In Figure 6.19, the graph that compares cell viability of cells after interaction with rhamnolipid and SDS, reaching a 50% cell viability, is reported. Results indicate that the 50% cell viability is reached at 400 µM rhamnolipid and at 300 µM SDS. To note, from one hand 400 µM rhamnolipid is over its CMC (160 µM), from the other hand 300 µM SDS is much lower than its CMC (8200 µM). This means that isolated RL molecules in solution seems to not show toxicity effects.

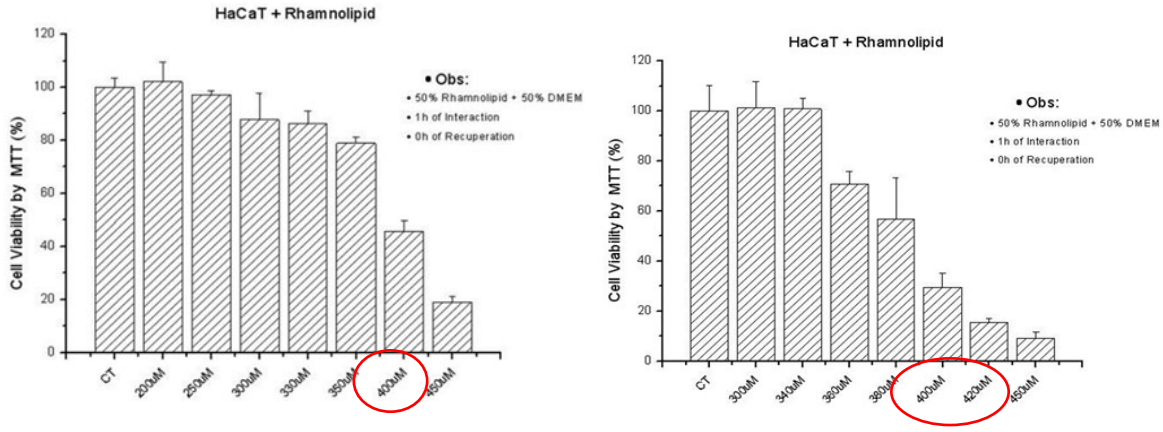

Figure 6.19: cell viability after MTT assay between different concentrations of rhamnolipid and cell culture.

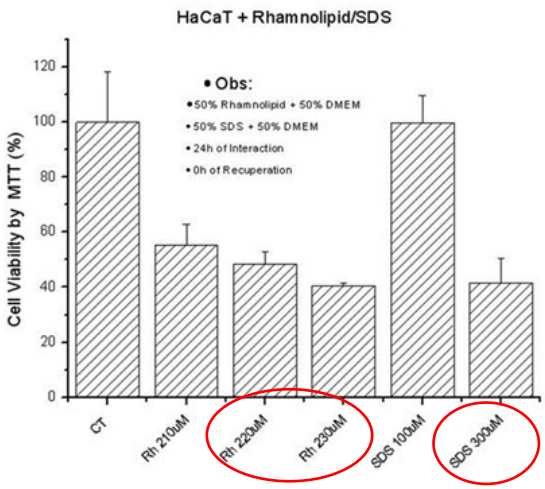

	SDS	Rhamnolipid
CMC (mM)	8.20	0.16
50% cell viability dose (mM)	0.30	0.38

Table 6.2 comparison between RLs and SDS, CMC and 50% Cell Viability dose

Figure 6.20: cell viability after MTT assay. Comparison between the rhamnolipid and the SDS

Chapter 7

Oil recovery

Enhanced oil recovery (EOR) is the technique or process where the physicochemical (physical and chemical) properties of the rock are changed to enhance the recovery of hydrocarbon. The properties of the reservoir fluid system which are affected by EOR process are chemical, biochemical, density, miscibility, interfacial tension (IFT)/surface tension (ST), viscosity and thermal. EOR often is called tertiary recovery if it is performed after waterflooding.

Three major categories of EOR have been found to be commercially successful to varying degrees:

- Thermal recovery, which involves the introduction of heat such as the injection of steam to lower the viscosity, or thin, the heavy viscous oil, and improve its ability to flow through the reservoir. Thermal techniques account for over 40 percent of U.S. EOR production, primarily in California.
- Gas injection, which uses gases such as natural gas, nitrogen, or carbon dioxide (CO_2) that expand in a reservoir to push additional oil to a production wellbore, or other gases that dissolve in the oil to lower its viscosity and improves its flow rate. Gas injection accounts for nearly 60 percent of EOR production in the United States.
- Chemical injection, which can involve the use of polymers to increase the effectiveness of waterfloods, or the use of detergent-like surfactants to help lower the surface tension that often prevents oil droplets from moving through a reservoir. Chemical techniques account for about one percent of U.S. EOR production. Each of these techniques has been hampered by its relatively high cost and, in some cases, by the unpredictability of its effectiveness.

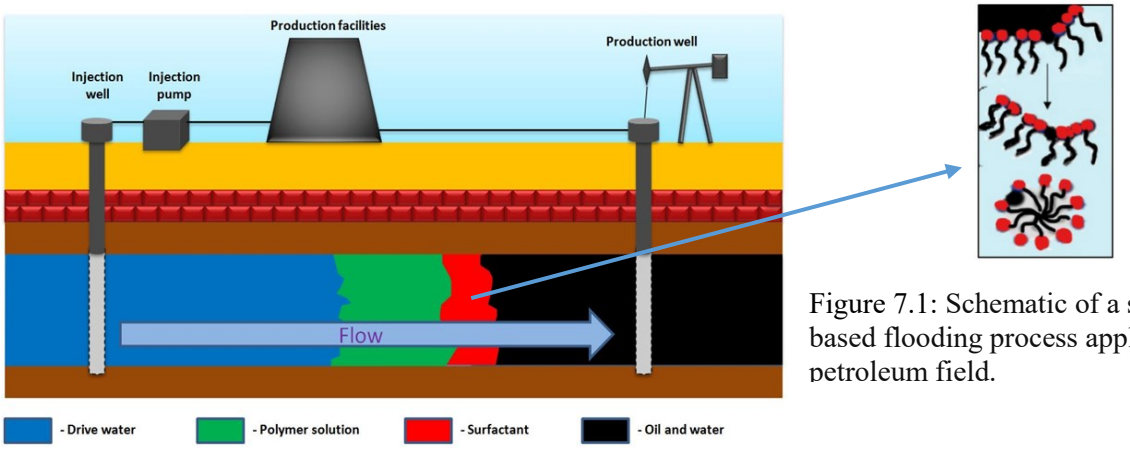

Figure 7.1: Schematic of a surfactant-based flooding process applied to a petroleum field.

7.1 Spectroscopy experiments

The spectroscopy experiments conducted in this case have been aimed at analyzing the extraction capacity of the rhamnolipids, in solution at different concentrations, in the presence of a constant amount of Kirkuk crude oil from Iraq field and comparing it with that of a synthetic detergent (C_{12}-C_{18}-7 OE) that presents a structure similar to the biosurfactant object of study.

The samples at different rhamnolipid concentrations and the same amount of Kirkuk oil, have been prepared and subjected to a quantitative spectrophotometric analysis, thus analyzing the absorbance values. The analysis has been conducted at 540 nm and a single-beam VIS spectrophotometer was used. The rhamnolipid concentrations adopted cover a range from 0.01 to 3 mM (hereafter shown in the table) and have been placed in contact with a fixed quantity of oil in order to obtain a fixed volume fraction of oil equal to 0.02. Under these conditions, two immiscible phases are formed. When the sample is stirred, the volume below the oily phase is taken, inserted in a 2.5 ml cuvette, and subjected to spectrophotometric analysis.

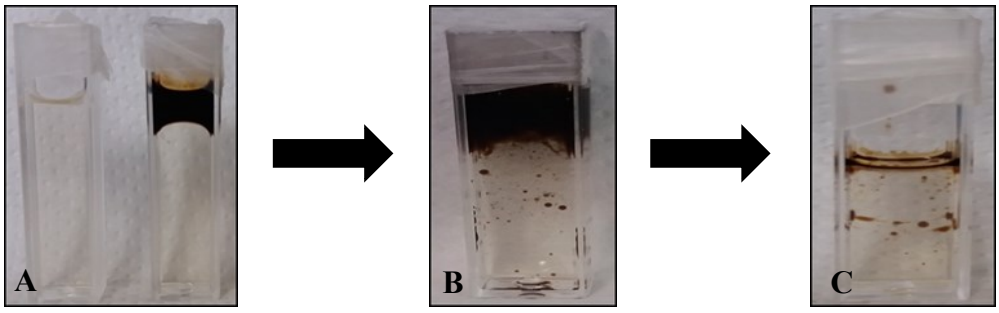

Figure 7.2: A) detergent sample in the presence and absence of oil; B) sample after stirring; C) volume under the oily phase which is subjected to spectrophotometric analysis.

Sample concentrations (mM)							
0.01	0.02	0.05	0.06	0.07	0.08	0.1	0.16
0.2	0.3	0.4	0.5	0.6	0.7	0.8	1
1.2	1.5	1.7	2	2.4	2.6	2.8	3

Table 7.1: sample concentration for spectroscopy experiments

The absorbance values of these samples were compared with those of a synthetic detergent (C_{12}-C_{18}-7OE). The preparation of the samples with the synthetic detergent was carried out in the same way as the previous ones.

After stirring and after leaving the tubes at rest for 24 hours, the aqueous phase was separated and its turbidity analyzed with the spectrophotometer, in order to evaluate the extraction capacity of the rhamnolipid against the oil and to compare it with that of the synthetic detergent C_{12}-C_{18}-7 OE. Absorbance measurements were conducted at a length of 540 nm.

In the graphs below, the respective absorbance values of both investigated surfactants were placed according to the different concentrations.

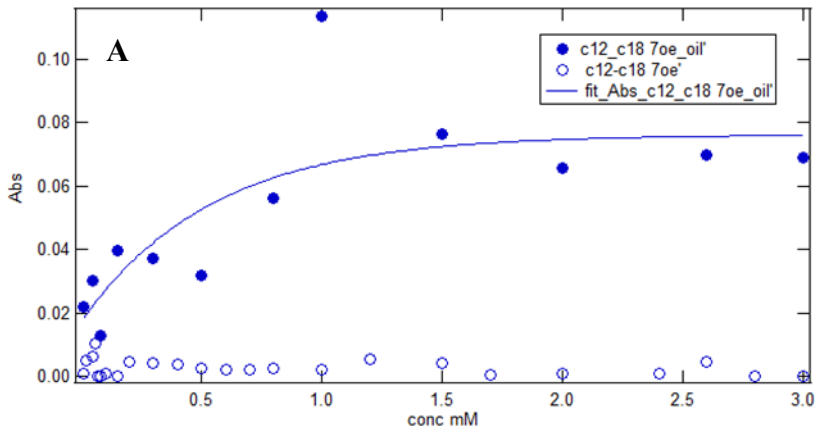

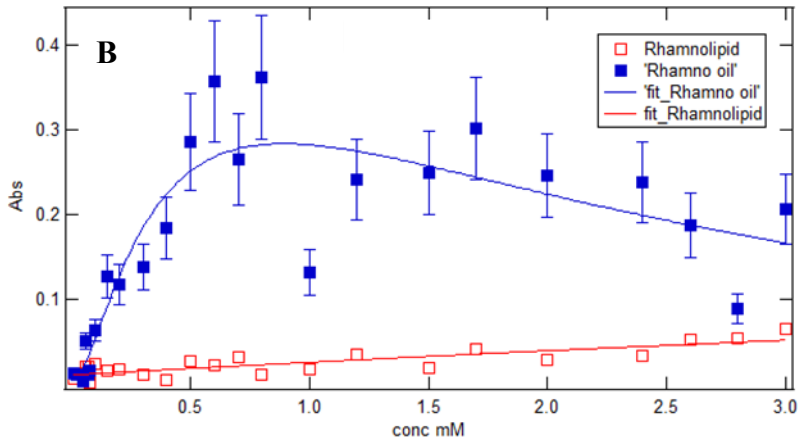

Figure 7.3: Concentration dependency of the absorbance of detergents with and without oil. A) C_{12}-C_{18}-7OE. B) rhamnolipid.

From the first graph we observe that the absorbance values of the synthetic detergent both in the presence and in the absence of oil are very low, but the addition of the oil causes an exponential increase in the absorbance. This indicates that the aqueous phase is enriched with oil, solubilized inside micelles formed by the detergent. However, the extraction capacity of the detergent is very low and reaches its maximum efficiency at a concentration of about 1.5 mM.

The second graph shows that the rhamnolipid has a much higher extraction capacity. In the presence of oil, the absorbance values are at least four times higher than those of the C_{12}-C_{18}-7OE. However, rhamnolipid has an absorbance peak in the concentration range between 0.5 and 1 mM, beyond which the absorbance seems to decrease until it reaches a plateau: this fact could indicate a structural rearrangement of the rhamnolipid (perhaps at a lamellar phase, as observed at higher concentrations) which also determines the slight absorbance increase observed when the lipid concentration varies in the absence of oil.

In conclusion, we can deduce from the absorbance values that the biosurfactant succeeds in solubilizing in a more efficient way, compared to the synthetic surfactant, the light part of the oil in particular in the concentration range between 0.5 and 1 mM. Moreover, it is inferred that the efficiency of the rhamnolipid is not proportional to its concentration.

To understand possible relations between the extraction capacity of the light part of the oil by the two detergents and the contact time between the aqueous phase and the oil, the absorbances were measured and compared after different time intervals. In particular, the absorbance

measurements were made after leaving the aqueous phase and oil in contact for 0, 24, 48 and 72 hours (up to 96 hours for the synthetic detergent).

The graphs obtained are shown in the Figure 7.4.

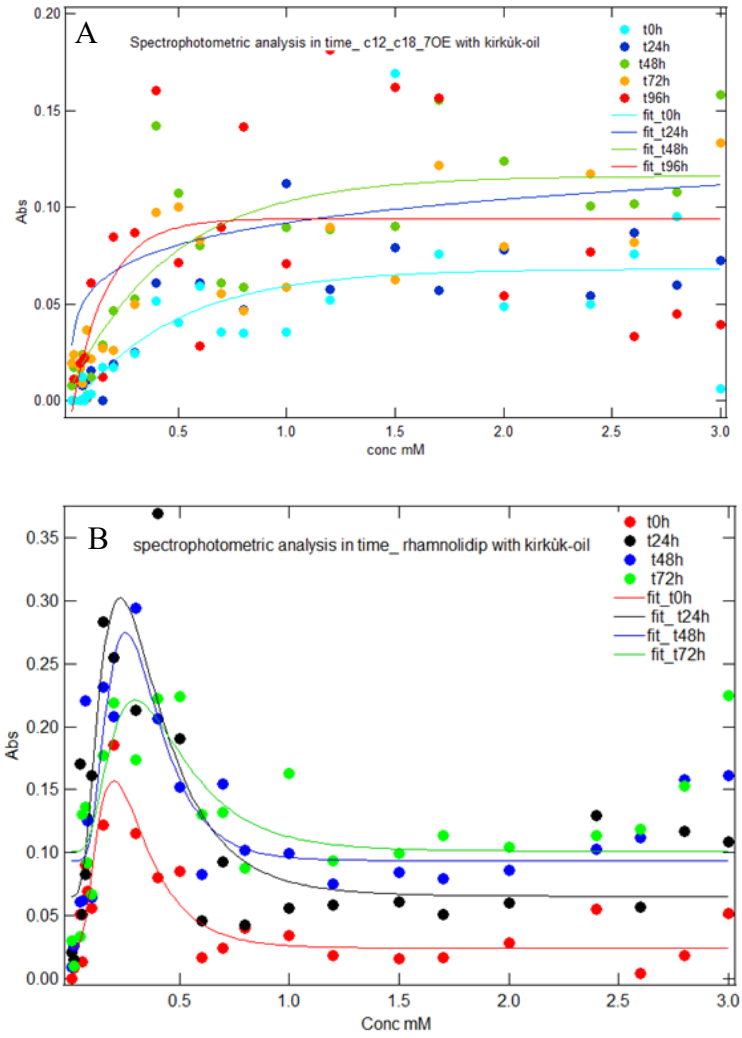

Figure 7.4:

Absorbance values as a function of surfactant concentration as time changes

A) C_{12}-C_{18}-7 OE

B) Rhamnolipid

The observed data suggest that the extraction capacity depends on the contact time, even if the trend as a function of the detergent concentration is not confirmed. It is interesting to note that rhamnolipid oil extraction seems to be the maximum between 24 and 48 hours of contact.

7.2 SAXS Experiments

The main motivation of this part of the work is to exploit the high brilliance properties of synchrotron SAXS technique for characterizing the structures formed by rhamnolipids in oil-

contaminated water solution in a wide range of physical-chemical conditions. The experiments reported here are of rhamnolipid solutions at concentrations of 10 mM, 15 mM, 25 mM, 35 mM, 47 mM. The same concentrations were analyzed in the presence of two oil volume fractions, 0.02 and 0.002, and at two temperatures, 10 and 22°C.

SAXS curves are reported in Figures 7.5. Their trend is qualitatively similar to preliminary results obtained with the Nanostar instrument, shown in Fig. 5.10. Hence, it would be possible also for these curves to apply the model of the interacting spherocylinders, discussed in the paragraph 5.2.2. In order to properly quantify the presence of oil within the micelles, we have applyied a chemical-physical approach, based on the concept of partition coefficient and by taking into account the volumetric contraints. These issues are discussed in the next paragraphs.

7.2.1 Partition cofficient

The composition of the sample is defined by two parameters: the molar concentration of rhamnolipids (R) molecules in water (W) solution, C_R, and the volume fraction of oil (O) in the solution, Φ_O.

For a sake of simplicity, it is assumed that oil molecules are only costituted by methylene groups CH_2. Hence the nominal molar concentration of CH_2 groups provided by oil can be written as

eq. 7.1
$$C_{CH_2,O} = \frac{\Phi_O d_O}{M_{CH_2}}$$

where d_O is the mass density of oil and M_{CH2} the molecular weight of CH_2.

We also introduce the nominal oil-CH_2 to rhamnolipid molar ratio

eq.7.2
$$x_{max} = \frac{C_{CH_2,O}}{C_R}$$

The concentration of CH_2 coming from oil dissolved in the sphero-cylindrical micelles (M) is

eq. 7.3
$$C_{CH_2,O,M} = C_R n_{CH_2,O,M} = C_R p x_{max}$$

where $n_{CH2;O;M}$ is the number of oil-CH_2 adsorbed by one rhamnolipid molecule and p is a parameter ranging from 0 to 1, which measures the overall capability of the rhamnolipid micelles to adsorbe oil.

The thermodynamic partition coefficient of oil between micelle and water can be written as

eq. 7.4 $$K = \frac{C_{CH_2,O,M}}{C_{CH_2,O,W}}$$

Since the nominal concentration of oil-CH2 is the sum of the corresponding concentrations in micelles and in water we have,

eq.7.5 $$K = \frac{C_{CH_2,O}}{C_{CH_2,O} - C_{CH_2,O,W}} = \frac{p}{1-p}$$

7.2.2 Volumetric constraints and electron densities

The paraffinic volume of one R-molecule in a micelle that has adsorbed oil is

eq. 7.6 $$v_1 = v_{CH_2}\left(n_{CH_2,R} + n_{CH_2,O,M} + n_{CH_3,R}r\right)$$

where v CH_2 is the molecular volume of the CH2 group, r is the ratio between the molecular volume of the terminal methyl group CH3 and the one of CH2 and $n_{CH2;\,R} = 12$, $n_{CH3;R} = 2$ are the numbers of CH2 and CH3 groups, respectively, in the paraffinic tails of the rhamolipid molecule.

By naming N_{agg} the aggregation number of the micelle, i.e. the number of R-molecules selfassembled in the micelle, the length L of the cylindrical part of the sphero-cylinder can be determined by the following equation

eq. 7.7 $$L = \frac{N_{agg}v_1 - \frac{4\pi}{3}R_{1,sc}^3}{\pi R_{1,sc}^2}$$

The electron density of the paraffinic part is thus

eq.7.8 $$\rho_1 = \frac{e_{CH_2}\left(n_{CH_2,R} + n_{CH_2,O,M} + e_{CH_3}n_{CH_3,R}\right)}{v_1}$$

where $e_{CH2;R} = 8$, $e_{CH3;R} = 9$ are the numbers of electrons provided by CH_2 and CH_3 groups, respectively.

The average volume of the polar domain occupied by one R-molecule in the micelle is

eq. 7.9 $$\nu_2 = \frac{\frac{4\pi}{3}R_{2,sc}^3 + \pi R_{2,sc}^2 L}{N_{agg}} - \nu_1$$

Since this volume is occupied by the dry polar head of R and by hydration water molecules, it is possible to calculate the average number of hydration water molecules per polar head of R,

eq. 7.10 $$n_{W,R} = \frac{\nu_2 - [\nu_{R1,sc.pol}\, x_{R1,sc} + \nu_{R2,sc,pol}(1 - x_{R1}sc)]}{d_{W,R}\, \nu_W}$$

where xR,$_{sc}$ is the molar fraction of mono-R (R1$_{sc}$) in the mixture of mono- and dimer-R (R2,$_{sc}$), ν $_{R1sc;pol}$ = 374,8 Å^3 and ν $_{R2sc;pol}$ = 613,8 Å^3 are the molecular volumes of the polar heads of R1,$_{sc}$ and R2,$_{sc}$ respectively, d $_{W;R}$ is the relative mass density of hydration water and v W ≅30 Å^3 is the molecular volume of water in the bulk solvent.

On this basis, the electron density of the sphero-cylindrical shell, corresponding of hydrated polar heads of R, can be easily calculated,

eq.7.11

$$\rho_2 = \frac{e_{R1sc,pol}\, x_{R1sc} + e_{R2sc,pol}\,(1 - x_{R1sc}) + e_W n_{W,R}}{\nu_2}$$

where $e_{R1;pol}$ = 162, $e_{R2;pol}$ = 240 and e_W = 10 are the numbers of electrons provided by R1$_{sc}$, R2$_{sc}$ and water, respectively.

Assuming that the oil molecules that are not adsorbed in the micelles form a separate phase on the top of the sample, the electron density of the solution that surrounds the micelles corresponds to the bulk water electron density,

eq. 7.12 $$\rho_3 = \frac{e_W}{\nu_W}$$

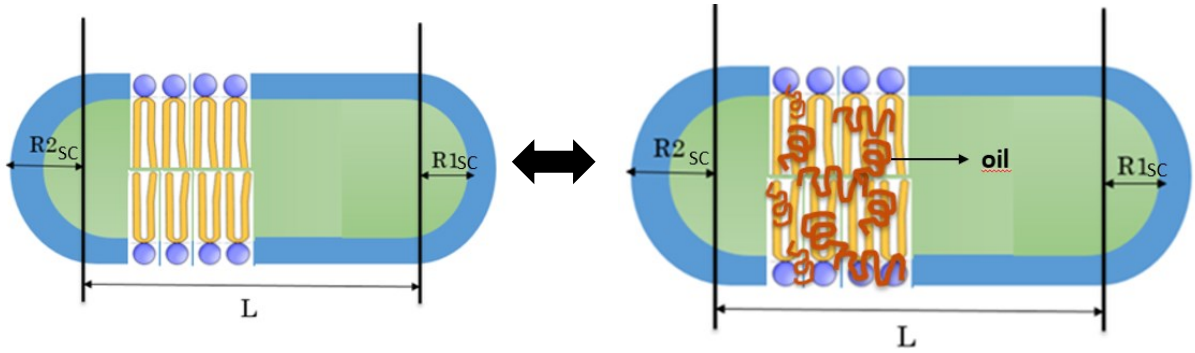

Figure 7.5: Graphic representation of the geometric model in the absence and presence of oil

7.2.3 Fitting results

All the equations developed for describing the system in term of partition coefficient and volumetric constraints have been inserted in the GENFIT software. Fitting results, shown as black solid lines in the Figs. 7.6 have been obtained by simultaneously analysing all the curves of each panel. The quality of the fit is very good, indicating the appropriateness of the adopted method. Fitting parameters are reported in Tables 7.2 and 7.3.

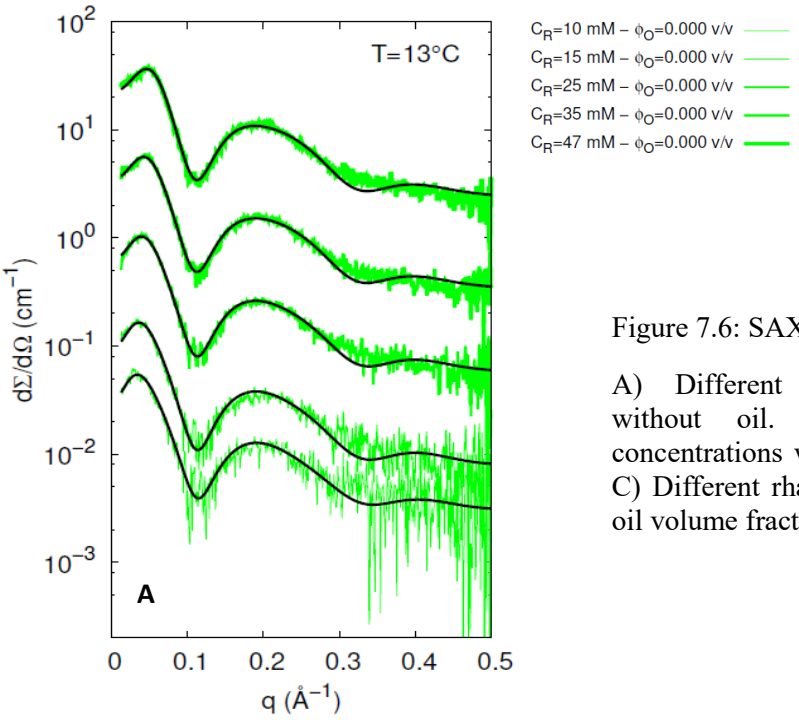

Figure 7.6: SAXS curves and best fit at 13°C.

A) Different rhamnolipid concentrations without oil. B) Different rhamnolipid concentrations wit oil volume fraction 0.002. C) Different rhamnolipid concentrations with oil volume fraction 0.02.

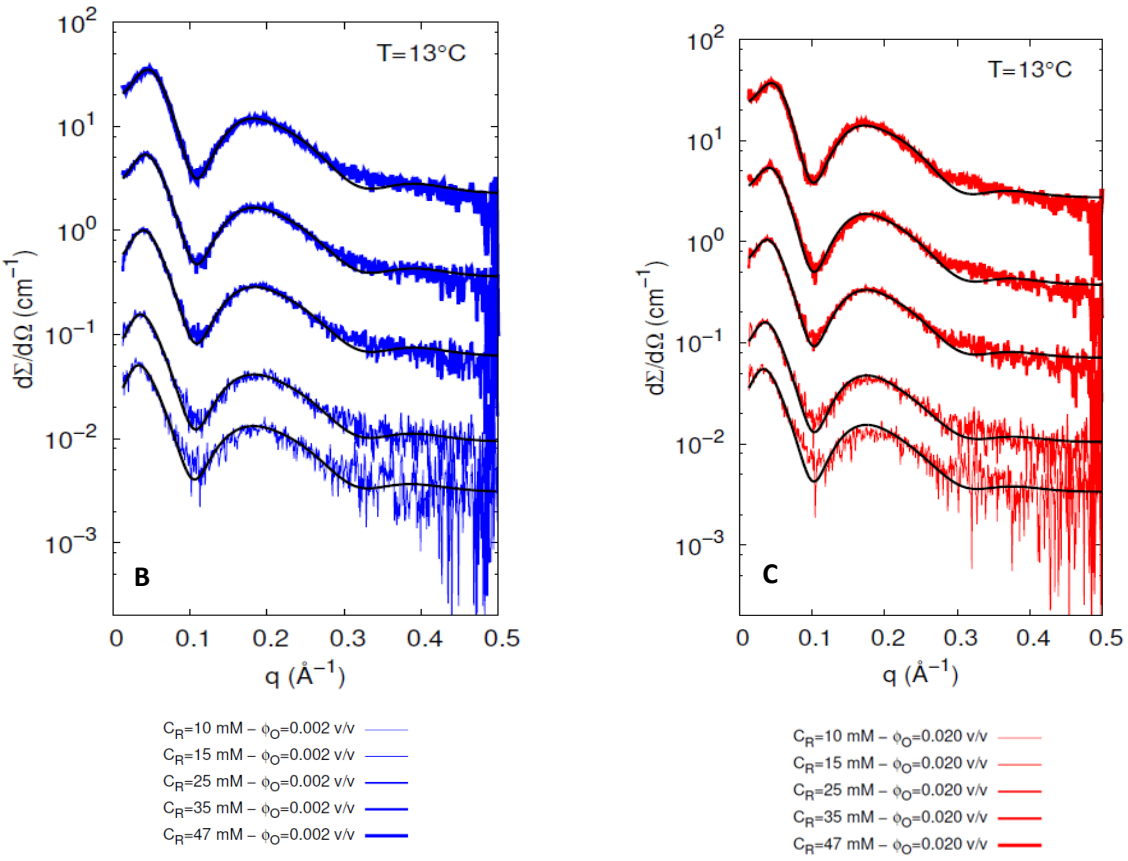

Fitting Parameters at 13°C	No oil	% v/v 0.002	% v/v 0.02
$R_{1,sc}$ (Å)	9.8 ± 0.2	10.93 ± 0.9	12.3 ± 0.3
δ (Å)	12.1 ± 0.1	11.90 ± 0.07	11.9 ± 0.2
ρ	-	0.19 ± 0.05	0.08 ± 0.03
N agg a	45.4 ± 0.8	40.8 ± 0.9	43 ± 2
N agg b	47.2 ± 0.9	41.7 ± 0.4	43 ± 2
N agg c	48.1 ± 0.9	42.7 ± 0.2	46 ± 2
N agg d	49.6 ± 0.8	43.6 ± 0.2	46 ± 2
N agg e	49.4 ± 0.7	44.2 ± 0.2	48 ± 2
ν_{CH2} (Å^3)	25.40 ± 0.04	25.09 ± 0.08	25.18 ± 0.05
r	1.454 ± 0.007	1.55 ± 0.02	1.56 ± 0.02
ν_W	29.9 ± 0.3	29.90 ± 0.3	30.0 ± 0.3
d_W	1.003 ± 1.004	1.00 ± 0.01	1.00 ± 0.01
J/N agg (k_B T)	0.007 ± 0.008	0.13 ± 0.02	0.18 ± 0.02
d (Å)	0±10	1.3 ± 0.2	1.01 ± 0.01
z/ N agg (q_e)	-0.197 ± 0.005	-0.22 ± 0.01	- 0.236 ± 0.06
γ	2.81 ± 0.02	2.75 ± 0.01	2.73 ± 0.05

Table 7.2: Summary table with the corresponding fitting parameters calculated using the GENFIT software

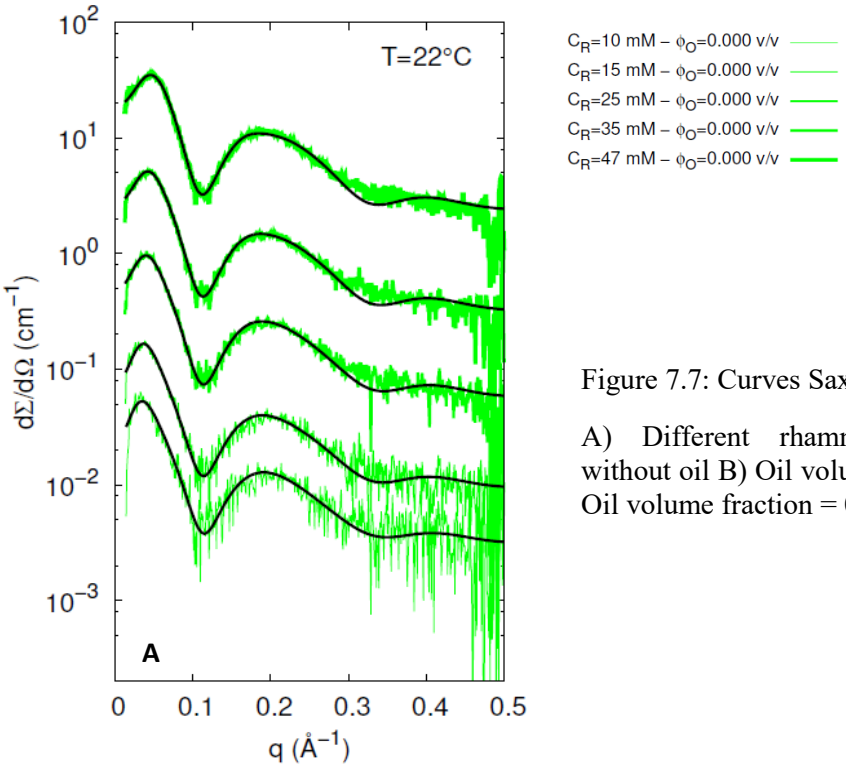

Figure 7.7: Curves Saxs at 22 °C.

A) Different rhamnolipid concentrations without oil B) Oil volume fraction = 0.002 C) Oil volume fraction = 0.02

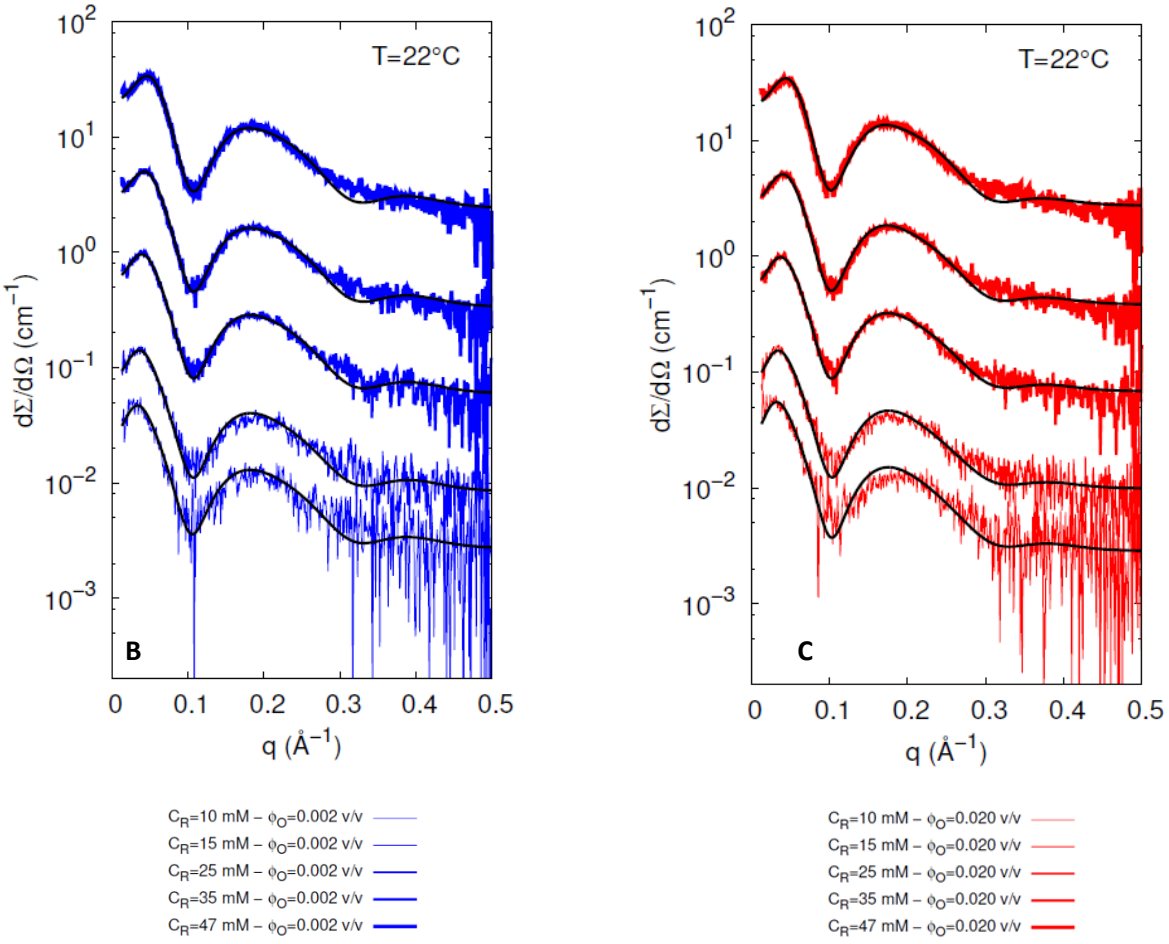

Fitting Parameters at 22°C	No oil	% v/v 0.002	% v/v 0.02
$R_{1,sc}$ (Å)	9.8± 0.3	10.5 ± 0.2	12.2 ± 0.3
δ (Å)	12.1 ± 0.2	12.2 ± 0.1	11.9 ± 0.2
ρ	-	0.13 ± 0.03	0.002 ± 0.002
N agg a	43 ± 1	44.0 ± 0.8	45 ± 1
N agg b	46 ± 1	45 ± 1	44 ± 1
N agg c	45 ± 1	47 ± 1	46 ± 1
N agg d	47 ± 2	48 ± 1	47 ± 1
N agg e	48 ± 2	49 ± 1	48.2 ± 0.9
ν_{CH2} (Å^3)	25.1 ± 0.2	25.5 ± 0.1	25.0 ± 0.2
r	1.54 ± 0.05	1.44 ± 0.04	1.60 ± 0.06
ν_W (Å^3)	29.9 ± 0.3	29.90 ± 0.05	29.99 ± 0.05
d_W	1.01 ± 1.01	1.001 ± 0.003	1.003 ± 0.001
J/N agg (k_B T)	0.05 ± 0.02	0.13 ± 0.03	0.13 ± 0.06
d (Å)	5±2	1.06 ± 0.04	1 ± 2
z/ N agg (q_e)	-0.23 ± 0.04	-0.23 ± 0.01	- 0.20 ± 0.01
γ	3.0 ± 0.4	2.89 ± 0.05	2.76 ± 0.02

Table 7.3: Summary table with the corresponding fitting parameters calculated using the GENFIT software.

Experimental data confirm that the presence of oil induces a change in the shape of the spherocylinder with consequent increase in size as confirmed in this image.

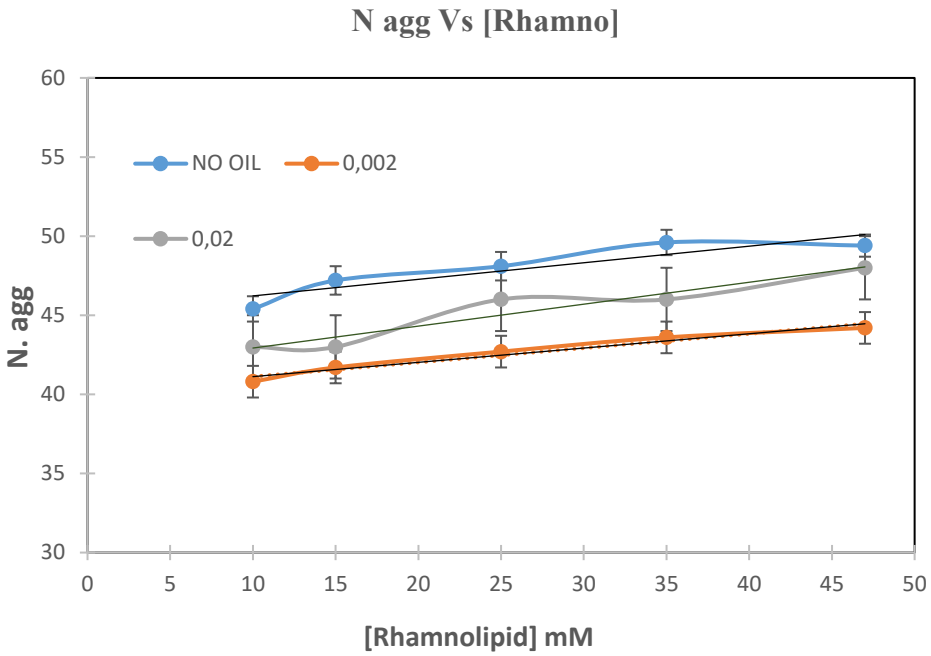

Figure 7.8: The aggregation number as a function of the concentration of Rhamnolipid. As the concentration increases, the number of aggregations increases that does not increase logically with the increase in oil

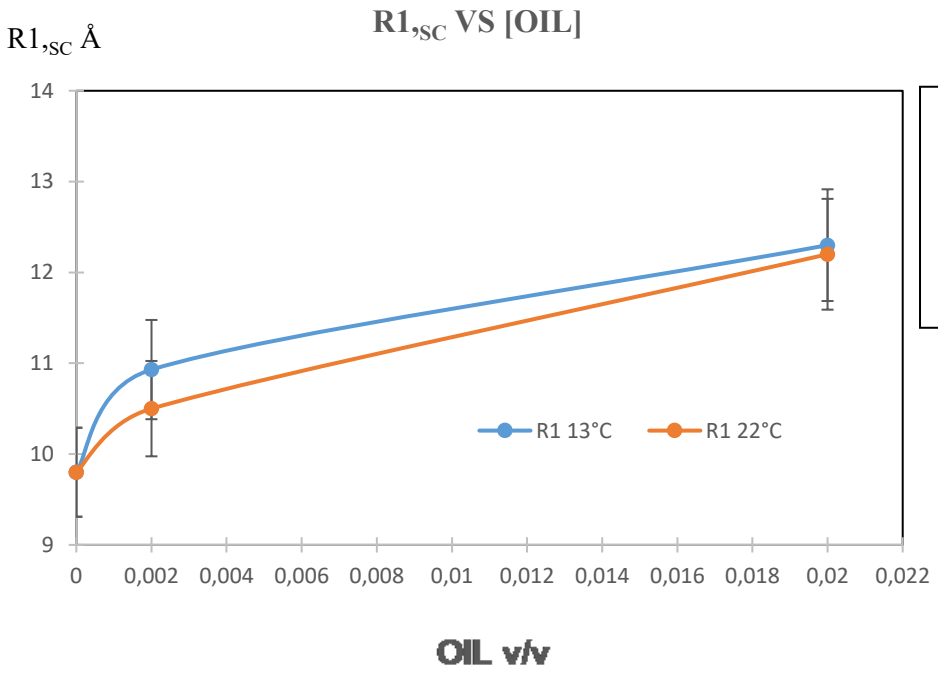

Figure 7.9: As the oil concentration increases, the value of the spherocylinder's internal radius increases

Subsequently we calculated the area per molecule and we have seen that both at 13 ° C and at 22 ° C this value does not increase much with the increase of the concentration of oil and remains about compelling as the concentration of rhamnolipid increases.

The values of the fitting parameter *p* allows the determination of the partition coefficient *K*, deserve some comments. From one hand, a unique value of *p* is able to determine good fitting

results of all the curves of a panel, which share the oil volume fraction and the temperature. From the other hand, we see that the values of p in different panels are quite different, suggesting that the oil recover into the rhamnolipid micelles cannot simply be described in terms of a unique mechanism and so from a unique partition coefficient.

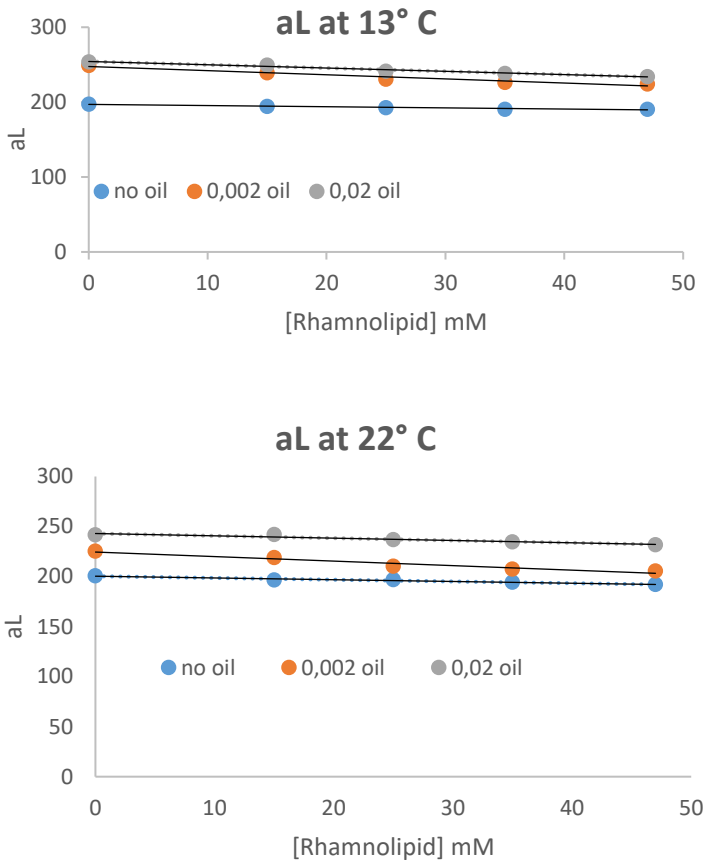

Figure 7.10: Area per molecule as a function of the ramnolipid concentration at 13 °C and 22°C.

7.3 Rhamnolipids in brackish water

Subsequently we analysed the behaviour of the rhamnolipids in brackish water to bring us closer to a practical purpose of possible application.

The experiments have been conducted at two temperatures, 10 and 25°C. Samples were prepared at 9 rhamnolipid pure water concentrations between 10 and 90 mM (at steps of 10 mM) and 5 different concentrations of crude oil volume fraction (0, 0.001, 0.005, 0.01 and 0.5).

To simulate sea or brackish water, the same conditions will be also investigated in the presence of following 4 combinations of salts:

1) 460 mM NaCl;

2) 46 mM NaCl, 1 mM $CaCl_2$ and 6 mM $MgSO_4$;

3) 92 mM NaCl, 2 mM $CaCl_2$ and 11 mM $MgSO_4$;

4) 229 mM NaCl, 5 mM $CaCl_2$ and 28 mM $MgSO_4$.

Considering our preliminary laboratory SAXS experiments the optimum q range is 0.01-0.40 $Å^{-1}$.

7.3.1 SAXS of mixtures of interacting spherocylinders and stacked bilayers

Data recorded at the ELETTRA synchrotron at different temperatures and in a wide range of rhamnolipid and oil concentrations as well as sodium, calcium and magnesium ions concentrations are shown in Figure 7.10. To note, the huge set of 360 curves has been distincted in 42 panels, where in each panel all samples share the temperature, the oil volume fraction and the concentration of the various salts. The only parameter that distinguishes the curves of a panel is the concentration of R, reported in mM unit beside each curve. At a first sight, the behaviour of SAXS curves deviates from the one of interacting spherocylinders and, in several circumstances, shows a typical lamellar peak, indicating the presence of large vesicles or almost flat bilayer. Hence, it can be assumed that, depending on sample compositions and on temperature, dispersions of rhamnolipids could be simultaneously present in the form of spherocylinders and of flat bilayers with a possible stacking order (Spinozzi, Mariani, Paccamiccio, & Amaral, 2010).

To check this assumption, each SAXS curve of the ELETTRA series has been analysed by using the GENFIT software by the following expression,

eq. 7.13 $$\frac{d\Sigma}{d\Omega}(q) = \frac{d\Sigma}{d\Omega_{SC}}(q) + \frac{d\Sigma}{d\Omega_{ib}}(q) + \frac{d\Sigma}{d\Omega_{sb}}(q)$$

eq. 7.14 $$\frac{d\Sigma}{d\Omega_{SC}}(q) = n_{SC}\, r_e^2\, P(q) S_M(q)$$

eq. 7.15 $$\frac{d\Sigma}{d\Omega_{ib}}(q) = \frac{\phi_{ib}}{t}\, r_e^2\, \frac{2\pi}{q^2}\, [A_b(q)]^2$$

eq. 7.16 $$\frac{d\Sigma}{d\Omega_{sb}}(q) = \frac{\phi_{sb}}{t}\, r_e^2\, \frac{2\pi}{q^2}\, [A_b(q)]^2 S_{PT}(q)$$

where the first term, labelled with the pedex "sc" describes the interacting spherocylinders particles and the other two terms refer to infinite bilayers and stacking of infinite bilayers, "ib" and "sb", respectively. In particular, the amplitude $A_b(q)$ represents the Fourier transform of a two electron density steps model, with mild transition among the steps,

eq 7.17
$$A_b(q) = 2\left[R_{1,b}(\rho_{1,b}-\rho_0)e^{-\frac{1}{2}(q\sigma_{1,b})^2} j_0(qR_{1,b}) + (\delta_b + R_{1,b})(\rho_{2,b}-\rho_{1,b})e^{-\frac{1}{2}(q\sigma_{2,b})^2} j_0\left(q(\delta_b + R_{1,b})\right)\right]$$

where $j_0(x)$ is the 0^{th} Bessel functions of fractional order. We have considered that a unique amplitude could be optimised for both ib and sc terms. The standard parameters of this amplitude are the thickness δ_b of the hydrated polar head of R and the thickness $R_{1,b}$ of the paraffinic moiety, which could include oil molecules, their corresponding electron densities $\rho_{2,b}$ and $\rho_{1,b}$ and the two parameters $\sigma_{2,b}$ and $\sigma_{1,b}$ the represents the widths of transition mild steps. The parameter t is the whole bilayer thickness, $t=2(\delta_b+R_{1,b})$; ϕ_{ib} and ϕ_{sb} represent the volume fractions of ib and sb structures, respectively. The stacking order is here described by the para-crystal structure factor, $S_{PT}(q)$, able to take into consideration distorted lamellar order of the so-called second type. Parameters of $S_{PT}(q)$ are the staking distance d, the distortion factor $g_d=\sigma_d / d$, being σ_d the Gaussian standard deviation of the isotropic distortion and N_d, the number of stacked bilayers.

To note, $r_e=2.8\cdot10^{-13}$ cm is the classical radius of the electron.

Volumetric constraints and electron densities

It is fundamental, for a proper analysis of SAXS data, in particular when the models applied to fit the data includes many adjustable parameters, to include all the constraints that arise from information known "a priori" with respect to the experiments. In particular, there are constraints due to sample compositions and constraint due the structural properties of the all the molecules forming the sample, such as molecular weights or molecular volumes (Matsuoka, Tanaka, Hashimoto, & Ise, 1987).

In the following, all those constraints are listed, together with the introduction of new parameters that allow to be easily optimised in a simple range of validity.

First of all, the composition of the sample is defined by the following parameters: the molar concentrations of rhamnolipids (R) molecules, NaCl, $CaCl_2$ and $MgSO_4$ dissolved in water (W) solution (C_R, C_{Na}, C_{Ca} and C_{Mg} respectively), and the volume fraction of oil (O) with respect to the whole volume of water solution and oil volume, ϕ_O. As in the previous case, it is assumed that oil molecules are only constituted by methylene groups, indicated with $CH_{2,O}$. On this basis, it is useful to introduce the nominal oil-CH_2 to rhamnolipid molar ratio,

eq. 7.18 $$n_{CH_2,O} = \frac{\phi_O d_O}{(1-\phi_O) C_R M_{CH_2}}$$

where d_O is the known density of oil.

The mass balance of the sample can be described by introducing the following useful molar fractions: F, the fraction of R in solution ($1-F$ is the fraction of precipitated R); W, the fraction of R forming sc with respect to R in solution; Z, the fraction of R forming ib with respect to R forming ib and sb; p, the fraction of $CH_{2,O}$ entrapped in sc; q, the fraction of $CH_{2,O}$ entrapped in both ib and sb; S, the fraction of Na^+ associated to the hydrated polar domain with respect to the Na-to-R ratio, $n_{Na^+}=C_{Na}/C_R$; T, the fraction of S associated with the polar head of sc.

Concerning the sc particles, by writing the whole area and paraffinic volume of one spherocylinder in terms of area per polar head, a_{sc}, and volume of the paraffinic part, $v_{1,sc}$, it possible to derive its aggregation number N_{agg} and the length L of its inner cylinder,

eq. 7.19 $$4\pi\left(R_{1,sc}+\delta_{sc}\right)^2 + 2\pi\left(R_{1,sc}+\delta_{sc}\right)L = N_{agg}a_{sc}$$

eq. 7.20 $$\frac{4\pi}{3} R_{1,sc}^3\, \pi R_{1,sc}^2\, L = N_{agg}\, v_{1,sc}$$

Indeed, the solution of the system of the two previous expressions gives

eq. 7.21 $$N_{agg} = \frac{4R_{1,sc}^4\pi + 16R_{1,sc}^3\pi\delta_{sc} + 12R_{1,sc}^2\pi\delta_{sc}^2}{3R_{1,sc}^2 a_{sc} - 6v_{1,sc}\delta_{sc} - 6R_{1,sc}v_{1,sc}}$$

eq. 7.22 $$L = \frac{12R_{1,sc}^2 v_{1,sc} + 24R_{1,sc} v_{1,sc} \delta_{sc} + 12 v_{1,sc} \delta_{sc}^2 - 4R_{1,sc}^3 a_{sc}}{3R_{1,sc}^2 a_{sc} - 6 v_{1,sc} \delta_{sc} - 6R_{1,sc} v_{1,sc}}$$

On the basis of the relationships already shown in the previous section, for the sc is then possible to determine the electron density of the paraffinic part,

eq. 7.23 $$\rho_{1,sc} = \frac{e_{CH_2}\left(n_{CH_2,R} + n_{CH_2,O}\, p(1-q)\right) + e_{CH_3} n_{CH_3,R}}{v_{1,sc}}$$

the average number of hydration water molecules *per* polar head of R, $n_{W,\,sc}$ and finally the electron density of the sphero-cylindrical shell, $\rho_{2,\,sc}$. To note, in the previous equation *p* and *q* are the molar fractions that describe the partition of oil among the different structures in the dispersion (Frühwirth, Fritz, Freiberger, & Glatter, 2004). The electron density of the polar domain is calculated by including the possible effect of counterions, here only considered the Na^+

eq. 7.24 $$v_{2,sc} = \frac{\frac{4\pi}{3} R_{2,sc}^3 + \pi R_{2,sc}^2 L}{N_{agg}} - v_{1,sc}$$

eq. 7.25 $$n_{W,sc} = \frac{v_{2,sc} - \left[v_{R1,pol} x_{R1} + v_{R2,pol}(1-x_{R1}) + v_{Na^+} S T n_{Na^+}\right]}{d_W\, v_W}$$

eq. 7.26 $$\rho_{2,sc} = \frac{e_{R1,pol} x_{R1} + e_{R2,pol}(1-x_{R1}) + e_W n_{W,R} + e_{Na^+} S T n_{Na^+}}{v_2}$$

where v_{Na^+}=4.44 Å^3 and e_{Na^+}=10 are the standard volume of number of electron of this cation.

The number density of spherocylinders results:

eq. 7.27 $$n_{sc} = \frac{FWN_A C_R}{N_{agg}\left(1 + C_R p n_{CH_2,O} v_{CH_2}\right)}$$

N_A being Avogadro's number.

Concerning the infinite bilayers (Spinozzi et al., 2010), the are simple relationships among the area of hydrated polar head of R, a_b, and the volume of the oil-enriched paraffinic part and hydrated polar head, all referred to one R molecule,

eq. 7.28 $$\nu_{1,b} = \nu_{CH_2}\left(n_{CH_2,R} + n_{CH_2,O}pq + n_{CH_3,R}r\right)$$

eq. 7.29 $$\nu_{2,b} = \nu_{pol} + \frac{n_{W,b}}{d_W \nu_W} + \nu_{Na^+}S(1-T)n_{Na^+} = a_b\delta_b$$

Also in this latter case, by considering a_b and δ_b among the free and adjustable parameters, the number of hydration water molecules, $n_{W,b}$ can be found, and, likewise, the two electron densities $\rho_{1,b}$ and $\rho_{2,b}$.

As a final remark, the volume fractions of bilayers, both isolated and stacked, which quantify the contribution of those structures, can be found be the following expressions,

eq 7.30 $$\phi_{ib} = \frac{F(1-W)ZN_AC_R\left(\nu_{1,b}+\nu_{2,b}\right)}{1+C_Rpn_{CH_2,O}\nu_{CH_2}}$$

eq.7.31 $$\phi_{sb} = \frac{F(1-W)(1-Z)N_AC_R\left(\nu_{1,b}+\nu_{2,b}\right)}{1+C_Rpn_{CH_2,O}\nu_{CH_2}}$$

Geometrical Model in brackish water

The rhamnolipid molecules assume dimensions and different configurations according to the organization to form a bilayer or a spherocylinder as this figure shows:

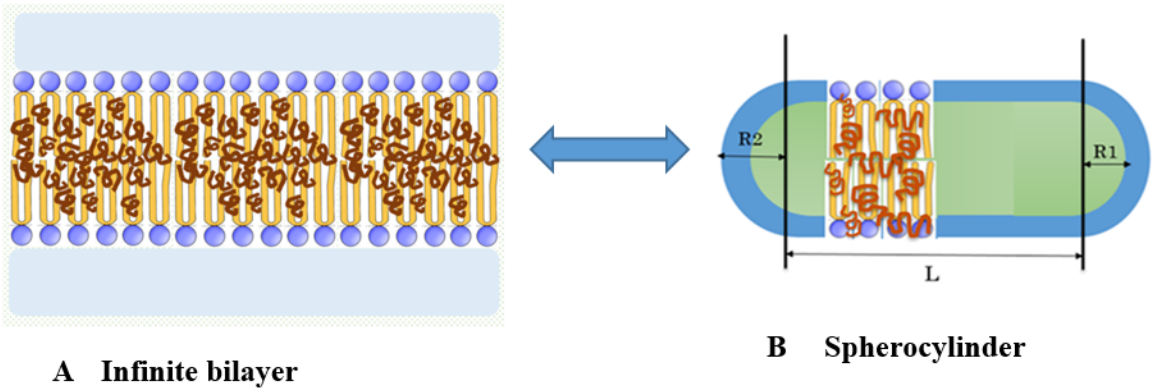

Figure 7.11 The two phases assumed by rhamnolipids in the presence of oil and salts. Situation in brackish water

Figure 7.12: A) Conical conformation of the rhamnolipid molecule in the bilayer structure. B) Conformation of the rhamnolipid molecule in the spherocylinder structure (cylinder shape).

7.3.2 Fitting results in brackish water

As in the previous case, the whole set of derived expressions has been entered in the Genfit software. Subsequently, each of the 360 curves reported in Figure 7.12 has been fitted with the model of the mixture of interacting spherocylinders and stacked bilayers, seen in paragraph 7.3.1. Fitting curves, shown as solid black lines in Figure 7.12, are well superimposed to experimental SAXS data in almost any case. Hence, the model is able to describe the behavior

of the investigated system in a very large set of different conditions. For a sake of completeness, the fitting parameters of the curves of each panel are reported in a group of three tabular panels, shown in Tables 7.4 - 7.46. The first of the three tabular panel indicates the parameters that distribute the various molecules (R, oil and salt) in the different structures. The second tabular panel shows the parameters related to the spherocylinders, whereas the last tabular panel refers to the isolated and stacked bilayers.

Some comments of the obtained results are hereafter listed.

- The *F* parameter in most cases is close to 1, indicating that rhamnolipid molecules are well dispersed in water. However, it decreases up to nearly 0.03 when the concentration of calcium and magnesium ions increases, confirming the low solubility of the biosurfactant in the presence of bivalent cations.
- The *W* parameters is often close to 1, indicating that spherocylinders are the most represantitive self-assembled structure of rhamnolipid in solution. However, in the presence of large amount of sodium *W* decreases up to approximatively 0.6.
- As for the values of *Z*, we can say that it tends to values close to 0 the molecules of rhamnolipid tend to stack themselves forming infinite bilayers. This also allows to have values of *d* around 30 Å, which confirm the results obtained in diffraction. When the *Z* values tend to 1 the bilayers are almost uncorrelated.
- As regards the values of a_{SC} and a_b, results suggest that a_{SC} has minimum values of 150 $Å^2$ up to maximum values of 280, whereas the values of a_b has an average value of 60-70 $Å^2$. This features confirms a completely different packing of RL in the two self-assembled structures.
- In the presence of oil, it is also important to analyze the parameters *p* and *q*. The value of *p* expresses the quantity of methylene groups incorporated in the rhamnolipid micelles with respect to the total amount of CH_2 coming from oil with respect to the RL concentration. The values of *p* are very low and similar, all lower than 0.05. With respect to the parameter *q*, we can say that when it is close to 1 all the oil in the water domain is inside the bilayer, while when it is close to 0 all the oil in water domain it is incorporated inside the spherocylinder. In our case we never get to extreme cases and the values of *q* are always close to 0.5. This means that oil can be embedded in RL indendently on the self-assemble structure.

•

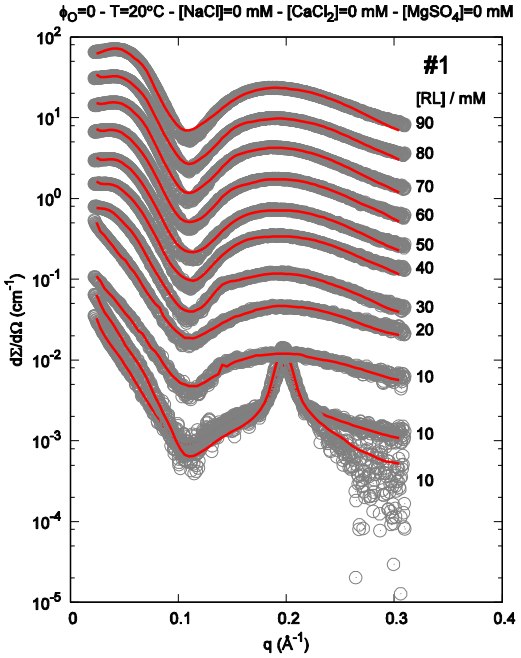
ϕ_O=0 - T=20°C - [NaCl]=0 mM - [$CaCl_2$]=0 mM - [$MgSO_4$]=0 mM
#1
[RL] / mM
90
80
70
60
50
40
30
20
10
10
10
dΣ/dΩ (cm^{-1})
q (Å^{-1})

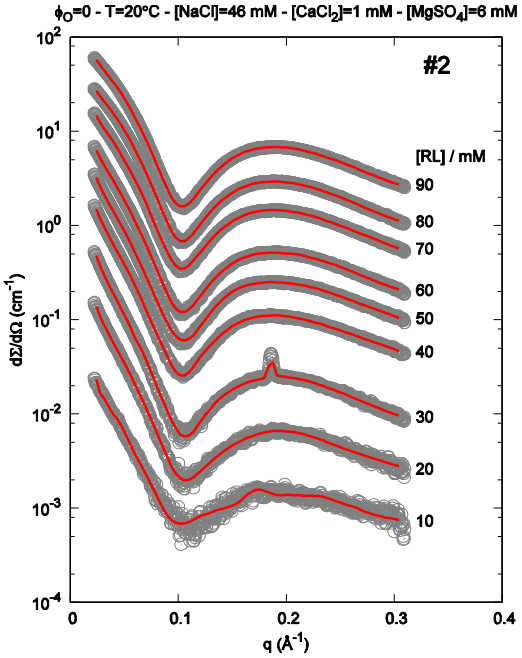
ϕ_O=0 - T=20°C - [NaCl]=46 mM - [$CaCl_2$]=1 mM - [$MgSO_4$]=6 mM
#2
[RL] / mM
90
80
70
60
50
40
30
20
10
dΣ/dΩ (cm^{-1})
q (Å^{-1})

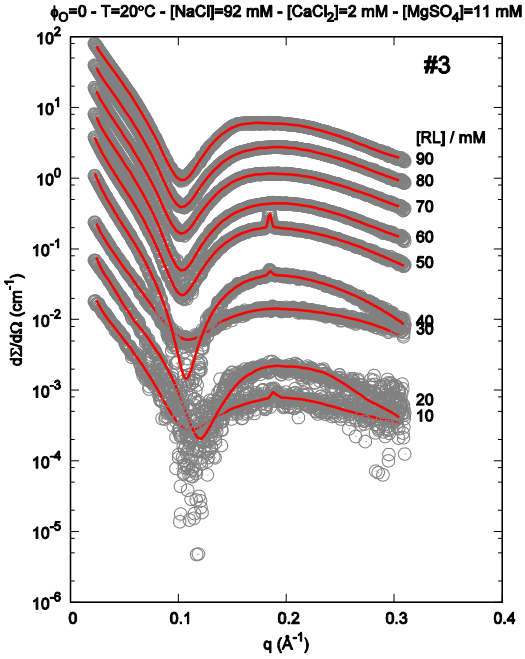
ϕ_O=0 - T=20°C - [NaCl]=92 mM - [$CaCl_2$]=2 mM - [$MgSO_4$]=11 mM
#3
[RL] / mM
90
80
70
60
50
40
30
20
10
dΣ/dΩ (cm^{-1})
q (Å^{-1})

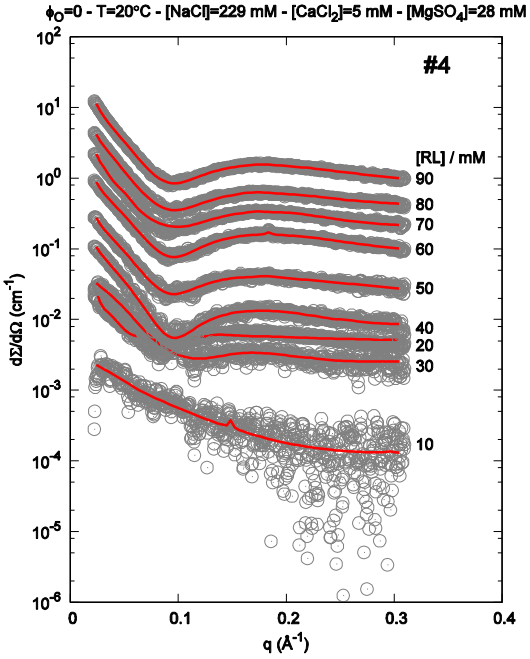
ϕ_O=0 - T=20°C - [NaCl]=229 mM - [$CaCl_2$]=5 mM - [$MgSO_4$]=28 mM
#4
[RL] / mM
90
80
70
60
50
40
20
30
10
dΣ/dΩ (cm^{-1})
q (Å^{-1})

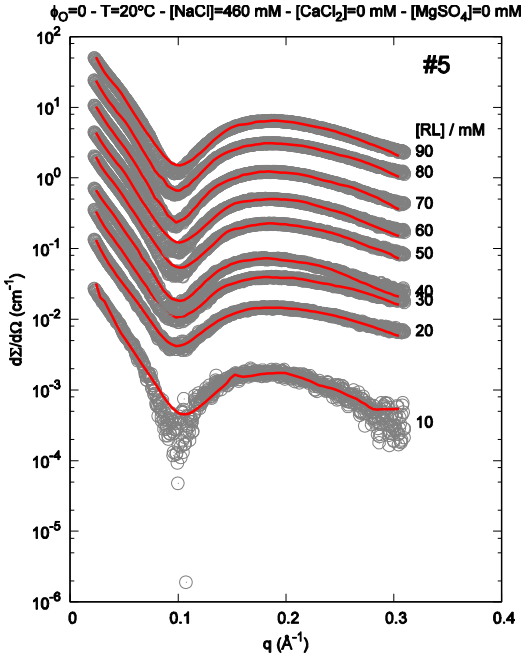
ϕ_O=0 - T=20°C - [NaCl]=460 mM - [$CaCl_2$]=0 mM - [$MgSO_4$]=0 mM
#5
[RL] / mM
90
80
70
60
50
40
30
20
10
dΣ/dΩ (cm^{-1})
q (Å^{-1})

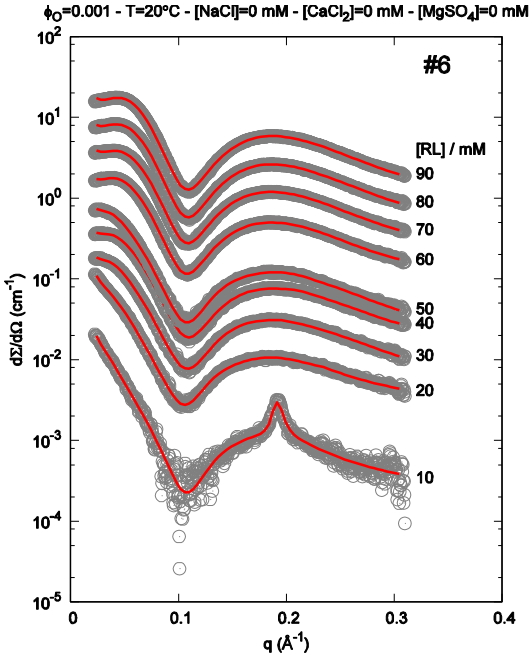
ϕ_O=0.001 - T=20°C - [NaCl]=0 mM - [$CaCl_2$]=0 mM - [$MgSO_4$]=0 mM
#6
[RL] / mM
90
80
70
60
50
40
30
20
10
dΣ/dΩ (cm^{-1})
q (Å^{-1})

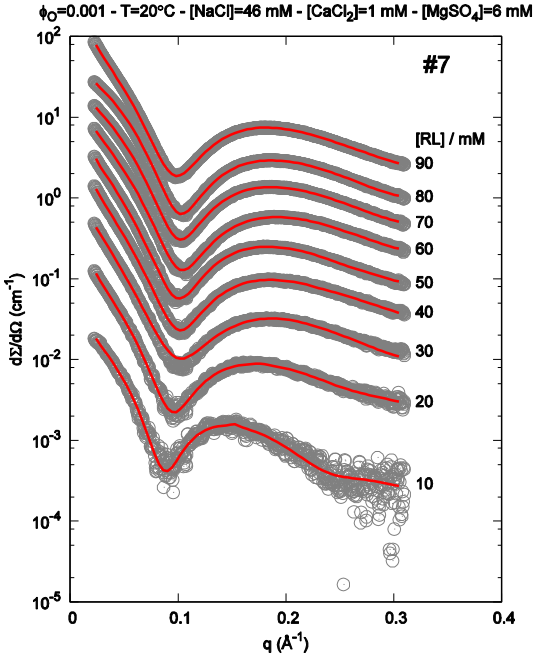
ϕ_O=0.001 - T=20°C - [NaCl]=46 mM - [$CaCl_2$]=1 mM - [$MgSO_4$]=6 mM
#7
[RL] / mM
90
80
70
60
50
40
30
20
10
dΣ/dΩ (cm^{-1})
q (Å^{-1})

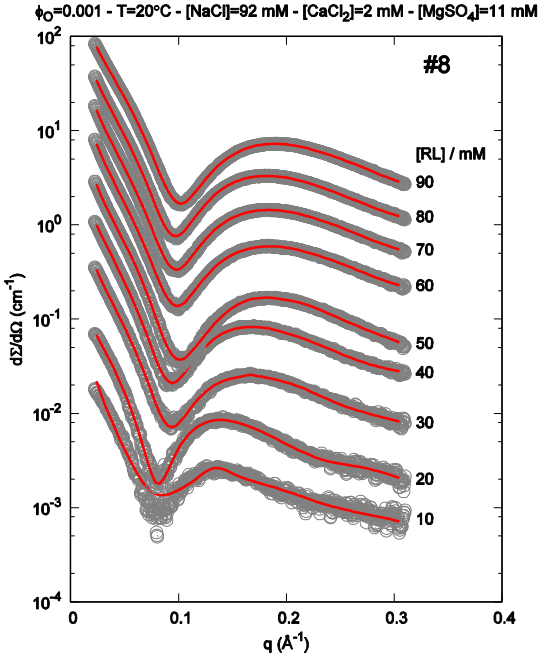
ϕ_O=0.001 - T=20°C - [NaCl]=92 mM - [$CaCl_2$]=2 mM - [$MgSO_4$]=11 mM
#8
[RL] / mM
90
80
70
60
50
40
30
20
10
dΣ/dΩ (cm^{-1})
q (Å^{-1})

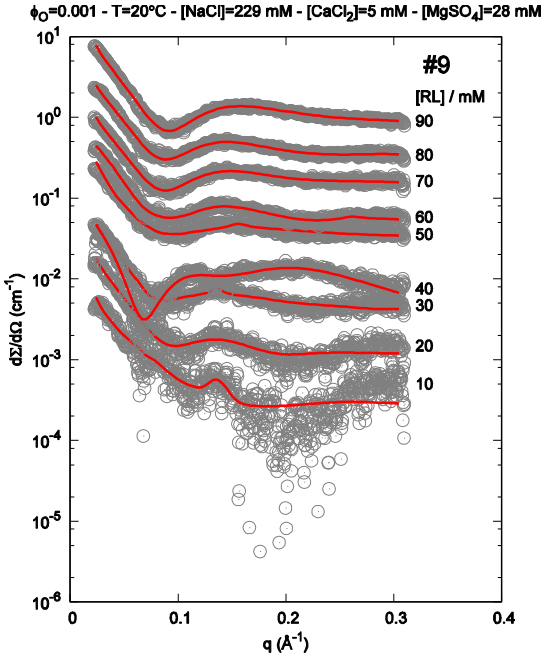
ϕ_O=0.001 - T=20°C - [NaCl]=229 mM - [$CaCl_2$]=5 mM - [$MgSO_4$]=28 mM
#9
[RL] / mM
90
80
70
60
50
40
30
20
10
dΣ/dΩ (cm^{-1})
q (Å^{-1})

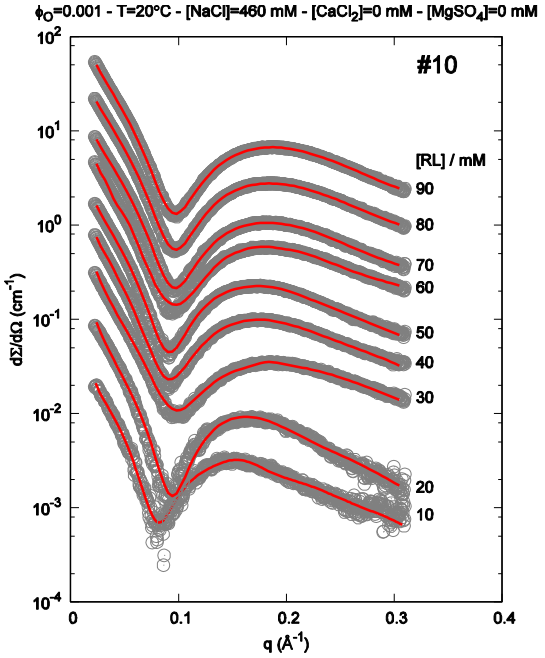
ϕ_O=0.001 - T=20°C - [NaCl]=460 mM - [$CaCl_2$]=0 mM - [$MgSO_4$]=0 mM
#10
[RL] / mM
90
80
70
60
50
40
30
20
10
dΣ/dΩ (cm^{-1})
q (Å^{-1})

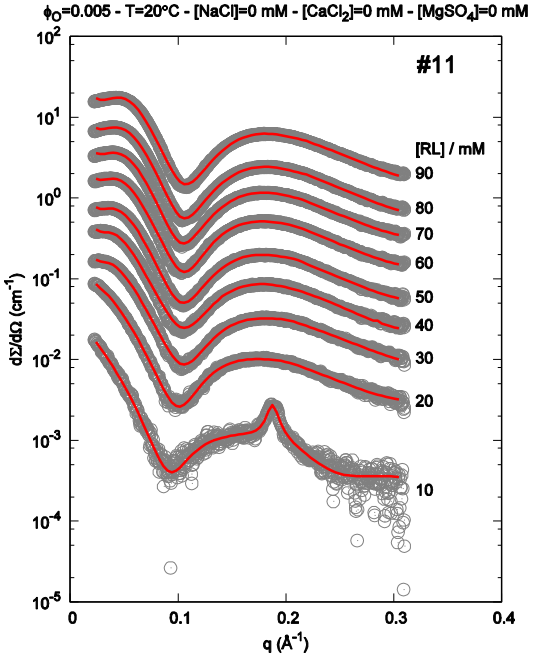
ϕ_O=0.005 - T=20°C - [NaCl]=0 mM - [$CaCl_2$]=0 mM - [$MgSO_4$]=0 mM
#11
[RL] / mM
90
80
70
60
50
40
30
20
10
dΣ/dΩ (cm^{-1})
q (Å^{-1})

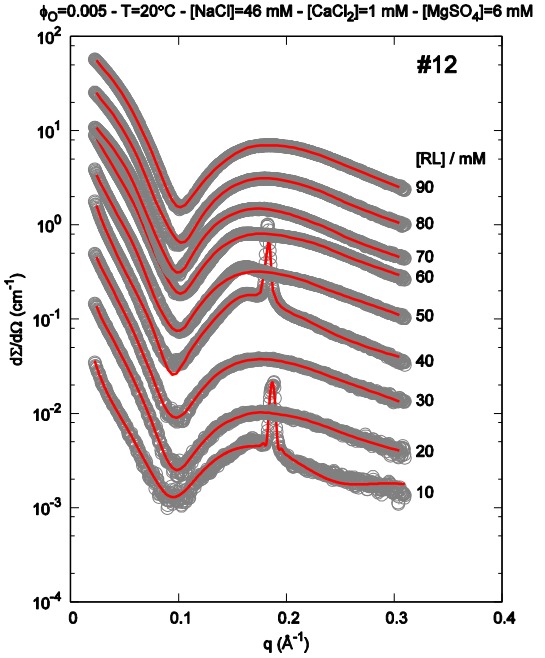
ϕ_O=0.005 - T=20°C - [NaCl]=46 mM - [$CaCl_2$]=1 mM - [$MgSO_4$]=6 mM
#12
[RL] / mM
90
80
70
60
50
40
30
20
10
dΣ/dΩ (cm^{-1})
q (Å^{-1})

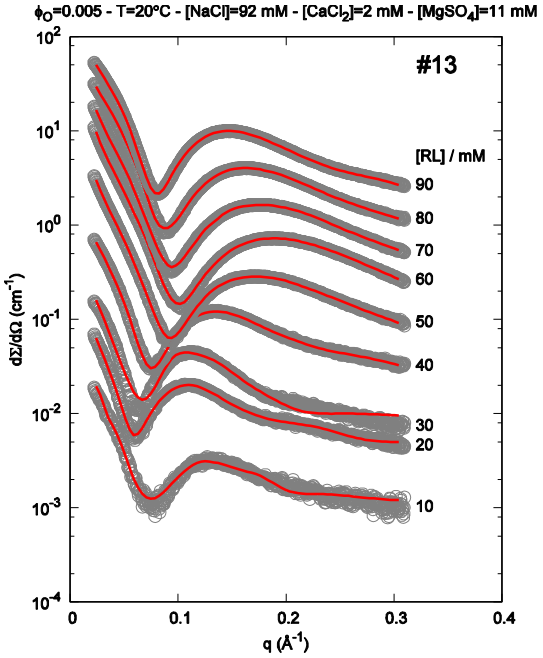
ϕ_O=0.005 - T=20°C - [NaCl]=92 mM - [$CaCl_2$]=2 mM - [$MgSO_4$]=11 mM
#13
[RL] / mM
90
80
70
60
50
40
30
20
10
dΣ/dΩ (cm^{-1})
q (Å^{-1})

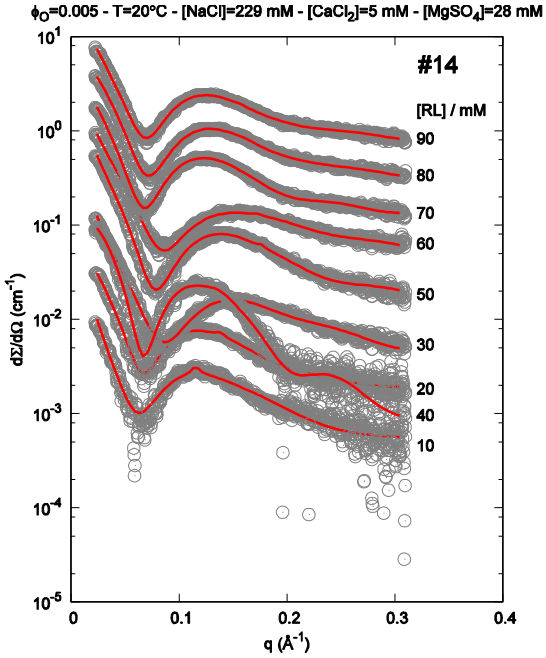
ϕ_O=0.005 - T=20°C - [NaCl]=229 mM - [$CaCl_2$]=5 mM - [$MgSO_4$]=28 mM
#14
[RL] / mM
90
80
70
60
50
30
20
40
10
dΣ/dΩ (cm^{-1})
q (Å^{-1})

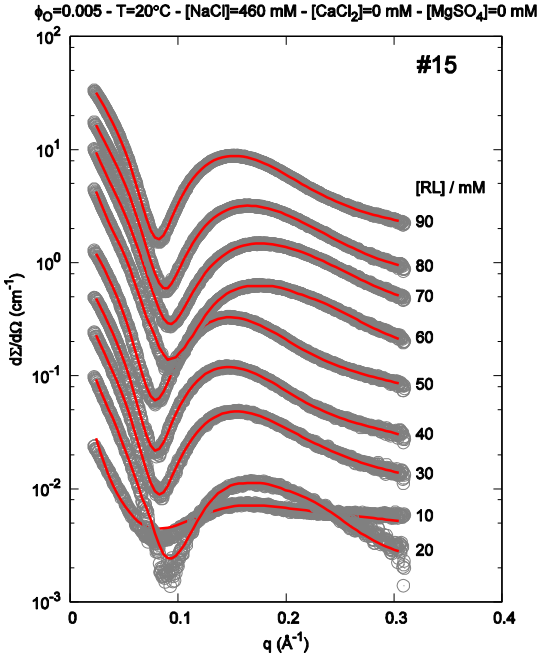
ϕ_O=0.005 - T=20°C - [NaCl]=460 mM - [$CaCl_2$]=0 mM - [$MgSO_4$]=0 mM
#15
[RL] / mM
90
80
70
60
50
40
30
10
20
dΣ/dΩ (cm^{-1})
q (Å^{-1})

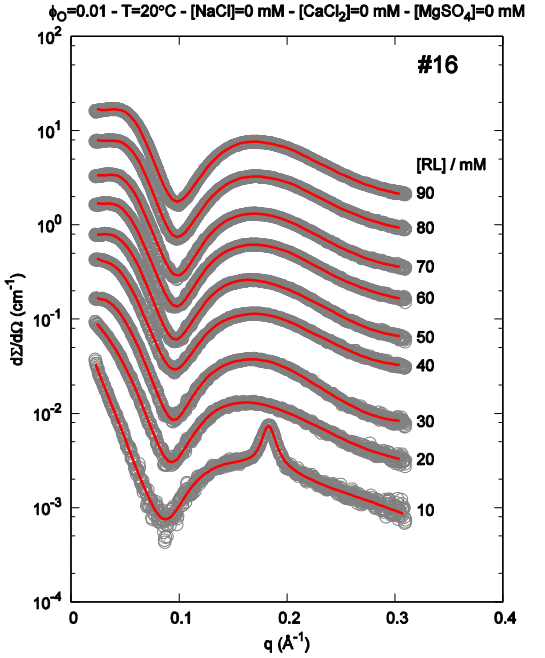
ϕ_O=0.01 - T=20°C - [NaCl]=0 mM - [$CaCl_2$]=0 mM - [$MgSO_4$]=0 mM
#16
[RL] / mM
90
80
70
60
50
40
30
20
10
dΣ/dΩ (cm^{-1})
q (Å^{-1})

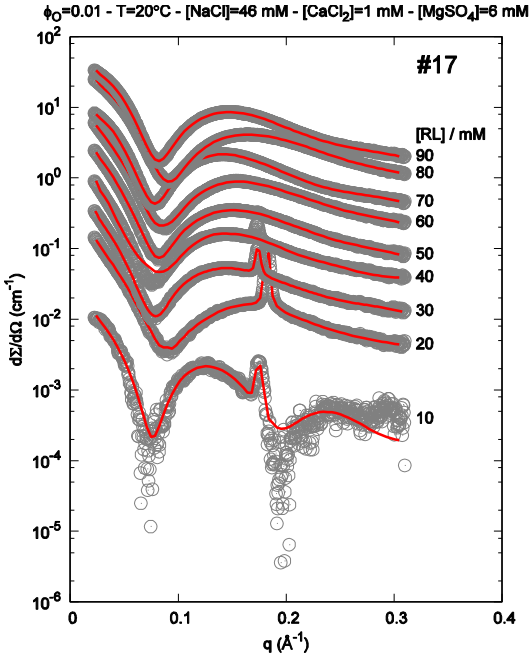
ϕO=0.01 - T=20°C - [NaCl]=46 mM - [CaCl2]=1 mM - [MgSO4]=6 mM
#17
[RL] / mM
90
80
70
60
50
40
30
20
10
dΣ/dΩ (cm-1)
q (Å-1)

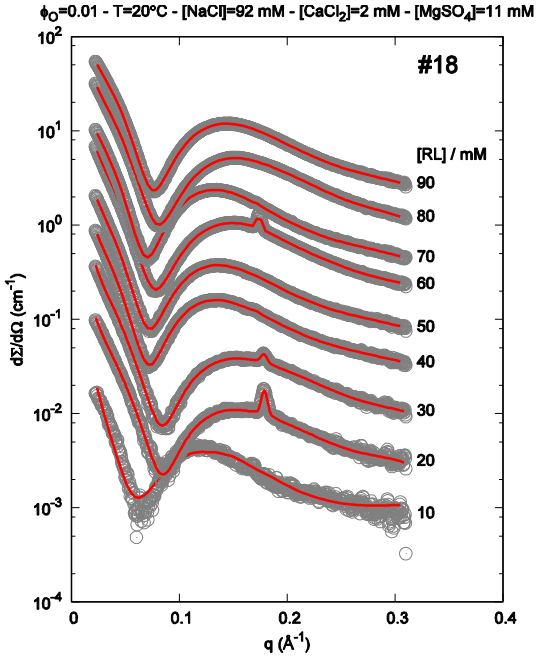
ϕO=0.01 - T=20°C - [NaCl]=92 mM - [CaCl2]=2 mM - [MgSO4]=11 mM
#18
[RL] / mM
90
80
70
60
50
40
30
20
10
dΣ/dΩ (cm-1)
q (Å-1)

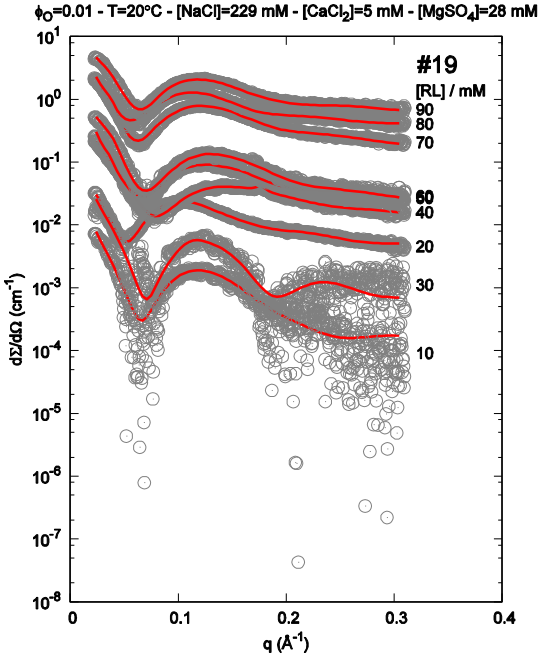
ϕO=0.01 - T=20°C - [NaCl]=229 mM - [CaCl2]=5 mM - [MgSO4]=28 mM
#19
[RL] / mM
90
80
70
60
40
20
30
10
dΣ/dΩ (cm-1)
q (Å-1)

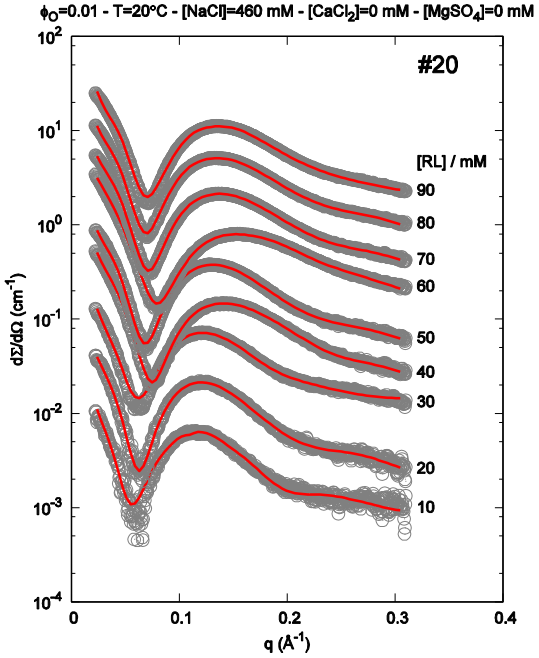
ϕO=0.01 - T=20°C - [NaCl]=460 mM - [CaCl2]=0 mM - [MgSO4]=0 mM
#20
[RL] / mM
90
80
70
60
50
40
30
20
10
dΣ/dΩ (cm-1)
q (Å-1)

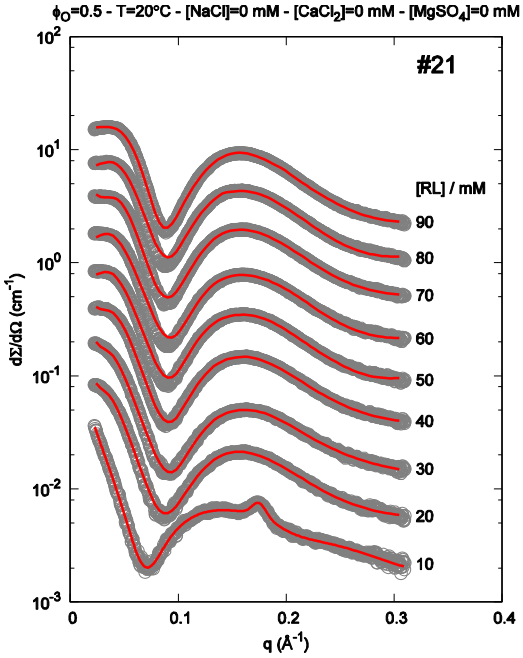
ϕO=0.5 - T=20°C - [NaCl]=0 mM - [CaCl2]=0 mM - [MgSO4]=0 mM
#21
[RL] / mM
90
80
70
60
50
40
30
20
10
dΣ/dΩ (cm-1)
q (Å-1)

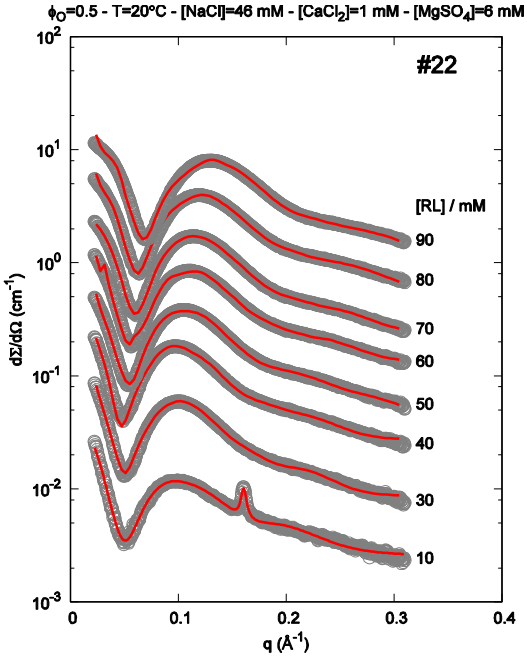
ϕO=0.5 - T=20°C - [NaCl]=46 mM - [CaCl2]=1 mM - [MgSO4]=6 mM
#22
[RL] / mM
90
80
70
60
50
40
30
10
dΣ/dΩ (cm-1)
q (Å-1)

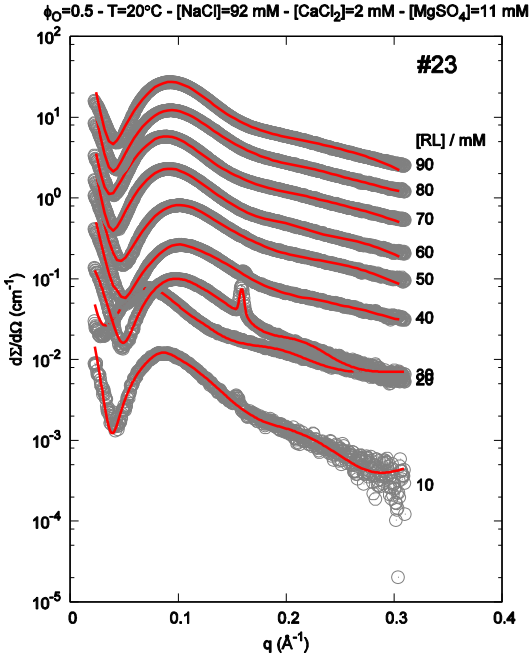
ϕO=0.5 - T=20°C - [NaCl]=92 mM - [CaCl2]=2 mM - [MgSO4]=11 mM
#23
[RL] / mM
90
80
70
60
50
40
10
dΣ/dΩ (cm-1)
q (Å-1)

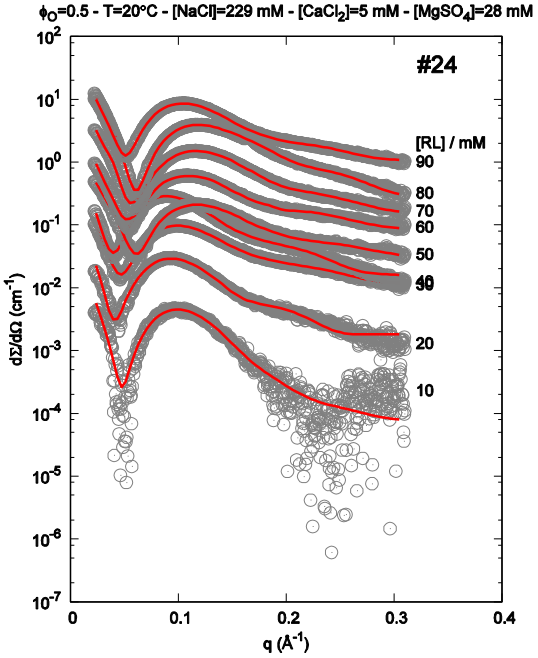
ϕO=0.5 - T=20°C - [NaCl]=229 mM - [CaCl2]=5 mM - [MgSO4]=28 mM
#24
[RL] / mM
90
80
70
60
50
20
10
dΣ/dΩ (cm-1)
q (Å-1)

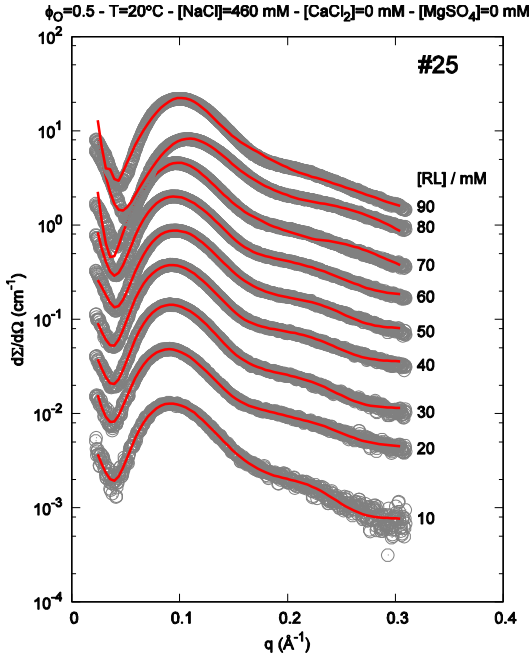
ϕ_O=0.5 - T=20°C - [NaCl]=460 mM - [$CaCl_2$]=0 mM - [$MgSO_4$]=0 mM
#25
[RL] / mM
90
80
70
60
50
40
30
20
10
dΣ/dΩ (cm^{-1})
q (Å^{-1})

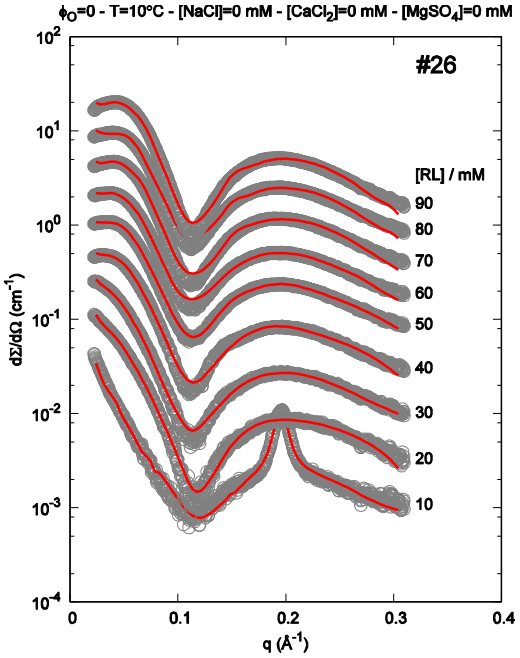
ϕ_O=0 - T=10°C - [NaCl]=0 mM - [$CaCl_2$]=0 mM - [$MgSO_4$]=0 mM
#26
[RL] / mM
90
80
70
60
50
40
30
20
10
dΣ/dΩ (cm^{-1})
q (Å^{-1})

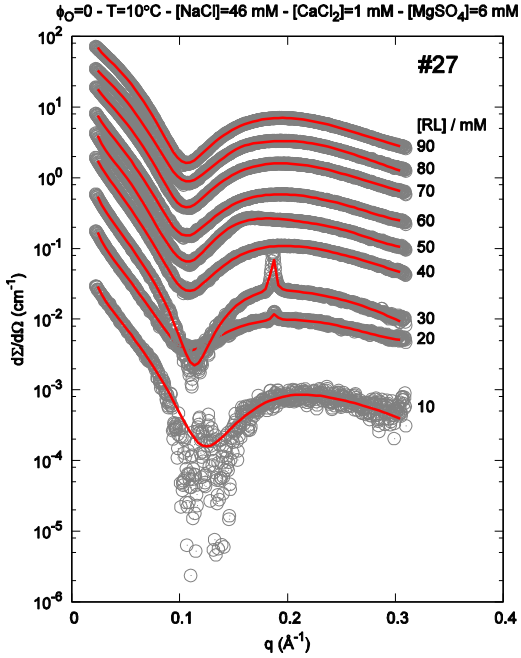
ϕ_O=0 - T=10°C - [NaCl]=46 mM - [$CaCl_2$]=1 mM - [$MgSO_4$]=6 mM
#27
[RL] / mM
90
80
70
60
50
40
30
20
10
dΣ/dΩ (cm^{-1})
q (Å^{-1})

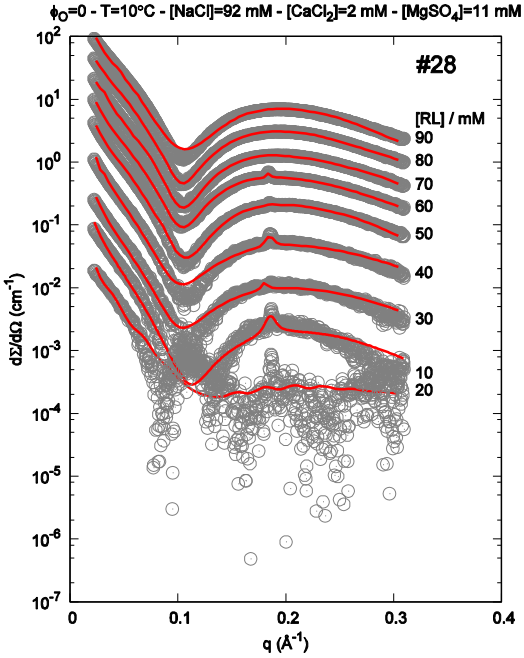
ϕ_O=0 - T=10°C - [NaCl]=92 mM - [$CaCl_2$]=2 mM - [$MgSO_4$]=11 mM
#28
[RL] / mM
90
80
70
60
50
40
30
10
20
dΣ/dΩ (cm^{-1})
q (Å^{-1})

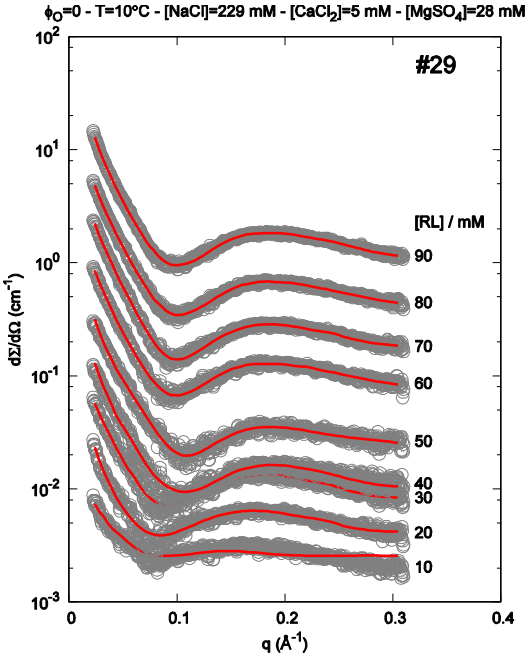
ϕ_O=0 - T=10°C - [NaCl]=229 mM - [$CaCl_2$]=5 mM - [$MgSO_4$]=28 mM
#29
[RL] / mM
90
80
70
60
50
40
30
20
10
dΣ/dΩ (cm^{-1})
q (Å^{-1})

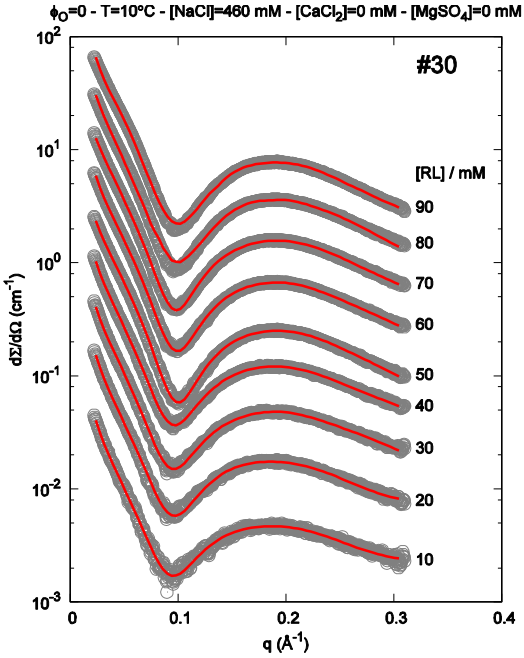
ϕ_O=0 - T=10°C - [NaCl]=460 mM - [$CaCl_2$]=0 mM - [$MgSO_4$]=0 mM
#30
[RL] / mM
90
80
70
60
50
40
30
20
10
dΣ/dΩ (cm^{-1})
q (Å^{-1})

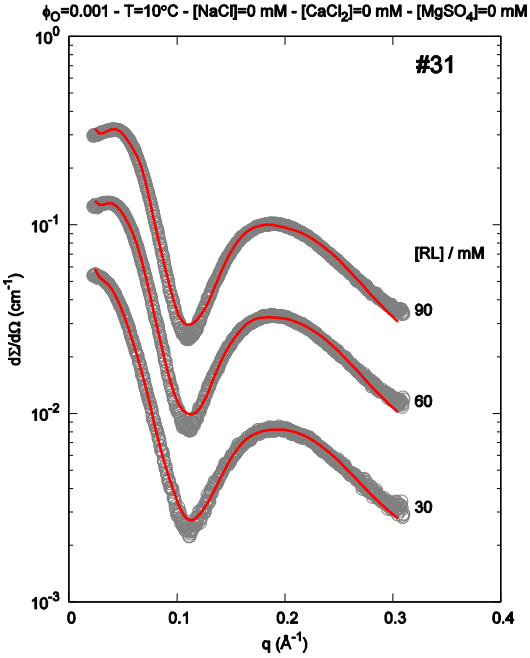
ϕ_O=0.001 - T=10°C - [NaCl]=0 mM - [$CaCl_2$]=0 mM - [$MgSO_4$]=0 mM
#31
[RL] / mM
90
60
30
dΣ/dΩ (cm^{-1})
q (Å^{-1})

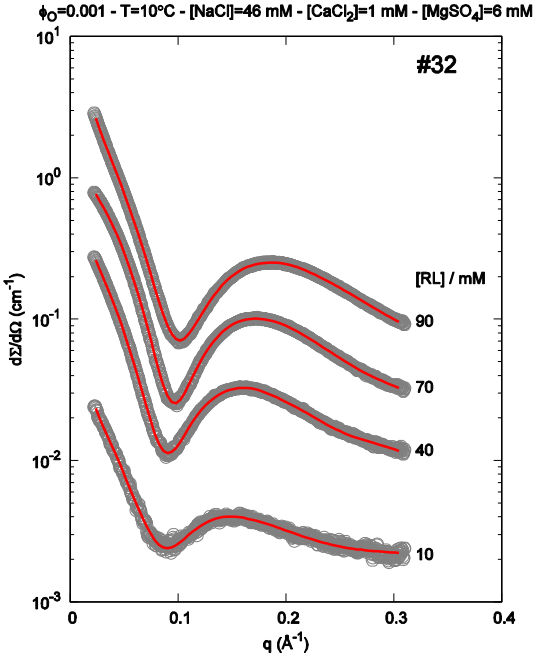
ϕ_O=0.001 - T=10°C - [NaCl]=46 mM - [$CaCl_2$]=1 mM - [$MgSO_4$]=6 mM
#32
[RL] / mM
90
70
40
10
dΣ/dΩ (cm^{-1})
q (Å^{-1})

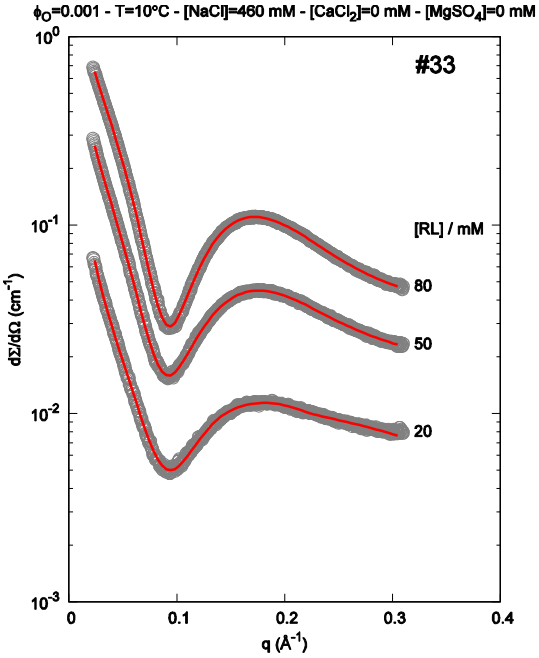
ϕ_O=0.001 - T=10°C - [NaCl]=460 mM - [$CaCl_2$]=0 mM - [$MgSO_4$]=0 mM
#33
[RL] / mM
80
50
20
dΣ/dΩ (cm^{-1})
q (Å^{-1})

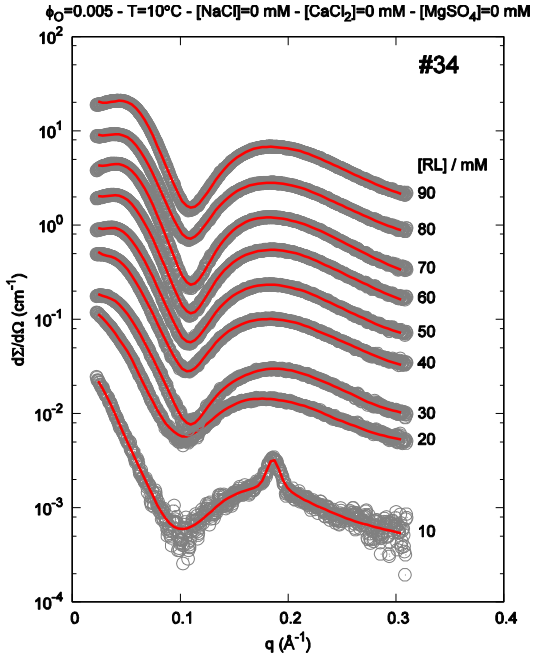
ϕ_O=0.005 - T=10°C - [NaCl]=0 mM - [$CaCl_2$]=0 mM - [$MgSO_4$]=0 mM
#34
[RL] / mM
90
80
70
60
50
40
30
20
10
dΣ/dΩ (cm^{-1})
q (Å^{-1})

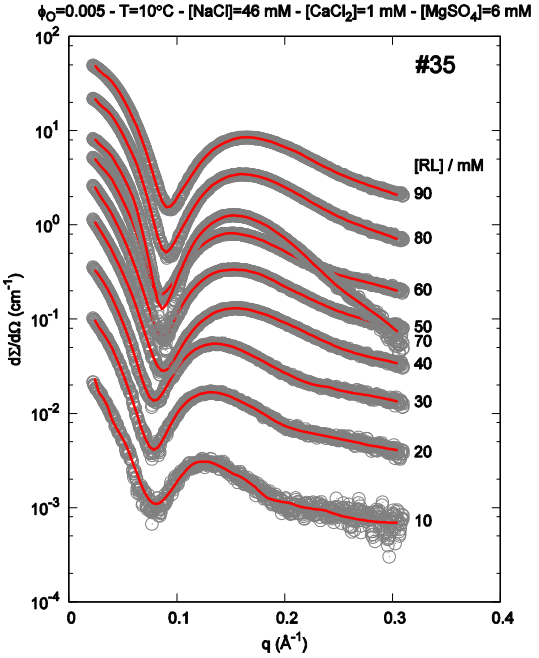
ϕ_O=0.005 - T=10°C - [NaCl]=46 mM - [$CaCl_2$]=1 mM - [$MgSO_4$]=6 mM
#35
[RL] / mM
90
80
60
50
70
40
30
20
10
dΣ/dΩ (cm^{-1})
q (Å^{-1})

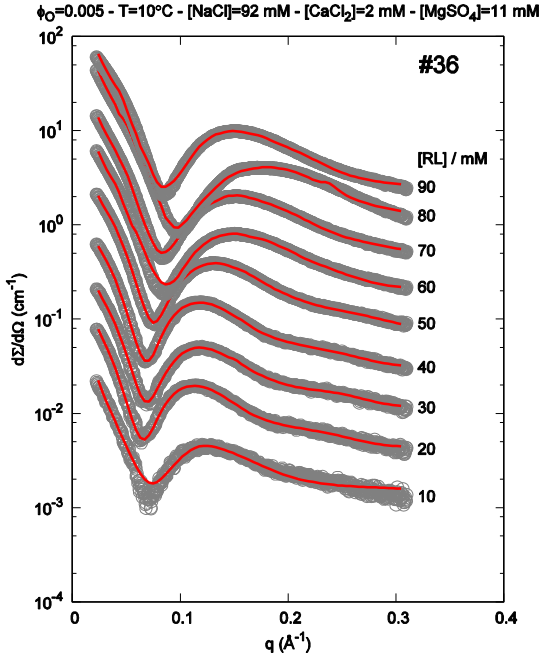
ϕ_O=0.005 - T=10°C - [NaCl]=92 mM - [$CaCl_2$]=2 mM - [$MgSO_4$]=11 mM
#36
[RL] / mM
90
80
70
60
50
40
30
20
10
dΣ/dΩ (cm^{-1})
q (Å^{-1})

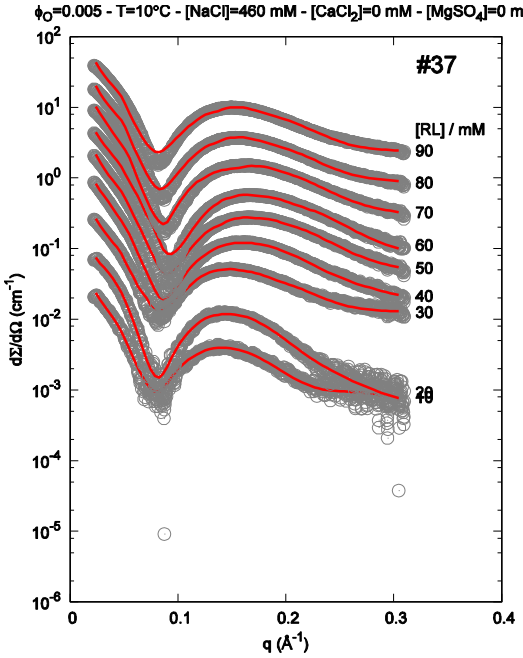
ϕO=0.005 - T=10°C - [NaCl]=460 mM - [CaCl2]=0 mM - [MgSO4]=0 mM
#37
[RL] / mM
90
80
70
60
50
40
30
dΣ/dΩ (cm-1)
q (Å-1)

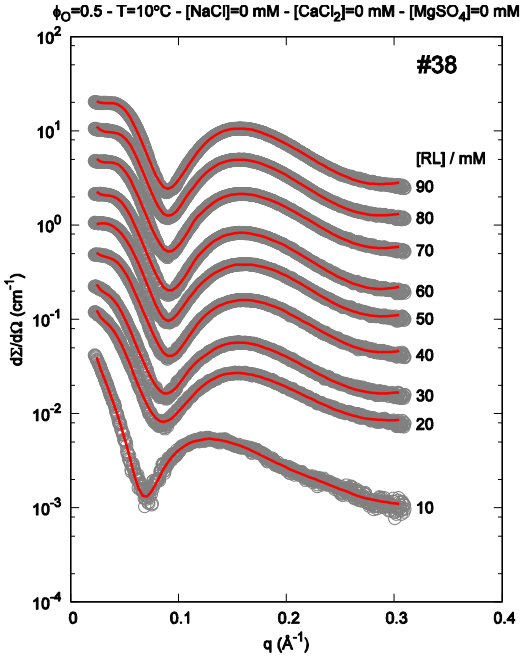
ϕO=0.5 - T=10°C - [NaCl]=0 mM - [CaCl2]=0 mM - [MgSO4]=0 mM
#38
[RL] / mM
90
80
70
60
50
40
30
20
10
dΣ/dΩ (cm-1)
q (Å-1)

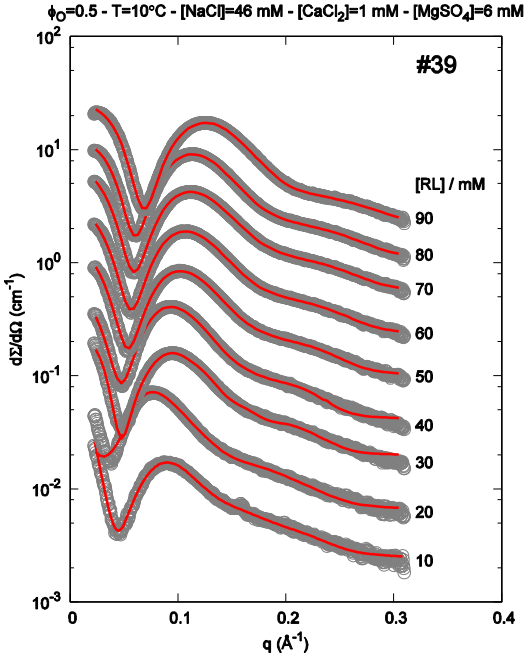
ϕO=0.5 - T=10°C - [NaCl]=46 mM - [CaCl2]=1 mM - [MgSO4]=6 mM
#39
[RL] / mM
90
80
70
60
50
40
30
20
10
dΣ/dΩ (cm-1)
q (Å-1)

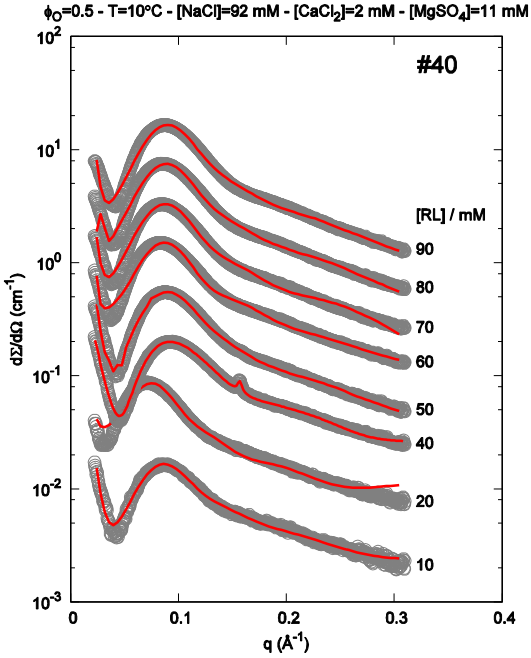
ϕO=0.5 - T=10°C - [NaCl]=92 mM - [CaCl2]=2 mM - [MgSO4]=11 mM
#40
[RL] / mM
90
80
70
60
50
40
20
10
dΣ/dΩ (cm-1)
q (Å-1)

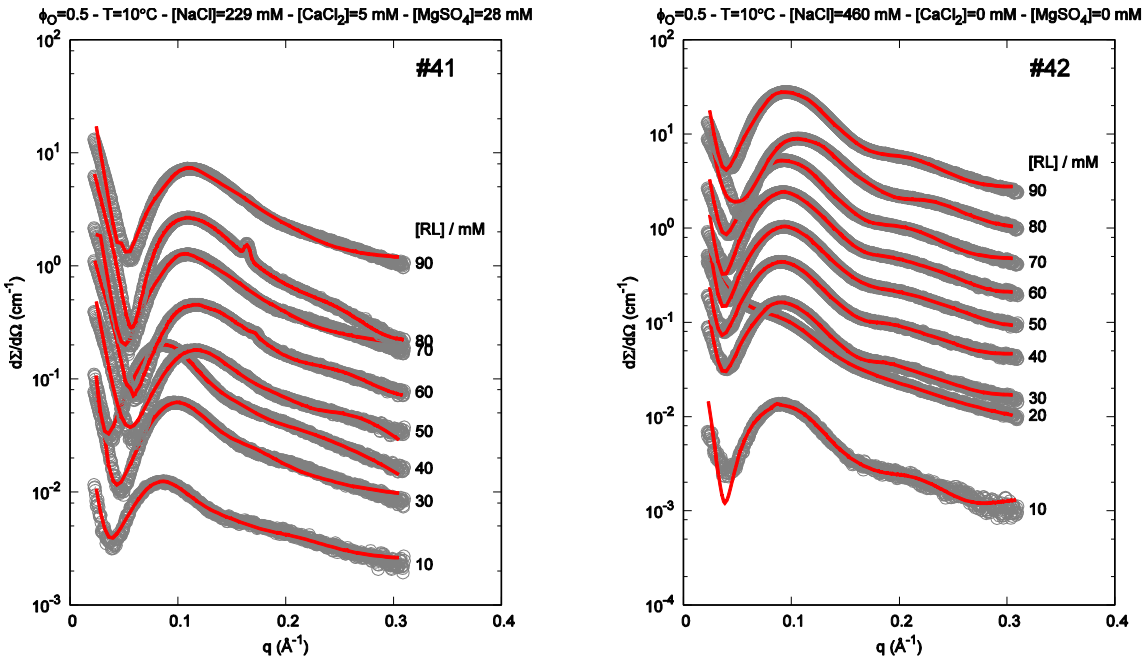

Figure 7.13: Curve fitting relative to different concentrations of rhamnolipids (from 10 to 90 mM), different concentrations and combinations of salt, and 5 different concentrations of kirkuk oil

C_R (mM)	F	W	Z	p	q	R	T
10	0.93±0.03	0.27±0.06	0.46±0.09	–	–	–	–
10	0.91±0.03	0.33±0.04	0.41±0.07	–	–	–	–
10	1.000±0.003	1.00±0.03	–	–	–	–	–
20	0.79±0.09	1.000±0.002	–	–	–	–	–
30	0.92±0.02	0.96±0.03	0.3±0.3	–	–	–	–
40	0.79±0.04	0.95±0.02	0.00±0.01	–	–	–	–
50	0.98±0.02	0.974±0.009	0.00±0.05	–	–	–	–
60	0.89±0.02	0.970±0.009	0.03±0.01	–	–	–	–
70	1.00±0.02	0.973±0.003	0.01±0.02	–	–	–	–
80	0.95±0.02	0.969±0.002	0.009±0.005	–	–	–	–
90	0.97±0.01	1.00±0.01	–	–	–	–	–

C_R (mM)	a_{sc} (Å^2)	δ_{sc} (Å)	$R_{1,sc}$ (Å)	L (Å)	N_{aggr}	$n_{W,sc}$	z q_o	J RT
10	250±30	15.1±0.8	10±4	150±70	120±30	70±10	−0.42±0.01	0.9±0.4
10	299.9±0.1	11.574±0.002	7.00±0.04	9000±2000	3300±800	68.2±0.4	−0.03±0.05	0.5±0.2
10	299.9±0.6	15.12±0.09	7.92±0.04	900±200	450±80	87.7±0.8	−0.82±0.04	1.000±0.002
20	298.4±0.4	16.2±0.4	8.07±0.05	1300±200	660±90	94±2	−0.86±0.03	0.897±0.005
30	298.2±0.6	15.0±0.2	8.38±0.02	220±10	133±6	83.9±0.7	−0.47±0.03	0.4±0.2
40	298.0±0.9	14.1±0.2	8.47±0.05	180±4	107±2	79.1±0.9	−0.67±0.07	1.0±0.4
50	297±1	14.4±0.1	8.46±0.05	165±9	102±4	79.2±0.9	−0.67±0.06	0.49±0.01
60	298.7±0.7	14.5±0.2	8.53±0.03	160±8	100±4	81±1	−0.6±0.1	0.1±0.1
70	298.3±0.9	14.65±0.09	8.61±0.03	149±2	95.6±0.8	80.6±0.7	−0.78±0.02	0.08±0.02
80	299.0±0.5	14.29±0.08	8.55±0.02	146±2	92.1±0.7	79.0±0.5	−0.83±0.01	0.11±0.03
90	300.0±0.2	14.5±0.1	8.58±0.03	150±3	95±2	80.4±0.8	−0.82±0.02	0.00±0.02

C_R (mM)	a_b (Å^2)	δ_b (Å)	$R_{1,b}$ (Å)	$n_{W,b}$	d (Å)	g_d	N_d
10	57±2	8.65±0.08	6.89±0.08	2.5±0.5	31.76±0.07	0.07±0.01	14±6
10	57±1	8.3±0.1	6.9±0.2	1.9±0.6	31.77±0.09	0.075±0.003	13±3
10	70.0±0.1	24.6±0.2	5.61±0.02	44.2±0.4	–	–	–
20	62.7±0.3	24.75±0.07	6.21±0.05	38.4±0.3	–	–	–
30	54±7	13±1	7.2±0.7	9±6	44±1	0.09±0.04	6±2
40	70±2	12.6±0.8	5.8±0.2	16±2	41±1	0.006±0.004	3.5±0.4
50	67.7±0.5	11.7±0.6	5.75±0.04	12±2	40±1	0.09±0.02	4±1
60	70±1	13.66±0.06	5.60±0.08	18.1±0.6	42.9±0.4	0.04±0.02	4±1
70	67±1	12.6±0.5	5.8±0.1	14±2	41.8±0.8	0.060±0.004	5.5±0.9
80	68±1	12.5±0.4	5.80±0.08	14±1	41.6±0.7	0.03±0.01	4±1
90	61.3±0.2	7±2	6.41±0.02	0±4	–	–	–

Table 7.4: Fitting parameters with the model of mixtures of interacting spherocylinders and stacked bilayers related to the curves shown in the panel #1: ϕ_O=0.0000, T=20°C, [NaCl]=0 mM, [$CaCl_2$]=0 mM, [$MgSO_4$]=0 mM.

C_R (mM)	F	W	Z	p	q	R	T
10	0.520±0.008	0.5224±0.0008	0.61±0.02	–	–	0.76±0.04	0.81±0.08
20	0.28±0.05	0.30±0.06	1.00±0.03	–	–	0.6±0.1	0.6±0.1
30	0.44±0.02	0.38±0.03	0.93±0.03	–	–	0.535±0.009	0.66±0.05
40	0.61±0.05	0.22±0.02	1.000±0.003	–	–	0.96±0.05	0.82±0.05
50	0.46±0.02	0.198±0.009	0.98±0.01	–	–	0.94±0.03	0.27±0.08
60	0.524±0.006	0.378±0.009	0.993±0.004	–	–	1.00±0.03	0.72±0.02
70	0.559±0.003	0.270±0.006	1.000±0.003	–	–	0.976±0.009	0.596±0.004
80	0.58±0.02	0.35±0.03	0.98±0.02	–	–	0.94±0.03	0.97±0.04
90	0.57±0.02	0.36±0.01	0.98±0.04	–	–	0.98±0.03	0.83±0.01

C_R (mM)	a_{sc} (Å^2)	δ_{sc} (Å)	$R_{1,sc}$ (Å)	L (Å)	N_{aggr}	$n_{W,sc}$	z q_o	J RT
10	261±7	13.79±0.01	8.6±0.1	7000±2000	4000±1000	64±2	−0.49±0.07	0.99±0.04
20	190±10	11.9±0.8	13.0±0.5	40±10	70±10	39±7	−0.0±0.1	1.00±0.07
30	250±10	16.0±0.4	9.3±0.2	1100±200	700±100	78±5	−0.20±0.09	1.0±0.3
40	299.4±0.9	16.7±0.1	9.7±0.1	150±20	111±9	98±1	−0.62±0.05	1.00±0.04
50	292±10	16.0±0.4	11.0±0.3	70±20	70±20	92±1	−0.66±0.09	0.0±0.4
60	261±5	12.5±0.1	11.8±0.1	27±1	44±2	58.2±0.9	−0.20±0.07	0.92±0.05
70	289±4	16.36±0.09	9.40±0.04	220±20	150±20	94±1	−0.82±0.07	0.994±0.003
80	300±1	13.3±0.2	11.31±0.05	26±1	39.0±0.9	72±1	−0.30±0.04	0.95±0.03
90	283±4	12.9±0.1	11.5±0.2	27±2	41±1	66±2	−0.51±0.04	0.979±0.009

C_R (mM)	a_b (Å^2)	δ_b (Å)	$R_{1,b}$ (Å)	$n_{W,b}$	d (Å)	g_d	N_d
10	70±4	9.6±0.4	6.1±0.4	8±2	36.4±0.6	0.10±0.02	0±10
20	68±1	8.5±0.2	6.0±0.1	5.5±0.6	33.4±0.6	0.06±0.03	50±1
30	69±8	8.5±0.4	5.9±0.8	6±3	33.8±0.1	0.03±0.05	31±1
40	67±2	8.0±0.8	6.4±0.2	4±2	30±2	0.067±0.008	0±30
50	66±2	6.7±0.2	6.6±0.3	0.8±0.7	27±3	0.03±0.04	0±10
60	69±2	7.3±0.6	6.1±0.2	3±2	30±1	0.10±0.05	20±10
70	63.21±0.08	7.9±0.2	6.71±0.01	2.7±0.4	34±3	0.004±0.004	0±20
80	68.8±0.5	6.9±0.5	6.18±0.09	2±1	29.9±0.3	0.100±0.001	0±20
90	69.39±0.05	6.8±0.4	6.14±0.01	1.8±0.9	30±1	0.095±0.001	6±1

Table 7.5: Fitting parameters with the model of mixtures of interacting spherocylinders and stacked bilayers related to the curves shown in the panel #2: ϕ_O=0.0000, T=20°C, [NaCl]=46 mM, [$CaCl_2$]=1 mM, [$MgSO_4$]=6 mM.

C_R (mM)	F	W	Z	p	q	R	T
10	0.06±0.01	0.5±0.2	0.97±0.08	–	–	0.59±0.02	0.7±0.1
20	0.24±0.04	0.53±0.01	1.0±0.2	–	–	0.56±0.02	0.71±0.03
30	0.23±0.05	0.83±0.05	1.0±0.1	–	–	0.64±0.06	0.32±0.09
40	0.19±0.01	0.56±0.01	0.99±0.03	–	–	0.63±0.02	0.00±0.07
50	0.88±0.04	0.47±0.04	0.969±0.006	–	–	0.23±0.02	0.61±0.03
60	0.34±0.05	0.35±0.06	0.90±0.07	–	–	0.63±0.08	0.3±0.1
70	0.41±0.02	0.45±0.02	0.97±0.01	–	–	0.68±0.02	0.28±0.09
80	0.43±0.03	0.39±0.03	0.95±0.02	–	–	0.58±0.08	0.17±0.05
90	0.471±0.006	0.537±0.006	0.97±0.01	–	–	0.58±0.03	0.3±0.1

C_R (mM)	a_{sc} (Å^2)	δ_{sc} (Å)	$R_{1,sc}$ (Å)	L (Å)	N_{aggs}	$n_{W,sc}$	z q_o	J RT
10	230±10	12.9±0.4	12±1	40±30	60±8	49±2	−0.7±0.3	0.0±0.3
20	230±10	11.65±0.04	9±1	3000±2000	1900±900	48±4	−1.0±0.5	0.59±0.05
30	250±10	9.1±0.6	10.4±0.4	26±2	32±3	38±4	−0.1±0.2	1.00±0.09
40	270±10	11.4±0.2	11.7±0.2	21±3	37±3	55±4	−0.03±0.05	1.000±0.002
50	284±5	12.9±0.1	11.2±0.1	23±3	38±2	62±1	−0.87±0.05	0.87±0.07
60	220±10	11.54±0.02	12.72±0.09	27±7	52±8	45±2	−0.00±0.03	1.0±0.3
70	294±4	13.0±0.1	11.44±0.09	24.4±0.6	38±1	69±1	−0.6±0.2	0.99±0.07
80	250±10	12.0±0.1	11.9±0.4	28±1	45±2	57±3	−0.473±0.008	0.94±0.05
90	235±5	11.57±0.03	12.25±0.07	26±1	47±2	48±1	−0.84±0.08	0.89±0.05

C_R (mM)	a_b (Å^2)	δ_b (Å)	$R_{1,b}$ (Å)	$n_{W,b}$	d (Å)	g_d	N_d
10	60.54±0.06	7±1	7.06±0.03	0±2	33±2	0.03±0.01	33.5±0.6
20	70±2	6±2	6.0±0.1	0±5	27±5	0.075±0.009	40±20
30	68.2±0.8	15.66±0.04	6.2±0.2	22.2±0.1	44.9±0.7	0.08±0.04	10±20
40	68±3	9.2±0.4	6.3±0.3	7±2	33.9±0.6	0.04±0.03	46±4
50	66.9±0.4	9.12±0.05	5.91±0.04	6.33±0.05	34.03±0.01	0.01±0.01	47±5
60	64±1	8±1	6.7±0.2	3±2	32±2	0.095±0.002	2.0±0.2
70	70±1	8.6±0.5	6.1±0.1	6±2	29.4±0.4	0.0515±0.0004	0±10
80	69.6±0.2	7.3±0.5	6.24±0.02	3±1	31.4±0.9	0.08±0.02	0±20
90	69.2±0.3	6.8±0.2	6.13±0.02	1.6±0.5	30.4±0.2	0.08±0.03	7.5±0.9

Table 7.6: Fitting parameters with the model of mixtures of interacting spherocylinders and stacked bilayers related to the curves shown in the panel #3: ϕ_O=0.0000, T=20°C, [NaCl]=92 mM, [$CaCl_2$]=2 mM, [$MgSO_4$]=11 mM.

C_R (mM)	F	W	Z	p	q	R	T
10	0.05±0.03	1.0±0.2	0.50±0.09	–	–	0.10±0.05	0.4±0.3
20	0.03±0.02	0.2±0.5	0.8±0.1	–	–	0.7±0.1	0.8±0.3
30	0.008±0.004	0.37±0.09	0.9±0.2	–	–	0.36±0.03	1.0±0.1
40	0.10±0.02	0.22±0.08	0.99±0.05	–	–	0.18±0.01	1.00±0.04
50	0.04±0.01	0.12±0.04	0.97±0.07	–	–	0.15±0.03	0.5326±0.0009
60	0.122±0.007	0.21±0.02	0.99±0.08	–	–	0.551±0.009	0.93±0.05
70	0.03±0.02	0.58±0.04	1.0±0.1	–	–	0.32±0.04	0.0±0.4
80	0.07±0.02	0.20±0.05	1.0±0.1	–	–	0.2±0.2	0.54±0.01
90	0.04±0.03	0.23±0.07	0.97±0.01	–	–	0.34±0.03	0.2±0.3

C_R (mM)	a_{sc} (Å^2)	δ_{sc} (Å)	$R_{1,sc}$ (Å)	L (Å)	N_{aggs}	$n_{W,sc}$	z q_o	J RT
10	217±2	18±2	13±2	90±40	130±30	62±7	−1.0±0.4	0.0±0.5
20	298±2	16±2	8±1	40000±20000	20000±10000	85±9	−0.00±0.08	0.1±0.4
30	260±40	17±4	12±1	60±60	80±40	80±30	−0.0±0.1	0.9±0.1
40	184±9	12.35±0.09	14±1	30±10	76±8	38±2	−0.01±0.08	0.87±0.06
50	300±20	17.4±0.3	13±3	30±20	55±6	99±4	−0.000±0.009	0.0±0.5
60	260±10	14.1±0.5	13±2	0±100	50±70	61±5	−0.19±0.03	0.94±0.03
70	236±6	15.8±0.2	9.7±0.1	2400±800	1700±600	77.5±0.7	−0.44±0.02	0.96±0.08
80	261±1	17±1	10.0±0.5	500±200	300±100	94±6	−0.3±0.3	0.9±0.2
90	300±8	15.9±0.9	12.4±0.9	30±30	50±20	90±6	−0.28±0.03	0.00±0.01

C_R (mM)	a_b (Å^2)	δ_b (Å)	$R_{1,b}$ (Å)	$n_{W,b}$	d (Å)	g_d	N_d
10	69±1	13.0±0.5	6.2±0.1	14±1	42.3±0.9	0.04±0.02	35.0±0.7
20	60.1±0.3	15±1	6.8±0.1	14±3	47±3	0.08±0.04	0±20
30	65.4±0.5	6±2	6.2±0.3	0±4	28±3	0.009±0.003	42±4
40	68.2±0.8	6±1	6.00±0.06	0±3	24±4	0.10±0.01	25±9
50	58±2	7.5±0.5	7.3±0.3	0±2	34±2	0.10±0.03	10±20
60	68±1	8.5±0.8	6.09±0.08	5±1	34±2	0.03±0.03	33±8
70	59±5	10±2	7.3±0.5	5±2	37±5	0.05±0.05	14±10
80	67±2	6.4±0.5	6.5±0.1	0±1	28±1	0.09±0.04	10±10
90	63.3±0.8	9±1	6.8±0.1	5±2	36±4	0.079±0.003	5±1

Table 7.7: Fitting parameters with the model of mixtures of interacting spherocylinders and stacked bilayers related to the curves shown in the panel #4: ϕ_O=0.0000, T=20°C, [NaCl]=229 mM, [$CaCl_2$]=5 mM, [$MgSO_4$]=28 mM.

C_R (mM)	F	W	Z	p	q	R	T
10	0.99±0.03	0.968±0.004	0.89±0.04	–	–	0.085±0.006	0.21±0.02
20	0.542±0.009	0.919±0.003	0.98±0.09	–	–	0.193±0.001	0.39±0.02
30	0.59±0.03	0.940±0.009	0.79±0.06	–	–	0.348±0.009	0.60±0.02
40	0.3±0.1	0.985±0.006	–	–	–	0.48±0.03	0.48±0.02
50	0.34±0.03	0.920±0.009	0.72±0.03	–	–	0.54±0.01	0.537±0.009
60	0.38±0.03	0.88±0.02	0.73±0.03	–	–	0.489±0.005	0.53±0.01
70	0.48±0.01	0.933±0.004	0.78±0.05	–	–	0.62±0.03	0.61±0.02
80	0.53±0.02	0.90±0.02	0.76±0.06	–	–	0.63±0.01	0.56±0.02
90	0.39±0.02	0.80±0.05	0.80±0.04	–	–	0.64±0.02	0.64±0.04

C_R (mM)	a_{ac} (Å^2)	δ_{ac} (Å)	$R_{1,ac}$ (Å)	L (Å)	N_{agg}	$n_{W,ac}$	z q_e	J RT
10	269±1	9.31±0.02	7.25±0.02	4000±2000	1600±800	45.3±0.2	−0.13±0.04	0.70±0.01
20	298.4±0.9	10.8±0.3	10.3±0.2	25±7	30±3	53±2	−1.0±0.3	0.0±0.2
30	280.6±0.7	13.0±0.2	8.21±0.03	832±8	416±7	64±1	−0.9±0.4	0.7±0.1
40	219±5	13.7±0.3	9.61±0.07	960±30	670±20	52±3	−0.3±0.1	0.26±0.06
50	253±2	13.45±0.08	9.08±0.06	444±7	274±5	60.9±0.8	−0.0±0.5	0.5026±0.0005
60	239±3	13.3±0.2	9.4±0.1	280±30	200±20	56.4±0.5	−0.4940±0.0007	0.19±0.05
70	264.6±0.7	12.71±0.08	8.50±0.02	820±20	440±10	60.8±0.3	−0.9999±0.0002	0.508±0.002
80	240±1	12.1±0.2	8.83±0.01	810±20	467±9	52±1	−0.97±0.01	0.011±0.005
90	235±2	12.9±0.2	9.25±0.05	420±20	280±10	54±2	−0.36±0.05	0.21±0.01

C_R (mM)	a_b (Å^2)	δ_b (Å)	$R_{1,b}$ (Å)	$n_{W,b}$	d (Å)	g_d	N_d
10	69.4±0.2	12.9±0.8	6.12±0.02	15±2	41±1	0.095±0.002	50±3
20	69±1	12.1±0.5	6.3±0.1	13±1	37±2	0.098±0.002	35±2
30	58±2	15±1	7.4±0.2	14±2	45±1	0.096±0.002	0±10
40	55±2	7.9±0.4	7.7±0.3	0.01±0.03	–	–	–
50	70.0±0.2	12.6±0.5	6.166±0.003	14±1	42.5±0.9	0.0011±0.0005	5±1
60	69.6±0.4	12.4±0.7	6.02±0.04	14±2	42±2	0.088±0.004	4.5±0.5
70	50.0±0.3	14.9±0.6	8.69±0.08	10.1±0.9	47±1	0.098±0.002	3.5±0.8
80	63±3	16±1	6.8±0.3	18±3	45.9±0.8	0.10±0.02	3.5±0.9
90	68.8±0.6	12.3±0.5	6.17±0.07	14±1	42±1	0.06±0.03	4.2±0.4

Table 7.8: Fitting parameters with the model of mixtures of interacting spherocylinders and stacked bilayers related to the curves shown in the panel #5: ϕ_O=0.0000, T=20°C, [NaCl]=460 mM, [$CaCl_2$]=0 mM, [$MgSO_4$]=0 mM.

C_R (mM)	F	W	Z	p	q	R	T
10	0.6±0.1	0.3±0.1	0.6±0.2	0.2±0.4	0.4±0.3	–	–
20	0.83±0.04	0.25±0.03	0.99±0.02	0.1±0.3	0.92±0.02	–	–
30	0.83±0.02	0.30±0.04	0.99±0.02	0.3±0.2	0.0±0.3	–	–
40	0.81±0.03	0.32±0.02	0.93±0.03	0.524±0.002	0.4±0.3	–	–
50	0.40±0.02	0.24±0.04	0.94±0.01	0.3±0.1	0.4±0.3	–	–
60	0.580±0.008	0.44±0.02	0.90±0.01	0.46±0.05	0.0±0.3	–	–
70	0.74±0.07	0.36±0.03	0.98±0.01	0.3±0.4	0.6±0.2	–	–
80	0.524±0.005	0.47±0.02	0.975±0.005	0.24±0.07	0.48±0.08	–	–
90	0.71±0.01	0.41±0.04	0.99±0.01	0.18±0.05	0.1±0.4	–	–

C_R (mM)	a_{ac} (Å^2)	δ_{ac} (Å)	$R_{1,ac}$ (Å)	L (Å)	N_{agg}	$n_{W,ac}$	z q_e	J RT
10	270±20	13.3±0.3	13±4	20±20	41±8	62±5	−0.43±0.02	0.5±0.1
20	247±5	15.0±0.4	11.0±0.2	79±8	87±8	70±3	−0.30±0.04	0.2±0.2
30	298±9	12.6±0.2	11.6±0.3	21±3	36±3	69±2	−0.27±0.05	0.013±0.006
40	244±2	11.3±0.1	12.28±0.08	22.2±0.9	42.0±0.7	50.8±0.6	−0.22±0.02	0.03±0.09
50	279±6	12.9±0.1	11.9±0.3	24±1	41±2	68±1	−0.38±0.06	0.50±0.04
60	268±8	12.1±0.2	12.1±0.2	21±2	39±3	60±2	−0.23±0.04	0.3±0.1
70	275±2	12.08±0.07	11.9±0.2	19.8±0.9	37.1±0.9	60.8±0.8	−0.24±0.02	0.2±0.4
80	254±2	11.544±0.005	12.10±0.08	20.9±0.2	39.9±0.4	53.4±0.6	−0.28±0.03	0.06±0.05
90	290±4	12.10±0.09	11.5±0.2	20±2	34±1	63.9±0.5	−0.27±0.02	0.28±0.05

C_R (mM)	a_b (Å^2)	δ_b (Å)	$R_{1,b}$ (Å)	$n_{W,b}$	d (Å)	g_d	N_d
10	70±5	9.4±0.9	5.7±0.8	8±3	32.8±0.3	0.079±0.005	28.5±0.8
20	69.5±0.3	7.4±0.4	6.0±0.2	3±1	27±2	0.10±0.01	33±3
30	64±1	7.0±0.4	6.6±0.1	1±1	32±1	0.10±0.04	26.9±0.2
40	67±1	6.3±0.1	6.41±0.05	0.00±0.01	30.1±0.2	0.054±0.001	4±1
50	64±1	6.6±0.7	6.69±0.09	0±2	31±1	0.06±0.01	0±20
60	70±2	6.1±0.3	6.1±0.3	0.1±0.6	29±1	0.055±0.001	3±1
70	65±2	6.5±0.2	6.6±0.1	0.00±0.08	28±1	0.09±0.02	10±20
80	68±1	6.2±0.4	6.27±0.08	0±1	29.0±0.8	0.10±0.05	7±3
90	70.0±0.3	6.04±0.02	6.09±0.05	0.00±0.01	27.6±0.7	0.01±0.03	10±20

Table 7.9: Fitting parameters with the model of mixtures of interacting spherocylinders and stacked bilayers related to the curves shown in the panel #6: ϕ_O=0.0010, T=20°C, [NaCl]=0 mM, [$CaCl_2$]=0 mM, [$MgSO_4$]=0 mM.

C_R (mM)	F	W	Z	p	q	R	T
10	0.06±0.01	0.515±0.004	1.0±0.1	0.18±0.06	0.85±0.08	0.61±0.01	0.70±0.08
20	0.83±0.06	0.23±0.07	0.984±0.005	0.988±0.006	0.4±0.2	0.99±0.03	1.00±0.01
30	0.91±0.02	0.8±0.1	0.98±0.02	0.98±0.09	0.5±0.3	0.86±0.06	0.92±0.09
40	0.63±0.05	0.17±0.01	1.00±0.04	0.06±0.03	0.99±0.02	0.96±0.02	1.00±0.03
50	0.70±0.06	0.33±0.01	0.985±0.005	0.37±0.07	0.9±0.1	0.98±0.02	0.87±0.04
60	0.86±0.04	0.49±0.02	0.995±0.006	0.17±0.05	1.00±0.05	0.91±0.01	1.00±0.01
70	0.76±0.01	0.320±0.009	0.997±0.003	0.12±0.07	0.960±0.008	0.98±0.09	1.00±0.03
80	0.75±0.05	0.39±0.04	0.997±0.003	0.42±0.09	1.0±0.4	1.0±0.1	0.999±0.003
90	0.71±0.06	0.31±0.02	1.00±0.03	0.13±0.05	0.9±0.4	1.00±0.08	0.96±0.02

C_R (mM)	a_{sc} (Å^2)	δ_{sc} (Å)	$R_{1,sc}$ (Å)	L (Å)	N_{aggs}	$n_{W,sc}$	z q_o	J RT
10	170±20	15±1	16±2	32±8	110±50	45±9	−0.09±0.04	0.69±0.09
20	179±7	12.37±0.07	15.1±0.7	31±8	83±7	33±1	−0.07±0.03	0.96±0.03
30	290±10	12.2±0.3	11.3±0.6	24±2	36±4	60±2	−0.02±0.05	0.98±0.02
40	236±6	16.4±0.3	10.3±0.1	270±40	230±30	76±3	−0.44±0.01	0.21±0.04
50	265±2	16.9±0.3	9.8±0.2	240±40	190±20	86.7±0.9	−0.2±0.1	0.13±0.03
60	192±7	10.2±0.2	13.0±0.2	24±2	53±2	30±2	−0.04±0.07	0.997±0.001
70	200±4	10.7±0.1	13.1±0.2	25±2	54±1	36±1	−0.14±0.06	0.99±0.03
80	185±6	10.1±0.2	13.4±0.2	24.8±0.7	57±2	31±2	−0.16±0.06	0.82±0.09
90	208±3	11.8±0.2	13.3±0.1	23±1	55±1	41±2	−0.01±0.08	0.86±0.07

C_R (mM)	a_b (Å^2)	δ_b (Å)	$R_{1,b}$ (Å)	$n_{W,b}$	d (Å)	g_d	N_d
10	51±2	12±1	8.7±0.5	7±2	41±5	0.0537±0.0008	20±10
20	60±6	8.3±0.6	7.1±0.5	2±3	35.6±0.6	0.08±0.03	10±10
30	62.0±0.3	7.3±0.4	7.0±0.3	1.0±0.8	34±2	0.08±0.02	0±20
40	57±4	7.6±0.2	7.2±0.4	1±1	34.2±0.9	0.00±0.01	50±20
50	59±2	7.2±0.2	7.2±0.1	0.0±0.5	29±3	0.10±0.05	10±20
60	64.1±0.9	6.6±0.3	6.4±0.1	0.0±0.7	28.1±0.7	0.067±0.004	10±20
70	67±1	6.28±0.09	6.3±0.1	0.0±0.2	29.2±0.4	0.07±0.03	28.0±0.4
80	67±2	6.3±0.3	6.4±0.2	0.0±0.2	30±1	0.04±0.02	10±20
90	58.7±0.7	7.8±0.4	6.97±0.09	1.1±0.6	29±1	0.0993±0.0008	30±10

Table 7.10: Fitting parameters with the model of mixtures of interacting spherocylinders and stacked bilayers related to the curves shown in the panel #7: ϕ_O=0.0010, T=20°C, [NaCl]=46 mM, [$CaCl_2$]=1 mM, [$MgSO_4$]=6 mM.

C_R (mM)	F	W	Z	p	q	R	T
10	0.9991±0.0008	0.66±0.03	0.88±0.03	0.56±0.02	1.00±0.02	0.02±0.02	0.70±0.06
20	0.56±0.01	0.14±0.03	1.00±0.04	0.3±0.5	0.69±0.07	0.05±0.02	0.50±0.06
30	0.39±0.05	0.21±0.05	0.98±0.01	0.3±0.3	1.00±0.07	0.0±0.3	0.90±0.05
40	0.77±0.06	0.28±0.03	0.995±0.009	1.00±0.09	0.4±0.2	0.02±0.08	0.5±0.2
50	0.83±0.06	0.19±0.02	0.988±0.007	0.508±0.002	0.9±0.3	0.017±0.008	0.4±0.2
60	0.85±0.02	0.27±0.01	0.97±0.03	0.49±0.03	0.88±0.06	0.00±0.07	0.56±0.01
70	0.6±0.1	0.27±0.06	0.986±0.004	0.1±0.2	0.0±0.4	0.0±0.1	0.10±0.06
80	0.70±0.06	0.22±0.01	0.985±0.006	0.14±0.04	0.4±0.3	0.4±0.1	0.83±0.08
90	0.773±0.009	0.34±0.03	0.995±0.008	0.17±0.08	0.5±0.2	0.05±0.02	0.0±0.4

C_R (mM)	a_{sc} (Å^2)	δ_{sc} (Å)	$R_{1,sc}$ (Å)	L (Å)	N_{aggs}	$n_{W,sc}$	z q_o	J RT
10	200±10	6.0±0.3	9.0±0.4	53±9	39±6	17±3	−0.00±0.02	0.99±0.01
20	213±3	16.9±0.5	16±1	30±20	90±10	67±2	−0.7±0.1	1.0±0.2
30	200±30	14±2	14.3±0.9	30±10	80±10	50±20	−0.1±0.2	1.00±0.04
40	206±2	13.1±0.9	14.3±0.8	30±20	70±20	49±4	−0.0±0.4	1.0±0.5
50	190±10	13.7±0.6	13.0±0.3	50±20	90±20	48±3	−0.7±0.2	0.3±0.5
60	193±4	11.5±0.2	13.5±0.2	27±2	62±1	39±2	−0.16±0.05	0.85±0.02
70	202±2	11.7±0.1	13.4±0.2	27±2	60.4±0.6	42.2±0.7	−0.0±0.2	1.00±0.06
80	194±5	11.2±0.2	13.9±0.2	23.8±0.9	60±2	38±2	−0.00±0.07	0.999±0.008
90	202±1	10.5±0.2	13.0±0.2	24±2	52±2	37±1	−0.1±0.1	0.66±0.04

C_R (mM)	a_b (Å^2)	δ_b (Å)	$R_{1,b}$ (Å)	$n_{W,b}$	d (Å)	g_d	N_d
10	62±1	14.8±0.3	8.2±0.3	18±1	46.8±0.7	0.10±0.04	0±20
20	69.986±0.006	6.9±0.6	6.3±0.4	2±2	29±2	0.098±0.002	29±4
30	67±3	10.2±0.4	6.4±0.5	10±1	38±2	0.10±0.02	50±10
40	67.4±0.8	9.4±0.9	6.4±0.2	8±2	34±2	0.10±0.03	26±8
50	68±1	7.9±0.4	6.2±0.2	4±1	29±2	0.096±0.003	10±20
60	69.6±0.1	9.6±0.2	6.06±0.04	9.1±0.4	32±2	0.10±0.01	4±10
70	69.9±0.9	10±1	5.9±0.2	10±3	32±1	0.09±0.01	0±20
80	70.0±0.4	9.1±0.6	6.11±0.04	8±2	30.4±0.4	0.095±0.007	0±20
90	70±2	8.2±0.4	6.0±0.2	6±1	31±2	0.05±0.01	6±4

Table 7.11: Fitting parameters with the model of mixtures of interacting spherocylinders and stacked bilayers related to the curves shown in the panel #8: ϕ_O=0.0010, T=20°C, [NaCl]=92 mM, [$CaCl_2$]=2 mM, [$MgSO_4$]=11 mM.

C_R (mM)	F	W	Z	p	q	R	T
10	0.0016±0.0004	0.4±0.2	0.1±0.3	0.96±0.02	0.999±0.009	0.90±0.04	0.78±0.06
20	0.018±0.008	0.3±0.3	1.00±0.05	0.70±0.04	0.66±0.02	0.5±0.2	0.9±0.2
30	0.04±0.01	0.13±0.02	0.90±0.09	0.95±0.08	0.879±0.003	0.53±0.02	1.0±0.1
40	0.153±0.004	0.015±0.007	0.89±0.05	0.999±0.009	0.68±0.06	0.61±0.03	1.00±0.02
50	0.04±0.01	0.2±0.1	0.90±0.07	0.53±0.07	0.99±0.03	0.2±0.1	0.0±0.1
60	0.02±0.01	0.2±0.1	0.9±0.4	0.4±0.5	0.0±0.4	0.63±0.07	1.00±0.05
70	0.032±0.005	0.26±0.06	1.00±0.08	0.8±0.4	0.537±0.003	0.66±0.03	0.73±0.09
80	0.08±0.02	0.20±0.07	1.00±0.07	0.69±0.03	0.50±0.03	0.1±0.2	0.998±0.001
90	0.11±0.01	0.21±0.08	1.00±0.02	0.92±0.03	0.68±0.05	0.5±0.2	0.88±0.06

C_R (mM)	a_{ac} (Å^2)	δ_{ac} (Å)	$R_{1,ac}$ (Å)	L (Å)	N_{aggs}	$n_{W,ac}$	z q_e	J RT
10	208±1	9±1	9±3	1000±3000	1000±1000	35±6	−0.469±0.003	0.2±0.3
20	207±1	18±1	21±4	0±40	90±20	55±3	−0.0±0.1	0.48±0.01
30	194±2	9.62±0.01	8.94±0.07	12000±5000	7000±3000	32±2	−0.41±0.02	0.2±0.3
40	100±20	16±1	24.8±0.9	20±10	260±60	22±5	−0.9±0.1	0.2±0.4
50	240±20	13±2	9±1	11000±5000	6000±3000	60±10	−0.1±0.3	0.89±0.07
60	100±20	11.57±0.02	18±2	70±30	230±60	17±2	−0.50±0.03	1.0±0.3
70	170±20	13±1	16.8±0.5	20±20	90±50	34±6	−0.40±0.02	1.0±0.5
80	130±30	10.9±0.5	17.8±0.7	20±20	110±60	21±7	−0.02±0.01	1.00±0.05
90	160±20	11.63±0.04	16±3	20±10	80±20	29±4	−0.45±0.01	0.0±0.4

C_R (mM)	a_b (Å^2)	δ_b (Å)	$R_{1,b}$ (Å)	$n_{W,b}$	d (Å)	g_d	N_d
10	53±8	11±3	11±1	4±8	46±8	0.018±0.009	5±1
20	69±1	6±9	6.2±0.2	0±20	30±20	0.00±0.02	0±20
30	62±2	16±2	7.3±0.3	19±4	46±1	0.099±0.002	30±1
40	69.99±0.06	8.5±0.6	6.29±0.06	5±1	30±1	0.05±0.02	0±30
50	65±1	11±2	6.9±0.1	8±3	40±3	0.09±0.03	10±20
60	70.0±0.4	6±2	6.0±0.2	0±5	24±6	0.10±0.03	34±2
70	69.97±0.04	6.1±0.7	6.37±0.07	0±2	30±1	0.10±0.04	20±10
80	70.0±0.4	6±1	5.975±0.009	0±2	28±2	0.07±0.05	29±1
90	69±2	6.9±0.4	6.2±0.2	2±1	30±1	0.0021±0.0007	31±1

Table 7.12: Fitting parameters with the model of mixtures of interacting spherocylinders and stacked bilayers related to the curves shown in the panel #9: ϕ_O=0.0010, T=20°C, [NaCl]=229 mM, [$CaCl_2$]=5 mM, [$MgSO_4$]=28 mM.

C_R (mM)	F	W	Z	p	q	R	T
10	0.29±0.07	0.0035±0.0005	0.77±0.07	0.594±0.005	0.2±0.1	0.49±0.04	0.973±0.003
20	0.24±0.05	0.07±0.02	1.00±0.01	0.97±0.05	1.00±0.01	0.5158±0.0008	0.97±0.02
30	0.29±0.02	0.016±0.001	0.977±0.009	0.93±0.02	0.3±0.1	0.864±0.009	0.925±0.005
40	0.49±0.07	0.059±0.002	0.90±0.03	0.3±0.2	0.0±0.2	0.639±0.004	0.958±0.003
50	0.269±0.009	0.16±0.02	0.9±0.1	0.01±0.05	0.6±0.1	0.757±0.009	0.883±0.005
60	0.44±0.02	0.118±0.008	1.000±0.002	0.137±0.006	0.1±0.2	0.679±0.005	0.94±0.02
70	0.35±0.04	0.20±0.01	0.90±0.05	0.3±0.1	0.534±0.009	0.71±0.01	0.880±0.009
80	0.36±0.03	0.260±0.009	0.96±0.02	0.46±0.06	0.67±0.03	0.607±0.009	0.81±0.02
90	0.44±0.07	0.23±0.02	0.97±0.05	0.4±0.2	0.66±0.09	0.61±0.08	0.792±0.009

C_R (mM)	a_{ac} (Å^2)	δ_{ac} (Å)	$R_{1,ac}$ (Å)	L (Å)	N_{aggs}	$n_{W,ac}$	z q_e	J RT
10	180±20	17.75±0.09	21.9±0.9	16±8	130±20	52±6	−0.0±0.1	0.94±0.03
20	270±10	9±5	18.8±0.4	16±8	20±20	160±40	−0.7±0.2	1.0±0.2
30	247.2±0.8	13.8±0.2	14.0±0.4	27±4	59±1	56.9±0.9	−0.13±0.07	0.97±0.01
40	208±2	16.9±0.2	12.2±0.3	260±60	280±50	61±1	−0.2±0.3	1.0±0.3
50	300±20	16.2±0.3	12.9±0.7	28±4	52±3	79±6	−0.1±0.1	1.00±0.06
60	167.0±0.5	13.71±0.09	11.67±0.02	2350±30	2290±30	37.0±0.4	−0.9±0.2	0.558±0.005
70	281±7	14.1±0.2	12.2±0.2	29±1	48±3	66±1	−0.04±0.04	1.000±0.007
80	262±6	12.87±0.09	12.3±0.2	28.4±0.4	48±2	59±1	−0.03±0.02	0.73±0.02
90	260±10	12.8±0.1	12.3±0.3	28±2	47±4	59±3	−0.06±0.09	0.74±0.06

C_R (mM)	a_b (Å^2)	δ_b (Å)	$R_{1,b}$ (Å)	$n_{W,b}$	d (Å)	g_d	N_d
10	69.2±0.4	12.2±0.8	6.7±0.2	14±2	40±2	0.10±0.05	2.5±0.3
20	51.1±0.4	8.3±0.4	9.2±0.2	0.0±0.7	35±2	0.058±0.002	36±1
30	60.80±0.06	7.1±0.1	7.60±0.06	0.1±0.3	34±3	0.060±0.002	10±20
40	62.2±0.5	7.0±0.2	7.18±0.09	0.4±0.6	33.4±0.6	0.100±0.004	2±3
50	66±2	8.9±0.4	6.8±0.2	5.2±0.4	34±1	0.0996±0.0004	3.5±0.5
60	62.8±0.4	6.77±0.06	6.98±0.06	0.05±0.02	32.5±0.3	0.065±0.001	0±20
70	67±1	8.0±0.5	6.56±0.08	4±1	34±1	0.099±0.008	2±2
80	69.1±0.5	7.5±0.2	6.58±0.06	3.1±0.5	33.0±0.6	0.046±0.006	3±3
90	69±1	7.6±0.6	6.6±0.1	3±1	33±1	0.04±0.03	3.1±0.4

Table 7.13: Fitting parameters with the model of mixtures of interacting spherocylinders and stacked bilayers related to the curves shown in the panel #10: ϕ_O=0.0010, T=20°C, [NaCl]=460 mM, [$CaCl_2$]=0 mM, [$MgSO_4$]=0 mM.

C_R (mM)	F	W	Z	p	q	R	T
10	0.62±0.03	0.43±0.08	0.5±0.2	0.24±0.09	0.86±0.06	–	–
20	0.41±0.06	0.5012±0.0003	1.0±0.1	0.003±0.005	0.0±0.4	–	–
30	0.560±0.002	0.54±0.01	0.93±0.03	0.002±0.006	0.0±0.5	–	–
40	0.42±0.04	0.83±0.08	0.96±0.03	0.00±0.02	0.8±0.1	–	–
50	0.533±0.003	0.82±0.01	0.91±0.08	0.01±0.02	1.00±0.04	–	–
60	0.59±0.02	0.77±0.05	0.96±0.02	0.05±0.02	0.96±0.06	–	–
70	0.67±0.03	0.74±0.01	0.96±0.02	0.12±0.02	0.2±0.2	–	–
80	0.61±0.05	0.78±0.04	0.986±0.006	0.08±0.01	0.3±0.3	–	–
90	0.64±0.05	0.81±0.06	0.99±0.01	0.05±0.01	0.3±0.3	–	–

C_R (mM)	a_{ac} (Å^2)	δ_{ac} (Å)	$R_{1,ac}$ (Å)	L (Å)	N_{agg}	$n_{W,ac}$	z q_o	J RT
10	140±20	11.58±0.02	16±2	40±10	120±10	24±4	−0.1±0.1	0.7±0.1
20	229±4	13.0±0.4	13.1±0.9	24±6	54±2	52.8±0.2	−0.24±0.02	0.61±0.03
30	293±3	13.2±0.2	11.6±0.3	21±3	37.8±0.7	69±1	−0.26±0.04	0.1±0.1
40	191±7	10.0±0.2	13.1±0.3	21±3	51±3	31±2	−0.21±0.05	0.1±0.3
50	219±4	11.529±0.002	12.7±0.1	22±2	49±2	42.2±0.8	−0.177±0.003	0.03±0.02
60	299.5±0.4	13.29±0.05	11.5±0.2	20±1	36.4±0.5	70.1±0.4	−0.29±0.03	0.06±0.01
70	235±4	11.56±0.03	12.5±0.2	21±1	45±1	47.2±0.9	−0.17±0.02	0.2±0.1
80	244.4±0.9	11.65±0.07	12.1±0.2	21±2	42.1±0.6	49.2±0.8	−0.17±0.01	0.02±0.05
90	246±9	11.4±0.3	12.0±0.2	20.9±0.8	41±1	48±4	−0.21±0.02	0.00±0.08

C_R (mM)	a_b (Å^2)	δ_b (Å)	$R_{1,b}$ (Å)	$n_{W,b}$	d (Å)	g_d	N_d
10	70.0±0.9	7.4±0.7	8±1	3±1	33.5±0.4	0.098±0.007	49±2
20	69±4	10±1	5.9±0.3	9±5	31±2	0.10±0.03	6±7
30	57±5	7.5±0.3	7.3±0.6	0±1	31±2	0.09±0.04	10±20
40	70±1	14±3	5.8±0.1	19±8	44±6	0.00±0.06	50±8
50	63±4	7.8±0.8	6.4±0.4	2±2	30±2	0.065±0.003	8±3
60	67.6±0.1	6.2±0.5	6.14±0.05	0±1	30±1	0.093±0.007	10±20
70	67±1	6.3±0.7	6.12±0.06	0±2	29±1	0.10±0.04	43±4
80	70±1	6.1±0.1	5.9±0.2	0.0±0.2	28.5±0.8	0.07±0.02	31±4
90	69.2±0.3	6.11±0.03	5.90±0.05	0.006±0.003	29±2	0.07±0.02	33±4

Table 7.14: Fitting parameters with the model of mixtures of interacting spherocylinders and stacked bilayers related to the curves shown in the panel #11: ϕ_O=0.0050, T=20°C, [NaCl]=0 mM, [$CaCl_2$]=0 mM, [$MgSO_4$]=0 mM.

C_R (mM)	F	W	Z	p	q	R	T
10	0.53±0.02	0.513±0.003	0.62±0.04	0.55±0.01	0.178±0.005	0.79±0.07	0.540±0.009
20	1.000±0.004	0.24±0.04	0.969±0.009	0.503±0.002	0.36±0.08	1.00±0.06	0.73±0.07
30	0.98±0.01	0.231±0.009	0.95±0.02	0.34±0.04	0.519±0.004	0.91±0.08	0.68±0.04
40	1.00±0.03	0.57±0.02	0.60±0.04	0.14±0.04	0.0±0.1	0.99±0.02	0.00±0.02
50	0.989±0.004	0.31±0.01	0.98±0.06	0.17±0.04	0.9±0.5	1.0±0.2	0.3±0.1
60	1.00±0.01	0.32±0.03	0.98±0.02	0.15±0.03	0.95±0.07	0.99±0.01	0.2±0.1
70	0.996±0.003	0.32±0.03	0.992±0.005	0.21±0.04	0.96±0.07	1.0±0.3	0.40±0.09
80	1.00±0.01	0.33±0.03	0.993±0.005	0.218±0.005	0.9±0.2	0.94±0.02	0.17±0.07
90	0.996±0.005	0.24±0.01	0.99±0.01	0.20±0.01	0.96±0.01	1.00±0.01	0.41±0.06

C_R (mM)	a_{ac} (Å^2)	δ_{ac} (Å)	$R_{1,ac}$ (Å)	L (Å)	N_{agg}	$n_{W,ac}$	z q_o	J RT
10	290±3	9.76±0.08	19.2±0.1	0.0±0.2	36.4±0.5	55±1	−0.44±0.04	0.6±0.2
20	229±9	12.03±0.05	14.6±0.2	31±3	62±5	51±2	−1.0000±0.0002	1.00±0.09
30	290±4	17.8±0.2	10.3±0.1	260±40	190±20	106±2	−0.7±0.3	0.555±0.006
40	280±20	14.0±0.6	13.5±0.1	16.8±0.9	44±3	71±10	−0.9997±0.0002	0.89±0.05
50	300.0±0.6	17.1±0.4	11.1±0.1	68±4	74±3	98±2	−1.00±0.02	0.65±0.07
60	300±5	16.6±0.2	10.8±0.1	71±2	72±1	96±2	−0.9±0.1	0.65±0.06
70	300±4	16.7±0.1	10.8±0.2	80±20	76±9	97±2	−1.0±0.2	0.58±0.03
80	290±5	15.8±0.3	10.8±0.2	70±10	71±7	89±4	−1.0±0.1	0.68±0.01
90	299.9±0.1	16.1±0.2	10.17±0.08	98±9	83±6	96±2	−0.59±0.08	0.65±0.01

C_R (mM)	a_b (Å^2)	δ_b (Å)	$R_{1,b}$ (Å)	$n_{W,b}$	d (Å)	g_d	N_d
10	62±1	7.9±0.1	8.3±0.2	2.1±0.5	33.61±0.02	0.001±0.007	31±2
20	70±1	8.8±0.6	7.0±0.3	7±2	36.5±0.5	0.05±0.03	0±20
30	63.4±0.9	6.7±0.7	7.5±0.1	0±2	30±2	0.093±0.009	2±4
40	62.6±0.8	8.98±0.05	6.8±0.1	4.8±0.3	34.40±0.06	0.034±0.004	49.7±0.5
50	65±2	6.5±0.2	7.1±0.3	0.01±0.01	29±2	0.08±0.01	2±3
60	65±2	6.5±0.2	7.0±0.2	0.0±0.2	27.0±0.8	0.081±0.003	7±1
70	67±2	6.3±0.2	6.9±0.2	0.0±0.1	27±2	0.082±0.009	10±10
80	67±1	6.38±0.08	6.8±0.1	0.0±0.2	26.8±0.7	0.083±0.006	10±10
90	65±1	6.5±0.1	6.9±0.1	0.00±0.02	27±1	0.080±0.002	5±4

Table 7.15: Fitting parameters with the model of mixtures of interacting spherocylinders and stacked bilayers related to the curves shown in the panel #12: ϕ_O=0.0050, T=20°C, [NaCl]=46 mM, [$CaCl_2$]=1 mM, [$MgSO_4$]=6 mM.

C_R (mM)	F	W	Z	p	q	R	T
10	0.53±0.02	0.513±0.003	0.62±0.04	0.55±0.01	0.178±0.005	0.79±0.07	0.540±0.009
20	1.000±0.004	0.24±0.04	0.969±0.009	0.503±0.002	0.36±0.08	1.00±0.06	0.73±0.07
30	0.98±0.01	0.231±0.009	0.95±0.02	0.34±0.04	0.519±0.004	0.91±0.08	0.68±0.04
40	1.00±0.03	0.57±0.02	0.60±0.04	0.14±0.04	0.0±0.1	0.99±0.02	0.00±0.02
50	0.989±0.004	0.31±0.01	0.98±0.06	0.17±0.04	0.9±0.5	1.0±0.2	0.3±0.1
60	1.00±0.01	0.32±0.03	0.98±0.02	0.15±0.03	0.95±0.07	0.99±0.01	0.2±0.1
70	0.996±0.003	0.32±0.03	0.992±0.005	0.21±0.04	0.96±0.07	1.0±0.3	0.40±0.09
80	1.00±0.01	0.33±0.03	0.993±0.005	0.218±0.005	0.9±0.2	0.94±0.02	0.17±0.07
90	0.996±0.005	0.24±0.01	0.99±0.01	0.20±0.01	0.96±0.01	1.00±0.01	0.41±0.06

C_R (mM)	a_{sc} (Å^2)	δ_{sc} (Å)	$R_{1,sc}$ (Å)	L (Å)	N_{aggs}	$n_{W,sc}$	z q_e	J RT
10	290±3	9.76±0.08	19.2±0.1	0.0±0.2	36.4±0.5	55±1	−0.44±0.04	0.6±0.2
20	229±9	12.03±0.05	14.6±0.2	31±3	62±5	51±2	−1.0000±0.0002	1.00±0.09
30	290±4	17.8±0.2	10.3±0.1	260±40	190±20	106±2	−0.7±0.3	0.555±0.006
40	280±20	14.0±0.6	13.5±0.1	16.8±0.9	44±3	71±10	−0.9997±0.0002	0.89±0.05
50	300.0±0.6	17.1±0.4	11.1±0.1	68±4	74±3	98±2	−1.00±0.02	0.65±0.07
60	300±5	16.6±0.2	10.8±0.1	71±2	72±1	96±2	−0.9±0.1	0.65±0.06
70	300±4	16.7±0.1	10.8±0.2	80±20	76±9	97±2	−1.0±0.2	0.58±0.03
80	290±5	15.8±0.3	10.8±0.2	70±10	71±7	89±4	−1.0±0.1	0.68±0.01
90	299.9±0.1	16.1±0.2	10.17±0.08	98±9	83±6	96±2	−0.59±0.08	0.65±0.01

C_R (mM)	a_b (Å^2)	δ_b (Å)	$R_{1,b}$ (Å)	$n_{W,b}$	d (Å)	g_d	N_d
10	62±1	7.9±0.1	8.3±0.2	2.1±0.5	33.61±0.02	0.001±0.007	31±2
20	70±1	8.8±0.6	7.0±0.3	7±2	36.5±0.5	0.05±0.03	0±20
30	63.4±0.9	6.7±0.7	7.5±0.1	0±2	30±2	0.093±0.009	2±4
40	62.6±0.8	8.98±0.05	6.8±0.1	4.8±0.3	34.40±0.06	0.034±0.004	49.7±0.5
50	65±2	6.5±0.2	7.1±0.3	0.01±0.01	29±2	0.08±0.01	2±3
60	65±2	6.5±0.2	7.0±0.2	0.0±0.2	27.0±0.8	0.081±0.003	7±1
70	67±2	6.3±0.2	6.9±0.2	0.0±0.1	27±2	0.082±0.009	10±10
80	67±1	6.38±0.08	6.8±0.1	0.0±0.2	26.8±0.7	0.083±0.006	10±10
90	65±1	6.5±0.1	6.9±0.1	0.00±0.02	27±1	0.080±0.002	5±4

Table 7.16: Fitting parameters with the model of mixtures of interacting spherocylinders and stacked bilayers related to the curves shown in the panel #12: ϕ_O=0.0050, T=20°C, [NaCl]=46 mM, [$CaCl_2$]=1 mM, [$MgSO_4$]=6 mM.

C_R (mM)	F	W	Z	p	q	R	T
10	0.037±0.004	0.31±0.02	0.497±0.002	0.36±0.01	0.46±0.04	0.700±0.004	0.83±0.02
20	1.0±0.2	0.53±0.05	1.00±0.03	0.9±0.2	0.514±0.009	0.76±0.08	0.62±0.04
30	0.87±0.02	0.64±0.06	0.5±0.2	0.91±0.05	0.70±0.04	0.52±0.02	0.76±0.07
40	0.8±0.2	0.55±0.01	0.91±0.03	0.84±0.06	0.48±0.09	0.93±0.02	0.63±0.03
50	0.90±0.05	0.28±0.03	0.96±0.02	0.29±0.02	0.2±0.1	0.61±0.03	0.63±0.02
60	0.997±0.004	0.34±0.02	1.000±0.002	0.27±0.02	0.20±0.05	0.74±0.02	0.34±0.01
70	0.997±0.002	0.31±0.02	0.992±0.004	0.33±0.06	0.82±0.09	0.96±0.04	0.64±0.05
80	0.98±0.02	0.35±0.03	0.92±0.04	0.35±0.03	0.60±0.02	0.88±0.07	0.48±0.02
90	0.99±0.01	0.43±0.03	1.0±0.1	0.37±0.01	0.4±0.1	0.89±0.03	0.64±0.07

C_R (mM)	a_{sc} (Å^2)	δ_{sc} (Å)	$R_{1,sc}$ (Å)	L (Å)	N_{aggs}	$n_{W,sc}$	z q_e	J RT
10	117±1	15.31±0.09	19.095±0.004	2700±200	5200±400	31.4±0.9	−0.451±0.003	0.0±0.1
20	160±10	17±1	22.9±0.8	32±2	171±9	45±7	−0.8±0.1	0.7±0.4
30	217±6	18.0±0.5	17.52±0.03	27±2	101±3	67±3	−0.46±0.03	0.6±0.1
40	206.5±0.9	15.5±0.5	17.7±0.4	25±4	93±4	57±2	−0.44±0.02	0.9±0.1
50	250±10	14.4±0.3	13.9±0.1	25±2	58±2	65±4	−0.31±0.09	0.63±0.02
60	203.3±0.2	13.9±0.3	11.4±0.1	200±10	198±8	55±1	−0.85±0.07	0.581±0.007
70	199±3	15.7±0.3	11.21±0.05	520±90	480±80	62±1	−0.85±0.03	0.985±0.003
80	184±7	16.1±0.6	12.8±0.3	210±20	260±20	58±4	−0.85±0.07	0.98±0.04
90	197±4	14.8±0.3	15.9±0.2	27±3	87±2	52±2	−0.5±0.1	0.71±0.07

C_R (mM)	a_b (Å^2)	δ_b (Å)	$R_{1,b}$ (Å)	$n_{W,b}$	d (Å)	g_d	N_d
10	61.67±0.03	8.2±0.6	9.5±0.3	3±1	35±2	0.09992±0.00003	4±2
20	70.0±0.8	12±2	8.7±0.5	14±4	46±5	0.03±0.01	50±20
30	65±2	23±1	8.9±0.3	35±2	64±1	0.10±0.04	3.4±0.5
40	60.29±0.07	8.6±0.7	8.5±0.2	3±1	35±2	0.01±0.02	0±10
50	54±2	7.9±0.5	7.9±0.2	0.0±0.8	33±2	0.10±0.02	3.5±0.2
60	56.1±0.7	7.6±0.1	7.6±0.1	0.12±0.09	30±2	0.001±0.003	50±5
70	60.9±0.1	7.9±0.3	7.52±0.07	2.1±0.6	35±1	0.082±0.008	10±20
80	60.4±0.2	7.7±0.3	7.44±0.07	1.4±0.7	30.3±0.8	0.00±0.03	2.5±0.2
90	54±5	7.9±0.3	8.1±0.5	0.2±0.8	34±3	0.05±0.02	5±2

Table 7.17: Fitting parameters with the model of mixtures of interacting spherocylinders and stacked bilayers related to the curves shown in the panel #13: ϕ_O=0.0050, T=20°C, [NaCl]=92 mM, [$CaCl_2$]=2 mM, [$MgSO_4$]=11 mM.

C_R (mM)	F	W	Z	p	q	R	T
10	0.4±0.1	0.001±0.003	0.97±0.02	0.0±0.4	0.02±0.01	0.66±0.01	0.96±0.01
20	0.09±0.05	0.2±0.4	1.0±0.2	0.5±0.2	0.3±0.1	0.5±0.2	0.85±0.02
30	0.10±0.02	0.07±0.02	1.00±0.02	0.5±0.2	0.979±0.006	0.71±0.05	0.79±0.02
40	0.07±0.03	0.4±0.1	0.9±0.3	0.59±0.02	0.55±0.04	0.6±0.1	0.85±0.07
50	0.15±0.04	0.44±0.05	0.99±0.07	0.2±0.3	0.3±0.2	0.50±0.03	0.82±0.06
60	0.10±0.03	0.19±0.04	0.99±0.03	0.1±0.2	0.97±0.02	0.8±0.3	0.88±0.04
70	0.04±0.02	0.40±0.09	0.62±0.07	0.83±0.09	0.8±0.2	0.92±0.08	0.76±0.05
80	0.16±0.02	0.4±0.1	0.97±0.02	0.64±0.09	0.8±0.3	0.47±0.02	1.00±0.01
90	0.13±0.03	0.30±0.08	0.99±0.03	0.24±0.05	0.68±0.05	0.852±0.005	0.87±0.03

C_R (mM)	a_{sc} (Å^2)	δ_{sc} (Å)	$R_{1,sc}$ (Å)	L (Å)	N_{aggs}	$n_{W,sc}$	z q_o	J RT
10	105±8	18±4	27.7±0.8	0±4000	0±8000	24±7	−0.3±0.1	0.1±0.4
20	200±40	18±2	20±5	30±20	140±80	60±20	−0.2±0.4	0.504±0.004
30	122±8	11.9±0.4	23±2	0±20	130±20	18±1	−0.0±0.2	1.0±0.5
40	150±20	17±2	20±1	40±20	170±70	38±8	−0.8±0.2	0.0±0.5
50	190±20	15±2	16±2	30±10	95±8	50±10	−0.0±0.5	1.0±0.5
60	150±30	13.0±0.7	17±2	30±10	120±20	30±10	−0.00±0.01	1.0±0.3
70	140±10	15.9±0.9	21.1±0.3	30±20	180±50	33±5	−1.0±0.3	0.0±0.5
80	150±30	15±1	18.7±0.2	26±8	130±20	34±10	−0.1±0.1	0.8±0.2
90	140±10	15±1	19±1	30±10	152±9	29±6	−1.0±0.5	0.5±0.4

C_R (mM)	a_b (Å^2)	δ_b (Å)	$R_{1,b}$ (Å)	$n_{W,b}$	d (Å)	g_d	N_d
10	59±3	20±2	6.7±0.4	23±2	55±4	0.100±0.004	28.1±0.9
20	61±5	13±1	8.3±0.8	12±4	45.3±0.7	0.09±0.04	36±1
30	62.1±0.4	11±2	8.7±0.8	8±3	39.8±0.9	0.09±0.04	50±20
40	65±2	15.1±0.9	7.3±0.2	17±1	46±2	0.10±0.05	10±10
50	63±5	10±1	6.7±0.9	7±4	36±2	0.00±0.06	25±4
60	69±5	10.3±0.8	6±1	9±1	36±3	0.0516±0.0008	26±1
70	57±7	13±2	9±1	10±3	44±4	0.0583±0.0009	2.1±0.3
80	61.5±0.2	11±1	7.4±0.5	8±3	39±2	0.10±0.04	10±20
90	63±2	12±1	6.7±0.2	10±2	40±3	0.10±0.01	30.2±0.3

Table 7.18: Fitting parameters with the model of mixtures of interacting spherocylinders and stacked bilayers related to the curves shown in the panel #14: ϕ_O=0.0050, T=20°C, [NaCl]=229 mM, [$CaCl_2$]=5 mM, [$MgSO_4$]=28 mM.

C_R (mM)	F	W	Z	p	q	R	T
10	0.981±0.006	0.17±0.02	1.00±0.01	0.651±0.006	0.10±0.01	0.118±0.004	0.78±0.02
20	0.90±0.07	0.66±0.04	1.00±0.04	0.58±0.03	0.58±0.02	0.169±0.005	0.74±0.01
30	1.0±0.1	0.553±0.009	1.000±0.009	0.50±0.01	0.538±0.001	0.26±0.01	0.76±0.04
40	1.0±0.2	0.567±0.009	0.98±0.03	0.7±0.2	0.83±0.06	0.29±0.02	0.71±0.03
50	0.9±0.1	0.53±0.02	0.99±0.02	0.508±0.007	0.69±0.08	0.32±0.01	0.76±0.05
60	1.00±0.01	0.55±0.02	0.99±0.01	0.371±0.005	0.3±0.1	0.395±0.005	0.82±0.02
70	0.98±0.06	0.37±0.02	0.979±0.009	0.35±0.02	0.5±0.2	0.47±0.02	0.81±0.02
80	1.00±0.02	0.42±0.06	0.997±0.001	0.504±0.001	0.58±0.04	0.48±0.01	0.75±0.05
90	0.90±0.03	0.48±0.02	0.99±0.05	0.41±0.03	0.508±0.001	0.483±0.009	0.81±0.01

C_R (mM)	a_{sc} (Å^2)	δ_{sc} (Å)	$R_{1,sc}$ (Å)	L (Å)	N_{aggs}	$n_{W,sc}$	z q_o	J RT
10	219±5	11.47±0.09	15.3±0.4	2200±400	1700±300	48±1	−0.0±0.4	0.2±0.2
20	250±7	14.9±0.3	10.7±0.2	1000±200	600±200	72±2	−0.6±0.3	0.63±0.08
30	252±6	13.8±0.3	14.7±0.1	23±2	57±1	58±2	−0.03±0.02	0.8±0.1
40	240±2	15.1±0.1	15.1±0.5	23±3	66±1	61.7±0.5	−0.1±0.1	0.9±0.2
50	238±4	14.7±0.2	15.0±0.2	23±1	65±2	59.7±0.8	−0.4±0.3	0.80±0.09
60	226±2	14.5±0.2	10.35±0.04	910±40	660±20	61±1	−0.92±0.05	0.02±0.01
70	210±4	11.52±0.01	13.8±0.2	25±3	57±2	38.6±0.8	−0.5±0.2	0.7±0.1
80	217±5	12.3±0.2	14.4±0.2	23±2	59±3	45±2	−0.490±0.005	1.0±0.2
90	229±6	14.2±0.3	14.79±0.09	23.7±0.6	64.7±0.6	55±3	−0.83±0.03	1.0±0.1

C_R (mM)	a_b (Å^2)	δ_b (Å)	$R_{1,b}$ (Å)	$n_{W,b}$	d (Å)	g_d	N_d
10	62±1	6.8±0.1	8.0±0.1	0.0±0.2	34±1	0.063±0.003	10±20
20	67.0±0.3	6.4±0.4	8.6±0.2	0±1	32.0±0.8	0.10±0.02	42±2
30	66±1	6.8±0.2	7.9±0.2	0.7±0.4	31±1	0.10±0.05	0±20
40	69.7±0.2	6.8±0.5	8.1±0.4	2±1	34±1	0.10±0.04	5±4
50	64±2	6.8±0.6	7.9±0.2	0±2	32.5±0.9	0.10±0.04	41±5
60	62.2±0.7	6.8±0.4	7.3±0.2	0.0±0.9	33.0±0.6	0.057±0.001	0±20
70	62.6±0.4	7.03±0.08	7.3±0.2	0.5±0.2	31.1±0.4	0.04±0.01	0±20
80	68±3	7.0±0.2	7.0±0.3	1.7±0.3	32±1	0.10±0.04	32±3
90	62.3±0.6	7.1±0.5	7.42±0.09	1±1	34±1	0.09±0.01	10±10

Table 7.19: Fitting parameters with the model of mixtures of interacting spherocylinders and stacked bilayers related to the curves shown in the panel #15: ϕ_O=0.0050, T=20°C, [NaCl]=460 mM, [$CaCl_2$]=0 mM, [$MgSO_4$]=0 mM.

C_R (mM)	F	W	Z	p	q	R	T
10	1.0±0.1	0.191±0.006	0.71±0.05	0.03±0.01	0.570±0.008	–	–
20	0.56±0.05	0.38±0.03	0.95±0.04	0.000±0.006	1.0±0.4	–	–
30	0.60±0.04	0.5±0.1	0.8±0.2	0.05±0.03	0.97±0.06	–	–
40	0.40±0.02	0.5043±0.0003	0.8±0.1	0.03±0.01	0.1±0.5	–	–
50	0.39±0.01	0.56±0.03	0.74±0.06	0.03±0.01	0.98±0.07	–	–
60	0.62±0.05	0.58±0.04	0.88±0.08	0.09±0.02	0.55±0.07	–	–
70	0.47±0.07	0.67±0.05	0.94±0.04	0.06±0.02	0.0±0.3	–	–
80	0.41±0.01	0.5027±0.0003	0.87±0.04	0.005±0.004	1.0±0.1	–	–
90	0.42±0.02	0.62±0.04	0.90±0.04	0.020±0.009	0.2±0.4	–	–

C_R (mM)	a_{sc} (Å^2)	δ_{sc} (Å)	$R_{1,sc}$ (Å)	L (Å)	N_{aggs}	$n_{W,sc}$	z q_o	J RT
10	216±4	17.7±0.2	13.3±0.5	80±30	130±20	71±3	−0.0±0.1	0.7±0.1
20	260±6	15.1±0.3	13.2±0.2	23±2	54±2	69±2	−0.2±0.1	0.2±0.3
30	270±10	14.7±0.4	12.7±0.9	25±8	51±4	73±6	−0.29±0.06	0.0±0.1
40	249±8	13.3±0.1	13.2±0.1	25±3	52±3	61±3	−0.33±0.03	0.02±0.03
50	300±20	14.7±0.5	12.5±0.2	22±1	44±2	79±7	−0.42±0.04	0.11±0.08
60	280±10	13.8±0.4	12.7±0.2	20.9±0.2	44±2	70±6	−0.469±0.007	0.11±0.07
70	267±3	13.0±0.2	12.77±0.05	20.1±0.6	43.4±0.7	63±2	−0.56±0.05	0.13±0.07
80	264±2	13.26±0.09	12.79±0.06	21.0±0.8	45.4±0.7	63.9±0.7	−0.495±0.002	0.12±0.05
90	261±2	12.9±0.2	12.72±0.02	21.0±0.7	44.5±0.6	61±1	−0.6±0.2	0.14±0.04

C_R (mM)	a_b (Å^2)	δ_b (Å)	$R_{1,b}$ (Å)	$n_{W,b}$	d (Å)	g_d	N_d
10	66±2	9.1±0.3	6.6±0.3	6±1	34.3±0.1	0.098±0.007	34±2
20	60.4±0.1	7.8±0.4	6.74±0.05	1.7±0.9	32±1	0.00±0.03	2±7
30	60.7±0.2	7±1	7.4±0.3	0±3	34±2	0.08±0.01	0±20
40	70±1	8.8±0.5	6.20±0.06	7.0±0.9	34.4±0.9	0.08±0.01	2.5±0.6
50	65±2	7±1	6.8±0.3	0±3	32±1	0.097±0.001	2.5±0.7
60	65±3	6.5±0.2	6.7±0.2	0.1±0.3	31±2	0.10±0.05	4±1
70	69±1	6.2±0.4	6.2±0.2	0.0±0.8	30±1	0.083±0.006	0±20
80	65.9±0.4	6.41±0.06	6.54±0.03	0.0±0.1	30.9±0.2	0.10±0.02	4±2
90	70±1	7.0±0.4	6.2±0.1	2±1	31.2±0.7	0.096±0.002	0±10

Table 7.20: Fitting parameters with the model of mixtures of interacting spherocylinders and stacked bilayers related to the curves shown in the panel #16: ϕ_O=0.0100, T=20°C, [NaCl]=0 mM, [$CaCl_2$]=0 mM, [$MgSO_4$]=0 mM.

C_R (mM)	F	W	Z	p	q	R	T
10	0.26±0.06	0.525±0.005	0.6±0.3	0.19±0.04	0.0±0.2	0.2±0.3	0.54±0.04
20	0.65±0.08	0.31±0.08	0.54±0.02	0.02±0.04	0.99±0.07	0.0±0.3	0.54±0.04
30	0.66±0.01	0.49±0.03	0.86±0.01	0.141±0.009	0.88±0.04	0.994±0.003	0.43±0.06
40	0.615±0.004	0.576±0.002	0.46±0.04	0.2198±0.0006	0.003±0.002	0.33±0.02	0.0±0.2
50	0.80±0.09	0.25±0.02	0.95±0.03	0.07±0.02	0.5±0.1	0.17±0.06	0.2±0.5
60	0.86±0.07	0.294±0.008	0.973±0.009	0.06±0.02	0.0±0.2	0.1±0.1	0.03±0.03
70	0.67±0.02	0.256±0.008	0.72±0.03	0.09±0.01	0.4±0.2	0.05±0.05	0.97±0.08
80	0.66±0.03	0.157±0.006	0.85±0.09	0.016±0.006	0.6±0.3	0.64±0.06	0.69±0.02
90	0.61±0.06	0.30±0.02	0.86±0.03	0.11±0.01	0.0±0.5	0.1±0.2	0.3±0.3

C_R (mM)	a_{sc} (Å^2)	δ_{sc} (Å)	$R_{1,sc}$ (Å)	L (Å)	N_{aggs}	$n_{W,sc}$	z q_o	J RT
10	256±4	16±1	23.2±0.7	0±3	75±6	77±7	−1.0±0.6	0.0±0.6
20	197±7	17.1±0.3	11.2±0.3	800±100	700±100	68±2	−0.6±0.3	0.1±0.3
30	180±8	14.4±0.7	16.6±0.2	26±2	95±3	44±4	−0.94±0.07	1.0±0.1
40	283.7±0.2	17.26±0.02	10.28±0.01	3090±40	1920±20	104.07±0.09	−0.83±0.07	0.05±0.05
50	192±8	14.9±0.3	15.9±0.3	30±3	92±4	52±4	−0.94±0.07	0.543±0.003
60	236±3	17.7±0.3	12.11±0.06	140±20	160±20	83±2	−0.480±0.003	1.0±0.2
70	217±3	17.32±0.05	16.7±0.5	23±4	90±3	69±2	−0.9±0.3	0.3±0.1
80	234±8	15.10±0.08	14.2±0.5	26±3	66±2	66±3	−0.4984±0.0005	0.0003±0.0004
90	239±5	16.4±0.3	15.1±0.2	27±2	75±2	73±3	−0.5±0.2	0.2±0.2

C_R (mM)	a_b (Å^2)	δ_b (Å)	$R_{1,b}$ (Å)	$n_{W,b}$	d (Å)	g_d	N_d
10	70.0±0.2	9.6±0.6	6±1	9±1	36±1	0.001±0.002	20±7
20	67±2	11±1	6.5±0.3	10±2	34.5±0.1	0.03±0.02	50±5
30	63±1	8.8±0.1	7.9±0.1	4.3±0.8	36.14±0.02	0.044±0.003	42±1
40	68.9±0.3	15.9±0.2	6.44±0.03	23.8±0.5	48.6±0.3	0.004±0.002	2.0±0.2
50	60.53±0.02	10±1	7.19±0.07	7±2	38±2	0.00±0.04	3.5±0.9
60	66.6±0.7	7.3±0.3	6.6±0.1	2.4±0.7	27.9±0.3	0.10±0.04	10±10
70	59±2	9.5±0.6	7.4±0.2	5±2	38±1	0.070±0.007	2.495±0.004
80	58±1	8.0±0.3	7.5±0.1	1.4±0.6	36±1	0.058±0.003	2.0±0.2
90	62.4±0.6	10±1	6.9±0.2	6±3	38±3	0.09±0.04	2.5±0.5

Table 7.21: Fitting parameters with the model of mixtures of interacting spherocylinders and stacked bilayers related to the curves shown in the panel #17: ϕ_O=0.0100, T=20°C, [NaCl]=46 mM, [$CaCl_2$]=1 mM, [$MgSO_4$]=6 mM.

C_R (mM)	F	W	Z	p	q	R	T
10	0.87±0.02	0.59±0.02	0.998±0.003	0.41±0.01	0.615±0.006	0.527±0.009	0.544±0.008
20	0.73±0.07	0.30±0.01	0.91±0.03	0.32±0.04	0.58±0.01	0.66±0.05	0.56±0.01
30	0.8±0.1	0.37±0.04	0.968±0.007	0.32±0.03	0.5±0.1	1.0±0.1	0.505±0.005
40	0.62±0.01	0.42±0.03	0.991±0.003	0.10±0.02	0.83±0.06	0.34±0.06	0.4±0.1
50	0.76±0.05	0.39±0.03	0.988±0.006	0.14±0.03	0.97±0.02	0.8±0.1	0.64±0.04
60	0.73±0.03	0.47±0.06	0.963±0.008	0.085±0.005	0.7±0.1	0.44±0.03	0.20±0.08
70	0.76±0.03	0.35±0.05	0.997±0.004	0.084±0.008	0.98±0.06	0.31±0.08	0.624±0.009
80	0.81±0.03	0.32±0.03	0.91±0.03	0.066±0.006	0.4±0.2	0.33±0.06	0.69±0.02
90	0.8±0.1	0.36±0.02	1.0±0.1	0.08±0.02	0.84±0.07	0.524±0.005	0.55±0.03

C_R (mM)	a_{ac} (Å^2)	δ_{ac} (Å)	$R_{1,ac}$ (Å)	L (Å)	N_{agg}	$n_{W,ac}$	z q_e	J RT
10	237±2	16.1±0.3	13.2±0.2	5300±700	4100±700	73±2	−0.377±0.004	1.0±0.1
20	180±10	11.3±0.2	17.3±0.6	27±10	83±7	36±4	−1.0±0.4	0.7±0.1
30	200±30	12.2±0.4	16.4±0.6	26±7	70±20	43±8	−1.00±0.04	0.1±0.3
40	223±2	17.9±0.1	16.1±0.1	28±2	91±1	70.8±0.5	−0.48±0.02	0.9±0.2
50	180±20	15.8±0.7	17.2±0.4	25±6	100±20	49±8	−0.4±0.1	0.9±0.1
60	251±4	16.2±0.4	14.8±0.1	22±1	65±2	72±3	−0.51±0.04	1.0±0.1
70	189±7	16.4±0.4	17.1±0.1	26±2	104±4	55±4	−0.10±0.02	1.0±0.2
80	245±3	16.1±0.3	14.5±0.2	26±2	68±2	71±2	−0.19±0.07	0.88±0.07
90	231±2	16.4±0.3	15.3±0.4	25±3	76.2±0.6	68±2	−0.55±0.01	0.99±0.04

C_R (mM)	a_b (Å^2)	δ_b (Å)	$R_{1,b}$ (Å)	$n_{W,b}$	d (Å)	g_d	N_d
10	66.0±0.8	7±2	13.0±0.2	0±4	43±4	0.064±0.003	0±10
20	69.9±0.4	7.9±0.7	8.6±0.3	4±2	35.2±0.2	0.03±0.04	28±1
30	70±3	7.9±0.6	7.7±0.6	4±2	35.2±0.2	0.05±0.02	31±4
40	69±5	10±1	6.8±0.8	10±4	37±1	0.08±0.05	31±2
50	56±4	8.2±0.2	8.6±0.7	1.1±0.8	35±2	0.055±0.002	10±20
60	62.5±0.4	10.0±0.3	7.16±0.05	6.9±0.5	36.11±0.08	0.00±0.01	26±1
70	64±2	9.7±0.7	7.1±0.2	7±2	36±2	0.064±0.003	49±4
80	66±1	10.7±0.6	6.6±0.1	10±2	36.6±0.6	0.100±0.005	2.2±0.2
90	69±4	9±1	6.5±0.3	6±3	33±2	0.068±0.008	2.50±0.01

Table 7.22: Fitting parameters with the model of mixtures of interacting spherocylinders and stacked bilayers related to the curves shown in the panel #18: ϕ_O=0.0100, T=20°C, [NaCl]=92 mM, [$CaCl_2$]=2 mM, [$MgSO_4$]=11 mM.

C_R (mM)	F	W	Z	p	q	R	T
10	0.04±0.08	0.31±0.08	0.97±0.06	0.523±0.004	0.6±0.1	0.22±0.09	0.50±0.08
20	0.42±0.09	0.40±0.04	1.0±0.1	0.05±0.05	1.0±0.2	0.16±0.02	0.70±0.08
30	0.020±0.007	0.97±0.02	0.8±0.4	1.00±0.05	0.9±0.1	0.70±0.07	0.1±0.3
40	0.2±0.2	0.41±0.03	0.94±0.03	0.22±0.09	0.58±0.06	0.32±0.07	0.71±0.08
50	0.07±0.04	0.533±0.005	1.00±0.03	0.674±0.009	0.19±0.02	0.64±0.05	0.67±0.05
60	0.4±0.2	0.3±0.3	1.0±0.4	0.39±0.05	0.0±0.4	0.5±0.1	0.69±0.08
70	0.3±0.3	0.33±0.06	1.00±0.02	0.42±0.09	0.64±0.09	0.82±0.08	0.81±0.08
80	0.5±0.1	0.30±0.03	0.83±0.04	0.66±0.04	0.010±0.004	0.49±0.03	0.77±0.03
90	0.20±0.07	0.61±0.03	1.0±0.2	0.54±0.06	1.0±0.3	0.55±0.02	0.5±0.1

C_R (mM)	a_{ac} (Å^2)	δ_{ac} (Å)	$R_{1,ac}$ (Å)	L (Å)	N_{agg}	$n_{W,ac}$	z q_e	J RT
10	280±30	18.0±0.6	22±3	10±10	80±30	100±10	−1.0±0.4	1.0±0.5
20	108±4	16.9±0.8	23±1	33±3	270±10	25±3	−0.1±0.1	0.8±0.5
30	105±5	12±2	24±2	11±5	170±20	16±4	−0.8±0.3	1.0±0.4
40	150±20	12.1±0.3	17.56±0.02	30±40	110±80	27±4	−0.0±0.3	1.0±0.2
50	118±4	13.79±0.08	18.2±0.1	3000±1000	6000±3000	25.4±0.9	−0.12±0.08	1.0±0.1
60	116±6	15.3±0.9	17.61±0.04	300±200	600±400	27±3	−0.15±0.07	1.0±0.3
70	114±4	18.0±0.6	17.69±0.09	400±100	900±200	32±2	−0.2±0.1	0.71±0.07
80	100.3±0.9	16.7±0.5	20.48±0.09	500±100	1300±300	26±1	−1.00±0.02	0.008±0.006
90	110±10	13.9±0.5	21±1	28±6	190±20	19±4	−1.000±0.003	0.000±0.005

C_R (mM)	a_b (Å^2)	δ_b (Å)	$R_{1,b}$ (Å)	$n_{W,b}$	d (Å)	g_d	N_d
10	68.3±0.7	10±2	15±1	8±6	54±5	0.01±0.03	0±20
20	60.2±0.1	15.9±0.6	7.4±0.3	16±1	49±1	0.08±0.04	2±3
30	50±9	10±4	17±3	0±10	56±3	0.078±0.007	0±20
40	65.8±0.4	10.7±0.6	7.1±0.4	9±1	36±1	0.08±0.01	50±10
50	61.42±0.09	10±1	7.56±0.07	6±2	40±2	0.091±0.008	49±7
60	70±1	18±1	5.5±0.8	26±2	51.0±0.9	0.10±0.04	10±20
70	70±2	12±2	6.9±0.3	12±6	42±7	0.07±0.03	0±20
80	60.6±0.5	19±2	6.49±0.07	22±3	56±3	0.0997±0.0003	2.0±0.7
90	69.9±0.6	17±2	6.9±0.5	22±5	49±5	0.00±0.05	0±10

Table 7.23: Fitting parameters with the model of mixtures of interacting spherocylinders and stacked bilayers related to the curves shown in the panel #19: ϕ_O=0.0100, T=20°C, [NaCl]=229 mM, [$CaCl_2$]=5 mM, [$MgSO_4$]=28 mM.

C_R (mM)	F	W	Z	p	q	R	T
10	0.59±0.03	0.5118±0.0008	1.00±0.03	0.41±0.04	0.05±0.03	0.002±0.004	0.66±0.06
20	0.529±0.005	0.6±0.1	0.9±0.1	0.3±0.2	0.0±0.3	0.080±0.008	0.6±0.2
30	0.97±0.07	0.56±0.02	1.00±0.03	0.26±0.05	0.91±0.03	0.33±0.02	0.69±0.05
40	0.5±0.2	0.48±0.07	0.8±0.1	0.13±0.04	0.2±0.1	0.33±0.02	0.74±0.04
50	0.63±0.06	0.49±0.06	0.73±0.02	0.33±0.01	0.04±0.08	0.358±0.006	0.76±0.03
60	0.58±0.03	0.22±0.02	0.85±0.09	0.04±0.04	0.0±0.2	0.31±0.02	0.88±0.06
70	0.42±0.07	0.42±0.02	0.76±0.02	0.15±0.01	0.2±0.2	0.387±0.005	0.73±0.03
80	0.49±0.08	0.48±0.07	0.74±0.05	0.20±0.08	0.7±0.3	0.5049±0.0005	0.73±0.06
90	0.6±0.1	0.49±0.03	0.9±0.1	0.19±0.05	0.7±0.2	0.41±0.02	0.59±0.04

C_R (mM)	a_{sc} (Å^2)	δ_{sc} (Å)	$R_{1,sc}$ (Å)	L (Å)	N_{aggs}	$n_{W,sc}$	z q_o	J RT
10	270±10	18.00±0.04	17.63±0.02	620±70	570±50	116±5	−0.0±0.4	1.00±0.06
20	280±60	16.6±0.4	18.5±0.1	26±3	70±20	90±20	−1.0±0.5	0.0±0.4
30	208±2	17.99±0.01	18.2±0.5	19±4	100±3	57.1±0.6	−0.24±0.08	0.0001±0.0007
40	252±4	16.3±0.5	15.3±0.3	27±4	71±4	69±3	−0.998±0.009	0.002±0.001
50	239±6	16.60±0.04	17.6±0.3	23±3	82±5	69±2	−0.9±0.2	0.002±0.004
60	280±20	17.0±0.4	14.8±0.3	19±3	60±6	82±4	−0.0±0.4	1.0±0.3
70	255±6	17.75±0.05	16.0±0.3	23±2	75±1	79±2	−0.97±0.07	0.003±0.001
80	240±10	17.8±0.1	16.5±0.4	22±1	82±6	72±4	−0.94±0.03	0.0±0.1
90	240±8	16.6±0.6	15.9±0.3	21±2	73±1	70±5	−1.00±0.01	0.001±0.002

C_R (mM)	a_b (Å^2)	δ_b (Å)	$R_{1,b}$ (Å)	$n_{W,b}$	d (Å)	g_d	N_d
10	70±4	13.1±0.3	6.8±0.1	18±2	42±1	0.00±0.04	0±20
20	69±4	13.58±0.04	6.5±0.8	18±2	43±2	0.01±0.04	2±2
30	68.0±0.5	13±2	8.3±0.4	15±5	48±6	0.082±0.008	0±20
40	69±2	11±1	6.6±0.3	12±3	40±3	0.072±0.009	2.5±0.2
50	57±2	9.9±0.5	7.9±0.2	4.6±0.5	40±1	0.09±0.04	2.5±0.3
60	70±1	8.8±0.3	6.3±0.1	7±1	33.0±0.9	0.10±0.05	3.5±0.6
70	63±2	10.4±0.2	7.3±0.3	8±1	39.3±0.7	0.040±0.006	2.5±0.1
80	57.4±0.6	9.0±0.5	8.3±0.2	3±1	39±1	0.05±0.02	2.5±0.2
90	70±3	11.1±0.9	6.7±0.2	12±3	39±1	0.00±0.03	2.4±0.2

Table 7.24: Fitting parameters with the model of mixtures of interacting spherocylinders and stacked bilayers related to the curves shown in the panel #20: ϕ_O=0.0100, T=20°C, [NaCl]=460 mM, [$CaCl_2$]=0 mM, [$MgSO_4$]=0 mM.

C_R (mM)	F	W	Z	p	q	R	T
10	0.83±0.02	0.22±0.02	0.90±0.05	0.0003±0.0001	1.00±0.08	–	–
20	0.45±0.02	0.48±0.07	1.00±0.07	0.00016±0.00008	0.83±0.05	–	–
30	0.3±0.2	0.50±0.02	1.00±0.04	0.0000±0.0002	0.6±0.3	–	–
40	0.34±0.07	0.64±0.04	0.99±0.02	0.0000±0.0002	1.0±0.4	–	–
50	0.26±0.04	1.0±0.1	–	0.00001±0.00004	0.61±0.03	–	–
60	0.221±0.003	1.000±0.003	–	0.00001±0.00005	0.9±0.4	–	–
70	0.30±0.06	0.78±0.06	0.68±0.01	0.0002±0.0003	0.494±0.009	–	–
80	0.32±0.01	0.98±0.01	–	0.0005±0.0002	0.0±0.2	–	–
90	0.36±0.02	0.60±0.02	0.98±0.02	0.00006±0.00007	0.5±0.1	–	–

C_R (mM)	a_{sc} (Å^2)	δ_{sc} (Å)	$R_{1,sc}$ (Å)	L (Å)	N_{aggs}	$n_{W,sc}$	z q_o	J RT
10	125±9	14.0±0.5	18.7±0.4	42±5	180±20	29±4	−0.13±0.09	0.0±0.4
20	206±1	12.7±0.4	14.8±0.2	19±4	62±5	47±2	−0.28±0.07	0.2±0.1
30	220±10	13.1±0.4	14.5±0.1	18±2	57±4	53±6	−0.50±0.02	0.61±0.05
40	236±7	13.3±0.2	14.0±0.1	19.7±0.8	54±2	57±3	−0.475±0.002	0.2±0.3
50	200.9±0.5	11.64±0.05	14.36±0.07	21.7±0.9	59.9±0.7	42.0±0.2	−0.48±0.01	0.32±0.09
60	234±2	12.49±0.09	13.73±0.07	20.4±0.3	51.2±0.3	54±1	−0.491±0.002	0.43±0.06
70	203±1	11.64±0.02	14.3±0.2	21.8±0.8	59.3±0.7	42.4±0.4	−0.4900±0.0005	0.16±0.09
80	212±4	11.94±0.07	14.26±0.07	21.1±0.7	57.1±0.9	45±2	−0.33±0.05	0.00±0.02
90	213.7±0.4	12.90±0.06	14.4±0.1	22±1	61.6±0.7	49.9±0.2	−0.44±0.02	0.10±0.06

C_R (mM)	a_b (Å^2)	δ_b (Å)	$R_{1,b}$ (Å)	$n_{W,b}$	d (Å)	g_d	N_d
10	63.3±0.6	9.7±0.6	7.4±0.3	7±1	35.9±0.1	0.079±0.005	12±2
20	70±1	13±1	6.31±0.07	18±4	43±3	0.04±0.02	2±3
30	70±2	12±2	6.24±0.07	15±5	40±5	0.08±0.04	41±3
40	69.997±0.008	11±2	6.2±0.1	14±5	38±4	0.087±0.005	50.0±0.5
50	59.7±0.7	14±1	7.4±0.1	16±2	–	–	–
60	59±7	21.6±0.6	7.6±0.8	31±6	–	–	–
70	69.7±0.9	12±1	6.4±0.1	15±3	41±2	0.00±0.04	2.5±0.2
80	70±2	13.5±0.3	6.3±0.2	19±2	–	–	–
90	61.8±0.4	7.0±0.3	7.08±0.07	0.3±0.7	32.0±0.8	0.100±0.003	40±10

Table 7.25: Fitting parameters with the model of mixtures of interacting spherocylinders and stacked bilayers related to the curves shown in the panel #21: ϕ_O=0.5000, T=20°C, [NaCl]=0 mM, [$CaCl_2$]=0 mM, [$MgSO_4$]=0 mM.

C_R (mM)	F	W	Z	p	q	R	T
10	0.61±0.07	0.22±0.03	0.91±0.01	0.0003±0.0001	0.71±0.07	0.65±0.02	0.82±0.02
30	0.64±0.02	0.45±0.02	0.56±0.03	0.0012±0.0004	0.0±0.1	0.33±0.07	0.62±0.08
40	0.91±0.04	0.62±0.02	0.66±0.06	0.0016±0.0003	0.7±0.1	0.8±0.1	0.5±0.1
50	0.94±0.04	0.36±0.02	0.66±0.03	0.00141±0.00006	0.50±0.08	0.70±0.04	0.989±0.003
60	0.93±0.02	0.45±0.01	0.602±0.002	0.00161±0.00006	0.2±0.1	0.542±0.001	0.30±0.08
70	0.95±0.02	0.43±0.02	0.81±0.03	0.0014±0.0001	0.66±0.05	0.34±0.06	0.90±0.05
80	0.97±0.05	0.36±0.02	0.80±0.03	0.0010±0.0001	0.609±0.008	0.569±0.007	1.00±0.01
90	0.981±0.009	0.41±0.01	0.78±0.04	0.00100±0.00005	0.5008±0.0002	0.72±0.06	0.79±0.08

C_R (mM)	a_{sc} (Å^2)	δ_{sc} (Å)	$R_{1,sc}$ (Å)	L (Å)	N_{agg}	$n_{W,sc}$	z q_o	J RT
10	109±6	18.000±0.002	24.0±0.3	51±6	330±30	28±2	−0.01±0.04	1.000±0.002
30	101±5	17.85±0.07	22.3±0.2	190±50	700±100	32±2	−0.42±0.03	0.2±0.2
40	116±4	17.96±0.06	22.7±0.2	54±6	300±20	35±1	−0.43±0.06	0.03±0.05
50	100.0±0.4	18.0±0.1	21.7±0.2	158±10	590±30	30.9±0.4	−0.31±0.09	0.24±0.08
60	109±3	17.6±0.3	19.4±0.3	302±9	800±40	36±2	−0.86±0.09	0.19±0.09
70	151±2	16.26±0.07	19.7±0.1	32.8±0.8	156±5	43.5±0.6	−0.37±0.06	0.07±0.03
80	127±4	17.1±0.3	17.8±0.1	148±5	376±9	40±3	−0.10±0.04	0.15±0.02
90	135±6	15.5±0.6	16.5±0.3	140±10	300±20	38±4	−0.455±0.007	0.22±0.04

C_R (mM)	a_b (Å^2)	δ_b (Å)	$R_{1,b}$ (Å)	$n_{W,b}$	d (Å)	g_d	N_d
10	63.9±0.3	11.9±0.2	7.6±0.2	10.4±0.3	39.10±0.05	0.06±0.01	50±3
30	51±6	8.3±0.8	8.6±0.7	0±3	38±1	0.074±0.002	2.5±0.5
40	65±1	9.5±0.4	7.5±0.3	6±1	37.4±0.8	0.00±0.02	2.5±0.5
50	67±1	11.0±0.5	7.0±0.1	11±1	41±1	0.00±0.03	2.1±0.2
60	62.9±0.1	8.5±0.2	7.2±0.1	3.9±0.5	33.9±0.6	0.100±0.004	2.6±0.5
70	60.058±0.009	7.04±0.05	7.81±0.04	0.0±0.1	29.7±0.1	0.060±0.001	3.5±0.5
80	69.97±0.06	7.5±0.4	6.57±0.08	4±1	31.9±0.6	0.059±0.001	2.5±0.5
90	68.5±0.3	6.3±0.1	6.67±0.03	0.2±0.2	28.8±0.3	0.0603±0.0003	3.1±0.3

Table 7.26: Fitting parameters with the model of mixtures of interacting spherocylinders and stacked bilayers related to the curves shown in the panel #22: ϕ_O=0.5000, T=20°C, [NaCl]=46 mM, [$CaCl_2$]=1 mM, [$MgSO_4$]=6 mM.

C_R (mM)	F	W	Z	p	q	R	T
10	0.61±0.02	0.41±0.04	0.91±0.01	0.0019±0.0004	0.632±0.002	0.12±0.04	0.4±0.4
20	0.9997±0.0002	0.47±0.02	0.82±0.01	0.0042±0.0002	0.997±0.002	0.56±0.03	0.70±0.05
30	0.63±0.04	0.42±0.03	0.92±0.02	0.00216±0.00008	0.999±0.009	0.76±0.05	0.86±0.02
40	0.96±0.02	0.46±0.02	0.914±0.008	0.00034±0.00003	0.77±0.07	0.517±0.002	0.521±0.003
50	0.97±0.01	0.511±0.006	0.85±0.02	0.00003±0.00001	0.86±0.06	0.07±0.07	0.75±0.03
60	0.81±0.05	0.519±0.007	0.86±0.02	0.00000±0.00004	0.566±0.003	0.24±0.01	0.66±0.04
70	0.9994±0.0003	0.550±0.003	0.85±0.02	0.0000004±0.0000002	0.3±0.3	0.26±0.05	0.57±0.02
80	0.84±0.06	0.47±0.02	0.90±0.01	0.00004±0.00001	0.0±0.4	0.55±0.02	0.46±0.02
90	0.86±0.04	0.53±0.01	0.82±0.01	0.0000±0.0001	1.0±0.1	0.28±0.08	0.53±0.03

C_R (mM)	a_{sc} (Å^2)	δ_{sc} (Å)	$R_{1,sc}$ (Å)	L (Å)	N_{agg}	$n_{W,sc}$	z q_o	J RT
10	200.71±0.05	7.3±0.4	16.6±0.6	2.0±0.9	37±3	24±2	−0.000±0.007	0.523±0.003
20	101±1	8.36±0.06	16.3±0.1	104±4	234±10	8.8±0.4	−0.99989±0.00007	0.03±0.01
30	118±1	17.9984±0.0008	23.1±0.2	41±1	270±6	31.6±0.5	−0.40±0.01	0.549±0.007
40	215.2±0.5	10.08±0.02	8.90±0.02	640±30	370±10	37.8±0.2	−0.0±0.1	0.40±0.06
50	201.4±0.4	8.2±0.4	9.9±0.2	80±20	65±10	27±2	−0.9981±0.0009	1.00±0.04
60	300±2	8.97±0.07	9.9±0.1	19.7±0.9	22.75±0.07	46.8±0.6	−1.0±0.4	0.50±0.06
70	284±9	7.6±0.2	10.0±0.1	14±2	19.1±0.8	35±2	−0.34±0.05	0.991±0.004
80	294±3	8.7±0.2	10.3±0.2	15±1	21.5±0.7	42.8±0.8	−0.3±0.1	1.00±0.01
90	282±8	9.9±0.4	9.3±0.1	46.8±0.5	36.6±0.8	50±4	−0.70±0.08	0.5014±0.0001

C_R (mM)	a_b (Å^2)	δ_b (Å)	$R_{1,b}$ (Å)	$n_{W,b}$	d (Å)	g_d	N_d
10	50.0±0.4	23±1	13±1	26±2	74±1	0.10±0.04	2.6±0.5
20	50.0000±0.0005	24.998±0.001	16.0±0.3	30.5±0.1	86.6±0.7	0.096±0.002	2.5±0.2
30	50.3±0.2	8.4±0.1	11.3±0.1	0.0±0.2	39.54±0.06	0.038±0.009	35±2
40	50.00±0.03	23.19±0.04	8.78±0.05	24.23±0.02	63.93±0.08	0.10±0.02	3.0±0.2
50	50.0±0.8	22.8±0.3	8.7±0.2	25±1	63.1±0.6	0.066±0.002	2.50±0.09
60	50.2±0.1	25.00±0.08	8.89±0.04	29.1±0.2	68.6±0.9	0.099±0.005	2.5±0.1
70	50.0002±0.0008	25.00000±0.00005	8.9599±0.0002	28.41±0.09	70.8±0.3	0.08±0.01	2.1±0.2
80	50.00±0.06	25.00±0.04	8.86±0.02	28.1±0.1	67.7±0.3	0.059±0.002	2.0±0.2
90	50.03±0.01	24.98±0.06	8.89±0.09	28.6±0.1	67.7±0.3	0.0987±0.0006	2.5±0.2

Table 7.27: Fitting parameters with the model of mixtures of interacting spherocylinders and stacked bilayers related to the curves shown in the panel #23: ϕ_O=0.5000, T=20°C, [NaCl]=92 mM, [$CaCl_2$]=2 mM, [$MgSO_4$]=11 mM.

C_R (mM)	F	W	Z	p	q	R	T
10	0.6±0.2	0.4±0.2	1.0±0.1	0.002±0.002	0.64±0.08	0.00±0.05	0.58±0.02
20	0.99±0.01	0.40±0.02	0.997±0.006	0.0038±0.0002	0.25±0.06	0.10±0.02	0.68±0.05
30	1.00±0.02	0.59±0.01	1.00±0.02	0.0016±0.0002	0.548±0.007	0.08±0.01	0.2±0.2
40	0.99±0.02	0.545±0.009	1.000±0.006	0.0020±0.0003	0.1±0.3	0.08±0.03	0.13±0.06
50	0.5±0.1	0.43±0.02	0.97±0.03	0.0023±0.0008	0.4±0.2	0.07±0.05	0.81±0.03
60	0.68±0.03	0.22±0.04	0.93±0.04	0.0025±0.0007	0.60±0.03	0.08±0.02	1.0±0.2
70	1.00±0.03	0.43±0.02	1.00000±0.00003	0.0044±0.0004	0.74±0.03	0.08±0.04	0.98±0.03
80	0.98±0.07	0.41±0.02	0.999±0.003	0.0038±0.0004	0.2±0.1	0.06±0.06	0.92±0.04
90	0.9±0.1	0.43±0.04	0.99±0.02	0.0033±0.0005	0.52±0.05	0.02±0.03	0.0±0.2

C_R (mM)	a_{sc} (Å^2)	δ_{sc} (Å)	$R_{1,sc}$ (Å)	L (Å)	N_{ssS}	$n_{W,sc}$	z q_o	J RT
10	140±50	18.0±0.4	25±2	20±20	200±70	40±20	−1.0±0.2	0.74±0.05
20	101±4	18.00±0.04	24.8±0.2	490±70	1500±200	33±2	−0.999±0.005	0.0±0.3
30	140±10	17±1	22.5±0.9	27±2	200±20	38±6	−0.45±0.01	0.0±0.1
40	130±10	18±2	24.5±0.6	30±2	230±20	41±9	−0.0±0.3	0.1±0.1
50	173±5	17.2±0.3	19.2±0.5	28±2	134±9	52±2	−0.6±0.2	0.1±0.3
60	100±1	18.0±0.2	19.88±0.09	360±30	1040±70	32.4±0.8	−0.032±0.007	0.68±0.02
70	108±2	18.0±0.1	18.4±0.1	400±30	1010±70	34.7±0.9	−0.95±0.02	0.98±0.05
80	160±10	15.8±0.6	19.9±0.4	34±6	150±10	44±6	−0.82±0.08	0.4±0.2
90	139±4	17.2±0.5	21.8±0.2	30±2	190±7	41±3	−0.9±0.4	0.28±0.09

C_R (mM)	a_b (Å^2)	δ_b (Å)	$R_{1,b}$ (Å)	$n_{W,b}$	d (Å)	g_d	N_d
10	50±8	19±2	12±1	18.1±0.8	65±2	0.096±0.004	40±20
20	53±2	20±1	9.5±0.5	21±1	63±3	0.05±0.02	19±7
30	68±3	16±1	7.0±0.4	22±2	50±3	0.09±0.05	20±10
40	66.8±0.4	18.1±0.5	6.7±0.5	27±1	54±2	0.061±0.003	26±6
50	70.0±0.2	12±2	6.42±0.07	15±6	42±5	0.02±0.01	10±20
60	68.0±0.9	9±1	7.0±0.2	7±4	35±3	0.03±0.01	0±20
70	68.8±0.4	15.2±0.3	7.3±0.1	21.8±0.6	46±1	0.065±0.002	0±10
80	69.4±0.4	17.1±0.6	6.50±0.09	27±1	48±3	0.04±0.02	28.1±0.4
90	69.7±0.3	15.4±0.8	6.6±0.1	23±2	44±3	0.10±0.04	39±2

Table 7.28: Fitting parameters with the model of mixtures of interacting spherocylinders and stacked bilayers related to the curves shown in the panel #24: ϕ_O=0.5000, T=20°C, [NaCl]=229 mM, [$CaCl_2$]=5 mM, [$MgSO_4$]=28 mM.

C_R (mM)	F	W	Z	p	q	R	T
10	0.516±0.004	0.519±0.004	0.98±0.02	0.0005±0.0002	0.2±0.2	0.054±0.006	0.81±0.05
20	0.95±0.04	0.34±0.07	0.63±0.03	0.0003±0.0003	0.62±0.02	0.071±0.005	0.97±0.04
30	0.39±0.02	0.49±0.01	1.0±0.2	0.00000±0.00009	0.97±0.08	0.072±0.004	0.78±0.04
40	0.48±0.02	0.54±0.01	0.9±0.1	0.0007±0.0002	0.2±0.4	0.20±0.02	0.70±0.05
50	0.46±0.01	0.53±0.03	1.00±0.02	0.00005±0.00002	1.0±0.1	0.189±0.006	0.69±0.02
60	0.81±0.04	0.49±0.04	0.9997±0.0006	0.0006±0.0002	0.0±0.3	0.19±0.02	0.60±0.01
70	0.95±0.02	0.414±0.008	0.837±0.006	0.000011±0.000008	0.79±0.02	0.19±0.02	0.363±0.007
80	1.00±0.04	0.556±0.004	0.737±0.009	0.00024±0.00004	0.87±0.05	0.26±0.01	0.504±0.002
90	0.998±0.001	0.206±0.004	0.73±0.03	0.00121±0.00005	0.01±0.04	0.348±0.008	0.41±0.01

C_R (mM)	a_{sc} (Å^2)	δ_{sc} (Å)	$R_{1,sc}$ (Å)	L (Å)	N_{ssS}	$n_{W,sc}$	z q_o	J RT
10	130±10	17.9±0.9	24.0±0.5	30±10	230±40	36±6	−1.0±0.5	0.0±0.5
20	125±4	18.0±0.7	23.0±0.6	35±6	240±20	34±2	−1.0±0.5	0.4±0.2
30	112±2	17.3±0.3	24.6±0.5	29±4	265±6	30±1	−0.471±0.005	0.15±0.07
40	119±3	17.3±0.4	24.7±0.2	28.8±0.4	250±10	30.5±0.8	−0.7±0.1	0.1±0.2
50	119±1	17.1±0.4	23.32±0.07	29±3	240±10	30.0±0.8	−1.0±0.2	0.0±0.1
60	130±2	17.2±0.3	22.96±0.06	25±3	204±9	34.5±0.9	−0.1±0.3	0.1±0.1
70	135.4±0.4	5.5±0.2	10.0±0.1	1610±40	1180±50	6.0±0.5	−0.30±0.02	0.64±0.01
80	161±3	5.15±0.05	10.8±0.1	41.2±0.9	46±1	7.3±0.5	−0.95±0.02	0.7±0.1
90	109±4	5.37±0.02	12.5±0.3	1430±20	1510±90	2.2±0.6	−0.99±0.02	0.678±0.007

C_R (mM)	a_b (Å^2)	δ_b (Å)	$R_{1,b}$ (Å)	$n_{W,b}$	d (Å)	g_d	N_d
10	57±5	16.0±0.3	8.1±0.6	15±2	52±1	0.084±0.002	2.5±0.3
20	66±1	8±1	6.9±0.2	4±3	35±3	0.040±0.009	3.5±0.7
30	68±1	18±2	6.6±0.1	27±4	50±2	0.00±0.05	3±1
40	66±1	17±1	6.9±0.3	21±3	47.5±0.9	0.09±0.02	2.6±0.5
50	70±2	18.1±0.5	6.3±0.2	27±2	51.9±0.8	0.09±0.04	47±3
60	62.8±0.2	13.5±0.5	7.0±0.2	14±1	45.8±0.9	0.0635±0.0006	3±1
70	51.8±0.8	22.8±0.2	8.4±0.1	24±1	62.9±0.4	0.019±0.008	2.5±0.2
80	50.1±0.1	19.8±0.1	8.97±0.04	18.5±0.2	57.6±0.2	0.09992±0.00005	2.2±0.1
90	50.0±0.3	21.5±0.1	8.92±0.06	20.5±0.3	60.8±0.2	0.09±0.04	2.50±0.04

Table 7.29: Fitting parameters with the model of mixtures of interacting spherocylinders and stacked bilayers related to the curves shown in the panel #25: ϕ_O=0.5000, T=20°C, [NaCl]=460 mM, [$CaCl_2$]=0 mM, [$MgSO_4$]=0 mM.

C_R (mM)	F	W	Z	p	q	R	T
10	0.999±0.002	0.5±0.1	0.29±0.06	–	–	–	–
20	0.88±0.05	0.85±0.02	0.3±0.3	–	–	–	–
30	0.78±0.08	0.70±0.07	1.00±0.04	–	–	–	–
40	0.72±0.04	0.952±0.003	0.000±0.003	–	–	–	–
50	0.79±0.09	0.97±0.03	0.00±0.08	–	–	–	–
60	0.993±0.009	0.97±0.01	0.69±0.04	–	–	–	–
70	0.88±0.03	0.956±0.005	0.00±0.07	–	–	–	–
80	0.88±0.03	0.96±0.01	0.4±0.2	–	–	–	–
90	0.92±0.04	0.968±0.003	0.000±0.004	–	–	–	–

C_R (mM)	a_{ac} (Å^2)	δ_{ac} (Å)	$R_{1,ac}$ (Å)	L (Å)	N_{agg}	$n_{W,ac}$	z q_o	J RT
10	226.1±0.6	12.15±0.07	8.58±0.06	3000±1000	1800±700	52.8±0.8	−0.92±0.03	0.687±0.006
20	178±5	10.4±0.6	10.0±0.2	200±50	170±30	31±3	−0.23±0.05	0.2±0.4
30	241±5	13.8±0.3	9.4±0.2	190±10	145±7	62±2	−0.27±0.04	0.0±0.4
40	300±4	10.8±0.2	10.1±0.3	22±1	28±1	56.7±0.9	−0.4±0.1	0.94±0.06
50	270±10	10.9±0.3	10.7±0.2	23.0±0.6	33±1	50±5	−0.33±0.05	1.00±0.04
60	247.6±0.9	13.57±0.04	9.22±0.02	160±5	119±3	61.3±0.4	−0.69±0.02	0.8±0.1
70	203±1	11.8±0.1	9.93±0.03	156±3	134±3	42.5±0.7	−0.58±0.06	0.98±0.09
80	268±8	13.00±0.09	9.2±0.1	92±2	72±4	63±2	−0.42±0.02	0.61±0.08
90	220±10	12.4±0.3	9.5±0.2	145±4	115±5	50±5	−0.72±0.03	0.7±0.2

C_R (mM)	a_b (Å^2)	δ_b (Å)	$R_{1,b}$ (Å)	$n_{W,b}$	d (Å)	g_d	N_d
10	68.1±0.2	7.85±0.09	5.83±0.06	3.9±0.2	32.2±0.2	0.084±0.002	20±3
20	67±1	12±3	5.8±0.1	13±7	41±6	0.006±0.007	2±2
30	66±1	6.4±0.2	6.0±0.1	0.0±0.1	25±1	0.10±0.03	25±4
40	50±9	13±1	8±1	8±6	43.7±0.5	0.01±0.04	2.5±0.2
50	52±9	11.8±0.8	8±1	7±5	42±2	0.09±0.03	4±2
60	69.88±0.02	6.048±0.002	5.54±0.01	0.0001±0.0001	23.17±0.06	0.100±0.008	10±10
70	70.0±0.9	12.2±0.3	5.58±0.08	14.9±0.9	40.6±0.7	0.09±0.02	5±2
80	68.7±0.5	12.6±0.5	5.73±0.04	15±1	42±1	0.02±0.05	5.7±0.2
90	70.0±0.4	12.9±0.1	5.56±0.06	16.4±0.5	41.9±0.2	0.001±0.003	5.1±0.8

Table 7.30: Fitting parameters with the model of mixtures of interacting spherocylinders and stacked bilayers related to the curves shown in the panel #26: ϕ_O=0.0000, T=10°C, [NaCl]=0 mM, [$CaCl_2$]=0 mM, [$MgSO_4$]=0 mM.

C_R (mM)	F	W	Z	p	q	R	T
10	0.11±0.04	0.4±0.1	1.0±0.5	–	–	0.95±0.04	0.7±0.1
20	0.3±0.1	0.5±0.1	0.967±0.004	–	–	1.0±0.1	0.44±0.07
30	0.8±0.1	0.48±0.07	0.83±0.03	–	–	0.91±0.04	0.77±0.03
40	0.95±0.01	0.59±0.04	0.99±0.02	–	–	0.45±0.02	0.4±0.1
50	1.00±0.01	0.35±0.02	0.90±0.03	–	–	0.98±0.05	0.82±0.06
60	0.97±0.03	0.39±0.01	0.978±0.008	–	–	0.85±0.04	0.92±0.04
70	0.992±0.006	0.61±0.06	0.996±0.002	–	–	0.85±0.06	0.91±0.04
80	0.93±0.03	0.97±0.02	0.02±0.03	–	–	0.9±0.2	0.40±0.09
90	0.8±0.1	0.64±0.05	0.99±0.01	–	–	0.74±0.05	0.84±0.09

C_R (mM)	a_{ac} (Å^2)	δ_{ac} (Å)	$R_{1,ac}$ (Å)	L (Å)	N_{agg}	$n_{W,ac}$	z q_o	J RT
10	270±20	12.4±0.2	10±1	40±20	47±10	59±5	−1.0±0.4	0.0±0.5
20	100±20	5.6±0.3	16±2	28±3	90±20	1±2	−1.000±0.002	0.65±0.05
30	278±7	11.9±0.1	11.0±0.1	22±2	35±2	55±1	−0.3±0.1	0.84±0.03
40	224±6	10.6±0.2	11.8±0.1	24±1	43±1	39±2	−0.02±0.03	0.81±0.04
50	244±2	14.8±0.2	11.34±0.09	64±1	78±1	64.8±0.3	−0.75±0.03	1.0±0.1
60	202.2±0.4	10.50±0.08	12.4±0.1	27±1	52.1±0.9	34.4±0.3	−0.28±0.06	1.00±0.02
70	250±10	11.3±0.3	11.7±0.3	22.2±0.8	40±2	46±4	−0.35±0.03	0.8±0.1
80	215±8	9.4±0.3	11.7±0.2	20.9±0.7	38.9±0.9	32±3	−0.30±0.02	0.81±0.08
90	231±5	10.8±0.2	11.9±0.2	22.3±0.5	42±2	41.6±0.9	−0.42±0.04	0.87±0.02

C_R (mM)	a_b (Å^2)	δ_b (Å)	$R_{1,b}$ (Å)	$n_{W,b}$	d (Å)	g_d	N_d
10	63±1	6.8±0.1	6.7±0.2	0.0±0.2	29±2	0.063±0.006	3.4±0.5
20	68±9	9.4±0.7	6±1	7±4	33±1	0.052±0.002	48±4
30	68±1	8.7±0.1	5.84±0.06	5.5±0.6	33.70±0.04	0.04±0.01	50±2
40	66.8±0.8	6.3±0.5	6.03±0.06	0.0±0.9	28±1	0.10±0.04	11±6
50	69.8±0.5	6.7±0.3	5.86±0.05	1.5±0.7	25.1±0.4	0.100±0.006	4.4±0.8
60	68.2±0.7	6.5±0.2	5.98±0.07	0.8±0.6	29.8±0.6	0.10±0.04	10±20
70	67±1	7.6±0.5	5.99±0.09	3±1	27±1	0.09±0.05	26±7
80	65±2	11.2±0.5	6.2±0.1	11±2	40±1	0.10±0.02	4±1
90	70±2	6.0±0.5	5.8±0.2	0.0±0.8	26±1	0.07±0.03	10±20

Table 7.31 : Fitting parameters with the model of mixtures of interacting spherocylinders and stacked bilayers related to the curves shown in the panel #27: ϕ_O=0.0000, T=10°C, [NaCl]=46 mM, [$CaCl_2$]=1 mM, [$MgSO_4$]=6 mM.

C_R (mM)	F	W	Z	p	q	R	T
10	0.07±0.02	0.68±0.09	0.99±0.01	–	–	0.724±0.005	0.549±0.003
20	0.273±0.002	0.70±0.01	0.900±0.008	–	–	0.927±0.009	0.6365±0.0004
30	0.32±0.01	0.36±0.02	0.980±0.007	–	–	0.87±0.01	0.759±0.001
40	0.5868±0.0005	0.40±0.03	0.957±0.007	–	–	0.914±0.002	0.667±0.007
50	0.60±0.02	0.26±0.02	0.994±0.005	–	–	0.68±0.02	0.511±0.002
60	0.46±0.03	0.2±0.1	0.990±0.003	–	–	0.96±0.03	0.48±0.06
70	0.5014±0.0001	0.25±0.02	1.00000±0.00004	–	–	0.73±0.06	0.32±0.07
80	0.77±0.03	0.130±0.003	1.00±0.03	–	–	0.71±0.02	0.74±0.05
90	0.52±0.05	0.33±0.05	1.000±0.003	–	–	0.8±0.1	0.3±0.1

C_R (mM)	a_{sc} (Å^2)	δ_{sc} (Å)	$R_{1,sc}$ (Å)	L (Å)	N_{aggs}	$n_{W,sc}$	z q_e	J RT
10	235.4±0.2	13.26±0.02	9.15±0.01	43000±4000	26000±2000	56.3±0.5	−0.988±0.004	0.68±0.04
20	235.56160±0.00008	13.26128±0.00004	9.15876±0.00001	996000±1000	595700±700	62.55±0.02	−0.48563±0.00003	0.5865±0.0003
30	235.65±0.02	13.27±0.01	9.159±0.003	293000±2000	175000±1000	65.5±0.1	−0.96±0.02	0.7281±0.0005
40	235.56070±0.00006	13.261330±0.000009	9.158884±0.000004	293600±200	175590±90	65.3±0.1	−0.716±0.008	0.880±0.004
50	189.0±0.5	11.4±0.3	10.18±0.08	830±40	620±40	42±1	−0.0±0.2	0.63±0.01
60	260±30	12.0±0.8	12.4±0.2	20.7±0.8	41±4	60±10	−1.000±0.009	0.8±0.1
70	218.0±0.9	12.12±0.03	9.33±0.04	4400±100	2720±80	54.3±0.1	−0.66±0.04	0.9974±0.0009
80	270±4	15.3±0.3	9.97±0.08	150±10	119±8	83±3	−0.3±0.3	0.0±0.2
90	234±3	12.8±0.4	9.1±0.2	2070±80	1250±90	61±2	−0.5±0.2	0.80±0.07

C_R (mM)	a_b (Å^2)	δ_b (Å)	$R_{1,b}$ (Å)	$n_{W,b}$	d (Å)	g_d	N_d
10	69.987±0.009	6.7±0.2	6.28±0.01	1.1±0.5	26.9±0.4	0.0912±0.0004	28.51±0.05
20	66.320±0.008	9.63±0.09	6.6444±0.0008	7.4±0.2	33.8±0.3	0.08272±0.00003	26.5664±0.0007
30	69.75±0.03	10.1±0.5	6.318±0.003	10±1	35±1	0.05183±0.00002	30.84±0.05
40	66.68±0.08	9.6±0.2	6.608±0.008	8.0±0.6	34.0±0.5	0.068±0.003	27.51±0.06
50	69.95±0.04	8.0±0.3	6.28±0.02	4.9±0.8	34±1	0.03±0.01	23±6
60	66±2	8.9±0.3	6.7±0.3	5.8±0.5	34.2±0.2	0.001±0.002	32.5±0.9
70	65.1±0.6	8.99±0.01	6.75±0.06	5.9±0.2	35.0±0.2	0.042±0.006	28.05±0.05
80	69.2±0.3	7.5±0.5	6.26±0.05	4±1	27.6±0.9	0.081±0.009	11±4
90	69±2	9±1	6.4±0.2	7±3	33±2	0.052±0.002	28±7

Table 7.32: Fitting parameters with the model of mixtures of interacting spherocylinders and stacked bilayers related to the curves shown in the panel #28: ϕ_O=0.0000, T=10°C, [NaCl]=92 mM, [$CaCl_2$]=2 mM, [$MgSO_4$]=11 mM.

C_R (mM)	F	W	Z	p	q	R	T
10	0.00±0.05	0.99±0.06	–	–	–	0.3±0.1	0.90±0.05
20	0.12±0.08	0.5015±0.0001	0.9±0.2	–	–	0.13±0.07	0.7±0.1
30	0.09±0.02	0.4±0.1	1.0±0.1	–	–	0.29±0.02	0.89±0.04
40	0.015±0.002	0.58±0.04	1.0±0.2	–	–	0.623±0.006	0.56±0.01
50	0.02±0.04	0.3±0.1	1.00±0.06	–	–	0.66±0.03	0.7±0.1
60	0.052±0.004	0.33±0.05	0.99±0.04	–	–	0.504±0.001	0.74±0.03
70	0.06±0.01	0.28±0.03	0.982±0.009	–	–	0.61±0.02	0.78±0.03
80	0.09±0.01	0.3±0.1	1.00±0.01	–	–	0.45±0.08	0.93±0.03
90	0.075±0.005	0.44±0.04	0.91±0.08	–	–	0.69±0.01	0.70±0.07

C_R (mM)	a_{sc} (Å^2)	δ_{sc} (Å)	$R_{1,sc}$ (Å)	L (Å)	N_{aggs}	$n_{W,sc}$	z q_e	J RT
10	100±10	14.1±0.4	16±1	2500±500	5000±1000	21±3	−0.1±0.2	0.5±0.1
20	110±90	9±2	14±3	200±100	400±200	10±20	−0.11±0.03	0.78±0.06
30	165±8	13.6±0.3	11.6±0.2	1200±400	1200±400	39±3	−1.0±0.3	0.90±0.04
40	108±3	8.7±0.3	13.4±0.2	2100±600	2800±700	10±2	−0.1±0.1	0.592±0.007
50	100±30	6±1	17.532±0.009	17±9	90±20	1±8	−0.003±0.006	0.85±0.08
60	180±10	13.4±0.3	11±1	900±400	800±300	46±5	−0.9±0.3	0.71±0.09
70	140±20	11.5±0.1	13±2	300±200	330±90	26±7	−0.5±0.1	0.72±0.03
80	142±8	11.61±0.05	12±1	800±400	900±400	27±2	−0.485±0.008	0.90±0.06
90	118±1	9.4±0.2	12.80±0.09	900±200	1100±300	14.4±0.6	−0.1±0.1	0.72±0.03

C_R (mM)	a_b (Å^2)	δ_b (Å)	$R_{1,b}$ (Å)	$n_{W,b}$	d (Å)	g_d	N_d
10	51±4	8.5±0.6	8.5±0.5	0.2±0.6	–	–	–
20	70±2	6±3	6.0±0.2	0±6	26±7	0.10±0.02	10±20
30	67.2±0.4	6.6±0.2	6.41±0.02	0.6±0.4	26±2	0.10±0.04	37±2
40	61.2±0.2	7.0±0.1	7.03±0.02	0.0±0.2	32.5±0.6	0.082±0.002	40±20
50	61.2±0.5	7.0±0.7	6.96±0.05	0±1	30±2	0.00±0.04	10±10
60	70.0±0.6	7.8±0.8	6.19±0.06	4±2	28.5±0.8	0.077±0.008	36±4
70	66±2	6.4±0.6	6.4±0.2	0±2	26±1	0.07±0.04	10±10
80	61.6±0.5	6.91±0.08	6.63±0.09	0.1±0.2	31.4±0.3	0.075±0.008	49±2
90	69.978±0.008	6±1	6.07±0.02	0±2	25±2	0.078±0.009	2±3

Table 7.33: Fitting parameters with the model of mixtures of interacting spherocylinders and stacked bilayers related to the curves shown in the panel #29: ϕ_O=0.0000, T=10°C, [NaCl]=229 mM, [$CaCl_2$]=5 mM, [$MgSO_4$]=28 mM.

C_R (mM)	F	W	Z	p	q	R	T
10	0.64±0.04	0.007±0.005	0.63±0.07	–	–	0.512±0.002	0.973±0.005
20	0.63±0.01	0.015±0.003	0.63±0.08	–	–	0.514±0.004	0.949±0.008
30	0.76±0.08	0.0066±0.0003	1.0±0.1	–	–	0.69±0.02	0.947±0.004
40	0.7±0.1	0.014±0.003	0.92±0.05	–	–	0.64±0.04	0.93±0.02
50	0.75±0.08	0.031±0.003	0.99±0.03	–	–	0.69±0.05	0.924±0.004
60	0.7±0.1	0.033±0.008	0.97±0.02	–	–	0.72±0.07	0.91±0.02
70	0.79±0.08	0.07±0.01	1.000±0.002	–	–	0.68±0.05	0.90±0.02
80	0.78±0.07	0.059±0.003	0.995±0.008	–	–	0.699±0.003	0.91±0.02
90	0.85±0.06	0.0463±0.0007	0.9999±0.0008	–	–	0.76±0.02	0.93±0.02

C_R (mM)	a_{sc} (Å^2)	δ_{sc} (Å)	$R_{1,sc}$ (Å)	L (Å)	N_{aggs}	$n_{W,sc}$	z q_e	J RT
10	299±8	15±2	18.9±0.3	9±2	41±6	120±5	−0.1±0.2	0.84±0.05
20	250±10	16.4±0.7	18.9±0.5	2±1	60±9	73±6	−0.46±0.08	0.9±0.4
30	170±10	12.3±0.3	16±2	30±10	90±20	32±2	−0.9±0.5	0.8±0.4
40	180±20	12.4±0.6	15.3±0.3	30±30	80±40	35±7	−0.6±0.2	0.81±0.08
50	205±4	12.2±0.5	13.8±0.9	30±9	65±5	40±3	−0.32±0.06	0.80±0.04
60	208±6	12.3±0.5	14.0±0.7	30±30	60±30	42±2	−0.7±0.2	0.8±0.3
70	230±10	12.5±0.1	12.9±0.3	32±6	58±9	47±4	−0.9±0.4	0.8±0.1
80	165±2	12.3±0.4	11.5±0.1	900±100	830±90	36±2	−0.46±0.06	0.8±0.1
90	154±2	12.28±0.07	12.2±0.1	510±70	560±80	33.2±0.6	−0.5±0.2	0.90±0.04

C_R (mM)	a_b (Å^2)	δ_b (Å)	$R_{1,b}$ (Å)	$n_{W,b}$	d (Å)	g_d	N_d
10	70±4	8±1	6.2±0.4	5±3	33±2	0.061±0.005	2.50±0.05
20	70±1	8.1±0.3	6.21±0.09	4±1	32±1	0.061±0.006	2.4±0.2
30	66±2	7.4±0.3	6.7±0.3	2±1	31.9±0.9	0.061±0.005	2.5±0.3
40	67±2	7.3±0.3	6.6±0.2	2±1	32±1	0.061±0.001	2.4±0.1
50	66±1	6.4±0.6	6.6±0.1	0±2	30±1	0.060±0.005	3.4±0.5
60	66.5±0.5	6.9±0.2	6.59±0.06	1.2±0.5	30.8±0.4	0.060±0.003	3±2
70	68±2	6.7±0.7	6.5±0.2	1±2	30±2	0.07±0.01	10±10
80	66.4±0.6	6.39±0.06	6.65±0.04	0.000±0.006	29.8±0.6	0.060±0.002	10±10
90	68±1	6.3±0.1	6.5±0.1	0.0±0.2	29.6±0.2	0.056±0.003	10±20

Table 7.34: Fitting parameters with the model of mixtures of interacting spherocylinders and stacked bilayers related to the curves shown in the panel #30: ϕ_O=0.0000, T=10°C, [NaCl]=460 mM, [$CaCl_2$]=0 mM, [$MgSO_4$]=0 mM.

C_R (mM)	F	W	Z	p	q	R	T
30	0.46±0.01	0.78±0.06	0.73±0.07	0.42±0.09	0.93±0.04	–	–
60	0.46±0.03	0.90±0.09	0.006±0.003	0.57±0.04	0.3±0.1	–	–
90	0.48±0.04	0.86±0.01	0.000±0.002	0.8±0.1	0.89±0.03	–	–

C_R (mM)	a_{sc} (Å^2)	δ_{sc} (Å)	$R_{1,sc}$ (Å)	L (Å)	N_{aggs}	$n_{W,sc}$	z q_e	J RT
30	163±3	10.8±0.1	11.1±0.1	200±20	210±20	32±1	−0.28±0.04	0.99±0.06
60	225±4	12.3±0.2	10.0±0.1	170±10	133±8	53±1	−0.40±0.02	0.2±0.2
90	190±2	11.0±0.2	10.59±0.03	157±2	143±2	39±1	−0.29±0.01	0.01±0.01

C_R (mM)	a_b (Å^2)	δ_b (Å)	$R_{1,b}$ (Å)	$n_{W,b}$	d (Å)	g_d	N_d
30	70±4	11±2	6.1±0.4	13±5	39±3	0.094±0.003	4.5±0.6
60	70±5	11±1	6.1±0.6	13±4	40±1	0.091±0.007	2.6±0.5
90	62.8±0.3	10.1±0.2	6.90±0.07	7.7±0.4	39.0±0.4	0.0993±0.0008	2.5±0.5

Table 7.35: Fitting parameters with the model of mixtures of interacting spherocylinders and stacked bilayers related to the curves shown in the panel #31: ϕ_O=0.0010, T=10°C, [NaCl]=0 mM, [$CaCl_2$]=0 mM, [$MgSO_4$]=0 mM.

C_R (mM)	F	W	Z	p	q	R	T
10	0.5±0.3	0.2±0.1	0.9987±0.0006	0.84±0.08	0.61±0.03	0.7±0.2	0.88±0.08
40	0.49±0.03	0.24±0.02	0.97±0.01	0.38±0.06	0.4±0.4	0.8±0.1	1.00±0.01
70	0.72±0.04	0.232±0.003	0.95±0.02	0.36±0.08	1.00±0.03	0.61±0.04	1.00±0.07
90	0.68±0.08	0.216±0.008	0.97±0.02	0.3±0.1	0.9±0.2	0.85±0.06	0.81±0.08

C_R (mM)	a_{sc} (Å^2)	δ_{sc} (Å)	$R_{1,sc}$ (Å)	L (Å)	N_{ass}	$n_{W,sc}$	z q_e	J RT
10	180±20	14±2	16±1	26±9	90±10	39±9	−0.992±0.004	0.09±0.06
40	165±8	12.9±0.5	15.8±0.2	30±2	96±7	37±3	−0.04±0.06	1.0±0.2
70	236±3	13.84±0.03	13.3±0.1	27±2	59±2	60.6±0.5	−0.45±0.03	1.000±0.005
90	216±6	12.15±0.03	13.2±0.1	24±3	55±4	48±1	−0.23±0.07	0.98±0.07

C_R (mM)	a_b (Å^2)	δ_b (Å)	$R_{1,b}$ (Å)	$n_{W,b}$	d (Å)	g_d	N_d
10	65±3	13.80±0.05	7.2±0.4	15±1	46±1	0.068±0.008	49.1±0.7
40	53±5	8.5±0.6	7.9±0.5	1±2	38±1	0.04±0.04	0±20
70	60.92±0.09	6.9±0.2	7.09±0.04	0.0±0.4	33±1	0.062±0.004	3±4
90	59±1	8.0±0.4	7.09±0.06	2.0±0.9	31±2	0.10±0.05	0±30

Table 7.36: Fitting parameters with the model of mixtures of interacting spherocylinders and stacked bilayers related to the curves shown in the panel #32: ϕ_O=0.0010, T=10°C, [NaCl]=46 mM, [$CaCl_2$]=1 mM, [$MgSO_4$]=6 mM.

C_R (mM)	F	W	Z	p	q	R	T
20	0.90±0.06	0.13±0.06	0.96±0.02	0.3±0.1	0.0±0.3	0.06±0.03	0.80±0.04
50	0.98±0.07	0.39±0.03	0.95±0.02	0.05±0.02	0.574±0.009	0.01±0.02	0.98±0.09
80	0.69±0.02	0.44±0.01	0.98±0.02	0.00±0.04	0.7±0.1	0.033±0.005	0.47±0.07

C_R (mM)	a_{sc} (Å^2)	δ_{sc} (Å)	$R_{1,sc}$ (Å)	L (Å)	N_{ass}	$n_{W,sc}$	z q_e	J RT
20	230±20	14±2	14.6±0.3	20±6	59±7	60±10	−0.40±0.04	1.0±0.2
50	299±1	14.7±0.2	11.9±0.2	24±1	43.2±0.8	78±1	−0.5±0.1	0.93±0.03
80	295±2	14.41±0.09	12.14±0.07	22±1	42±1	75.6±0.3	−0.493±0.002	0.80±0.03

C_R (mM)	a_b (Å^2)	δ_b (Å)	$R_{1,b}$ (Å)	$n_{W,b}$	d (Å)	g_d	N_d
20	69.3±0.5	8±1	6.13±0.02	5±3	32±3	0.09±0.04	4±6
50	69.999±0.002	7.5±0.6	5.85±0.07	4±2	32±1	0.10±0.02	2.9±0.7
80	69.97±0.04	6.8±0.3	5.92±0.03	1.8±0.8	29.3±0.8	0.086±0.008	4±1

Table 7.37: Fitting parameters with the model of mixtures of interacting spherocylinders and stacked bilayers related to the curves shown in the panel #33: ϕ_O=0.0010, T=10°C, [NaCl]=460 mM, [$CaCl_2$]=0 mM, [$MgSO_4$]=0 mM.

C_R (mM)	F	W	Z	p	q	R	T
10	1.0±0.1	0.5±0.2	0.7±0.2	0.21±0.03	0.96±0.02	–	–
20	0.40±0.04	0.58±0.03	0.86±0.02	0.10±0.05	0.09±0.04	–	–
30	0.5126±0.0009	0.32±0.02	1.00±0.03	0.02±0.04	0.01±0.02	–	–
40	0.603±0.006	0.530±0.004	0.98±0.02	0.001±0.007	0.61±0.03	–	–
50	0.49±0.03	0.73±0.02	0.99±0.01	0.001±0.002	0.511±0.002	–	–
60	0.67±0.07	0.61±0.05	0.999±0.007	0.13±0.04	0.3±0.5	–	–
70	0.49±0.05	0.617±0.006	0.999±0.002	0.06±0.05	0.98±0.02	–	–
80	0.43±0.03	0.68±0.02	0.96±0.04	0.03±0.01	0.88±0.06	–	–
90	0.519±0.004	0.55±0.03	0.96±0.01	0.01±0.02	0.5±0.3	–	–

C_R (mM)	a_{sc} (Å^2)	δ_{sc} (Å)	$R_{1,sc}$ (Å)	L (Å)	N_{agg}	$n_{W,sc}$	z q_e	J RT
10	240±9	16.3±0.5	12±3	60±30	90±10	69±2	−0.2±0.1	0.7±0.2
20	240±10	14.7±0.6	10.2±0.4	300±100	200±80	72±3	−0.32±0.01	0.1±0.5
30	243.0±0.8	14.0±0.1	11.0±0.1	81±6	84±5	66.8±0.8	−0.31±0.01	0.0±0.2
40	225±2	11.34±0.08	12.6±0.1	22±1	46.5±0.5	45.3±0.9	−0.39±0.02	0.4±0.1
50	245±1	11.68±0.04	12.20±0.07	20.6±0.7	41.8±0.4	50.6±0.4	−0.372±0.002	0.3±0.1
60	284±4	12.23±0.06	11.8±0.2	20±1	36.2±0.3	64±2	−0.51±0.01	0.22±0.02
70	245±8	11.4±0.1	12.3±0.1	19.8±0.3	41±1	50±3	−0.43±0.02	0.32±0.04
80	279±1	12.37±0.09	11.8±0.1	21±1	37.4±0.4	62.5±0.8	−0.36±0.06	0.00±0.06
90	270±10	11.9±0.2	11.8±0.1	20±1	36±2	59±4	−0.497±0.004	0.13±0.04

C_R (mM)	a_b (Å^2)	δ_b (Å)	$R_{1,b}$ (Å)	$n_{W,b}$	d (Å)	g_d	N_d
10	67±4	6.6±0.5	8.1±0.3	1±1	33.8±0.3	0.07±0.03	20±20
20	70.00±0.06	13±1	6.00±0.03	17±2	41±2	0.09±0.05	3±2
30	69.3±0.4	6.1±0.5	6.09±0.03	0±1	24±2	0.084±0.004	36±1
40	61.9±0.9	7.0±0.2	6.70±0.09	0.4±0.4	30.2±0.5	0.0523±0.0003	10±20
50	66±2	6.4±0.6	6.2±0.2	0±1	28±1	0.0551±0.0009	10±10
60	69.6±0.2	6.08±0.01	6.11±0.02	0.02±0.02	28.1±0.3	0.009±0.004	48.6±0.5
70	69.99±0.02	6.038±0.002	6.1±0.1	0.0001±0.0001	26.8±0.2	0.0736±0.0008	48±3
80	67±2	6.4±0.2	6.3±0.2	0.01±0.03	29±2	0.10±0.02	7±4
90	69±2	6.1±0.3	6.1±0.2	0.0±0.4	29.5±0.5	0.10±0.04	10±20

Table 7.38: Fitting parameters with the model of mixtures of interacting spherocylinders and stacked bilayers related to the curves shown in the panel #34: ϕ_O=0.0050, T=10°C, [NaCl]=0 mM, [$CaCl_2$]=0 mM, [$MgSO_4$]=0 mM.

C_R (mM)	F	W	Z	p	q	R	T
10	0.65±0.01	0.72±0.02	0.89±0.05	0.13±0.03	0.93±0.02	0.09±0.02	0.3±0.1
20	0.3±0.1	0.66±0.08	0.9±0.1	0.9±0.3	0.65±0.05	1.0±0.1	0.2±0.2
30	0.65±0.03	0.26±0.06	0.98±0.01	0.06±0.07	0.4±0.4	0.02±0.07	1.0±0.3
40	0.48±0.02	0.46±0.01	1.00±0.01	0.21±0.02	0.95±0.02	0.96±0.02	0.39±0.07
50	0.33±0.02	0.32±0.04	0.93±0.03	0.01±0.02	0.62±0.02	0.97±0.01	0.4±0.1
60	0.74±0.06	0.27±0.02	0.999±0.004	0.07±0.01	0.88±0.04	0.91±0.07	0.86±0.08
70	0.262±0.003	0.60±0.04	1.000±0.004	0.07±0.02	0.96±0.01	1.0±0.2	0.24±0.07
80	0.348±0.006	0.36±0.02	1.0000±0.0008	0.00±0.02	0.1±0.2	0.98±0.08	0.2±0.2
90	0.45±0.02	0.35±0.02	0.996±0.007	0.00±0.03	0.4±0.2	1.00±0.05	0.12±0.09

C_R (mM)	a_{sc} (Å^2)	δ_{sc} (Å)	$R_{1,sc}$ (Å)	L (Å)	N_{agg}	$n_{W,sc}$	z q_e	J RT
10	220.6±0.8	16.77±0.04	10.31±0.08	6100±100	4800±100	73.6±0.4	−0.05±0.04	0.84±0.06
20	270±20	17.8±0.7	17.516±0.008	20±3	75±6	90±10	−0.97±0.01	0.0±0.5
30	231±5	17.5±0.2	15.6±0.3	28±2	85±4	75±2	−0.0±0.3	1.0±0.2
40	266±4	15.8±0.2	13.7±0.4	27±4	60±3	78±1	−0.04±0.03	0.993±0.007
50	274±3	17.1±0.3	14.0±0.4	26±5	63±3	88±3	−1.00±0.01	0.59±0.04
60	194±1	17.95±0.02	12.72±0.08	197±6	256±6	67.5±0.6	−0.83±0.05	1.0±0.5
70	199±2	17.4±0.3	12.35±0.04	193±10	236±9	68±2	−0.90±0.02	0.95±0.03
80	240±10	17.7±0.4	11.4±0.2	180±20	180±20	87±5	−1.0±0.1	0.76±0.08
90	271±5	18.00±0.04	10.6±0.2	177±10	156±3	98±1	−0.98±0.02	0.79±0.04

C_R (mM)	a_b (Å^2)	δ_b (Å)	$R_{1,b}$ (Å)	$n_{W,b}$	d (Å)	g_d	N_d
10	67.4±0.8	17.0±0.5	7.8±0.4	25±1	54±1	0.097±0.001	0±20
20	69±2	6±2	9.7±0.8	0±6	36±4	0.082±0.007	4±4
30	70±2	6±1	6.3±0.3	0±2	26±2	0.10±0.05	30±10
40	65.5±0.4	6.5±0.1	7.40±0.05	0.0±0.3	27.8±0.9	0.09±0.05	32±7
50	70.0±0.8	9.6±0.5	6.3±0.1	9±1	37±2	0.09±0.04	3.5±0.8
60	70±2	9.0±0.6	6.2±0.2	7±2	34±1	0.00±0.02	41±3
70	55±2	8.4±0.1	7.9±0.3	1.5±0.7	33±2	0.056±0.004	20±10
80	70±5	7.7±0.6	6.3±0.5	4±2	30.8±0.9	0.073±0.006	26.6±0.2
90	69.1±0.7	6.2±0.9	6.33±0.08	0±2	29.8±0.4	0.10±0.02	34±2

Table 7.39: Fitting parameters with the model of mixtures of interacting spherocylinders and stacked bilayers related to the curves shown in the panel #35: ϕ_O=0.0050, T=10°C, [NaCl]=46 mM, [$CaCl_2$]=1 mM, [$MgSO_4$]=6 mM.

C_R (mM)	F	W	Z	p	q	R	T
10	0.7±0.2	0.4±0.2	0.88±0.05	0.46±0.06	0.4±0.2	0.0±0.2	0.9±0.2
20	0.58±0.08	0.74±0.06	0.99±0.04	0.8±0.1	0.75±0.05	0.75±0.08	0.58±0.02
30	0.28±0.04	0.48±0.08	0.99±0.02	0.4±0.2	0.72±0.03	1.0±0.2	0.8±0.1
40	0.51±0.05	0.520±0.008	0.978±0.008	0.83±0.06	0.63±0.01	1.00±0.03	0.64±0.07
50	0.519±0.007	0.6±0.1	0.93±0.03	0.53±0.05	0.61±0.02	0.95±0.07	0.3±0.1
60	0.78±0.05	0.86±0.04	0.04±0.08	0.44±0.03	0.71±0.03	1.0±0.2	0.6±0.1
70	0.99±0.04	0.60±0.03	1.000±0.004	0.51±0.02	0.3±0.1	1.00±0.02	0.511±0.003
80	0.982±0.007	0.371±0.008	0.959±0.005	0.39±0.03	0.494±0.009	0.821±0.008	0.45±0.08
90	1.00±0.04	0.70±0.06	0.9993±0.0004	0.42±0.03	0.54±0.01	0.9±0.1	0.74±0.03

C_R (mM)	a_{sc} (Å^2)	δ_{sc} (Å)	$R_{1,sc}$ (Å)	L (Å)	N_{agg}	$n_{W,sc}$	z q_e	J RT
10	229±10	16±1	19±2	27±8	91±9	69±2	−0.7±0.4	0.67±0.06
20	170±20	18±1	21±1	27±4	150±30	50±10	−1.0±0.2	0.5±0.2
30	150±8	16.7±0.8	20.2±0.2	29±2	160±10	39±4	−0.59±0.04	0.4±0.1
40	183±6	17.9±0.6	19.9±0.1	26±1	132±3	58±4	−0.9±0.3	0.49±0.08
50	230±20	18.0±0.5	16.6±0.4	26±3	90±8	75±6	−0.97±0.04	0.65±0.04
60	233±2	17.88±0.09	10.60±0.02	1190±30	950±30	82.8±0.3	−0.99±0.08	0.53±0.01
70	221±2	18.00±0.02	11.81±0.08	520±30	490±20	81±1	−0.5±0.1	0.47±0.03
80	227.1±0.4	16.613±0.009	10.64±0.05	1540±5	1202±2	80.2±0.3	−0.33±0.02	0.44±0.04
90	229±1	18.00±0.01	10.89±0.04	1010±10	840±20	82.9±0.3	−0.87±0.05	0.57±0.02

C_R (mM)	a_b (Å^2)	δ_b (Å)	$R_{1,b}$ (Å)	$n_{W,b}$	d (Å)	g_d	N_d
10	59±9	17±2	9±2	20±5	53±4	0.049±0.009	0±10
20	61.0±0.2	8.6±0.5	10.8±0.6	3.2±0.9	41±2	0.10±0.02	12±8
30	58±5	9.8±0.5	9±1	5±3	42±2	0.08±0.02	32±7
40	60±3	9.4±0.9	9.1±0.5	5±2	40±1	0.08±0.03	10±20
50	58±3	8.6±0.5	8.4±0.4	2±1	39±2	0.10±0.05	10±20
60	70.00±0.04	14.03±0.04	6.71±0.08	19.2±0.2	46.5±0.3	0.005±0.006	2.5±0.2
70	56±2	7.6±0.3	8.1±0.2	0.0±0.5	32.3±0.5	0.012±0.003	30±9
80	67.0±0.6	6.34±0.06	6.86±0.08	0.001±0.003	26.4±0.3	0.098±0.001	47±7
90	60.6±0.2	7.07±0.04	7.51±0.02	0.16±0.09	31.74±0.09	0.10±0.05	41±4

Table 7.40: Fitting parameters with the model of mixtures of interacting spherocylinders and stacked bilayers related to the curves shown in the panel #36: ϕ_O=0.0050, T=10°C, [NaCl]=92 mM, [$CaCl_2$]=2 mM, [$MgSO_4$]=11 mM.

C_R (mM)	F	W	Z	p	q	R	T
10	0.999±0.008	0.68±0.02	1.00±0.08	0.20±0.03	0.57±0.01	0.0000±0.0009	0.4±0.4
20	0.5±0.1	0.75±0.06	0.73±0.03	0.31±0.09	0.60±0.03	0.04±0.01	0.53±0.02
30	0.49±0.06	0.93±0.03	1.00±0.02	0.28±0.01	0.63±0.01	0.09±0.05	0.80±0.03
40	0.7±0.1	0.63±0.06	0.993±0.004	0.34±0.02	0.75±0.09	0.20±0.01	0.67±0.07
50	0.83±0.07	0.7±0.1	0.97±0.01	0.46±0.03	0.75±0.08	0.178±0.003	0.4±0.2
60	0.8±0.1	0.72±0.09	1.00±0.01	0.27±0.01	0.553±0.008	0.180±0.009	0.88±0.04
70	0.515±0.006	0.57±0.03	1.0000±0.0002	0.10±0.03	0.86±0.03	0.178±0.006	0.90±0.05
80	0.58±0.04	0.61±0.03	1.00±0.05	0.02±0.02	0.7±0.1	0.02±0.02	0.82±0.07
90	0.508±0.007	0.73±0.08	0.99±0.06	0.09±0.03	0.0±0.5	0.13±0.02	0.78±0.08

C_R (mM)	a_{sc} (Å^2)	δ_{sc} (Å)	$R_{1,sc}$ (Å)	L (Å)	N_{agg}	$n_{W,sc}$	z q_e	J RT
10	134±8	15.1±0.4	15.9±0.1	200±200	300±300	36±3	−1.0±0.5	0.0±0.5
20	201.5±0.3	17.7±0.3	12.9±0.3	240±40	280±50	70±3	−0.42±0.01	0.52±0.01
30	240±9	17.999±0.002	10.7±0.3	1000±30	800±50	86±5	−0.3±0.4	0.98±0.02
40	230±10	17.0±0.4	11.3±0.3	270±30	250±40	75±6	−0.1±0.4	0.2±0.1
50	230±10	16.1±0.6	10.7±0.2	500±80	410±70	74±7	−0.06±0.05	0.21±0.08
60	224±1	15.52±0.03	10.246±0.004	920±50	710±40	67.5±0.5	−0.09±0.03	0.11±0.05
70	231.1±0.6	17.9±0.2	10.44±0.05	1300±60	1040±60	82.2±0.8	−0.462±0.009	0.81±0.09
80	234±1	18.00±0.06	10.47±0.08	510±20	430±20	83.3±0.8	−1.0±0.5	0.4±0.1
90	240±10	18.000±0.005	10.7±0.2	510±40	430±50	85±4	−0.9±0.3	0.2±0.2

C_R (mM)	a_b (Å^2)	δ_b (Å)	$R_{1,b}$ (Å)	$n_{W,b}$	d (Å)	g_d	N_d
10	54±9	7.8±0.5	9±1	0±2	37±3	0.0513±0.0001	50±30
20	69.4±0.5	6.1±0.2	7.1±0.2	0.0±0.5	26.4±0.9	0.05±0.03	3.5±0.9
30	66±1	6.8±0.2	7.3±0.2	0.8±0.5	28.4±0.8	0.020±0.003	0±30
40	63±3	6.8±0.4	7.7±0.4	0±1	34±1	0.10±0.04	40±4
50	63.2±0.9	6.8±0.5	7.8±0.2	0.0±0.9	34±1	0.10±0.04	40±20
60	60.8±0.2	7.0±0.2	7.28±0.04	0.0±0.4	32.1±0.7	0.00±0.02	38±2
70	64±1	6.6±0.2	6.8±0.2	0.05±0.02	30.7±0.3	0.09±0.01	20±10
80	69.96±0.03	6.0±0.3	6.0±0.1	0.0±0.6	27.9±0.5	0.066±0.006	50±20
90	70±2	6.1±0.2	6.1±0.2	0.02±0.02	27±2	0.10±0.04	40±20

Table 7.41: Fitting parameters with the model of mixtures of interacting spherocylinders and stacked bilayers related to the curves shown in the panel #37: ϕ_O=0.0050, T=10°C, [NaCl]=460 mM, [$CaCl_2$]=0 mM, [$MgSO_4$]=0 mM.

C_R (mM)	F	W	Z	p	q	R	T
10	0.558±0.005	0.19±0.07	1.00±0.02	0.0007±0.0003	0.98±0.05	–	–
20	0.73±0.04	0.67±0.02	1.000±0.008	0.0000±0.0002	0.97±0.08	–	–
30	0.512±0.006	0.91±0.03	0.8±0.1	0.000002±0.000003	0.63±0.04	–	–
40	0.71±0.04	0.84±0.04	1.00±0.06	0.00010±0.00004	0.7±0.1	–	–
50	0.89±0.06	0.99±0.04	–	0.00033±0.00004	1.00±0.09	–	–
60	0.75±0.02	0.945±0.006	0.9±0.1	0.00008±0.00003	0.98±0.08	–	–
70	0.667±0.008	0.96±0.02	0.79±0.05	0.00001±0.00004	1.0±0.1	–	–
80	0.8±0.1	0.95±0.02	0.96±0.05	0.0001±0.0002	0.6±0.3	–	–
90	0.74±0.05	0.91±0.01	0.93±0.06	0.0001±0.0001	0.71±0.06	–	–

C_R (mM)	a_{sc} (Å^2)	δ_{sc} (Å)	$R_{1,sc}$ (Å)	L (Å)	N_{agg}	$n_{W,sc}$	z q_e	J RT
10	130±10	17±2	20.2±0.9	38±7	200±30	39±9	−0.23±0.07	0.95±0.06
20	128±6	9.3±0.2	16.5±0.2	22±4	93±9	16.0±0.7	−0.18±0.02	0.3±0.4
30	127±4	8.3±0.4	16.05±0.06	22.1±0.9	85±3	13±2	−0.16±0.03	0.2±0.2
40	124±3	8.6±0.2	16.23±0.05	23±1	91±3	13±1	−0.27±0.03	0.00±0.08
50	126±2	8.45±0.06	16.11±0.09	21.7±0.5	87±1	12.9±0.4	−0.07±0.01	0.99±0.01
60	121±3	8.3±0.2	16.2±0.1	22.3±0.7	91±2	11±1	−0.16±0.04	0.05±0.02
70	122±1	8.1±0.2	16.19±0.07	21.9±0.8	88±2	11.4±0.7	−0.20±0.02	0.02±0.01
80	140±20	9.9±0.6	15.6±0.4	22.0±0.8	82±7	20±6	−0.24±0.09	0.00±0.03
90	129±1	8.98±0.07	16.1±0.1	22.5±0.4	88.6±0.6	14.9±0.3	−0.16±0.02	0.03±0.01

C_R (mM)	a_b (Å^2)	δ_b (Å)	$R_{1,b}$ (Å)	$n_{W,b}$	d (Å)	g_d	N_d
10	61.3±0.4	13.8±0.2	8.4±0.8	15.5±0.6	49±1	0.04±0.01	50±4
20	58±3	14.6±0.4	7.0±0.2	15±2	46±1	0.09±0.04	2.1±0.2
30	69.1±0.4	21±1	5.96±0.03	38±4	57±3	0.10±0.01	0±20
40	59±3	9.0±0.7	6.9±0.4	4±2	32.1±0.6	0.05±0.01	36±2
50	55±2	11±2	7.6±0.3	6±4	–	–	–
60	69±1	19±2	5.77±0.08	33±4	54±3	0.100±0.001	35±1
70	70.0±0.1	19±2	5.78±0.02	33±5	55±5	0.10±0.01	28.6±0.2
80	69.8±0.1	21±2	5.7±0.1	36±5	58±2	0.053±0.003	16±9
90	51±4	8±1	8.0±0.5	0±3	37±2	0.09±0.04	49.8±0.7

Table 7.42: Fitting parameters with the model of mixtures of interacting spherocylinders and stacked bilayers related to the curves shown in the panel #38: ϕ_O=0.5000, T=10°C, [NaCl]=0 mM, [$CaCl_2$]=0 mM, [$MgSO_4$]=0 mM.

C_R (mM)	F	W	Z	p	q	R	T
10	0.89±0.05	0.57±0.03	0.57±0.02	0.0012±0.0001	0.524±0.009	0.77±0.05	0.5075±0.0006
20	0.93±0.03	0.36±0.04	0.9±0.1	0.0007±0.0001	0.57±0.02	0.2±0.1	0.99±0.04
30	0.86±0.03	0.54±0.01	0.42±0.08	0.0016±0.0001	0.1±0.5	0.10±0.02	0.86±0.03
40	0.60±0.03	0.42±0.03	0.997±0.009	0.0009±0.0001	0.54±0.02	0.999±0.007	1.00±0.01
50	0.55±0.03	0.44±0.02	0.984±0.008	0.00088±0.00004	0.9±0.1	1.00±0.05	1.00±0.03
60	0.73±0.03	0.40±0.05	0.97±0.06	0.0010±0.0001	0.50±0.02	1.0±0.1	1.00±0.05
70	0.62±0.02	0.48±0.02	0.96±0.05	0.0011±0.0002	0.512±0.009	0.977±0.005	0.95±0.02
80	0.46±0.05	0.565±0.006	0.97±0.01	0.0009±0.0003	0.92±0.06	0.05±0.03	0.95±0.03
90	0.68±0.08	0.513±0.006	0.92±0.08	0.0010±0.0003	0.53±0.01	0.97±0.05	1.00±0.06

C_R (mM)	a_{sc} (Å^2)	δ_{sc} (Å)	$R_{1,sc}$ (Å)	L (Å)	N_{agg}	$n_{W,sc}$	z q_e	J RT
10	117±7	16.8±0.7	27.2±0.7	27±4	270±30	29±4	−0.33±0.06	0.3±0.1
20	112±6	18.00±0.01	26.6±0.8	26±3	290±40	31±2	−0.61±0.05	0.85±0.02
30	121±9	17.5±0.4	24.3±0.5	52±5	290±20	39±4	−0.6±0.1	0.3±0.3
40	116±4	18.0±0.2	25.0±0.5	31.5±0.9	270±10	33±2	−0.29±0.06	0.99±0.02
50	133±1	18.0±0.1	22.7±0.2	28.2±0.7	212±3	39.7±0.7	−0.44±0.02	0.76±0.06
60	150±10	18.0±0.2	21.6±0.3	27±4	180±20	47±4	−0.39±0.09	0.52±0.01
70	162±2	18.00±0.02	20.5±0.4	26±2	153±3	51.3±0.8	−0.34±0.03	0.78±0.09
80	163±5	17.8±0.1	20.11±0.08	25±3	147±7	52±2	−0.41±0.01	0.27±0.09
90	180±2	16.2±0.2	18.6±0.3	21.1±0.4	110±3	52±1	−0.7±0.1	0.6±0.3

C_R (mM)	a_b (Å^2)	δ_b (Å)	$R_{1,b}$ (Å)	$n_{W,b}$	d (Å)	g_d	N_d
10	65.5±0.5	13.72±0.03	8.4±0.1	14.3±0.5	47±1	0.081±0.002	2.5±0.2
20	68.3±0.7	16.4±0.8	7.07±0.05	23±2	49±1	0.072±0.005	2.3±0.1
30	52±2	8.1±0.2	8.7±0.4	0.0±0.2	38.46±0.08	0.095±0.003	3.5±0.5
40	63.1±0.5	16.7±0.8	7.42±0.05	21±2	52.67±0.07	0.00±0.03	50±1
50	54±2	10±1	8.7±0.3	4±2	43±3	0.056±0.002	0±10
60	51.1±0.5	9.0±0.4	9.0±0.2	1.3±0.6	41.0±0.6	0.10±0.02	5±2
70	50±3	9.4±0.5	9.2±0.6	2±2	40.1±0.7	0.100±0.009	5±1
80	50.1±0.4	8.5±0.2	9.2±0.2	0.1±0.4	39.9±0.5	0.10±0.03	6±6
90	55±3	7.7±0.6	8.3±0.3	0±2	35±1	0.097±0.005	5±7

Table 7.43: Fitting parameters with the model of mixtures of interacting spherocylinders and stacked bilayers related to the curves shown in the panel #39: ϕ_O=0.5000, T=10°C, [NaCl]=46 mM, [$CaCl_2$]=1 mM, [$MgSO_4$]=6 mM.

C_R (mM)	F	W	Z	p	q	R	T
10	1.00±0.05	0.514±0.007	0.73±0.07	0.0014±0.0005	1.0±0.2	0.05±0.04	0.0±0.2
20	0.9999±0.0004	0.346±0.005	0.73±0.01	0.00296±0.00005	1.0000±0.0008	0.20±0.04	0.85±0.02
40	1.00±0.01	0.538±0.008	0.974±0.009	0.00071±0.00006	0.93±0.03	0.72±0.04	0.745±0.003
50	0.99980±0.00002	0.314±0.001	0.81±0.01	0.00091±0.00002	0.99852±0.00008	0.72±0.01	0.586±0.002
60	0.993±0.005	0.39±0.04	0.57±0.05	0.0003±0.0001	0.88±0.06	0.5019±0.0004	0.68±0.02
70	0.998±0.001	0.499±0.005	0.70±0.02	0.000019±0.000009	0.94±0.02	0.66±0.05	0.63±0.01
80	0.997±0.003	0.310±0.009	0.709±0.009	0.00049±0.00003	0.99±0.02	0.38±0.06	0.87±0.04
90	1.0000±0.0003	0.346±0.008	0.70±0.04	0.00056±0.00004	1.00±0.01	0.40±0.04	0.87±0.04

C_R (mM)	a_{sc} (Å^2)	δ_{sc} (Å)	$R_{1,sc}$ (Å)	L (Å)	N_{aggs}	$n_{W,sc}$	z q_e	J RT
10	200±10	11.8±0.5	11.8±0.4	100±20	110±20	43±3	−0.09±0.06	0.6±0.2
20	242±3	12.10±0.05	16.52±0.08	0.3±0.2	42.7±0.8	53.5±0.9	−0.312±0.002	0.00006±0.00008
40	126±3	18.00±0.01	23.1±0.2	27±2	224±9	33.3±0.7	−0.490±0.005	0.74±0.03
50	193.81±0.05	11.155±0.002	9.948±0.001	1740±3	1219±2	39.24±0.02	−0.612±0.003	0.948±0.002
60	218±7	10.2±0.7	10.4±0.2	84±4	74±2	37±4	−0.13±0.05	0.96±0.02
70	228±2	8.87±0.09	9.42±0.01	89.0±0.5	63.2±0.3	33.3±0.7	−0.44±0.06	0.91±0.04
80	197.2±0.4	10.653±0.006	9.67±0.01	1699±3	1126±4	38.3±0.2	−0.83±0.05	0.4±0.1
90	187±1	10.04±0.07	9.99±0.07	633±5	452±5	33.4±0.2	−0.27±0.04	0.536±0.006

C_R (mM)	a_b (Å^2)	δ_b (Å)	$R_{1,b}$ (Å)	$n_{W,b}$	d (Å)	g_d	N_d
10	60±4	25.0±0.1	11.4±0.7	38±4	73±3	0.100±0.005	2.5±0.2
20	50.0003±0.0002	25.000±0.002	13.97±0.08	30.64±0.04	82.9±0.1	0.0950±0.0006	2.02±0.09
40	50.019±0.009	8.6±0.3	9.17±0.09	0.1±0.4	40.1±0.3	0.056±0.003	50±3
50	50.000±0.003	25.000±0.005	9.55±0.02	28.010±0.005	70.6±0.4	0.0597±0.0002	2.0±0.2
60	50.02±0.01	24.9999±0.0001	9.12±0.07	27.17±0.05	69.8±0.5	0.1000±0.0006	2.4±0.1
70	50.04±0.02	24.992±0.004	8.9606±0.0002	27.21±0.03	69.7±0.3	0.088±0.006	2.5±0.1
80	50.00±0.01	25.0000±0.0003	9.13±0.02	28.32±0.08	69.7±0.1	0.097±0.001	2.05±0.09
90	50.0012±0.0005	24.9994±0.0003	9.17±0.02	28.6±0.1	68.7±0.3	0.10±0.03	2.47±0.02

Table 7.44: Fitting parameters with the model of mixtures of interacting spherocylinders and stacked bilayers related to the curves shown in the panel #40: ϕ_O=0.5000, T=10°C, [NaCl]=92 mM, [$CaCl_2$]=2 mM, [$MgSO_4$]=11 mM.

C_R (mM)	F	W	Z	p	q	R	T
10	0.97±0.01	0.62±0.04	0.81±0.09	0.0018±0.0002	0.97±0.01	0.10±0.02	0.34±0.05
30	0.997±0.003	0.29±0.03	0.78±0.03	0.0010±0.0001	0.92±0.02	0.12±0.04	0.37±0.06
40	1.000±0.002	0.561±0.006	0.794±0.009	0.00004±0.00002	1.00±0.02	0.15±0.02	0.504±0.002
50	0.97±0.04	0.62±0.01	0.79±0.01	0.00002±0.00001	0.0±0.3	0.11±0.01	0.60±0.06
60	0.981±0.009	0.37±0.02	0.994±0.005	0.0043±0.0002	0.909±0.004	0.745±0.004	0.71±0.02
70	0.983717±0.000005	0.33833±0.00003	0.87±0.01	0.0007472±0.0000001	0.989191±0.000002	0.231121±0.000003	0.288402±0.000003
80	0.49±0.04	0.49±0.02	0.975±0.005	0.00256±0.00007	0.89±0.09	0.87±0.01	0.61±0.02
90	0.992±0.004	0.19±0.01	0.878±0.009	0.00134±0.00001	0.997±0.001	0.31±0.03	0.32±0.07

C_R (mM)	a_{sc} (Å^2)	δ_{sc} (Å)	$R_{1,sc}$ (Å)	L (Å)	N_{aggs}	$n_{W,sc}$	z q_e	J RT
10	219±2	12.7±0.2	11.4±0.4	100±20	100±10	49±2	−0.12±0.03	0.605±0.009
30	289±3	15.9±0.5	8.7±0.1	1400±500	800±300	90±4	−0.02±0.04	0.992±0.003
40	211±4	6.0±0.1	10.9±0.1	14±1	24.3±0.5	16.6±0.8	−0.32±0.05	0.999±0.003
50	202.5±0.2	5.0±0.6	12±2	0±20	18±7	11±3	−0.5±0.2	0.63±0.03
60	106.1±0.7	17.5±0.2	17.77±0.03	1240±20	2740±50	30.4±0.9	−0.97±0.04	0.76±0.02
70	294.961±0.002	11.518700±0.000001	9.9050±0.0006	33.79±0.01	34.975±0.003	56.722±0.001	−0.348108±0.000002	0.637163±0.000008
80	130.5±0.9	15.5±0.3	21.67±0.06	27±1	181±5	30.7±0.7	−0.98±0.03	0.93±0.03
90	291±1	13.9±0.2	8.25±0.06	560±50	290±20	77.0±0.8	−0.313±0.004	0.566±0.002

C_R (mM)	a_b (Å^2)	δ_b (Å)	$R_{1,b}$ (Å)	$n_{W,b}$	d (Å)	g_d	N_d
10	62.0±0.9	25.00±0.02	11.9±0.8	38±1	74±4	0.094±0.003	2.4±0.7
30	61.06±0.09	24.6±0.2	7.9±0.1	36.5±0.3	65.0±0.4	0.068±0.003	2.50±0.09
40	50.0008±0.0004	24.99997±0.00004	9.00±0.02	27.6±0.1	71.2±0.3	0.087±0.008	2.5±0.2
50	53±1	19.2±0.8	7.8±0.2	20±2	56.0±0.5	0.09±0.03	2.4±0.2
60	66.2±0.3	8.6±0.1	8.4±0.1	4.6±0.3	36.7±0.2	0.0631±0.0007	39±3
70	53.2311±0.0008	20.6±0.2	8.0948±0.0002	22.0±0.4	61.2±0.4	0.085533±0.000002	2.5566±0.0002
80	50.03±0.06	9.24±0.08	9.9±0.1	1.2±0.1	38.28±0.06	0.02±0.02	25±1
90	60.7±0.2	21.6±0.1	7.364±0.002	29.8±0.2	57.9±0.3	0.100±0.003	3.2±0.2

Table 7.45: Fitting parameters with the model of mixtures of interacting spherocylinders and stacked bilayers related to the curves shown in the panel #41: ϕ_O=0.5000, T=10°C, [NaCl]=229 mM, [$CaCl_2$]=5 mM, [$MgSO_4$]=28 mM.

C_R (mM)	F	W	Z	p	q	R	T
10	0.999±0.006	0.83±0.02	0.99±0.01	0.0037±0.0001	0.962±0.005	0.13±0.01	0.4±0.1
20	1.0±0.1	0.504±0.004	1.00±0.01	0.0025±0.0002	0.24±0.09	0.55±0.09	0.795±0.007
30	1.00±0.07	0.58±0.02	0.90±0.02	0.0046±0.0004	0.92±0.04	0.28±0.04	0.66±0.02
40	0.74±0.07	0.56±0.02	0.83±0.04	0.0043±0.0001	0.76±0.04	0.48±0.05	0.77±0.03
50	1.00±0.04	0.63±0.02	0.87±0.05	0.0040±0.0004	0.89±0.03	0.32±0.04	0.57±0.03
60	1.00±0.08	0.58±0.04	1.00±0.09	0.0040±0.0003	0.998±0.002	0.27±0.03	0.54±0.01
70	1.000±0.001	0.71±0.03	0.84±0.02	0.00478±0.00007	0.93±0.02	0.50±0.04	0.60±0.01
80	0.74±0.08	0.738±0.004	0.3±0.1	0.0038±0.0002	0.90±0.04	0.50±0.02	0.56±0.01
90	0.94±0.03	0.69±0.01	0.82±0.04	0.0041±0.0002	0.99±0.02	0.53±0.01	0.62±0.02

C_R (mM)	a_{sc} (Å^2)	δ_{sc} (Å)	$R_{1,sc}$ (Å)	L (Å)	N_{aggs}	$n_{W,sc}$	z q_n	J RT
10	285.6±0.5	17.80±0.05	18.74±0.05	0.01±0.02	58.7±0.4	83±1	−0.20±0.08	0.98±0.02
20	295±10	5.2±0.4	22.0±0.2	21.8±0.6	19±1	190±10	−0.0±0.5	0.58±0.08
30	300±6	5.1±0.1	14.9±0.2	12.2±0.5	11.6±0.4	116±6	−0.1±0.4	0.8±0.1
40	280±10	5.4±0.3	15.9±0.1	12.2±0.8	15±2	110±10	−0.1±0.1	0.89±0.04
50	300±20	5.1±0.4	14.1±0.2	10.7±0.7	11±2	100±10	−0.6±0.2	0.2±0.4
60	300±2	5.1±0.4	14.6±0.2	12.2±0.3	11±1	119±1	−0.5±0.3	0.70±0.03
70	300.0±0.2	5.0±0.1	14.37±0.05	11.7±0.1	11.0±0.3	108±2	−0.00±0.05	0.526±0.006
80	299.7±0.8	5.01±0.09	13.7±0.3	10.1±0.7	10.6±0.2	96±8	−0.8±0.3	0.738±0.007
90	296±2	5.01±0.02	14.69±0.04	12.42±0.07	11.3±0.1	117±2	−0.04±0.04	0.60±0.02

C_R (mM)	a_b (Å^2)	δ_b (Å)	$R_{1,b}$ (Å)	$n_{W,b}$	d (Å)	g_d	N_d
10	46.1±0.2	11.2±0.7	22.7±0.4	3±1	72.7±0.6	0.10±0.03	33±3
20	60±5	13±1	8±1	12±4	46±1	0.05±0.04	10±20
30	39±2	17.6±0.9	17.2±0.8	9±2	74.6±0.8	0.1000±0.0003	2.7±0.4
40	31.2±0.4	14.9±0.1	18.64±0.07	1.3±0.4	72.1±0.4	0.1000±0.0008	2.2±0.3
50	31.2±0.7	13.8±0.3	18.0±0.2	0.1±0.2	64±3	0.091±0.004	2.2±0.2
60	30.7±0.2	16.2±0.4	17.6±0.2	2.6±0.5	68±2	0.100±0.002	2.1±0.2
70	32.4±0.6	19.2±0.5	16.7±0.3	6.6±0.8	77±1	0.095±0.002	3.4±0.5
80	34±1	15.5±0.7	15.1±0.6	3±1	64.5±0.5	0.10±0.01	2.2±0.1
90	29.8±0.8	18.4±0.6	16.9±0.3	4±1	74±1	0.095±0.002	2.5±0.5

Table 7.46: Fitting parameters with the model of mixtures of interacting spherocylinders and stacked bilayers related to the curves shown in the panel #42: ϕ_O=0.5000, T=10°C, [NaCl]=460 mM, [$CaCl_2$]=0 mM, [$MgSO_4$]=0 mM.

Chapter 8

Conclusion and future insights

The idea of studying a class of biosurfactants was born from a collaboration already started for years with Prof. Rosangela Itri of the University of São Paulo in Brazil and the group of Molecular Biophysics at DiSVA. From this collaboration, the main issue that has inspired my PhD work emerged: the environmental impact that hydrocarbon contaminants have in water and soil, damaging not only the environment but also the micro-organisms and the fauna involved.

One of the main problems that limits the availability of biosurfactants is their production and purification, which are not the research skills of the group of Molecular Biophysics at DiSVA. Hence, we have decided to investigate with biophysical methods the properties of a commercial biosurfactant, the rhamnolipid.

Rhamnolipids can be widely applied in many industries including petroleum, food, agriculture and bioremediation etc. *Pseudomonas aeruginosa* is still the most competent producer of rhamnolipids, but its pathogenicity may cause safety and health concerns during large-scale production and applications. Therefore, extensive studies have been carried out to explore safe and economical methods to produce rhamnolipids. Various metabolic engineering efforts have also been applied to either *P. aeruginosa* for improving its rhamnolipid production and diminishing its pathogenicity, or to other non-pathogenic strains by introducing the key genes for safe production of rhamnolipids. The three key enzymes for rhamnolipid biosynthesis, RhlA, RhlB and RhlC, are found almost exclusively in *Pseudomonas* sp. and *Burkholderia* sp., but have been successfully expressed in several non-pathogenic host bacteria to produce rhamnolipids in large scales. The composition of mono- and di-rhamnolipids can also be modified through altering the expression levels of RhlB and RhlC. In addition, cell-free rhamnolipid synthesis by using the key enzymes and precursors from non-pathogenic sources is thought to not only eliminate pathogenic effects and simplify the downstream purification processes, but also to circumvent the complexity of quorum sensing system that regulates rhamnolipid biosynthesis. The pathogenicity of *P. aeruginosa* can also be reduced or eliminated through in vivo or in vitro enzymatic degradation of the toxins such as pyocyanin during rhamnolipid production. The rhamnolipid production cost can also be significantly reduced if

rhamnolipid purification step can be bypassed, such as utilizing the fermentation broth or the rhamnolipid-producing strains directly in the industrial applications of rhamnolipids.

The toxicity tests we have conducted in this work were aimed to determine the possible environmental impact that these surfactants have if they were used for bioremediation processes as well as for possible applications in medicine. Preliminary tests have been carried out that should in future be completed with an analysis of the possible effect that the use of rhamnolipid can have on microorganisms, soil and waters. Treating different concentrations of rhamnolipid with GUVs, we have found that, when the concentrations of RLs is higher than the CMC value, morphological changes of GUV occur (budding formation, fission), while if the interaction occurs with the erythrocytes, RLs above CMC provoke haemolysis.
A similar effect has been revealed when RLs interact with the keratocinotic cells of the skin: results show that the cellular viability reaches 50% at a RLs concentration few times higher than the CMC.

The X-ray diffraction experiments have allowed understanding the general organization of high concentration of RLs at dispersed in water. Under these conditions, RLs are organized in a lamellar phase which is slowly lost as soon as more water concentrations are reached. In fact, through the SAXS technique we have obtained that, in diluted conditions, RLs are organized into a structure that can be traced back to the geometric model of the spherocylinder. SAXS results have allowed to measure the shape and size of spherocylinders and their variations at different concentrations of oil. We have also analysed with SAXS RLs in brackish water. The presence of salts seems to have an influence on the structural organization of the rhamnolipids. In fact, next to the geometric model of the spherocylinder, these are organized again in contiguous lamellar phases.

Future experiments could be devoted to analysing the behaviour of rhamnolipids in sea water, where the concentration of salts is high. Moreover, toxic effects of RLs on the micro-organisms present in contaminated sites can be envisaged. In this regard, it would be necessary to analyse the RLs biodegradability after their application for removing heavy hydrocarbons from contaminated sites.

The present study has integrated knowledges and techniques in the fields of Physics, Chemistry, Biology as well as Biophysics. Beside, it is necessary not only to go deeply inside in the nature of RLs, but also to produce them possibly at low cost. Their application requires personnels skilled in several disciplines

and technologies. We are only at the beginning, but we have already clear ideas on how to proceed step by step toward a better environmental protection from hydrocarbons contamination.

BIBLIOGRAPHY

A. GUINIER, G. F. (n.d.). Small-angle scattering of X-rays - André Guinier, Gérard Fournet - 1955. Retrieved October 3, 2018, from https://books.google.it/books/about/Small_angle_scattering_of_X_rays.html?id=5zRRAAAAMAAJ&redir_esc=y

Akashi, K., Miyata, H., Itoh, H., Kinosita, K., & Jr. (1996). Preparation of giant liposomes in physiological conditions and their characterization under an optical microscope. *Biophysical Journal*, *71*(6), 3242–3250. https://doi.org/10.1016/S0006-3495(96)79517-6

Akbarzadeh, A., Rezaei-Sadabady, R., Davaran, S., Joo, S. W., Zarghami, N., Hanifehpour, Y., … Nejati-Koshki, K. (2013). Liposome: classification, preparation, and applications. *Nanoscale Research Letters*, *8*(1), 102. https://doi.org/10.1186/1556-276X-8-102

Angelova, M. I., & Dimitrov, D. S. (1986). Liposome electroformation. *Faraday Discussions of the Chemical Society*, *81*(0), 303. https://doi.org/10.1039/dc9868100303

Angelova, M. I., Soléau, S., Méléard, P., Faucon, F., & Bothorel, P. (1992). Preparation of giant vesicles by external AC electric fields. Kinetics and applications. In *Trends in Colloid and Interface Science VI* (pp. 127–131). Darmstadt: Steinkopff. https://doi.org/10.1007/BFb0116295

Baeurle, S. A., & Kroener, J. (2004). Modeling Effective Interactions of Micellar Aggregates of Ionic Surfactants with the Gauss-Core Potential. *Journal of Mathematical Chemistry*, *36*(4), 409–421. https://doi.org/10.1023/B:JOMC.0000044526.22457.bb

Barbosa, L. R. S., Ortore, M. G., Spinozzi, F., Mariani, P., Bernstorff, S., & Itri, R. (2010). The Importance of Protein-Protein Interactions on the pH-Induced Conformational Changes of Bovine Serum Albumin: A Small-Angle X-Ray Scattering Study. *Biophysical Journal*, *98*(1), 147–157. https://doi.org/10.1016/J.BPJ.2009.09.056

Baroni, A., Buommino, E., De Gregorio, V., Ruocco, E., Ruocco, V., & Wolf, R. (2012). Structure and function of the epidermis related to barrier properties. *Clinics in Dermatology*, *30*(3), 257–262. https://doi.org/10.1016/j.clindermatol.2011.08.007

Benincasa, M. (2007). Rhamnolipid Produced from Agroindustrial Wastes Enhances Hydrocarbon Biodegradation in Contaminated Soil. *Current Microbiology*, *54*(6), 445–

449. https://doi.org/10.1007/s00284-006-0610-8

Bernardino de la Serna, J., Perez-Gil, J., Simonsen, A. C., & Bagatolli, L. A. (2004). Cholesterol rules: direct observation of the coexistence of two fluid phases in native pulmonary surfactant membranes at physiological temperatures. *The Journal of Biological Chemistry*, *279*(39), 40715–40722. https://doi.org/10.1074/jbc.M404648200

Bezlyepkina, N., Gracià, R. S., Shchelokovskyy, P., Lipowsky, R., & Dimova, R. (2013). Phase diagram and tie-line determination for the ternary mixture DOPC/eSM/cholesterol. *Biophysical Journal*, *104*(7), 1456–1464. https://doi.org/10.1016/j.bpj.2013.02.024

Boukamp, P., Petrussevska, R. T., Breitkreutz, D., Hornung, J., Markham, A., & Fusenig, N. E. (1988a). Normal keratinization in a spontaneously immortalized aneuploid human keratinocyte cell line. *The Journal of Cell Biology*, *106*(3), 761–771. https://doi.org/10.1083/JCB.106.3.761

Boukamp, P., Petrussevska, R. T., Breitkreutz, D., Hornung, J., Markham, A., & Fusenig, N. E. (1988b). Normal keratinization in a spontaneously immortalized aneuploid human keratinocyte cell line. *The Journal of Cell Biology*, *106*(3), 761–771. https://doi.org/10.1083/JCB.106.3.761

Das, K., & Mukherjee, A. K. (2007). Crude petroleum-oil biodegradation efficiency of Bacillus subtilis and Pseudomonas aeruginosa strains isolated from a petroleum-oil contaminated soil from North-East India. *Bioresource Technology*, *98*(7), 1339–1345. https://doi.org/10.1016/J.BIORTECH.2006.05.032

De Cássia, R., Silva, F. S., Almeida, D. G., Rufino, R. D., Luna, J. M., Santos, V. A., & Sarubbo, L. A. (2014). Applications of Biosurfactants in the Petroleum Industry and the Remediation of Oil Spills. *OPEN ACCESS Int. J. Mol. Sci*, *15*, 15. https://doi.org/10.3390/ijms150712523

Desai, J. D., & Banat, I. M. (1997a). Microbial production of surfactants and their commercial potential. *Microbiol. Mol. Biol. Rev.*, *61*(1), 47–64. Retrieved from https://mmbr.asm.org/content/61/1/47.long

Desai, J. D., & Banat, I. M. (1997b). Microbial production of surfactants and their commercial potential. *Microbiology and Molecular Biology Reviews : MMBR*, *61*(1), 47–64. Retrieved from http://www.ncbi.nlm.nih.gov/pubmed/9106364

Deyrieux, A. F., & Wilson, V. G. (2007). In vitro culture conditions to study keratinocyte differentiation using the HaCaT cell line. *Cytotechnology*, *54*(2), 77–83. https://doi.org/10.1007/s10616-007-9076-1

Estes, D. J., & Mayer, M. (2005). Giant liposomes in physiological buffer using electroformation in a flow chamber. *Biochimica et Biophysica Acta (BBA) - Biomembranes*, *1712*(2), 152–160. https://doi.org/10.1016/J.BBAMEM.2005.03.012

Evans, D. F., & Wennerström, H. (1999). *The colloidal domain : where physics, chemistry, biology, and technology meet*. Wiley-VCH. Retrieved from https://www.wiley.com/en-us/The+Colloidal+Domain%3A+Where+Physics%2C+Chemistry%2C+Biology%2C+and+Technology+Meet%2C+2nd+Edition-p-9780471242475

Faraday, M. (1857). The Bakerian Lecture: Experimental Relations of Gold (and Other Metals) to Light. *Philosophical Transactions of the Royal Society of London*, *147*(0), 145–181. https://doi.org/10.1098/rstl.1857.0011

Frühwirth, T., Fritz, G., Freiberger, N., & Glatter, O. (2004). Structure and order in lamellar phases determined by small-angle scattering. *Journal of Applied Crystallography*, *37*(5), 703–710. https://doi.org/10.1107/S0021889804012956

Garach-Jehoshua, O., Ravid, A., Liberman, U. A., Reichrath, J., Glaser, T., & Koren, R. (1998). Upregulation of the calcium-dependent protease, calpain, during keratinocyte differentiation. *The British Journal of Dermatology*, *139*(6), 950–957. Retrieved from http://www.ncbi.nlm.nih.gov/pubmed/9990355

Gharaei-Fa, E. (2011). Biosurfactants in Pharmaceutical Industry (A Mini-Review). *American Journal of Drug Discovery and Development*, *1*(1), 58–69. https://doi.org/10.3923/ajdd.2011.58.69

Hänel, K., Cornelissen, C., Lüscher, B., Baron, J., Hänel, K. H., Cornelissen, C., … Baron, J. M. (2013). Cytokines and the Skin Barrier. *International Journal of Molecular Sciences*, *14*(4), 6720–6745. https://doi.org/10.3390/ijms14046720

Hartley, G. S., & Runnicles, D. F. (n.d.). The Determination of the Size of Paraffin-Chain Salt Micelles from Diffusion Measurements. *Proceedings of the Royal Society of London. Series A, Mathematical and Physical Sciences*. Royal Society. https://doi.org/10.2307/97274

Hishida, M., Seto, H., & Yoshikawa, K. (2005). Smooth/rough layering in liquid-crystalline/gel state of dry phospholipid film, in relation to its ability to generate giant vesicles. https://doi.org/10.1016/j.cplett.2005.06.045

Horger, K. S., Estes, D. J., Capone, R., & Mayer, M. (2009). Films of Agarose Enable Rapid Formation of Giant Liposomes in Solutions of Physiologic Ionic Strength. *Journal of the American Chemical Society*, *131*(5), 1810–1819. https://doi.org/10.1021/ja805625u

Husen, P., Arriaga, L. R., Monroy, F., Ipsen, J. H., & Bagatolli, L. A. (2012). Morphometric image analysis of giant vesicles: a new tool for quantitative thermodynamics studies of phase separation in lipid membranes. *Biophysical Journal*, *103*(11), 2304–2310. https://doi.org/10.1016/j.bpj.2012.10.031

I.D Robb. (n.d.). Specialist surfactants / edited by I.D. Robb. - Version details - Trove. Retrieved September 25, 2018, from https://trove.nla.gov.au/work/22866909?q&versionId=27733053

Karsa, D. R., Goode, J. M., & Donnelly, P. J. (1991). General Detergents. In *Surfactants Applications Directory* (pp. 37–60). Dordrecht: Springer Netherlands. https://doi.org/10.1007/978-94-011-3038-7_3

Keller, B. U., Hedrich, R., Vaz, W. L., & Criado, M. (1988). Single channel recordings of reconstituted ion channel proteins: an improved technique. *Pflugers Archiv : European Journal of Physiology*, *411*(1), 94–100. Retrieved from http://www.ncbi.nlm.nih.gov/pubmed/2451217

Krimm, S. (1980). The hydrophobic effect: Formation of micelles and biological membranes, Charles Tanford, Wiley-Interscience, New York, 1980, 233 pp. price: $18.50. *Journal of Polymer Science: Polymer Letters Edition*, *18*(10), 687–687. https://doi.org/10.1002/pol.1980.130181008

Makkar, R. S., & Rockne, K. J. (2003). COMPARISON OF SYNTHETIC SURFACTANTS AND BIOSURFACTANTS IN ENHANCING BIODEGRADATION OF POLYCYCLIC AROMATIC HYDROCARBONS. *Environmental Toxicology and Chemistry*, *22*(10), 2280. https://doi.org/10.1897/02-472

Manaargadoo-Catin, M., Ali-Cherif, A., Pougnas, J.-L., & Perrin, C. (2016). Hemolysis by surfactants--A review. *Advances in Colloid and Interface Science*, *228*, 1–16.

https://doi.org/10.1016/j.cis.2015.10.011

Martins, W. K., Severino, D., Souza, C., Stolf, B. S., & Baptista, M. S. (2013). Rapid screening of potential autophagic inductor agents using mammalian cell lines. *Biotechnology Journal*, *8*(6), 730–737. https://doi.org/10.1002/biot.201200306

Matsuoka, Tanaka, Hashimoto, & Ise. (1987). Elastic scattering from cubic lattice systems with paracrystalline distortion. *Physical Review. B, Condensed Matter*, *36*(3), 1754–1765. Retrieved from http://www.ncbi.nlm.nih.gov/pubmed/9943012

Micallef, L., Belaubre, F., Pinon, A., Jayat-Vignoles, C., Delage, C., Charveron, M., & Simon, A. (2009). Effects of extracellular calcium on the growth-differentiation switch in immortalized keratinocyte HaCaT cells compared with normal human keratinocytes. *Experimental Dermatology*, *18*(2), 143–151. https://doi.org/10.1111/j.1600-0625.2008.00775.x

Mohan, P. K., Nakhla, G., & Yanful, E. K. (2006). Biokinetics of biodegradation of surfactants under aerobic, anoxic and anaerobic conditions. *Water Research*, *40*(3), 533–540. https://doi.org/10.1016/J.WATRES.2005.11.030

Mulligan, C. N. (2005a). Environmental applications for biosurfactants. *Environmental Pollution*, *133*(2), 183–198. https://doi.org/10.1016/J.ENVPOL.2004.06.009

Mulligan, C. N. (2005b). Environmental applications for biosurfactants. *Environmental Pollution*, *133*(2), 183–198. https://doi.org/10.1016/J.ENVPOL.2004.06.009

Muñoz, S., Sebastián, J. L., Sancho, M., & Álvarez, G. (2014). Elastic energy of the discocyte–stomatocyte transformation. *Biochimica et Biophysica Acta (BBA) - Biomembranes*, *1838*(3), 950–956. https://doi.org/10.1016/J.BBAMEM.2013.10.020

Muthusamy, K., Gopalakrishnan, S., Ravi, T. K., & Sivachidambaram, P. (n.d.-a). Biosurfactants: Properties, commercial production and application. *Current Science*. Current Science Association. https://doi.org/10.2307/24100627

Muthusamy, K., Gopalakrishnan, S., Ravi, T. K., & Sivachidambaram, P. (n.d.-b). Biosurfactants: Properties, commercial production and application. *Current Science*. Current Science Association. https://doi.org/10.2307/24100627

naim kosaric. (n.d.). Biosurfactants and Their Application for Soil Bioremediation. Retrieved

September 26, 2018, from http://ftb.com.hr/archives/100-volume-39-issue-no-4/709-biosurfactants-and-their-application-for-soil-bioremediation

Ortore, M. G., Spinozzi, F., Mariani, P., Paciaroni, A., Barbosa, L. R. S., Amenitsch, H., … Russo, D. (2009). Combining structure and dynamics: non-denaturing high-pressure effect on lysozyme in solution. *Journal of the Royal Society, Interface*, *6 Suppl 5*(Suppl 5), S619-34. https://doi.org/10.1098/rsif.2009.0163.focus

Perfumo, A., Rancich, I., & Banat, I. M. (2010). Possibilities and challenges for biosurfactants use in petroleum industry. *Advances in Experimental Medicine and Biology*, *672*, 135–145. Retrieved from http://www.ncbi.nlm.nih.gov/pubmed/20545279

Rahman, P. K. S. M., & Gakpe, E. (2008). Production, Characterisation and Applications of Biosurfactants-Review. *Biotechnology(Faisalabad)*, *7*(2), 360–370. https://doi.org/10.3923/biotech.2008.360.370

Randhawa, K. K. S., & Rahman, P. K. S. M. (2014). Rhamnolipid biosurfactants—past, present, and future scenario of global market. *Frontiers in Microbiology*, *5*. https://doi.org/10.3389/FMICB.2014.00454

Reeves, J. P., & Dowben, R. M. (1969). Formation and properties of thin-walled phospholipid vesicles. *Journal of Cellular Physiology*, *73*(1), 49–60. https://doi.org/10.1002/jcp.1040730108

Rodrigues, L., Banat, I. M., Teixeira, J., & Oliveira, R. (2006). Biosurfactants: potential applications in medicine. *Journal of Antimicrobial Chemotherapy*, *57*(4), 609–618. https://doi.org/10.1093/jac/dkl024

Sánchez, M., Aranda, F. J., Teruel, J. A., Espuny, M. J., Marqués, A., Manresa, Á., & Ortiz, A. (2010). Permeabilization of biological and artificial membranes by a bacterial dirhamnolipid produced by Pseudomonas aeruginosa. *Journal of Colloid and Interface Science*, *341*(2), 240–247. https://doi.org/10.1016/J.JCIS.2009.09.042

Schindler, H. (1980). Introduction to Biological Membranes | A good chance missed, Mahendra Kumar Jain, Roger Curtis Wagner (Eds.), John Wiley and Sons, New York and Basel (1980), p. xiii + 382, 0 471 03471 1. *Trends in Neurosciences*, *3*(10), XXII. https://doi.org/10.1016/S0166-2236(80)80081-6

Schoop, V. M., Fusenig, N. E., & Mirancea, N. (1999). Epidermal Organization and

Differentiation of HaCaT Keratinocytes in Organotypic Coculture with Human Dermal Fibroblasts. *Journal of Investigative Dermatology*, *112*(3), 343–353. https://doi.org/10.1046/J.1523-1747.1999.00524.X

Schurer, N., Kohne, A., Schliep, V., Barlag, K., & Goerz, G. (1993). Lipid composition and synthesis of HaCaT cells, an immortalized human keratinocyte line, in comparison with normal human adult keratinocytes. *Experimental Dermatology*, *2*(4), 179–185. https://doi.org/10.1111/j.1600-0625.1993.tb00030.x

Sinibaldi, R., Ortore, M. G., Spinozzi, F., Carsughi, F., Frielinghaus, H., Cinelli, S., … Mariani, P. (2007). Preferential hydration of lysozyme in water/glycerol mixtures: A small-angle neutron scattering study. *The Journal of Chemical Physics*, *126*(23), 235101. https://doi.org/10.1063/1.2735620

Spinozzi, F., Ferrero, C., Ortore, M. G., De Maria Antolinos, A., & Mariani, P. (2014). GENFIT: software for the analysis of small-angle X-ray and neutron scattering data of macro-molecules in solution. *Journal of Applied Crystallography*, *47*(Pt 3), 1132–1139. https://doi.org/10.1107/S1600576714005147

Spinozzi, F., Mariani, P., & Ortore, M. G. (2016). Proteins in binary solvents. *Biophysical Reviews*, *8*(2), 87–106. https://doi.org/10.1007/s12551-016-0193-y

Spinozzi, F., Mariani, P., Paccamiccio, L., & Amaral, L. Q. (2010). New lamellar phase with pores in the chain-melting regime of an anionic phospholipid dispersion. *Journal of Physics: Conference Series*, *247*(1), 012019. https://doi.org/10.1088/1742-6596/247/1/012019

Spring KR, D. M. "Introduction to F. M. N. M. R. 2008-09-28. (n.d.). Bio-Rad ZOE™. Retrieved October 15, 2018, from https://www.zoe-bio-rad.com/?WT.mc_id=170125000405&WT.srch=1&WT.knsh_id=c8e4e229-c2bd-4a59-8aaa-57f39b39dfb9

Traudel, K., & Merten, S. (2017). Possible Food and Agricultural Application of Microbial Surfactants: An Assessment. In *Biosurfactants and Biotechnology* (pp. 183–210). Routledge. https://doi.org/10.1201/9781315138428-8

Vaz, W. L. C., Kapitza, H. G., Stuempel, J., Sackmann, E., & Jovin, T. M. (1981). Translational mobility of glycophorin in bilayer membranes of

dimyristoylphosphatidylcholine. *Biochemistry*, *20*(5), 1392–1396. https://doi.org/10.1021/bi00508a055

Walde, P., Cosentino, K., Engel, H., & Stano, P. (2010). Giant Vesicles: Preparations and Applications. *ChemBioChem*, *11*(7), 848–865. https://doi.org/10.1002/cbic.201000010

Zhang, F., Skoda, M. W. A., Jacobs, R. M. J., Martin, R. A., Martin, C. M., & Schreiber, F. (2007). Protein Interactions Studied by SAXS: Effect of Ionic Strength and Protein Concentration for BSA in Aqueous Solutions. *The Journal of Physical Chemistry B*, *111*(1), 251–259. https://doi.org/10.1021/jp0649955

Zhao, Z., Wang, Q., Wang, K., Brian, K., Liu, C., & Gu, Y. (2010). Study of the antifungal activity of Bacillus vallismortis ZZ185 in vitro and identification of its antifungal components. *Bioresource Technology*, *101*(1), 292–297. https://doi.org/10.1016/j.biortech.2009.07.071